Université catholique de Louvain
Louvain Drug Research Institute
Medicinal Chemistry Research Group

CONFIDENTIAL

Investigating the acyl-CoA synthetase long-chain family member 4 (ACSL4) inhibition and substrate specificity: a pathway to targeting ferroptosis-related diseases and cancer

Romain Marteau

Thesis director: Professor Raphaël Frédérick
Thesis Co-supervisor: Doctor Séverine Ravez

Thesis submitted in fulfillment of the requirements for a PhD degree in Biomedical and Pharmaceutical Sciences

Thesis director

Professor Raphaël Frédérick

Université catholique de Louvain, Belgium

Thesis co-supervisor

Doctor Séverine Ravez

Université de Lille, France

President of the Jury

Professor Giulio G. Muccioli

Université catholique de Louvain, Belgium

Jury members

Doctor Corinne Lionne

Centre de biologie structurale, France

Professor Trisha J. Grevengoed

University of Copenhagen, Denmark

Professor Oliver Feron

Université catholique de Louvain, Belgium

Professor Emmanuel Hermans

Université catholique de Louvain, Belgium

Acknowledgments

Au terme de cette palpitante aventure, je tiens à exprimer ma profonde gratitude envers vous tous qui m'avez accompagné, instruit, soutenu, nourri, diverti et rassuré, sans qui ce travail n'aurait jamais abouti.

Je souhaite tout particulièrement remercier les membres du jury, les professeurs Muccioli, Hermans et Feron qui ont suivi ce projet depuis ses débuts, ainsi que les professeures Lionne et Grevengoed, qui m'ont fait l'honneur d'accepter de participer en tant que membre externe. Merci pour votre temps, votre intérêt, la pertinence de vos questions, remarques et suggestions qui ont donné lieu à des échanges captivants, et enrichi ce travail de vos expertises respectives.

Je tiens à également à remercier le professeur Raphaël Frédérick d'avoir accepté d'être mon promoteur de mémoire d'abord puis de thèse. Vous avez ouvert votre porte à un étudiant moyen qui ne savait pas très bien où il allait et je ne suis pas sûr que j'aurais pris le même pari si j'avais été à votre place. L'atmosphère de liberté que vous cultivez au laboratoire constitue un terrain particulièrement fertile à la créativité et aux découvertes. La confiance que vous m'avez accordée tout au long de ce parcours a été un atout majeur. Je ne sais pas si elle trouve son origine dans ce match de ping-pong épique, où, ravitaillé par Séverine, je m'étais finalement imposé après une compétition acharnée. Quoi qu'il en soit, peu de temps après vous me proposiez une thèse dans une chambre obscure du sud de la France, en compagnie de personnes peu recommandables. Proposition que je rejetais d'abord…

Je remercie Séverine de tout mon cœur, pour avoir été le pilier de cette thèse et de ma formation de chercheur. Depuis le tout début, tu m'as enseigné ce qu'il y a de plus important en recherche expérimentale : la rigueur indispensable à l'obtention de résultats interprétables et à l'élaboration de conclusions solides. Et ce n'était pas gagné d'avance. Durant l'encadrement de mon mémoire puis en tant que directrice de thèse, tu m'as transmis ta passion pour les enzymes et ton amour des belles courbes. Tu as été un soutien inestimable face aux problèmes, bugs et autres obstacles qui sont les réels défis auxquels est confronté tout expérimentateur. Au travail, tu m'as toujours estimé, inclus, orienté subtilement et défendu quand il le fallait. Tu m'as accueilli chez toi des semaines durant pour venir manipuler en équipe sur les paillasses lilloises, ce qui m'a appris énormément de choses et fait avancer le projet considérablement. Bref, dans ces mers houleuses que sont les thèses au CMFA, tu étais le phare au loin. Mais tu es bien plus que cela. Tu es une amie précieuse avec qui j'ai eu la chance de partager des moments incroyables en dehors du travail et j'espère bien que ça continuera. Merci aussi à Chris, Gaston et maintenant Baptiste, pour leur hospitalité légendaire.

Merci Jamal de m'avoir accueilli au sein du projet Ferroptose, mais aussi pour ton regard critique, parfois difficile à entendre, mais toujours juste, et constructif. Réussir à te convaincre a toujours été pour moi un gage de solidité scientifique. Aux côtés de Séverine, tu formes un duo parfaitement complémentaire, et je suis convaincu que l'étude d'ACSL4 a encore de très belles années devant elle.

Dans un terreau aussi propice, le projet a vite suscité de l'engouement et l'équipe s'est développée jusqu'à devenir une jungle luxuriante, même si d'aucuns la qualifieraient plutôt de secte. Ce foisonnement d'apprentis

chercheurs a permis l'émergence de compétences pointues et complémentaires, accélérant les découvertes et créant de nouvelles branches à explorer. Un immense merci à toute la team Ferroptose : aux filles chimistes, Emeline, Juliette, Ilona et Karine, et aux garçons biochimistes, Alex, Darius et Noah. Travailler à vos côtés a toujours été un plaisir.

Je tiens aussi à remercier tout le CMFA, avec qui j'ai partagé les paillasses, les pipettes défectueuses, les corvées, les meetings intempestifs et toutes les autres joies inhérentes à la vie de laborantin. Merci à Alex, Alice, Ariana, Arina, Asia, Ben, Bouazza, Boubou, Caro, Chiara, Didier, Esra, Ferran, François, Giuditta, Juhans, Julien, Karine, Léo, Marie-Sophie, les Marines, Maxime, Perrine, Quentin et Séraphin. Le CMFA ce ne sont pas juste des « collègues », n'en déplaise à Séraphin, mais une sorte de famille un peu dégénérée. L'humour y est très potache et l'âge mental incroyablement jeune. Il ne serait pas étonnant d'y voir un étron artificiel être livré au bureau voisin par voiture téléguidée. On y fête tout ce qui peut être fêté, mange tout ce qui peut être mangé et le petit verre de fin de semaine a la fâcheuse tendance à finir en karaoké à quatre heures du matin. On y fait du sport aussi de temps en temps, entre le tournoi de foot annuel, les séances de badminton, d'escalade, de course à pied, les descentes de rivière sauvage… et des activités plus artistiques, bien que ce soit souvent très abstrait. En d'autres termes, on ne fait pas sa thèse au CMFA, on vit au CMFA pendant sa thèse.

Je me dois de remercier quelques spécimens en particulier.

Merci à Mar1, première du nom, d'avoir supporté mes espièglerie et ricanements de bureau même si tu as rapidement trouvé une parade : la nourriture. En nous nourrissant à intervalle régulier, tu ralentissais ainsi notre

débit d'âneries, nos bouches étant trop pleines pour communiquer efficacement. Aujourd'hui encore, alors que ta thèse est terminée depuis bientôt deux ans, tu continues à m'alimenter. Je ne suis pas tout à fait sûr de comprendre pourquoi… Tu as laissé à la postérité du labo une teinte inoubliable, le marron Marine (RVB 132-98-53), qui égaiera à jamais nos présentations. Avec le temps, tu t'es peu à peu désensibilisée à ces facéties, au point de me tolérer au quotidien. Merci de continuer inlassablement à me supporter, malgré ma transformation en ermite de cette dernière année.

Au cours de ma thèse, une nouvelle Marine, plus jeune, plus endurante et plus odorante a établi ses quartiers dans notre bureau : Mar2. Très vite, une coalition s'est formée avec la Marine préexistante, pour notre plus grand malheur à tous. Néanmoins, ton arrivée au labo a révélé en moi une vocation insoupçonnée de coach sportif. Merci pour tous ces kilomètres parcourus ensemble, et j'attends toujours de te voir à l'entrainement pour ce fameux triathlon olympique.

Merci à Darius, mon allié de toujours contre la tyrannie marine. Arrivé au CMFA pour ton mémoire au début de ma thèse, on m'a confié la lourde responsabilité de t'encadrer… mais en réalité, c'était plutôt un encadrement mutuel. On a appris et progressé ensemble. Tu as ensuite commencé une thèse et grâce à ta passion pour les échelles, tu as rapidement grimpé pour devenir un chercheur de haut niveau qui publie dans *Télé-Moustique*. J'ai pu partager avec toi mes plus grandes fiertés de thèse : ton apprentissage du sifflement pour devenir un vrai pinson ainsi que notre culture du patatier, donnant naissance à Mar3. Aujourd'hui, tu t'es reproduit scientifiquement et la descendance du projet Ferroptose au CMFA est assurée. Ça a été un réel bonheur de travailler avec toi pendant toutes ces années.

Merci Léo de m'avoir informé que l'université n'avait trouvé personne pour le poste d'assistant en chimie analytique et analyse instrumentale, ce qui a fortement influencé ma décision de candidater, étant donné ma nature résolument opportuniste. Comme l'a élégamment résumé Martin par la suite : « Bro, ils avaient le choix entre toi et une chaise vide ». Pourtant Léo, à peine étais-je arrivé au CMFA, que tu m'accusais de sabotage, allumant le feu d'une rivalité LDH-ACSL4 dont les braises rougeoient encore bien après ton départ. Sache toutefois que cette hostilité envers LDH s'est propagée au reste du labo et qu'on utilise désormais le label « qualité LDH » pour décrire toute entreprise dont l'organisation et la réalisation semblent approximatives.

Je tiens à exprimer ma profonde gratitude à l'éminent professeur Spillier, grand supervisioneur du CMFA, qui m'a transmis son goût prononcé pour les molécules bien carrées, bien symétriques. Merci à Séraphin de m'avoir malaxé de manière hebdomadaire pour m'aider à survivre cette dernière année, et merci à Julien de l'avoir fait de manière ponctuelle. Merci à Chiara d'accepter de faire des concours de cuisine italienne avec moi, alors que je ne suis ni italien, ni grand cuisinier. Merci à Esra d'avoir effectué mes commandes avec autant de diligence que de gentillesse, malgré le fait que je ne dise pas toujours bonjour. Merci à Arina de m'avoir fait l'honneur d'être son meilleur ennemi. Merci à Asia d'être heureuse de me voir resurgir de mon trou après des mois d'absence. Merci à Caro de perpétuellement veiller à la propreté des écuries d'Augias que sont les labos du CMFA. Merci à François d'avoir autant bichonné cette vieille bique d'HPLC-MS. Merci à Juhans d'être aussi beau. Merci à Perrine, ma pote rugbyman.

Être assistant, c'est aussi, à parts égales, enseigner et je tenais à remercier de tout cœur l'autre pilier de ma thèse, avec qui j'ai eu le plaisir de partager la

quasi-totalité de mes vendredis durant ces sept dernières années : Marie-France. Les TPs d'analyse du vendredi, ce sont des longues journées qui commencent à 8h avec le petit-déjeuner et finissent vers 17h après le goûter. Entre temps il y a la collation de 10h, le diner, le chocolat de 13h (avec le café) et l'encas de 15h. Heureusement ton énergie et ta bonne humeur nous ont toujours permis de voir le bout du jour. J'ai énormément appris sur le plan pratique à tes côtés : en vous observant, toi et Maude, démonter des pompes ou déboucher des injecteurs en urgence avant le petit-déjeuner… mais aussi siphonner des éviers d'étudiants prêts à déborder, ou réparer la seule imprimante compatible avec la machine de Turing connectée aux GC. J'ai également énormément appris sur le plan pédagogique en observant la subtilité du cocktail de rigueur scientifique, de sollicitude et d'autorité avec lequel tu accompagnes les étudiants. Tu réussis à instaurer une atmosphère de travail bienveillante et chaleureuse, qui rend ces longues journées de titrage bien plus agréables pour les étudiants et pour nous. J'espère que ces heureux moments à tes côtés ne seront pas les derniers, pour ne pas avoir à te faire *d'Impossibles adieux*.

Ces TPs, c'était avant tout un travail d'équipe, où il fallait sans cesse réapprendre les couleurs primaires à des enfants de 20 ans. Merci à toute l'équipe sans qui il aurait été impossible de ne pas mettre fin à ses jours au bout de deux heures. Merci à Maude d'avoir assuré d'une main de maître toute la partie technique nécessaire au bon déroulement des TPs. Merci à Justine d'avoir initié le processus de modernisation de l'encodage. Merci à Adam pour ses gros bras. Merci à la relève, Marie-Sophie et Eloïse d'être venu nous soulager cette dernière année. Merci à tous d'avoir accepté de faire les gros yeux à ma place pour me permettre de garder le bon rôle. Travailler

à vos côtés a toujours été un réel bonheur. Enfin, merci aux étudiants d'avoir été intéressés et indulgents.

Cette thèse je ne l'aurais probablement jamais faite sans feu mon colloc, Martin. Bro, c'est toi qui m'as poussé vers la recherche en master, puis qui as insisté pour que je continue en thèse, allant même jusqu'à m'accueillir en ton sein pour t'assurer que je n'abandonnerais pas en cours de route. En m'invectivant fréquemment de « flaque de pus » ou autres analogies fleuries, tu as su trouver les mots qui m'ont aidé à avancer. On a partagé bien plus qu'un appartement. On a plus ou moins le même travail, le même labo, les mêmes centres d'intérêts, le même morphotype, la même phobie des coiffeurs, et même plus ou moins les mêmes noms. Ça en a perturbé plus d'un, MF la première. Je dois dire que moi aussi il m'est parfois arrivé de douter… En emménageant chez toi je ne me doutais pas que j'allais avoir une deuxième colocataire. Merci Alice d'avoir focalisé sur toi une partie de l'attention malicieuse de Martin, et pour tous ces moments de bonheur partagés à trois, Avenue de Mai.

Enfin, je souhaite remercier ma famille pour m'avoir fait tomber dans la marmite scientifique quand j'étais petit, pour avoir toujours été là, pour m'avoir encouragé quoi que je fasse, pour son aide inestimable tout au long de cette thèse… et pour le cidre aussi.

Abbreviations

14:0	Myristate
16:0	Palmitate
16:1ω-7	Palmitoleate
17:0	Heptadecanoate
18:0	Stearate
18:1ω-9 (E)	Elaidate
18:1ω-9 (Z)	Oleate
18:2ω-6	Linoleate
18:3ω-3	α-linolenate
18:3ω-6	γ-linolenate
20:0	Arachidate
20:1ω-9	Ecosenoate
20:2ω-6	Eicosadienoate
20:3ω-6	Dihomo-γ-linolenate
20:3ω-9	Eicosatrienoate
20:4ω-6	Arachidonate
20:5ω-3	Eicosapentaenoate
22:1ω-9	Docosenoate
22:4ω-6	Adrenate
22:6ω-3	Docosahexaenoate
AA	Arachidonate

AA-CoA	Arachidonoyl-CoA
AdA	Adrenate
ACBP	Acyl-coa binding protein
ACC	Acyl-CoA carboxylase
ACN	Acetonitrile
ACOT2	Acyl-CoA thioesterase 2
ACP	Acyl-carrier protein
ACS	Acyl-CoA synthetase
ACSBG	Acyl-CoA synthetase bubblegum
ACSL	Acyl-CoA synthetase long chain family
ACSM	Acyl-CoA synthetase medium chain
ACSS	Acyl-CoA synthetase short chain
ACTH	Adrenocorticotropin
AD	Alzheimer's disease
AdA-CoA	Adrenoyl-CoA
ADME	Absorption, distribution, metabolism and excretion
AGPAT	Acylglycerol phosphate acyltransferase
AKT	Protein kinase B
ALOX	Arachidonate lipoxigenase
ALS	Amyothrophic lateral sclerosis
AMP	Adenosine monophosphate
ANL	Acyl-CoA/NRPS/Luciferase
ANOVA	Analysis of variance
ApCpp	α,β-methyleneadenosine-5'-triphosphate
$_{app}K_D$	Apparent dissociation constant

AR	Androgen receptor
ATP	Adenosine triphosphate
Aβ	Amyloid β
BC	Breast cancer
BODIPY	Bore-dipyrromethene
cAMP	Cyclic adenosine monophosphate
CARM1	Coactivator-associated arginine methyltransferase 1
cas9	Caspase 9
CD36	Cluster of differentiation 36
CD8	Cluster of differentiation 8
CDP	Cytidine-diphosphate
CE	Cholesteryl ester
CL	Cardiolipin
CoA	Coenzyme A
CoQ10	Coenzyme Q10
COX	Cyclooxygenase
CRC	Colorectal cancer
CRISPR	Clustered Regularly Interspaced Short Palindromic Repeats
CRPC	Castration-resistant prostate cancer
cryo-EM	Cryogenic electron microscopy
CYP	Cytochrome P450
D5D	Delta 5 desaturase
D6D	Delta 6 desaturase
DAG	Diacylglycerol

DGAT	Diacylglycerol acyltransferase
diHETE	Dihydroxy eicosatetraeboic acid
DMEM	Dulbecco modified Eagle's Medium
DMSO	Dimethylsulfoxide
DNA	Deoxyribonucleic acid
DPPH	2,2-Diphenyl 1-picrylhydrazyl
DSF	Differential scanning fluorimetry
DTT	Dithiothreitol
EC1	Enoyl-CoA isomerase 1
EC_{50}	Half maximal effective concentration
ECH1	Enoyl-CoA hydratase 1
ECO	Econazole
EDTA	Ethylenediaminetetraacetic acid
EET	Epoxy eicosatrienoic acid
ELOVL	Ketoacyl-CoA synthetase
EMT	Epithelial-to-mesenchymal transition
EPOX	Epoxygenase
ER	Endoplasmic reticulum
ER	Estrogen receptor
FA	Fatty acids
FABP	Fatty acid binding protein
FADH2	Flavin adenine dinucleotide
FAO	Mitochondrial β-oxidation
FAS	Fatty acid synthase
FATP	Fatty acid transport protein

FBDD	Fragment-based drug design
FDA	Food and drug agency
Fer-1	Ferrostatin-1
$FINO_2$	Endoperoxide ferroptosis inducer
FITC	Fluorescein isothiocyanate
FLUCO	Fluconazole
FSP1	Ferroptosis suppressor protein 1
Fsp^3	Fraction of sp^3 carbons
GDNF	Glial cell line-derived neurotrophic factor
GPAT	Glycerol-3-phosphate acyltransferase
GPCR	G protein–coupled receptors
GPL	Glycerophospholipid
GPX4	Glutathione peroxidase 4
GSH	Gluthatione
HCC	Hepatocellular carcinoma
HCHFD	High-cholesterol high-fat diet
HD	Huntington's disease
HDx-MS	Hydrogen-deuterium exchange mass spectrometry
HER2	Human epidermal growth factor receptor 2
HETE	Hydroxy eicosatetraenoic acid
HFD	High-fat diet
HpETE	Hydroperoxy eicosatetraenoic acid
HTT	Huntingtin
HUFA	Highly unsaturated fatty acid
IC_{50}	Half maximal inhibitory concentration

IPTG	Isopropyl-β-D thiogalactopyranoside
IR	Ischemia-reperfusion
IRI	Ischemia-reperfusion injury
ITC	Isothermal titration calorimetry
ITRA	Itraconazole
k_{cat}/K_m	Catalytic efficiency
K_D	Dissociation constant
K_m	Michaelis constant
KO	Knockout
LB	Lysogeny broth
LCFA	Long-chain fatty acid
LC-MS	Liquid chromatography - mass spectrometry
LC-MS/MS	Liquid chromatograpy - tandem mass spectrometry
LC-TRAP	Living-cell-target accessibility profiling
LD	Lipid droplet
LE	Ligand efficiency
LED	Light-emitting diode
LH	Luteinizing hormone
LHPP	Phospholysine phosphohistidine inorganic pyrophosphate phosphatase
LHUMES	Lund human mesencephalic
LogD	Distribution coefficient
LogP	Partition coefficient
LOX	Lipoxygenase
LPA	Lysophosphatidic acid

LPCAT3	Lysophosphatidylcholine acyltransferase 3
LPLAT	Lysophospholipid acyltransferase
LPS	Lipopolysaccharide
MAG	Monoacylglycerol
MAM	Mitochondria-associated membranes
MCFA	Medium-chain fatty acid
MD	Molecular dynamics
MESG	2-Amino-6-mercapto-7-methylpurine riboside
mHTT	Mutated huntingtin
MPP^+	1-Methyl-4-phenylpyridinium
MPTP	Methyl-4-phenyl-1,2,3,6-tetrahydropyridine
mRNA	Messenger ribonucleic acid
MST	Microscale thermophoresis
MUFA	Monounsaturated fatty acid
MW	Molecular weight
NAD	Nicotinamide adenine dinucleotide
NADH	Nicotinamide adenine dinucleotide
NADP	Nicotinamide adenine dinucleotide phosphate
NDD	Neurodegenerative disease
NEDD4	Neural precursor cell expressed developmentally down-regulated protein 4
NF-κB	Nuclear factor kappa-light-chain-enhancer of activated B cells
NMR	Nuclear magnetic resonnance
NRPS	Non-ribosomal peptide synthetase

NTA	Nitrilotriacetic acid
OC	Ovarian cancer
OD_{600}	Optical density at a wavelength of 600 nm
OGD	Oxygen-glucose deprivation
O-GlcNAc	*O*-linked β-*N*-acetylglucosamine
OH·	Hydroxyl radical
P450scc	Cholesterol side-chain cleavage enzyme
PA	Phosphatidic acid
PA-CoA	Palmitoyl-CoA
PAINS	Pan-assay interference motif
PAL	Photoaffinity labeling
PAP-1	Phosphatidate phosphatases 1
PBS	Phosphate buffer saline
PC	Phosphatidylcholine
PC	Prostate cancer
PCK2	Phosphoenol pyruvate carboxykinase 2
PCR	Polymerase chain reaction
PD	Parkinson's disease
PE	Phosphatidylethanolamine
PG	Phosphatidylglycerol
PG	Prostaglandin
pH	Potential of hydrogen
PI	Phosphatidylinositol
Pi	Orthophosphate
PI3K	Phosphoinositide 3-kinase

PIO	Pioglitazone
PKA	Protein kinase A
PKC	Protein kinase C
PL	Phospholipid
PLA	Phospholipase A
PLO·	Phospholipid alkoxyl radical
PLOO·	Phospholipid peroxyl radical
PLOOH	Phospholipid hydroperoxides
PM	Plasma membrane
PMA	Phorbol 12-myristate 13-acetate
PNP	Purine nucleoside phosphorylase
POR	Cytochrome P450 oxidoreductase
PPAR	Peroxisome proliferator-activated receptor
PPi	Inorganic pyrophosphate
PR	Progesterone receptor
PS	Phosphatidylserine
PTM	Post-translational modification
PUFA	Polyunsaturated fatty acid
QNBC	Quadruple-negative breast cancers
RBBP6	RB Binding Protein 6
rBFGF	Recombinant basic fibroblast growth factor
RCD	Regulated cell death
RNF25	Ring finger protein 25
ROS	Reactive oxigen species
ROSI	Rosiglitazone

rpm	Rotation per minute
RSL3	Oncogenic-RAS-selectively lethal
RTA	Radical trapping antioxidants
SAR	Structure-activity relationship
SCD	Stearoyl-CoA desaturase
SCFA	Short-chain fatty acid
SD	Standard deviation
SDS-PAGE	Sodium dodecyl sulfate polyacrylamide gel electrophoresis
SEM	Standard error of means
SENP1	Sentrin-specific protease 1
SERTA	Sertaconazole
SFA	Saturated fatty acid
SKP2	S-phase kinase-associated protein 2
SL	Sphingolipid
SLC27A	Solute carier family 27 family
SMC	Smooth muscle cell
SN	Substantia nigra
SOSA	Selective optimization of side activity
Sp1	Specificity protein 1
SPR	Surface plasmon resonance
SREBP1	Sterol regulatory element-binding protein 1
StAR	Steroidogenic acute regulatory protein
STD	Saturation transfer difference
SUMO	Small ubiquitin-like Modifier

$t_{1/2}$	Half-life
TAG	Triacylglycerol
TAM	Tamoxifen
TCA	Tricarboxylic acid cyle
T_m	Melting temperature
TNBC	Triple-negative breast cancers
TNM	Tumor-Node-Metastasis
TRIM9	Tripartite motif containing 9
Tris	Tris(hydroxymethyl)aminomethane
TRO	Troglitazone
TSA	Thermal shift assay
TSPO	Translocator protein
***tt*LC-FACS**	Thermus thermophilus fatty-acyl CoA synthetase
TZD	Thiazolidinedione
v_0	Initial velocity
VEGF	Vascular endothelial growth factor
VLCFA	Very long-chain fatty acid
V_{max}	Maximum initial velocity
YAP1	Yes-associated protein 1
β-ox	β-Oxidation
ΔT_m	Thermal shift
ω-ox	ω-Oxidation

Table of content

INTRODUCTION

1. Fatty acids

Fatty acids (FAs) are essential components of lipids, which, along with proteins, carbohydrates and nucleic acids, constitute the major classes of biological molecules (1). FAs fulfill diverse roles in living organisms. Their oxidation is highly exergonic, serving as a primary energy source for humans and contributing roughly 30% of total energy intake (2). FAs can be stored long-term as triacylglycerol (TAG) in adipose tissue and mobilized during energy deprivation. Additionally, as fundamental constituents of phospholipids (PLs), FAs form the structural backbone of cell membranes, playing a vital role in defining their properties and functions.

FAs consist of a carboxylate group with an aliphatic chain containing 2 to 40 carbon atoms (3), (4). They are categorized based on their carbon chain length, the number of double bonds, and their position. The classification based on FA chain length can vary slightly between studies (5). Here, we will consider that short-chain FAs (SCFAs) contain 2 to 6 carbon atoms, medium-chain FAs (MCFAs) range from 8 to 12 carbon atoms, long-chain FAs (LCFAs) span 14 to 22 carbon atoms, and very long-chain FAs (VLCFAs) have 24 or more carbon atoms. Most FAs contain an even number of carbon atoms, as their synthesis and degradation processes occur in two-carbon increments (2).

1.1. Long-chain fatty acids (LCFAs)

LCFAs are further classified into three primary groups based on the number of double bonds in their structures: saturated fatty acids (SFAs), which have no double bonds; monounsaturated fatty acids (MUFAs), containing a single double bond; and polyunsaturated fatty acids (PUFAs), characterized by two to six double bonds (6). In some contexts, the term highly unsaturated fatty acid (HUFA) is used to describe LCFAs with more than three double bonds. LCFAs account for most of FAs (5,6), and, for simplicity, will hereafter be referred to simply as FAs. Representative FAs of each class are presented in **Figure 1**.

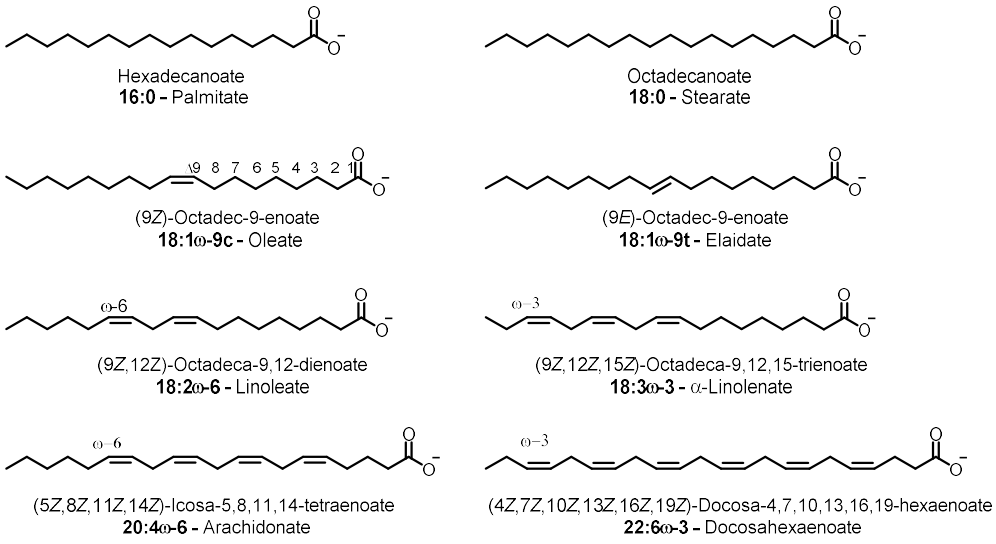

Figure 1: Chemical structures of representative FAs. Representative FAs include SFAs (palmitate and stearate), MUFAs (oleate and elaidate), and PUFAs. PUFA examples include essential FAs (linoleate and α-linolenate) and some derivatives highly unsaturated (arachidonate and docosahexaenoate).

SFAs are the most prevalent FAs, usually comprising 30-40% of the total FAs in animal tissues, with palmitic acid (16:0) and stearic acid (18:0) being the primary constituents (7). Beyond their common functions with other FAs, myristate (14:0) and palmitate (16:0) have unique roles in post-translational modifications (PTMs), specifically in *N*-myristoylation and side-chain palmitoylation, respectively. These modifications are involved in key cellular processes, including protein trafficking, protein-protein interactions, and protein-membrane interactions.

The majority of MUFAs feature a single *cis* double bond between the 9th and 10th carbons. This results in a distinct orientation of the adjacent carbons across the double bond, giving the molecule a curved structure (2). The primary representatives of this group are oleate (18:1ω-9), vaccenate (18:1ω-7) and palmitoleate (16:1ω-7). Some MUFAs of exogenous origin, such as elaidate (18:1ω-9t), exist in the *trans* configuration. This configuration produces a straight structure with physicochemical properties resembling those of SFAs.

PUFAs, excluding mead acid (20:3ω-9) (8), cannot be synthesized *de novo*. When not directly obtained from the diet, they are derived from the essential precursors linoleate (18:2ω-6) and α-linolenate (18:3ω-3) (9). Most PUFAs feature exclusively *cis* double bonds. These bonds are typically non-conjugated and separated by an sp^3 carbon atom, which confers high flexibility to the acyl chain (10). At this bis-allylic position, hydrogens are preferentially abstracted by peroxyl radicals, rendering PUFAs highly

susceptible to lipid peroxidation (11). However, a small fraction of PUFAs with conjugated double bonds, primarily isomers of linoleate (18:2ω-6), can also be obtained from dietary sources. The unique properties and functions of PUFAs stem from two primary modes of action: serving as precursors for signaling lipids and as fundamental building blocks of membranes (12). This will be discussed in sections 2.10. and 2.11.

2. Fatty acid metabolism

2.1. Uptake

Most FAs in the body are derived from the diet, primarily as TAGs, which are hydrolyzed in the intestinal lumen (9). Due to their minimal water solubility, FAs are incorporated into bile acid micelles in the intestine and transported through the systemic circulation bound to albumin. Additionally, FAs are carried in the systemic circulation as TAGs within lipoproteins, where they are locally released via hydrolysis by lipoprotein lipases.

The mechanism by which FAs enter cells remains a subject of debate. Some studies suggest that neutral FAs passively diffuse across the plasma membrane (13). However, as FAs are predominantly negatively charged at physiological pH, such diffusion by flip-flop mechanism is unlikely to be favored (9). Instead, several plasma membrane FA transporters have been

identified, and it is estimated that approximately 90% of cellular uptake is protein-mediated. Different mechanisms are involved in protein-mediated FA uptake. Transporters, such as CD36 and fatty acid transport proteins (FATPs), directly facilitate FA entry into cells. Activators, including long-chain acyl-CoA synthetases (ACSLs) and binders, such as fatty acid binding proteins (FABPs), contribute to limiting FA efflux. As FATPs also exhibit acyl-CoA synthetase activity for VLCFAs, the precise mechanisms underlying their role in cellular FA uptake remain under investigation (14). Once inside the cell, FAs are transported and distributed either by FABPs in their free form or by acyl-CoA binding protein (ACBP) if activated (15).

2.2. *De novo* synthesis

SFAs, primarily palmitate (16:0), can be *de novo* synthesized from surplus carbohydrates (9). This de novo biosynthesis takes place in lipogenic tissues, including the liver, adipose tissue, and lactating mammary glands.

De novo FA biosynthesis is an iterative process that occurs in the cytosol, involving acetyl-CoA, malonyl-CoA, NADPH, and the large, dimeric, multidomain enzyme fatty acid synthase (FAS) (16). The process begins with acetyl-CoA, the primer substrate, which is repeatedly extended by malonyl-CoA building blocks, adding two carbons at a time and releasing CO_2 during each condensation step. The β-carbon of the condensation product is processed by a NADPH-dependent reduction, followed by a dehydration and an additional NADPH-reduction. At each step, the substrate is transferred between domains while tethered to the 4′-phosphopantetheine prosthetic

group of the acyl carrier protein (ACP) domain. The growing of the substrate continues through successive addition of malonyl moieties, culminating in the formation of palmitoyl-thioester, which is subsequently cleaved to release palmitate (16:0).

2.3. Elongation

FAs from all sources can undergo modification through elongation and desaturation. Elongation primarily occurs in the endoplasmic reticulum (ER) and involves the addition of two carbon units to existing SFAs, MUFAs, or PUFAs using malonyl-CoA (3). While this process is mechanistically similar to *de novo* synthesis, elongation is carried out by multiple distinct enzymes. Initially, FAs are activated into acyl-CoA by an ACSL. Subsequently, four independent enzymes mediate successive steps of condensation, reduction, dehydration, and a final reduction. The initial condensation reaction, catalyzed by one of the seven ketoacyl-CoA synthetases (ELOVL1-7), is the rate-limiting step that determines FA specificity.

2.4. Desaturation

FAs can undergo further modification through the action of various FA desaturases, which catalyze stereospecific dehydrogenation reactions to introduce double bonds into the aliphatic chain (17).

Stearoyl-CoA desaturases (SCDs) are Δ9 desaturases localized in the ER, where they convert SFAs into MUFAs by introducing a double bond between

the 9th and 10th carbon atoms. SCDs require prior activation of the FA into fatty acyl-CoA and preferentially utilize palmitoyl- and stearoyl-CoAs as substrates. The process is dependent on molecular oxygen (O_2) and involves electron transfer through NAD(P)H, cytochrome b5 reductase, and cytochrome b5.

Humans lack Δ12 and Δ15 desaturases, which restricts endogenous desaturation to positions beyond the Δ9 carbon (2). Consequently, dietary intake of linoleate (18:2ω-6) and α-linolenate (18:3ω-3) is necessary for synthesizing all ω-6 and ω-3 series PUFAs. PUFA biosynthesis from these essential FAs requires sequential desaturation by Δ5 and Δ6 desaturases (D5D and D6D, respectively), elongation by ELOVLs, and, in the case of docosahexaenoate (22:6ω-3), peroxisomal β-oxidation (**Figure 2**) (18).

Figure 2. Biosynthetic pathway of ω-6 and ω-3 PUFAs. The synthesis of ω-6 and ω-3 PUFA series begins with the essential precursors linoleate (18:2ω-6) and α-linolenate (18:3ω-3), respectively. The pathway includes sequential desaturation and elongation steps, with peroxisomal β-oxidation (β-Ox) contributing to the final processing of very long-chain PUFAs. Adapted from (3).

2.5. Degradation

The primary pathway for FA degradation is mitochondrial β-oxidation (FAO), which involves approximately 20 proteins (19). The process begins with the mitochondrial import of acyl-CoAs via the carnitine shuttle system. Once inside the mitochondria, the cyclic FAO process shortens acyl-CoA molecules by sequentially removing two carboxy-terminal carbon atoms as acetyl-CoA. Each cycle involves four enzymatic steps, starting with the dehydrogenation of acyl-CoA, which introduces a *trans* double bond between the α and β carbons (**Figure 3**). This is followed by hydration at the β carbon, oxidation of the resulting alcohol into a ketone, and, finally, cleavage of the 3-ketoacyl-CoA to yield acetyl-CoA and an acyl-CoA shortened by two carbons. FAO cycles continue and, as acyl-CoA molecules are progressively shortened, distinct enzymes with substrate preferences for shorter chain lengths take over within the FAO machinery. This process enables FAs to be completely degraded. In addition to supplying acetyl-CoA for the tricarboxylic acid (TCA) cycle and ketogenesis, FAO generates $FADH_2$ and NADH, which directly fuel the respiratory chain. To degrade MUFAs and PUFAs, auxiliary enzymes, including reductases and isomerases, reposition various double bonds into the *trans*-2 configuration, enabling enoyl-CoAs to reenter the FAO cycle (20).

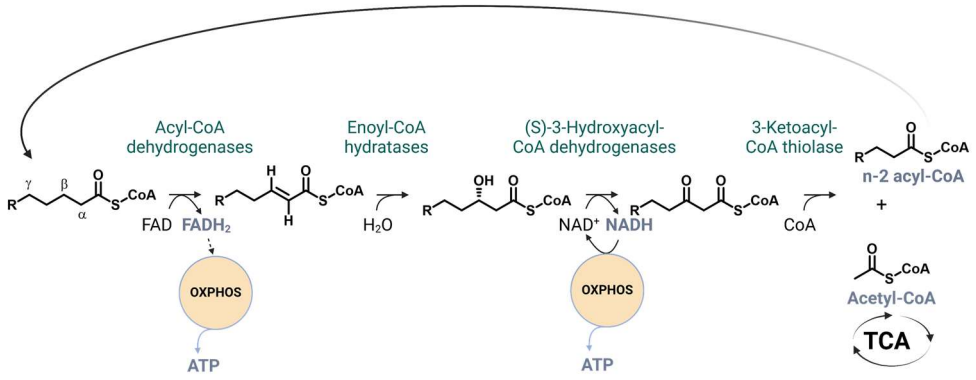

Figure 3. FA β-Oxidation pathway. The four sequential steps of β-oxidation and the chemical structures of the intermediates are depicted. The two-carbon shortened acyl-CoA re-enters the β-oxidation cycle for further processing. Adapted from (19).

2.6. Fatty acid as a building block

FAs serve as fundamental building blocks for the synthesis of more complex lipids, including glycerolipids and glycerophospholipids (GPLs) (9).

Glycerolipids are a group of neutral lipids characterized by a glycerol backbone esterified with one (1- and 2-monoacylglycerols), two (1,2- and 1,3-diacylglycerols), or three (triacylglycerol; TAG) FAs. The primary functions of TAGs are to act as a reservoir of FAs for energy production and the synthesis of membrane lipids (21). TAGs are stored in cells within small organelles called lipid droplets (LDs) and transported through the systemic circulation, packaged in lipoproteins.

GPLs consist of a lipophilic component, formed by 1,2-diacylglycerols (DAG), and a hydrophilic head group attached to the *sn*-3 hydroxyl group of

the glycerol backbone via a phosphodiester bond (22). Several different head groups (choline, ethanolamine, serine, inositol or glycerol) give rise to distinct classes of GPLs (**Figure 4**) with specific properties. The amphipathic nature of GPLs drives their assembly into membrane bilayers, which act as selective barriers to the extracellular environment and delineate intracellular organelles. In addition, GPLs act as a reservoir of precursors for the synthesis of lipid mediators, such as eicosanoids.

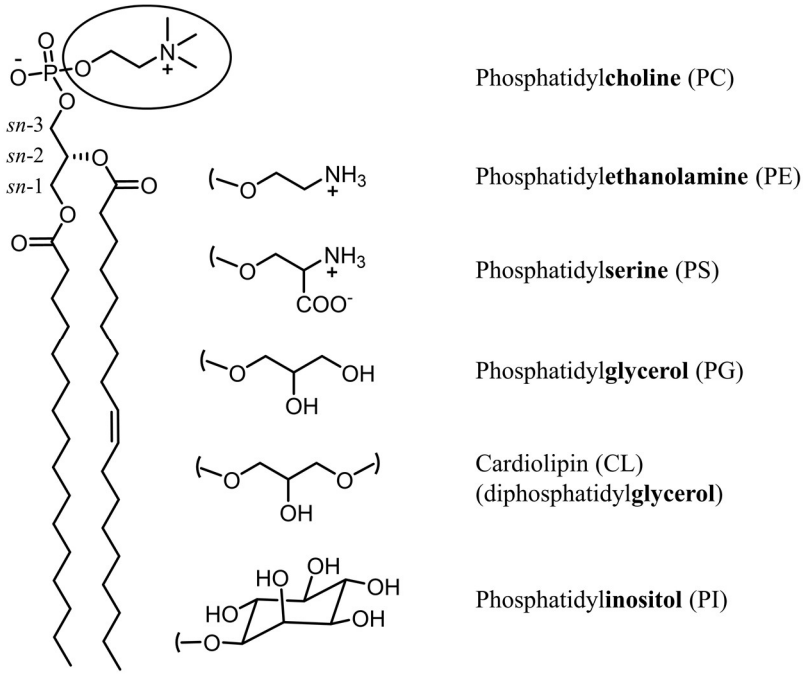

Figure 4. Different hydrophilic head groups define distinct phospholipid species. The glycerophospholipid (GPL) structure on the left represents 1-palmitoyl-2-oleoyl-sn-phosphatidylcholine. On the right, various hydrophilic head groups can replace the circled choline, giving rise to different GPL species. Adapted from (23).

2.7. Triacylglycerol synthesis

TAG synthesis occurs primarily in adipose tissue, the liver, and the intestine (9), and it is thought to take place mainly in the ER (21). This process involves two distinct pathways: the glycerol phosphate pathway and the monoacylglycerol (MAG) pathway. Both pathways depend on acyl-CoAs as FA donors (24). The glycerol phosphate pathway is nearly ubiquitous and primarily relies on the reduction of a glycolytic intermediate to generate glycerol-3-phosphate (9). This glycerol-3-phosphate backbone undergoes two sequential esterifications with FAs by two different acyltransferases, resulting in the formation of phosphatidic acid (PA) (**Figure 5**). Subsequently, PA is dephosphorylated by a phosphatase, yielding DAG. The final step, which is common to both pathways, involves the acylation of DAG to form TAG. The MAG pathway is primarily active in enterocytes of the small intestine, where it mediates the re-esterification of 2-MAG derived from dietary fat hydrolysis.

2.8. Glycerophospholipid synthesis

The synthesis of GPLs involves multiple pathways and numerous enzymes distributed across various organelles, including the ER, mitochondria, peroxisomes, and Golgi apparatus (25). However, the ER and Golgi apparatus are the main sites of GPL biosynthesis in most primary cells. Phosphatidylcholine (PC) and phosphatidylethanolamine (PE) comprise the majority of GPLs. Their synthesis begins in a manner analogous to TAG synthesis, starting with the formation of DAG (**Figure 5**) (22). Subsequently,

specific transferases utilize activated cytidine-diphosphate (CDP) derivatives of choline and ethanolamine to attach the polar head groups to DAG. Phosphatidylserine (PS), on the other hand, cannot be synthesized *de novo* and is instead produced through a head-group exchange between PC or PE and serine. Unlike PC and PE, phosphatidylinositol (PI), phosphatidylglycerol (PG), and cardiolipin (CL) are synthesized from PA, which acts as a precursor for cytidine-diphosphate-1,2-diacylglycerol (CDP-DAG). As a result, the dephosphorylation of PA to DAG represents a crucial regulatory step in phospholipid biosynthesis and energy storage. The polar head groups can also be interconverted through additional reactions, such as methylations, which converts PE to PC, and decarboxylation, which transforms PS into PE.

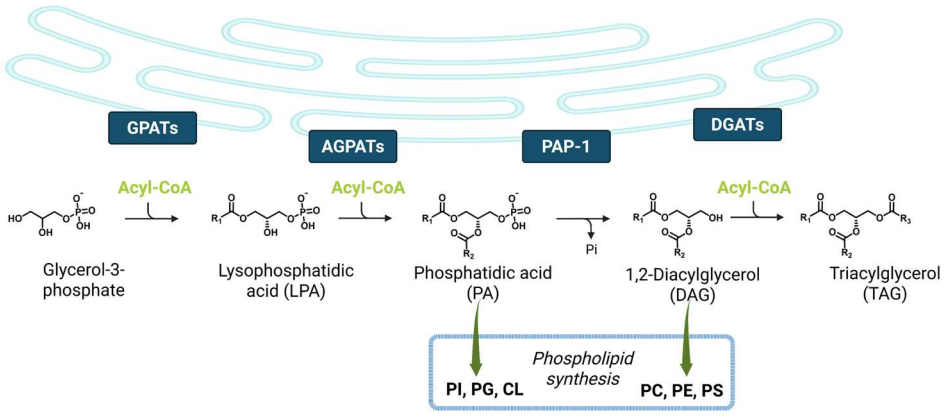

Figure 5. The crossroads of TAG and GPL synthesis. TAG and GPL synthesis both begin with the acylation of glycerol-3-phosphate, yielding lysophosphatidic acid (LPA), followed by a second acylation to produce PA. PA serves as a precursor for PI, PG, and CL. Alternatively, PA can be dephosphorylated to generate DAG, which undergoes a third acylation to form TAG or serves as an intermediate for the

synthesis of PC, PE, and PS. GPATs, glycerol-3-phosphate acyltransferases; AGPATs, acylglycerol phosphate acyltransferases; PAP-1, phosphatidate phosphatases 1; DGATs, diacylglycerol acyltransferases.

2.9. Fatty acid remodeling in glycerophospholipids

Similar to the interconversion of polar head groups after GPL synthesis, the FA composition of GPLs can also be modified (26). Given the vast diversity of FAs in humans and their two possible positions (*sn*-1 and *sn*-2) on the glycerol backbone, thousands of potential combinations give rise to an equally diverse array of GPL species. To fine-tune the membrane composition of GPLs, extensive remodeling of FAs, primarily at the *sn*-2 position, occurs through coordinated reactions involving phospholipases A (PLAs), ACSLs, transacylases, and lysophospholipid acyltransferases (LPLATs). This process, known as the Lands' cycle, is crucial for tailoring the GPL compositions of membranes, enabling variation across different cell types, organelles, and between inner and outer membranes. It plays vital roles, such as generating disaturated GPLs that function as surfactants in the lungs or enriching membranes with PUFAs.

2.10. Fatty acid influence on phospholipid structure and function

On average, the first FA of a GPL is typically a SFA, while the second is either a MUFA or a PUFA (10). However, significant variations in this pattern exist across different membranes. Simple organisms lack PUFAs, highlighting the essential role of the MUFA/SFA ratio in maintaining basic cellular functions. This ratio is typically low in membranes with protective

barrier functions, such as the apical membranes of epithelial cells or lung surfactant, and tends to be high in membranes involved in biosynthetic activities, such as the endoplasmic reticulum (ER). This can be attributed to the intrinsic shapes of MUFA- and SFA-GPLs. SFA-GPLs are cylindrical and tightly packed, which limits the membrane permeability (**Figure 6A and 6B**). Conversely, MUFA-containing GPLs exhibit a conical shape that disrupts membrane organization and generates large water-accessible packing defects. This supports the anchoring of cytosolic proteins to the ER or ER-derived membranes involved in biogenic processes.

Unlike SFA- and MUFA-GPLs, which possess a defined intrinsic shape, PUFA-GPLs can adopt multiple conformations of comparable energy, alternating between cones, cylinders and hairpins (**Figure 6C**). Like MUFAs, PUFAs in GPLs increase membrane disorder and reduce membrane thickness. However, the packing defects caused by PUFA-GPLs are more superficial, as their highly flexible tails tend to fill these voids. The greater structural flexibility they impart minimize the packing stress that results from the fast conformational changes of membrane proteins or the mechanical work of membrane-bending proteins. As a result, PUFA-GPLs are particularly abundant in membranes hosting fast reactions like phototransduction and neurotransmission as well as in membranes that undergo important bending, such as those involved in endocytosis. Additionally, PUFA-GPLs are often regarded as enhancers of membrane fluidity, though quantitative evidence demonstrating a greater effect compared to MUFAs remains limited (12).

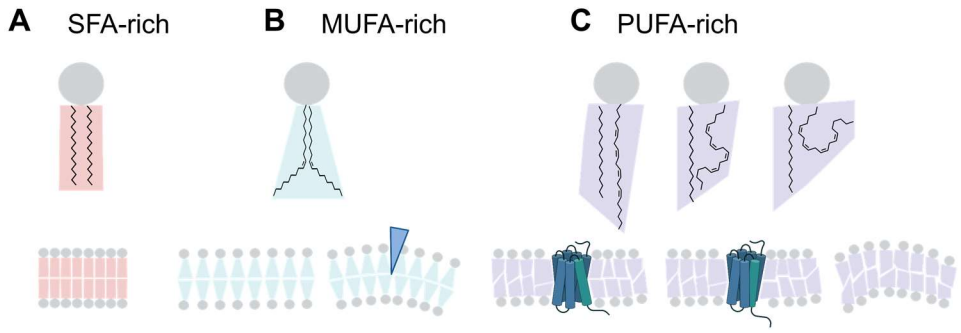

Figure 6. Conformational differences between saturated, monounsaturated, and polyunsaturated acyl-Chains influence membrane properties. (**A**) SFA-rich GPLs adopt a cylindrical shape, enabling tight packing and forming effective barrier membranes. (**B**). MUFA-rich GPLs exhibit a conical shape, creating large packing defects that facilitate protein adsorption (blue triangle). (**C**) PUFA-rich GPLs are highly adaptable, minimizing mechanical stress induced by rapid protein conformational changes (exemplified by G-protein coupled receptor). Adapted from (10).

2.11. Involvement of PUFAs as precursors of lipid mediators

Multiple lipid mediators are derived from PUFAs and are produced downstream of GPL synthesis during the deacylation-reacylation (Lands' cycle) process (27). Among these mediators are eicosanoids, a group of bioactive, oxygenated compounds derived from 18-22 carbon PUFAs (28). Arachidonate (20:4ω-6) serves as the primary precursor for more than a hundred distinct eicosanoids. These are synthesized through three major pathways, collectively referred to as the "arachidonate cascade": the cyclooxygenase (COX), lipoxygenase (LOX), and epoxygenase (EPOX) pathways (**Figure 7**).

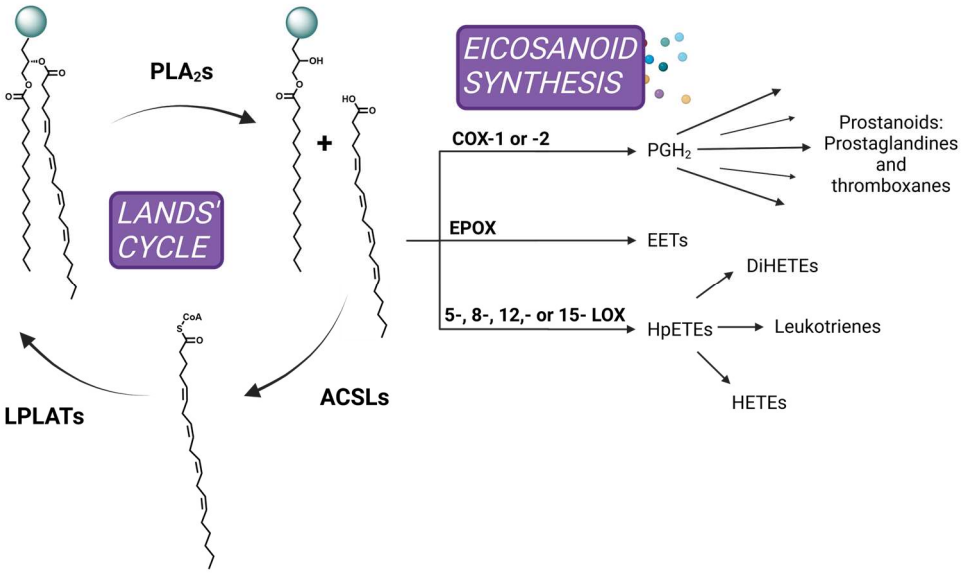

Figure 7. Phospholipid Remodeling Mobilizes PUFAs for Eicosanoid Synthesis. PLA_2s release PUFAs from GPLs, providing substrates for eicosanoid synthesis via the COX, EPOX and LOX pathways. The reacylation of free PUFAs into GPLs by ACSLs and LPLATs constrains eicosanoid synthesis. PGH_2, prostaglandin H_2; EET, epoxy eicosatrienoic acids; HpETEs, hydroperoxy eicosatetraenoic acids; diHETEs, dihydroxy eicosatetraenoic acids; HETEs, hydroxy eicosatetraenoic acids.

Eicosanoids are synthesized on demand in response to external stimuli, such as hormonal signals (28). The process begins with the release of free PUFAs from GPLs via calcium-dependent PLA_2-mediated hydrolysis. These liberated PUFAs are then converted into various eicosanoids through the three major pathways. Once synthesized, eicosanoids are released from the cell to exert local effects, in an autocrine and paracrine manner, by binding to class I G protein–coupled receptors (GPCRs). Their effects are typically short-lived, lasting only seconds to minutes before degradation. To prevent prolonged eicosanoid synthesis after stimulation, it is thought that free

arachidonate is rapidly converted back to arachidonoyl-CoA (AA-CoA) and reesterified into GPLs via the reacylation step of Lands' cycle (29).

Eicosanoids regulate diverse biological processes, notably in immune defense and inflammation. While arachidonic acid (20:4ω-6) is the dominant precursor, other ω-6 and ω-3 PUFAs also serve as substrates for eicosanoid synthesis. Generally, eicosanoids derived from ω-6 PUFAs are considered pro-inflammatory, whereas those derived from ω-3 PUFAs, such as eicosapentaenoate (20:5ω-3) and docosahexaenoate (22:6ω-3), are often linked to pro-resolving activities. However, exceptions to these generalizations are well-documented (12).

2.12. The central role of acyl-CoA activation in fatty acid metabolism

Most of the numerous metabolic fates of FAs, including β-oxidation, elongation, desaturation, and the synthesis of FA-derived lipids such as TAGs, GPLs, cholesteryl esters (CE), and sphingolipids (SL), require their initial activation to acyl-CoAs (30). This critical activation step is catalyzed by long-chain acyl-CoA synthetases (ACSLs), positioning them as key regulators of FA metabolism (**Figure 8**). Beyond FA activation, ACSLs facilitate FA uptake and even participate in the regulation of eicosanoid synthesis, one of the few metabolic pathways that do not necessitate acyl-CoA formation. By limiting the availability of PUFA precursors, ACSLs ensure that lipid mediator production remains transient. The following section

will explore the pivotal role of ACSLs, with a specific focus on the fourth isoform, ACSL4.

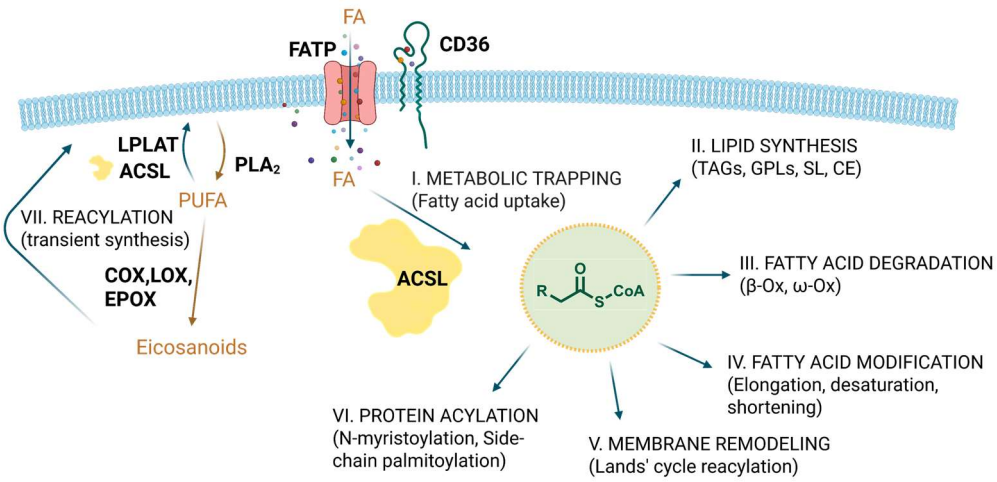

Figure 8. Central role of ACSLs in FA metabolism. FAs enter the cell via FATPs, CD36, or passive diffusion. Once inside the cell, ACSLs catalyze FA conversion into acyl-CoAs, effectively trapping them (I) and directing them toward diverse metabolic pathways: synthesis of complex lipids (TAGs, GPLs, SL, and CE) (II), degradation via β- and ω-oxidation (III), elongation and desaturation (IV), membrane remodeling (V), and protein acylation (VI). By modulating free PUFA levels, ACSLs also influence eicosanoid synthesis (VII). β-ox, β-oxidation ; ω-ox, ω-oxidation. Inspired by (30).

3. ACS family

3.1. Classification

ACSs are members of the Acyl-CoA/NRPS/Luciferase (ANL) superfamily of enzymes, defined structurally by a large *N*-terminal domain and a smaller *C*-terminal domain linked by a flexible hinge (**Figure 9**) (31). The active site resides at the interface of these two domains. A key feature of this superfamily is their conserved catalytic mechanism, which includes the formation of an adenylated intermediate as the first step in a two-step reaction process (32).

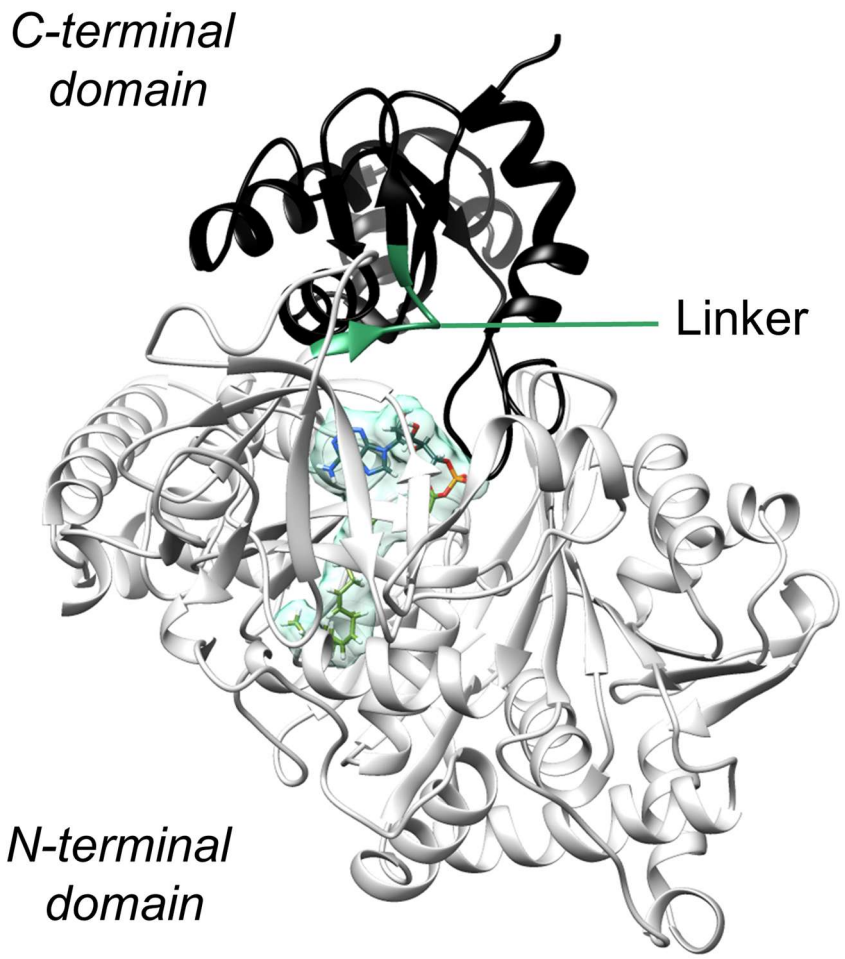

Figure 9. General ANL structure illustrated through ACSL4 model. The figure shows a refined AlphaFold 2 model of ACSL4_v1 in complex with an acyl-AMP intermediate (green sticks) (33). The structure features the large *N*-terminal domain (grey), the small *C*-terminal domain (black), and the connecting flexible linker (green).

Acyl-CoA synthetases (ACSs) are classified into five subfamilies based on the chain length of their prefered FA substrates (34). Short-chain synthetases

(ACSSs) activate FAs ranging from C2 to C4, medium-chain synthetases (ACSMs) target FAs from C4 to C12, and long-chain synthetases (ACSLs) process FAs from C12 to C22. Bubblegum synthetases (ACSBG) specialize in FAs spanning C14 to C24, while very-long-chain synthetases (SLC27A family) handle FAs from C18 to C26.

3.2. ACSL isoforms

Humans express five isoforms of ACSLs (ACSL1, ACSL3, ACSL4, ACSL5, and ACSL6), each with multiple spliced variants (34). These enzymes catalyze the formation of a thioester bond between a FA and coenzyme A (CoA) via an ordered Bi Uni Uni Bi ping-pong mechanism, as demonstrated by kinetic studies across various organisms (35,36). The catalytic mechanism has been further elucidated through the crystallographic structure of *Thermus thermophilus* ACSL (*tt*LC-FACS), the sole structural representative of this subfamily (37). The process begins with ATP binding (**Figure 10**), which induces a significant conformational change that brings the *C*-terminal domain closer to the *N*-terminal domain. This conformational closure opens the FA gate tunnel, allowing the FA to enter the catalytic cavity. The reaction proceeds with the formation of an acyl-AMP intermediate and the release of pyrophosphate (PPi). In the second step, CoA replaces AMP, resulting in the production of fatty acyl-CoA.

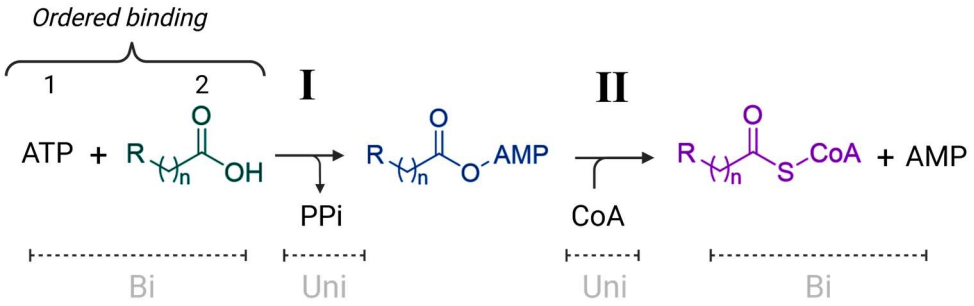

Figure 10. Catalytic mechanism of ACSLs. The reaction proceeds through two sequential steps: (I) ATP binds, followed by the FA, forming an acyl-AMP intermediate and releasing PPi. (II) CoA then replaces AMP, resulting in the formation of acyl-CoA and AMP.

Although the five ACSL isoforms catalyze the same reaction, they exhibit significant differences in sequence identity (38,39). In rats, two distinct clusters emerge upon comparing their sequence identities. The first cluster comprises ACSL1, ACSL5, and ACSL6, while the second consists of ACSL3 and ACSL4. Within each cluster, the isoforms share approximately 60% sequence identity with each other. However, between clusters, only about 30% sequence identity is observed.

Despite these variations, five motifs are highly conserved (40), as highlighted in the sequence alignment of *tt*LC-FACS with *h*ACSL isoforms (**Figure 11**). Comparative analysis of these motifs with the crystal structure of *tt*LC-FACS has provided valuable insights into the ACSL mechanism (37).

Figure 11. Amino acid sequence alignment of *h*ACSLs and *tt*LC-FACS. A multiple sequence alignment of *h*ACSL4_v2 (O60488), *h*ACSL1_v2 (P33121), *h*ACSL3 (O95573), *h*ACSL5_v1 (Q9ULC5), *h*ACSL6_4 (Q9UKU0), and *tt*LC-FACS (Q5SKN9) was performed using ClustalO and visualized with Jalview. The five conserved motifs are boxed. The *C*-terminal domain, the linker region, and the putative transmembrane domain of ACSL4_v2 are indicated. The gating residue of *tt*LC-FACS (Trp234) and its proposed counterpart in *h*ACSL4 (Tyr318) are highlighted in orange. ACSL4 residues reported to undergo post-translational modifications are highlighted in purple. Adapted from (33).

Motif I includes the P-loop, described in the *tt*LC-FACS structure, which binds the phosphate of ATP/AMP and ensures proper substrate orientation. Motif II contains the L-motif of *tt*LC-FACS, which functions as a linker between the *N*-terminal and *C*-terminal domains and is essential for the ATP-induced conformational change. Mutational analysis has further revealed its involvement in determining FA chain-length specificity (41). Motif III is associated with ATP/AMP binding, stabilizing the adenine moiety via a conserved tyrosine. Motif IV forms part of the gate domain in *tt*LC-FACS, preventing FA entry before ATP binding, with steric hindrance mediated by Trp234. This tryptophan is absent in the human ACSL isoforms, but a tyrosine (Tyr318 in ACSL4) or a phenylalanine has been proposed to fulfill a similar role (**Figures 11-12**) (34). Finally, motif V contains a highly conserved lysine believed to play a crucial role in stabilizing the closed conformation by interacting with residues in motif II. The different motifs are illustrated on the refined AlphaFold 2 structural model of ACSL4 (33), in **Figure 12**.

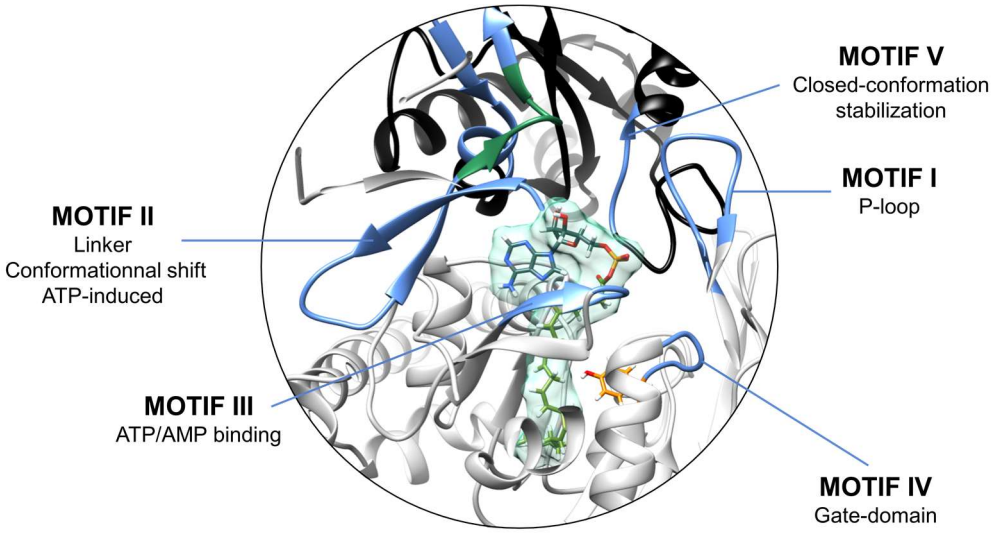

Figure 12. Conserved motifs within the ACSL family illustrated through the structural model of ACSL4. The figure presents a magnified view of the catalytic cavity of the refined AlphaFold 2 model of ACSL4 in complex with the acyl-AMP intermediate (green sticks). The *N*-terminal domain is depicted in grey, the *C*-terminal domain in black, the linker in green and the five sequence motifs conserved across the ACSL family are highlighted in blue. The proposed gating residue of *h*ACSL4 (Tyr318) is indicated in orange.

The distinct ACSL isoforms differ in tissue distribution, subcellular localization, and substrate specificity (29,39,42–46). These variations led to the proposition that each isoform plays a specialized role in directing selective FAs toward specific metabolic fates (47). This concept is strongly supported by extensive gain- and loss-of-function studies combined with lipidomic analyses (48,49,58,59,50–57).

4. ACSL4 specificities

4.1. Variants and tissue distribution

ACSL4 is localized on the Xq23 chromosome and produces two distinct variants through alternative splicing (60,61). The shorter variant, ACSL4_v1, consists of 670 amino acids and lacks the initial 41 *N*-terminal amino acids present in ACSL4_v2, which are predicted to function as an integral membrane association domain (56). ACSL4_v1 was identified as a membrane-associated protein rather than an integral membrane protein, based on observations that it could be washed from rat liver fractions using high salt concentrations (62).

ACSL4_v2 appears to be brain-specific (61), whereas *ACSL4_v1* transcripts are expressed across a wide range of tissues, with the highest levels observed in steroidogenic tissues in rats (29). In humans, *ACSL4_v1* gene expression is highest in the placenta, testis, ovary, spleen, and adrenal cortex (60). ACSL4_v1 is also expressed in most areas of the brain, except in the cerebellum and corpus callosum, where ACSL4_v2 is the only variant expressed (63).

4.2. Subcellular localization

Immunofluorescence and subcellular fractionation studies have revealed a strong association of ACSL4 with the endoplasmic reticulum (ER) (56,63–

66). Additionally, the enzyme was localized to lipid droplets (LD) (56,64,67,68), mitochondria-associated membranes (MAM) (49,62,69), the plasma membrane (PM) (56,64), peroxisomes (62), the cytosol (56), and secretory vesicles (70).

Küch et al. explored the differential subcellular localization of the two ACSL4 variants (56). ACSL4_v1 was found to localize primarily to the inner surface of the PM, including microvilli, with partial presence in the cytosol. In contrast, ACSL4_v2 was predominantly associated with the ER and LD.

A recent study, however, suggested that ACSL4 exhibits a widespread distribution throughout the cell (66). It has been proposed that the specific localization of ACSL4_v1, which is not an intrinsic membrane protein, is facilitated through interactions with other proteins (62).

4.3. Fatty acid preference

Since its early characterization, ACSL4 has been shown to convert a broad range of FAs, with a marked preference for arachidonate (20:4ω-6) and eicosapentaenoate (20:5ω-3) as substrates (29). The enzyme's catalytic efficiency (k_{cat}/K_m) for these PUFAs was found to be more than 10-fold higher than for palmitate (16:0) (29,71). However, other studies reported contradictory findings, showing comparable k_{cat}/K_m values for both arachidonate (20:4ω-6) and palmitate (16:0) (39,46). These discrepancies highlight that the determination of kinetic parameters is highly influenced by

the experimental design, including the specific constructs and methodologies employed (46).

The comparison of ACSL4_v1 and ACSL4_v2 using a consistent methodology, revealed that both variants exhibit comparable activities and similar FA preferences (72).

Despite the wide range of FAs converted by purified ACSL4, studies in the more complex environment of sf-9 cell lysates overexpressing ACSL4 revealed that only highly unsaturated fatty acids (HUFAs) were metabolized (58). This suggests the presence of a regulatory mechanism that governs its FA preference in more intricate environnements.

ACSL4, like other ACSLs, is also capable of metabolizing signaling eicosanoids such as epoxy eicosatrienoic acids (EETs) and hydroxy eicosatetraenoic acids (HETEs) (46).

4.4. Regulation of ACSL4 expression

The regulation of ACSL4 is intricate, encompassing multiple layers of control. Various pathophysiological stimuli, including ischemia (73), and epithelial-mesenchymal transition (74) enhance ACSL4 expression via the transcription factor Sp1 and the transcription coregulator YAP, respectively. Additionally, studies have shown that diet significantly influences ACSL4 expression in the liver. Specifically, a high-cholesterol high-fat diet (HCHFD) induces ACSL4 expression through PPAR-δ activation (75),

whereas a high-fat diet (HFD) suppresses its expression (76). However, this diet-regulated expression of ACSL4 is tissue-dependent, as HFD induces its expression in gonadal adipocytes (59).

Hormones, including insulin (55) and androgens (77), have been shown to repress *ACSL4* expression, whereas adrenocorticotropin (78) and angiotensine II (79) induces its expression. In addition, studies have identified multitude of miRNAs capable of regulating ACSL4 expression at the mRNA level, as reviewed in this work (80).

4.5. Regulation of ACSL4 stability

ACSL4 is subject to multiple post-translational modifications (PTMs) that modulate its stability (**Figures 11,13**), particularly via the ubiquitin-proteasomal pathway. Notably, arachidonate, its preferred substrate, has been reported to promote ACSL4 degradation through this pathway (76). Proteomic analysis further identified an interaction between ACSL4 and the intracellular vesicular transport factor p115 (81). This interaction, which is enhanced by arachidonate, accelerates ACSL4 degradation. Interestingly, arachidonate-induced degradation occurs independently of p115, suggesting that arachidonate either acts upstream of p115 or engages an alternative mechanism. Further studies are needed to clarify the precise role of p115 in ACSL4 turnover.

Additionally, ACSL4 stability is regulated by CARM1-mediated methylation at Arg339 (82). This modification promotes the recruitment of RNF25,

leading to ACSL4 ubiquitination and proteasomal degradation. TRIM9 and RBBP6 have also been identified as potential E3 ubiquitin ligases involved in ACSL4 degradation.

Phosphorylation also plays a key role in ACSL4 regulation. AKT-mediated phosphorylation of ACSL4 at Thr624 enhances its recognition at Lys621 by SKP2 (83). This interaction triggers ACSL4 polyubiquitination and subsequent degradation through the lysosomal pathway. Conversely, the phosphatase LHPP dephosphorylates AKT, thereby preventing ACSL4 phosphorylation and degradation.

The stability of ACSL4 is further modulated by SUMOylation, with deSUMOylation mediated by the SENP1 protease under hypoxic conditions, promoting ACSL4 degradation (84).

Immunoprecipitation assays have demonstrated an interaction between ACSL4 and O-GlcNAc transferase (85). Since ACSL4 is stabilized by the substrates of this transferase in cells, it is suggested that this stabilization is mediated through O-GlcNAcylation.

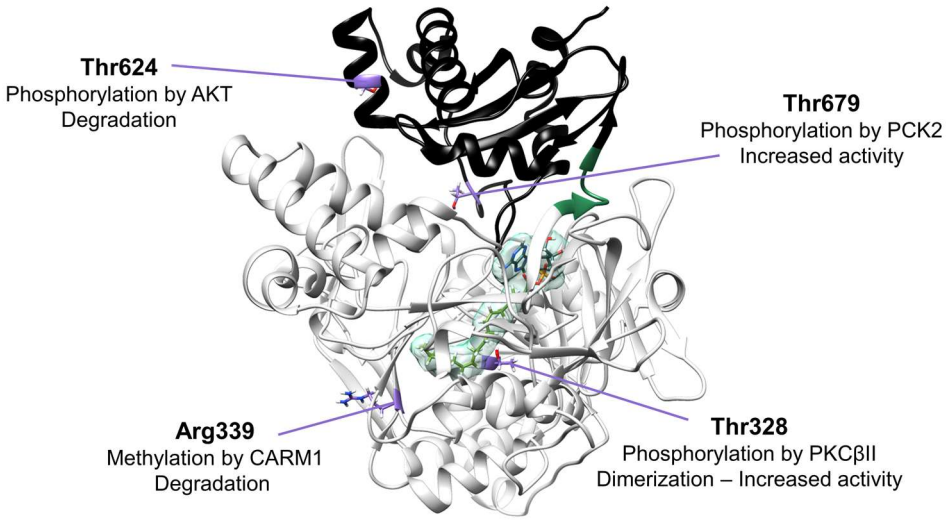

Figure 13. Post-translational modifications (PTMs) of ACSL4. Refined AlphaFold 2 model of ACSL4 bound to the acyl-AMP intermediate (green sticks), highlighting the four residues known to undergo PTMs (shown in purple). The *N*-terminal domain is depicted in grey, the *C*-terminal domain in black, and the linker in green.

4.6. Regulation of ACSL4 activity

Other PTMs regulate ACSL4 activity (**Figure 13**). Stimulation of steroidogenic cells by ACTH promotes the phosphorylation of ACSL4 dimeric form (69). In vitro phosphorylation assays suggest that protein kinase A (PKA) and protein kinase C (PKC) are involved. Phosphorylation by the two kinases occurs independently at distinct sites, resulting in opposing effects on ACSL4 activity: phosphorylation by PKA enhances its activity, while phosphorylation by PKC diminishes it.

In a different context, lipid peroxidation-mediated phosphorylation of PKCβII activates the kinase, which then phosphorylates ACSL4 at Thr328, promoting its dimerization and enhancing its activity (86).

Additionally, mitochondrial phosphoenolpyruvate carboxykinase 2 (PCK2) phosphorylates ACSL4 at Thr679, further increasing its activity (87).

The multilayered regulatory system governing ACSL4 activity and turnover suggests that it is a highly dynamic protein involved in transient physiological responses.

4.7. Structure

Limited structural information is available for ACSL4, primarily due to the absence of a resolved crystal structure. Current insights are mostly based on the dimeric structure of *tt*LC-FACS, which shares only about 20% sequence identity (37% sequence homology) with ACSL4 (37). However, several observations suggest functional similarities between the two proteins. Studies (69,86), indicate that ACSL4_v1 also likely functions as a dimer. Additionally, ATP binding induces a comparable conformational change, as evidenced by the stabilization of the ACSL4 *C*-terminal domain in hydrogen-deuterium exchange mass spectrometry (HDx-MS) (33).

Other related crystal structures differ substantially. For example, the monomeric FATP/ACSVL from *Mycobacterium tuberculosis* features a hydrophobic tunnel running through the entire protein, enabling FAs to bind

in the catalytic cavity while remaining partially embedded in the membrane (88). The human medium-chain ACSM2A, which also functions as a monomer, does not exhibit an ordered binding of ATP followed by FA (89). Moreover, it displays a domain alternation mechanism, common to many ANL enzymes (32), in which the *C*-terminal domain undergoes a major rotation between the adenylate-forming and thioester-forming reactions, exposing opposite faces to the *N*-terminal domain. Notably, this large-scale conformational shift has not been observed in *tt*LC-FACS (37). Finally, low-resolution cryogenic electron microscopy (cryoEM) structures and mutagenesis analyses have shown that ACSL1 is active as a monomer (90). Altogether, these diverse structural observations demonstrate the high degree of heterogeneity within the ACS enzyme family.

The AlphaFold 2 *in silico* model of ACSL4_v2 predicts the local three-dimensional positioning of amino acids with high accuracy (91), with over 95% of residues assigned a high or very high confidence score (**Figure 14A**). However, although individual domains are reliably modeled, their relative spatial arrangement is predicted with lower confidence (**Figure 14B**). This likely reflects the intrinsic flexibility of the interdomain linker, as well as the use of homologous structures resolved in distinct conformational states during AI-based model generation. Nevertheless, homology models (92) and AlphaFold-predicted structures (33,93) have been effectively utilized to investigate the binding mode of small molecules to ACSL4.

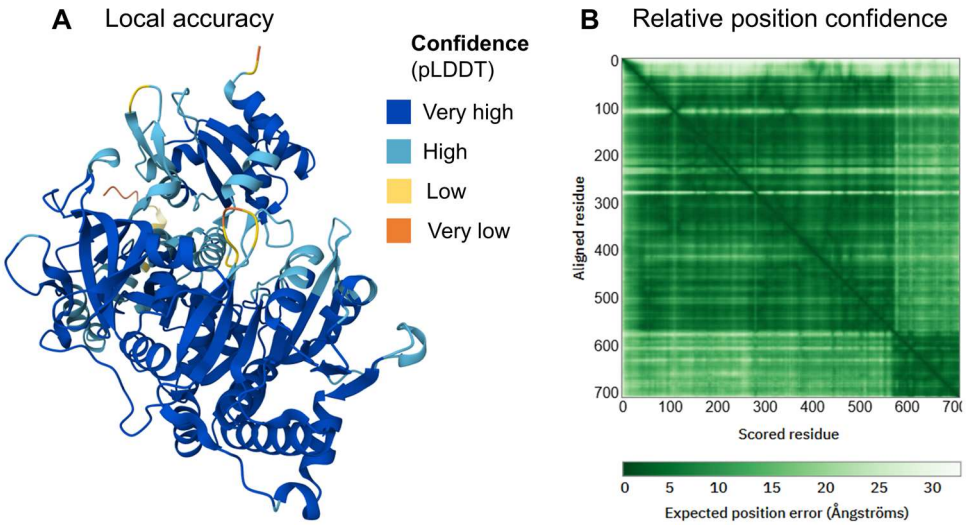

Figure 14. Confidence metrics of the AlphaFold 2 model of ACSL4_v2 (91). (A) Per-residue confidence scores based on the predicted local distance difference test (pLDDT), reflecting high local structural accuracy across most of the protein. (B) Predicted aligned arror (PAE) plot assessing the confidence in the relative positioning of residue pairs, revealing lower confidence in the spatial arrangement between domains.

5. Physiological role of ACSL4

5.1. Fatty acid uptake

All ACSLs enhance overall cellular FA uptake (56,94–97). This uptake mechanism is primarily attributed to the inability of amphipathic acyl-CoAs to passively diffuse through membranes, unlike FAs. Consequently, thioesterification of FAs to acyl-CoAs prevents their efflux, effectively

trapping them within the cell or organelle. However, the downstream metabolic utilization of acyl-CoAs also influences FA uptake, contributing to a broader yet incompletely understood phenomenon known as "metabolic trapping". Notably, the construction of an ACSL4 variant exclusively localized to the outer mitochondrial membrane demonstrated that the enhanced uptake of arachidonic acid is independent of ACSL4's subcellular localization (56).

5.2. Shaping membrane composition

Due to its unique substrate preference, ACSL4 channels arachidonate into various phospholipid species through membrane remodeling (59,98). Depending on the study, its incorporation is observed in specific PLs, including PC (56,58,68,99), PI (56,99,100), and PE (58,100,101). ACSL4 also facilitates the integration of other PUFAs into PLs, such as adrenate (22:4ω-6) (101), eicosapentaenoate (22:5ω-3), docosahexaenoate (22:6ω-3) (59), and contributes to PUFA incorporation into TAGs (68,100). Since ACSL4 deficiency results in a reciprocal increase in the incorporation of other FAs, such as oleate (18:1ω-9), this suggests that ACSL isoforms compete to shape the cellular phospholipidome (98). Interestingly, ACSL4 exerts a localized influence on membrane composition, as demonstrated by the reduced incorporation of arachidonate into ER membranes when ACSL4 is restricted to the mitochondria (56). This suggests that acyl-CoAs are preferentially utilized at the membranes where they are synthesized.

5.3. Regulation of eicosanoid synthesis - Inflammation

It has long been established that eicosanoid synthesis is primarily constrained by the availability of its precursors, mainly arachidonate, which must first be released by PLA_2s from esterified stores in complex lipids (**Figure 7)** (102). Given ACSL4's specificity in channeling the re-esterification of arachidonate, the enzyme effectively limits the levels of precursors available for eicosanoid synthesis. Consistently, ACSL4 overexpression in human arterial smooth muscle cells (SMCs) attenuates cytokine-induced prostaglandin (PG)E_2 release, whereas its inhibition enhances PGE_2 production (100). Likewise, *ACSL4* knockdown or ACSL4 inhibition significantly increases interleukin-1β-stimulated PG synthesis in rat fibroblastic 3Y1 cells (99,103). Furthermore, in bone marrow-derived macrophages from ACSL4-deficient mice, LPS-dependent PG release is markedly enhanced (58). *ACSL4* knockout in mice leads to the overproduction of COX-derived eicosanoids and exacerbates LPS-induced systemic inflammation, resulting in more severe symptoms and higher mortality (104). Together, these studies suggest that ACSL4 deficiency may promote inflammation by amplifying the stimulus-dependent release of COX-derived lipid mediators. However, conflicting results have been observed in mice with myeloid-specific ACSL4 deficiency, where opsonized zymosan-stimulated eicosanoid synthesis and the associated inflammatory response are attenuated (98). These conflicting results have been attributed to differences in the timing of ACSL4 targeting, varying between acute and long-term inhibition (100). According to this hypothesis, constitutive ACSL4 activity maintains a reservoir of

arachidonate, and long-term silencing depletes this pool, thereby limiting eicosanoid production. In contrast, acute ACSL4 inhibition does not deplete the pool of arachidonate but prevents its reacylation, thereby promoting sustained eicosanoid synthesis after stimulation. Further studies are required to elucidate this phenomenon and to define more precisely the role of ACSL4 in inflammation.

5.4. Regulation of eicosanoid synthesis - Steroidogenesis

ACSL4 contributes to steroidogenesis by regulating eicosanoid production through an alternative metabolic pathway, known as the ACSL4-ACOT2 axis (**Figure 15**) (105). The rate-limiting step in steroidogenesis is the transport of cholesterol to the inner mitochondrial membrane, where P450scc catalyzes its conversion into pregnenolone (106). This cholesterol transport is mediated by the steroidogenic acute regulatory protein (StAR), whose expression is transcriptionally regulated by trophic hormones (107). Additionally, adrenocorticotropin (ACTH) or the second messenger cAMP also stimulate ACSL4 synthesis in adrenal and Leydig cells, respectively (78). In these cells, ACSL4, along with acyl-CoA thioesterase 2 (ACOT2), participates in the intramitochondrial transport of arachidonate (108,109). The exact transport mechanism remains unclear but begins with ACSL4 converting arachidonate into arachidonoyl-CoA (AA-CoA). It is speculated that AA-CoA binds to ACBP, enabling its mitochondrial entry via the translocator protein (TSPO) (105). Inside the mitochondria, ACOT2 hydrolyzes the thioester bond, releasing free arachidonate, which is then metabolized through the LOX

(110,111) or EPOX pathways (112). The resulting eicosanoids transcriptionally enhance StAR expression, thereby promoting steroidogenesis. In addition, the steroidogenic role of ACSL4 may stem from its involvement in cholesteryl ester (CE) formation, as CEs serve as an important reservoir of cholesterol for steroid synthesis (113). Notably, steroid tissue-specific ACSL4 ablation in mice results in a 50% reduction in adrenal CE storage, disrupting steroidogenesis exclusively in males (114). In contrast, female mice heterozygous for ACSL4 deficiency exhibit reduced fertility accompanied by morphological uterine changes (115). However, whether this phenotype is linked to the ACSL4-ACOT2 axis remains unclear, as the observed increase in uterine PG levels is also associated with disrupted steroidogenesis and impaired fertility.

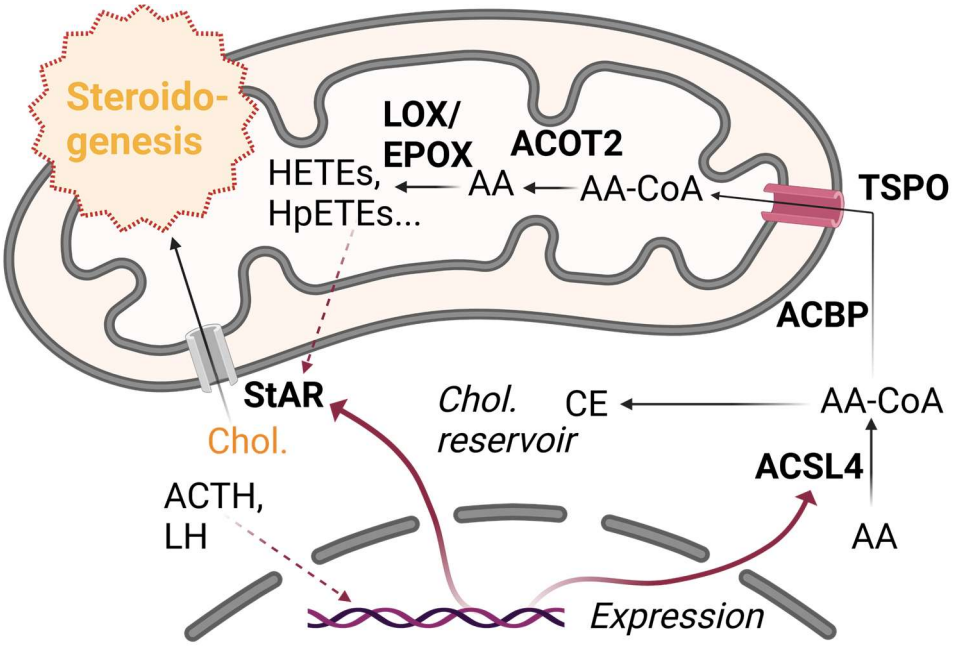

Figure 15. ACSL4's role in steroidogenesis. ACTH and luteinizing hormone (LH) stimulate StAR and ACSL4 expression. ACSL4 converts arachidonate (AA) into arachidonoyl-CoA (AA-CoA), which binds ACBP for transport and enters mitochondria via TSPO. Inside, ACOT2 releases AA, which is processed into eicosanoids by LOX and EPOX. These eicosanoids enhance StAR transcription, promoting cholesterol transport to the inner mitochondria membrane. Additionally, ACSL4 contributes to increasing the cellular cholesterol pool as CE.

5.5. Regulation of eicosanoid synthesis – Insulin secretion

Beyond inflammation and steroidogenesis, the eicosanoid-regulating role of ACSL4 also influences insulin secretion. *ACSL4* knockdown in the pancreatic INS 832/13 β-cell line increases the secretion of epoxy eicosatrienoic acids (EETs) (116), leading to impaired glucose-stimulated insulin secretion (70). However, in this context, rather than limiting the availability of the precursor

arachidonate for EET synthesis, ACSL4 is believed to regulate EET levels by directly producing EET-CoAs, which are subsequently incorporated into membranes.

5.6. Brain development

ACSL4 plays a role in brain development, as suggested by the identification of null mutations in *ACSL4* associated with non-syndromic X-linked mental retardation in two families (61,117). In *Drosophila larvae*, null mutation of *dAcsl*, the functional homolog of ACSL4, significantly reduces the number of glial and neuronal cells and impairs axonal targeting (118). This phenotype can be rescued by wild-type ACSL4 but not by patient-derived mutants. Further mechanistic investigations reveals that the null mutation leads to axonal aggregation of membranous organelles, synaptic defects, and impaired retrograde transport (119). Additionally, gene knockdown studies in rat hippocampal neurons suggest that ACSL4 is involved in dendritic spine generation (63).

Several lines of evidence, though conflicting, also point to a role for ACSL4 in neuronal differentiation. *ACSL4* knockout in embryonic stem cells markedly attenuates induced neuronal differentiation (120), whereas another study reports the opposite effect, showing that *ACSL4* knockdown promotes neural stem cell differentiation (121). The mechanisms by which ACSL4 contributes to neural development remain unclear, and further research is needed to determine whether disrupted eicosanoid regulation, altered membrane composition, or other pathways are involved.

6. Pathophysiological role of ACSL4

ACSL4 activity is also linked to various pathological conditions, including cancers and disorders associated with ferroptosis, a form of regulated cell death. The following section will first introduce ferroptosis, highlighting ACSL4's role and its involvement in related diseases. The second part will explore the enzyme's role in cancer.

6.1. Ferroptosis overview

The term ferroptosis was coined in 2012 to describe a novel form of regulated cell death that is biochemically, morphologically, and genetically distinct from other known mechanisms (such as apoptosis or necroptosis) (122). The ultimate executioner of ferroptosis is the accumulation of phospholipid hydroperoxides (PLOOHs), a process positioned at the intersection of reactive oxygen species (ROS) biology, iron regulation, and lipid metabolism (**Figure 16**) (123).

6.1.1. Iron-dependent lipid peroxidation

The mechanisms initiating lipid peroxidation in ferroptosis are not fully understood but likely involve iron-dependent enzymatic and non-enzymatic processes (124). Among PL structures, PUFA acyl chains, characterized by weak bis-allylic C–H bonds, are the most susceptible to peroxidation. At this position, a radical chain reaction can be initiated either by spontaneous

hydrogen abstraction or by hydroxyl radical (OH·)-mediated abstraction, likely generated through the iron-catalyzed Fenton reaction. Subsequently, the addition of O_2 to the bis-allylic radical forms a phospholipid peroxyl radical (PLOO·), which can react with neighboring lipids, generating PLOOHs and a new radical. Initiation can also be triggered by iron-dependent enzymes, such as specific LOXs (125) or cytochrome P450 oxidoreductase (POR) (126), leading to PLOOH formation. In the presence of labile iron and oxygen, the Fenton reaction further produces alkoxyl (PLO·) or PLOO· radicals from PLOOH, which drives the propagation of the chain reaction. Eventually, this process leads to the generation of numerous secondary products that decompose into highly reactive electrophiles, such as 4-hydroxynonenal and malondialdehyde. These electrophiles react with nucleophilic sites on DNA and proteins, ultimately compromising membrane integrity and causing membrane rupture. Ferroptosis can be experimentally induced by endoperoxide compounds ($FINO_2$), which initiate lipid peroxidation, likely through a Fenton reaction (127). In contrast, endogenous lipophilic radical trapping antioxidants (RTAs) such as α-tocopherol (vitamin E) (128) and exogenous RTAs, including ferrostatin-1 (122) and liproxstatin-1 (129), terminate lipid autoxidation and inhibit ferroptosis (130).

As iron drives the amplification of lipid peroxidation, it serves as a hallmark of ferroptosis. Various physiological processes that alter cellular labile iron levels influence sensitivity to ferroptosis. Iron import mechanisms mediated by transferrin and its receptor (131), as well as the autophagic degradation of ferritin, the cellular iron reservoir (132), promote ferroptosis. Conversly,

mechanisms that facilitate iron export confer resistance to ferroptosis (133,134). Small molecule iron chelators, such as deferoxamine are able to prevent ferroptosis (122).

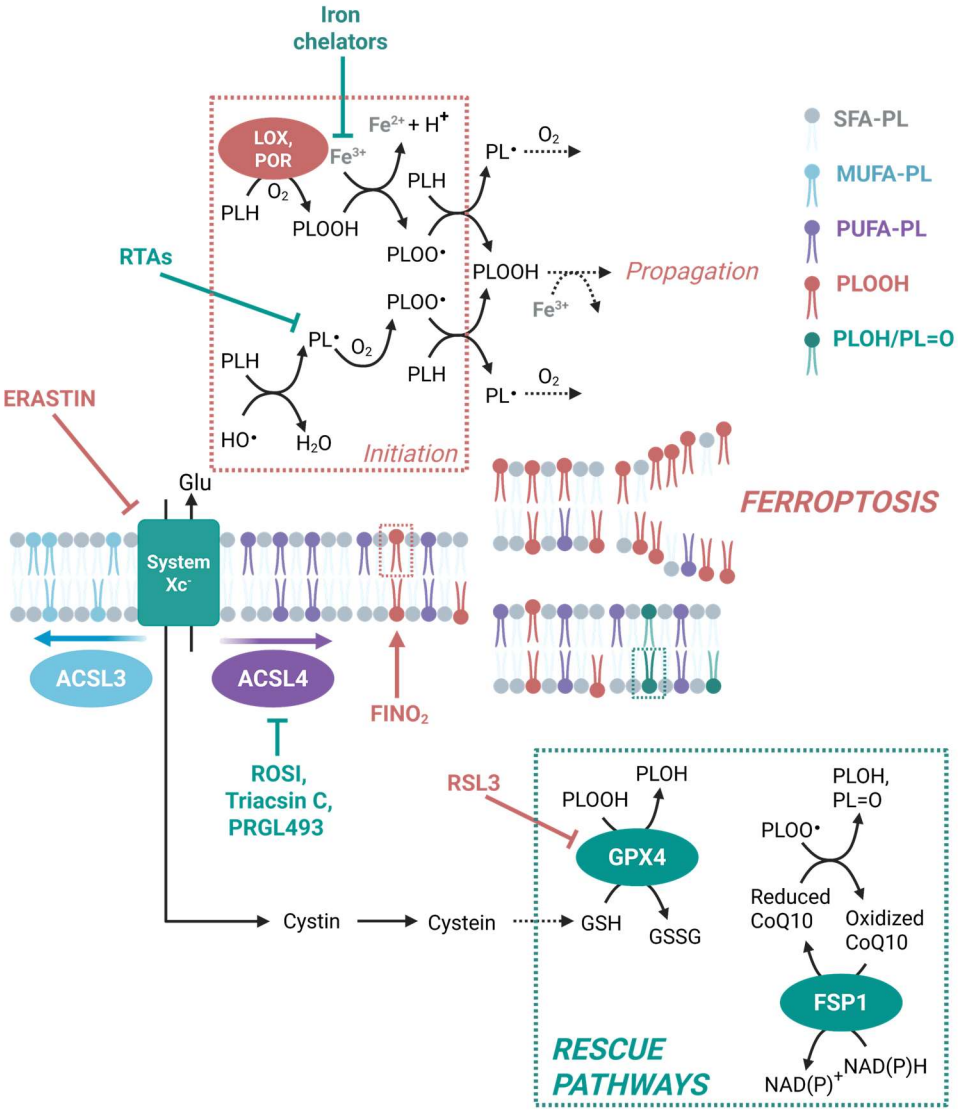

Figure 16. Overview of the ferroptosis mechanism. Ferroptosis occurs when lipid peroxidation surpasses a critical threshold, overwhelming cellular defense mechanisms. ACSL4 promotes ferroptosis by incorporating highly peroxidizable PUFAs into phospholipids (PUFA-PL), whereas ACSL3 counteracts this by favoring MUFA incorporation (MUFA-PL). The mechanisms initiating peroxidation are iron-

dependent and can be enzymatically driven by lipoxigenases (LOXs) or cytochrome oxidoreductase (POR) or mediated via free radicals. Once phospholipid hydroperoxide (PLOOH) are produced, Fenton reaction, involving iron and oxygen propagates the radical chain reaction. Rescue pathways include GSH-dependent GPX4, which directly reduces PLOOH to alcohol (PLOH) derivatives, and NAD(P)H-dependent FSP1, which reduces oxidized endogenous lipophilic antioxidant such as CoQ10. Ferroptosis is experimentally induced by direct GPX4 inhibition with RSL3 or by depleting GSH through system xc^- inhibition with Erastin. Additionally, $FINO_2$ compounds trigger ferroptosis via endoperoxide-mediated lipid peroxidation. Ferroptosis can be suppressed by radical-trapping antioxidants (RTAs), iron chelators, or ACSL4 inhibitors (ROSI, Triacsin C, PRGL493).

6.1.2. Rescue systems

To prevent the accumulation of lipid peroxides and the onset of ferroptosis, cells employ various detoxification pathways. Glutathione peroxidase 4 (GPX4) plays a key role in reducing PLOOHs to their corresponding alcohol derivatives, using gluthatione (GSH) as cofactor (135). Notably, its conditional knockout in mice was shown to induce lipid peroxidation and non-apoptotic cell death even before the term ferroptosis was coined (128). Consistently, the direct inhibition of GPX4 by the covalent inhibitor RSL3 (136) or the inhibition of system x_c^- by Erastin (137), which is involved in cystine import, the precursor of GSH required for GPX4 activity, induce ferroptosis. Inhibiting GPX4 activity constitutes the primary strategy employed to induce ferroptosis in most studies. GPX4 plays a pivotal role in ferroptosis prevention, but it is now clear that it operates alongside other protective systems. Genome-wide screens have identified ferroptosis suppressor protein 1 (FSP1) as an independent ferroptosis regulator (138,139). Mechanistically, FSP1 is recruited to the plasma membrane after

myristoylation, where it recycles oxidized lipophilic RTAs, such as Coenzyme Q_{10} or vitamin E, to their reduced form using NAD(P)H as cofactor.

6.1.3. Lipid metabolism

Due to the propensity of PUFA-PLs to undergo peroxidation, enzymes that increase PUFA incorporation into membrane PLs play a crucial role in driving ferroptosis. Two independent genome-wide haploid and CRISPR-cas9 genetic screens, have uncovered the proferroptotic role of ACSL4 (101,140). The genetic deletion of *ACSL4* confers resistance to RSL3-induced ferroptosis and enables *GPX4* knockout pfa1 cells to proliferate for months (101). Interestingly, this effect is specific to the ACSL4 isoform, as the genetic deletion of other *ACSL* family members does not confer any protection. In addition, the sustained cell viability in the presence of RSL3 is associated with the prevention of lipid peroxidation, as assessed using the lipid peroxidation-sensitive dye BODIPY 581/591 C11. Together, these findings confirm that *ACSL4* knockout effectively prevents ferroptosis. Further (oxo)lipidomics investigation reveals that specific PLs are the preferential substrates for oxidation during ferroptosis (57). In pfa1 cells, treatment with RSL3 or *GPX4* knockout results in an increase of oxygenated arachidonate (AA, 20:4ω-6) and adrenate (AdA, 22:4ω-6) containing PE species. Moreover, *ACSL4* knockout considerably decreases the levels of AA-CoA and AdA-CoA, as well as those of AA and AdA containing PE, along with their oxidized forms in the case of RSL3-treated cells. The finding that

exogenous AA-OOH-PE, but not AA-OOH-CoA, potently enhances RSL3-induced ferroptosis in *ACSL4* knockout cells demonstrates that oxidative damage occurs directly on PE rather than through the re-esterification of preoxidized FAs.

Similar results to those observed with *ACSL4* knockout were obtained with the pharmacological inhibition of ACSL4 using thiazolidinedione (TZD) compounds such as rosiglitazone (ROSI) (101). ROSI protects against RSL3-induced ferroptosis and treated cells present the same changes in the phospholipidome. ROSI has been marketed as a PPARγ agonist, but its antiferroptotic activity is independent of PPARγ, as it is retained in *PPARγ* knockout cells. In addition, ACSL4 inhibition by ROSI in TAM-inducible *GPX4* knockout mice, which typically succumb to renal failure within 12 days, significantly extends their survival.

Beyond its role in enriching membranes with oxidizable FAs and sensitizing cells to ferroptosis, ACSL4 also serves as a key regulatory point in the process. ACSL4 actively participates in a feedforward loop where protein kinase C beta type isoform 2 (PKCβII) senses early lipid peroxidation and responds by phosphorylating ACSL4 at Thr328 (86). This phosphorylation enhances ACSL4 activity, promoting PUFA incorporation into membranes and increasing ferroptosis susceptibility. In addition, several signaling pathways regulate ferroptosis sensitivity by modulating ACSL4 expression (73,74), and ACSL4 itself is considered a biomarker for monitoring ferroptosis (123,141).

The incorporation of PUFA-CoAs into PLs is catalyzed by one of fifteen lysophospholipid acyltransferases (LPLATs), each exhibiting preferences for specific substrates (142). Among them, lysophosphatidylcholine acyltransferase 3 (LPCAT3), involved in the remodeling pathway, has been identified in a genetic screen to have an important role in ferroptosis induction (140). However, *LPCAT3* knockout only provides mild protection against RSL3-induced ferroptosis, suggesting that additional LPLATs might be involved in the esterification of AA and AdA to PE (101). Together, these data strongly support the idea that a specific death signal, driven by distinct oxidized PLs, such as AA- and AdA-PE, directs cells toward ferroptosis. The underlying mechanism remains unclear but may involve the specific localization of PE within cells or its particular arrangement in membranes, which could facilitate the binding of peroxidation-initiating proteins such as LOX.

In contrast to the ferroptosis-sensitizing role of PUFAs, exogenous MUFA supplementation or increased biosynthesis via stearoyl-CoA desaturase 1 protects against ferroptosis by displacing oxidizable PUFAs from PLs in an ACSL3-dependent (125,143,144).

6.2. Ferroptosis in physiology

Whether ferroptosis plays a role in normal physiology or merely represents an adverse consequence of cellular iron and oxygen utilization, which cells have evolved to regulate, remains unclear. Ferroptosis might be involved in tumor suppression, since multiple tumor suppressors, including p53, sensitize

cancer cells to ferroptosis (145,146). It could also play a role in immune surveillance as, CD8+ T cells production of interferon-γ, suppresses system x_c^- and stimulates ACSL4, inducing tumor cell ferroptosis (147,148). Recent studies go further, demonstrating that ferroptosis, propagated by trigger waves, drives a massive, spatially restricted cell death event during muscle remodeling in the embryonic avian limb (149). These findings provide the first evidence of ferroptosis as a tissue-sculpting mechanism during organismal development.

6.3. Ferroptosis in pathologies

In contrast to its putative role in normal physiology, ferroptosis has been implicated in a wide range of human pathologies, including cancer, ischemia-reperfusion injuries (IRI), and neurodegenerative diseases (NDD). After briefly discussing the implication of ferroptosis in cancer and the potential therapeutic benefits of its induction, the focus will shift to ferroptosis-related diseases where its inhibition, particularly through ACSL4 inhibition, emerges as a promising treatment strategy.

6.3.1. Ferroptosis in cancer

The discovery of ferroptosis originates from studies on novel antitumoral compounds that selectively target RAS-mutated cancer cells (150,151). The two ferroptosis inducers RSL3 (oncogenic-RAS-selectively lethal) and Erastin derive their names from this original design. Since then, classical ferroptosis inducers have been shown to be lethal to a wide range of cancer

cells, as reviewed here (152). Additionally, several marketed drugs, including targeted therapies (sorafenib), chemotherapy agents (cisplatin), anti-inflammatory drugs (sulfasalazine), and lipid-lowering drugs (simvastatin), all with antitumor activity, are also capable of inducing ferroptosis. Furthermore, ferroptosis has been implicated in the death mechanism of immunotherapy and radiotherapy-treated cancer cells (147,153). The susceptibility of cancer cells to ferroptosis is thought to stem from their heightened metabolic activity and increased ROS load. This vulnerability is particularly pronounced in mesenchymal and dedifferentiated cancer cells, which are typically resistant to conventional treatments, as well as in therapy-persister cancer cells (154–156). This positions ferroptosis induction as a promising approach for developing novel antitumoral treatments.

6.3.2. Ferroptosis and ACSL4 in ischemia-reperfusion injuries

Ischemia-reperfusion (IR) is a pathological condition caused by the temporary restriction and subsequent restoration of blood supply to an organ (157). It underlies various disorders, including heart attack, stroke, acute kidney injury and is a major concern in organ transplantation. While the ischemic phase induces hypoxia, reperfusion, though essential for survival, triggers oxidative damage and cell death, ultimately exacerbating tissue injury. Dysregulation of key ferroptosis regulators has been observed in various rodent models of IR injuries. For instance, GPX4 is downregulated in the kidney (158), and heart (159), ACSL4 is upregulated in the lung (160) and intestine (73), and 15-LOX is activated in the heart (161,162) during IR. More

specifically, these dysregulations occur during the ischemic phase, priming cells for ferroptosis, which is triggered early during reperfusion, as evidenced in a mouse model of intestinal IR (**Figure 17**) (73).

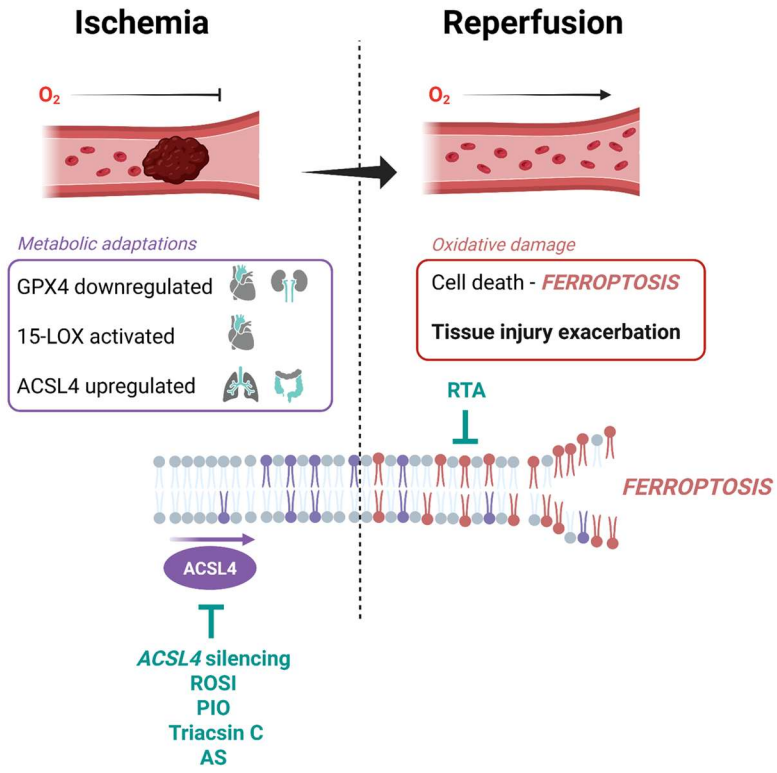

Figure 17. Role of ferroptosis in ischemia-reperfusion injury (IRI). Metabolic adaptations during the ischemic phase increase cellular susceptibility to the oxidative stress of reperfusion, leading to cell death, partly through ferroptosis, and exacerbating tissue damage. Targeting ferroptosis, either by inhibiting ACSL4 prior to reperfusion or by blocking lipid peroxidation with radical trapper antioxidant (RTA), can mitigate tissue injury. PIO, pioglitazone; AS, AS-252424.

Furthermore, ferroptosis inhibitors, such as RTAs (ferrostatin-1 and liproxstatin-1) alleviate tissue damages in rodent models of IR affecting the heart (163), liver (129), lung (160), kidney (164), intestine (73) and brain (133). Similar protective effects are observed when targeting ACSL4. Knockdown of *ACSL4* reduces IR-induced lipid ROS accumulation and cell lethality in lung epithelial cells (160). Moreover, inhibition of ACSL4 by ROSI prevents ferroptosis and improves pulmonary function in a mouse model of lung IR. Consistently in the intestine, *ACSL4* silencing rescues IR-induced cell death and decreases lipid peroxidation in Caco-2 cells, while ROSI protects against intestinal IR injuries and mitigates intestinal barrier dysfunction *in vivo* (73). ACSL4 expression also influences the outcome of acute IR brain injuries across different models (165). In an oxygen-glucose deprivation (OGD) model using N27 neuronal cultures, which are highly sensitive to ferroptosis, *ACSL4* knockout confers resistance to OGD/reperfusion-induced toxicity, whereas ACSL4 overexpression increases vulnerability. Similarly, in various rodent models of brain IR, ACSL4 overexpression exacerbates injury by increasing infarct volume, worsening neurological scores, and impairing motor coordination, while *ACSL4* knockout has the opposite effect. Consistently, ACSL4 inhibition by pioglitazone (PIO) or triacsin C provides neuroprotection *in vitro* and improves functional outcomes *in vivo*.

Recently, AS-252424, a known PI3-kinase inhibitor repositioned as an ACSL4 inhibitor, has been shown to suppress ferroptosis and protect against IR-induced acute kidney and liver injuries in mouse models (93).

However, it is important to highlight that in these studies, inhibitors are administered at least one hour before ischemia induction to allow sufficient time for proper phospholipid remodeling. The unpredictability and often-extreme acuteness of conditions such as stroke and ischemic heart injuries provide only a narrow window for intervention. Whether ferroptosis inhibitors, particularly ACSL4 inhibitors, could be effective as crisis treatments remain to be demonstrated.

In organ transplantation, however, IR is inevitable but predictable. Administration of RTAs during organ preservation alleviates cold IR injuries in donor lungs (166) and livers (167) and prevents cardiomyocyte cell death and neutrophil recruitment in heart transplant recipients (168). Further investigations are required to determine whether ACSL4 inhibitors could be used in this context.

6.3.3. Ferroptosis and ACSL4 in neurodegeneration

For a long time, brain iron accumulation and its abnormal deposition in specific regions associated with motor and cognitive dysfunctions have been linked to ageing and various neurodegenerative diseases (169). With the identification of an iron-dependent cell death, the role of ferroptosis in neurodegeneration has become an area of intense investigation. Emerging evidence suggests that ferroptosis is implicated in the pathological development of neurodegenerative diseases, including Alzheimer's disease (AD), Parkinson's disease (PD), amyotrophic lateral sclerosis (ALS), and Huntington's disease (HD).

AD is the most common neurodegenerative disease and it is characterized by extracellular accumulation of amyloid β (Aβ)-plaques and intracellular neurofibrillary tangles of hyperphosphorylated tau protein. AD progressively affects memory, cognition, and behavior. In addition, there is a close association between AD and cardiac anomalies, as Aβ-plaques often deposit in the heart. Primary evidence of ferroptosis involvement in AD comes from studies where conditional knockout of *GPX4* in the mouse forebrain leads to symptoms resembling AD (170). Notably, these symptoms can be ameliorated by the administration of ferroptosis inhibitors such as RTAs. Consistently, the overexpression of GPX4 in 5xFAD mice, a widely used model of AD, reduces neurodegeneration and improves their learning and memory abilities (171). There is also substantial evidence highlighting the close interconnection between Aβ pathology and ferroptosis. In post-mortem human brain tissues, Aβ plaques exhibit dysregulation of several ferroptosis biomarkers, including reduced GPX4 levels, with these alterations worsening as AD pathology progresses (172). Additionally, ferroptosis inhibition by RTAs reduces Aβ-like aggregation and lipid peroxidation in a human brain organoid model of AD. Notably, ACSL4 deficiency in 5xFAD mice decreases both Aβ plaque load and lipid peroxidation in the brain (173). Furthermore, Triacsin C-mediated ACSL4 inhibition completely prevents Aβ-induced cell toxicity and contractile dysfunction in cardiomyocytes from wild-type mice (174).

After AD, PD is the second most prevalent neurodegenerative disorder. It is characterized by the progressive loss of dopaminergic neurons in the

substantia nigra (SN), leading to motor symptoms such as tremor, rigidity, and bradykinesia. A key hallmark of PD is the accumulation of intracellular α-synuclein aggregates, which interact with cellular membranes, causing permeabilization, ion flux disruption, and altered membrane conductance (175,176). Numerous ferroptosis biomarkers, such as decreased GPX4 and FSP1 and increased ACSL4 levels, are observed in the SN of 1-methyl-4-phenyl-1,2,3,6-tetrahydropyridine (MPTP)-induced PD mouse model (177). Consistently, ACSL4 is overexpressed in neurons, microglia and endothelial cells from the SN of PD patients (178). Interestingly, the locomotor behavioral deficit and neuronal loss are alleviated by ferroptosis inhibition with an RTA in MPTP-treated mice (179). In addition, *ACSL4* knockdown or its inhibition by Triacsin C enhances the survival of N27 and N2a cells exposed to 1-methyl-4-phenylpyridinium (MPP^+), the toxic metabolite of MPTP, while also reducing lipid ROS levels (178). Furthermore, *ACSL4* knockdown or treatment with Triacsin C protects against dopaminergic neuronal death and mitigates parkinsonian phenotypes in MPTP-treated mice. Several studies also highlight interconnections between α-synuclein aggregation and ferroptosis. Labile iron accelerates the spontaneous oxidation of dopamine into a nucleophilic dopamine quinone (180) which covalently binds to GPX4 and promotes its degradation (181) via the ubiquitin pathway (182). The E3 ubiquitin ligase responsible for GPX4 degradation, NEDD4, is upregulated by α-synuclein, one of its substrates. This supports a model in which α-synuclein, dopamine, and iron cooperate to drive ferroptosis. Furthermore, *in vitro* studies on cortical neurons reveal that lipid peroxidation facilitates the interaction between α-synuclein aggregates and membranes,

while α-synuclein oligomers further promote lipid ROS accumulation (183). Notably, the toxicity of α-synuclein aggregates is completely abolished by iron chelators or RTAs *in vitro*. Finally, overexpression of human α-synuclein in the primary cortex of mice induces ferroptosis, leading to the loss of parvalbumin interneurons and impaired motor learning (184). However, the conditional knockout of *GPX4* in mouse dopaminergic neurons induces only prodromal PD symptoms, including an anxiety-related phenotype, without causing neurodegeneration or motor dysfunction (185). This suggests that dopaminergic neurons are at least partially resistant to ferroptosis. It has been hypothesized that the co-dependence of α-synucleinopathy and ferroptosis may explain why models based on a single factor alone fail to recapitulate the later-stage phenotypes of PD (183).

In ALS, degeneration affects motor neurons, leading to progressive weakness, paralysis, and ultimately respiratory failure. Unlike dopaminergic neurons, motor neurons in ALS are particularly vulnerable to ferroptosis. The conditional *GPX4* knockout in mouse neurons leads to preferential degeneration of spinal motor neurons, paralysis and death (186). Moreover, forced expression of GPX4 in ALS mouse models significantly delays motor neuron degeneration and disease progression (187). Additionally, multi-omics analysis in spinal motor neurons of ALS human induced pluripotent stem cells reveals dysregulated lipid metabolism and elevated arachidonate levels, suggesting that ACSL4 might be involved in this ferroptosis vulnerability (188).

HD is characterized by progressive cognitive, behavioral and motor dysfunctions associated with short life spans. Neurodegeneration in HD is caused by a mutation in *HTT* that results in the expression of a toxic mutated huntingtin (mHTT). Expression of mHTT alone does not induce ferroptosis but greatly sensitizes neurons to Erastin-induced ferroptosis (189). Furthermore, *ACSL4* knockout or inhibition by ROSI or troglitazone (TRO) completely prevents this increased susceptibility. However, *ACSL4* knockout in an HD mouse model does not significantly extend their lifespan.

Inhibiting ferroptosis may offer a promising strategy to mitigate the progression of several neurodegenerative diseases. Targeting ACSL4 appears particularly compelling, especially in AD and PD, where its implication has been more extensively investigated (**Figure 18**).

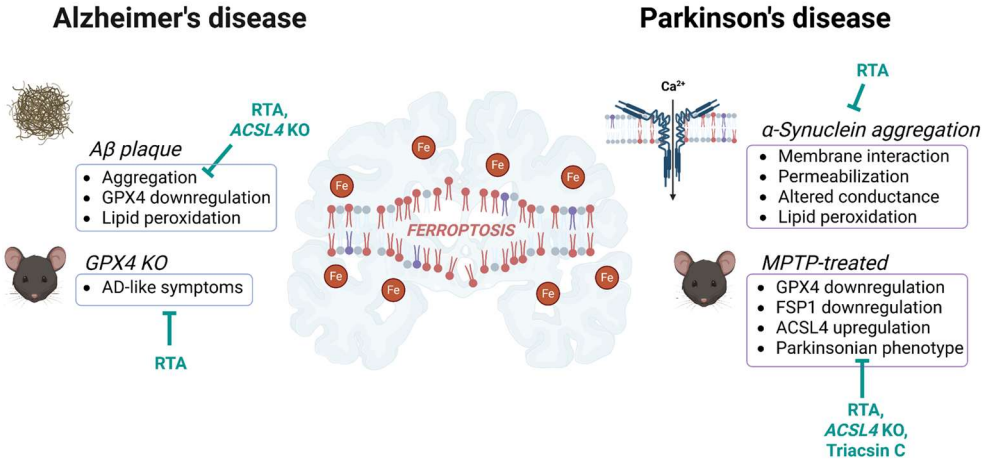

Figure 18. Targeting ferroptosis as a therapeutic strategy in Alzheimer's and Parkinson's disease.

6.4. Role of ACSL4 in cancer

Considering the pivotal roles of ACSL4 in various biological processes, including lipid metabolism, inflammation, steroidogenesis, and ferroptosis, its impact on cancer is highly context-dependent. Depending on the cancer type, subtype and stage, ACSL4 can either promote tumor proliferation or inhibit cancer cell growth. Specifically, ACSL4 is upregulated in several cancers, including prostate (190), liver (191,192), and colon (193) cancers, while it is downregulated in others, such as lung (194) and leukemia (195). Typically, in cancers with high ACSL4 expression (e.g. liver and prostate cancers), increased levels are generally associated with an unfavorable prognosis, whereas in cancers with low ACSL4 expression (e.g. lung cancer), decreased levels predict poor prognosis (190,194,196). Because of this, ACSL4 may serve as a risk, diagnostic and prognostic biomarker (197). In the following section, cancers in which ACSL4 plays a pro-tumoral role and where ACSL4 inhibition represents a potential therapeutic strategy will be discussed.

6.4.1. Hepatic cancer

Multiple studies have shown that ACSL4 is overexpressed in human hepatocellular carcinoma (HCC) (64,191,198–200). Moreover, ACSL4 expression correlates with TNM stage, and survival analysis indicate a significant reduction in overall and disease-free survival in HCC patients with high ACSL4 expression (199,200). ACSL4 contributes to the reprogramming of lipid metabolism in HCC cells. Silencing ACSL4 in Huh7 and SMMC-

7721 cells considerably reduces lipid content, including levels of FAs, TAGs and cholesterol (201). Mechanistically, ACSL4 stabilizes the oncoprotein c-Myc by inhibiting its degradation through the ubiquitin-proteasomal pathway (200). In turn, c-Myc transcriptionally regulates the expression of sterol regulatory element-binding protein 1 (SREBP1), the master regulator of lipogenesis, which promotes the expression of several lipogenic enzymes, including ACC, FAS, and SCD (201). Cancer cells benefit from *de novo* FA synthesis, as it supplies essential structural components, serves as an energy source, and generates key signaling molecules that support tumor growth and progression (202). Another study reveals that hexokinase 2 enhances FAO by promoting ACSL4 expression (203).

Silencing *ACSL4* restricts the proliferation of HCC cells, such as Hep3B, Huh7 and C3A cells, whereas forced *ACSL4* expression in SNU-398, Bel-7402, and PLC/PRF5 cells, which naturally exhibit low expression, promotes cell growth (191,192,200,203). Furthermore, the growth-restricting effects of *ACSL4* silencing are recapitulated with ACSL4 inhibition by Triacsin C or ROSI (200,203). Finally, ACSL4 depletion in HCC xenografts mouse model significantly reduces tumor growth (200). Together these data suggest that inhibiting ACSL4 might be a potential approach to impair HCC progression.

However, the pro-ferroptotic role of ACSL4 may also contribute to the antitumoral activity of sorafenib, the first-line treatment for HCC. Beyond its inhibition of multiple angiogenesis-associated kinases, sorafenib exerts its cytotoxic effects by inducing ferroptosis through system xc^- inhibition

(137,204). ACSL4 expression is negatively-correlated with sorafenib IC_{50} values in a panel of HCC cell lines and *ACSL4* knockdown reduces sorafenib efficacy *in vitro* and *in vivo* (205). This is reflected in patients, where those with higher ACSL4 expression generally show a better response to sorafenib.

6.4.2. Colorectal cancer

ACSL4 is overexpressed at both mRNA and protein levels in colon adenocarcinoma compared to adjacent normal tissues (193,206,207). Notably, this upregulation appears to emerge during the transition from adenoma to adenocarcinoma, as adenomas exhibit ACSL4 expression levels comparable to normal tissue (193). Additionally, the tumor promoter PMA elevates ACSL4 levels in Int407 intestinal cancer cell line. In two independent statistical analyses of stage II colorectal cancer (CRC) patient samples, high ACSL4 expression correlates with poorer clinical outcomes (208). Furthermore, a multivariable model demonstrates that the combined overexpression of ACSL4, ACSL1, and stearoyl-CoA desaturase (SCD) is associated with a significantly increased risk of relapse, with greater predictive power and statistical strength than any of these genes alone.

Silencing *ACSL4* in colorectal cancer (CRC) cell line HCT116, significantly reduces cell proliferation and invasion (207). In contrast, overexpression of ACSL4 has the opposite effect, promoting cell proliferation and invasion. The combined overexpression of ACSL4, ACSL1, and SCD in DLD-1 CRC cells induce a mesenchymal-like morphology, provokes the disruption of membrane-associated E-cadherin expression and the translocation of β-

catenin from the membrane to the nucleus (208). Accordingly, the expression of epithelial markers is downregulated, while the expression of epithelial-to-mesenchymal transition (EMT) genes is upregulated. No morphological changes, mislocalization of E-cadherin, or alterations in epithelial marker expression are observed in cells singly overexpressing any of these genes, indicating that their cooperative activity is required to drive EMT. Moreover, the combined overexpression enhances migration, invasion and cell survival capabilities without affecting proliferation.

Several mechanisms underlying the pro-tumoral role of ACSL4 in CRC have been identified. Notably, ACSL4 appears to enhance vascular endothelial growth factor (VEGF) signaling, as suggested by the correlation between ACSL4 expression, VEGF receptor levels, and increased secretion of VEGF *in vitro* (207). Moreover, exogenous arachidonate, can induce apoptosis through caspase 3 activation in CRC (HT-29) and other cell lines (206). Therefore, the elevated levels of ACSL4 and COX-2 observed in CRC may function as an apoptosis-evading mechanism by reducing the availability of free arachinodate (20:4ω-6). Additionally, ACSL4 contributes to the ACSL-SCD axis in driving an EMT-like metabolic shift in CRC, although its precise role in this process remains unclear.

ACSL inhibition by Triacsin C induces apoptosis in HT-29 cells, and this effect is enhanced when combined with COX-2 inhibition by sulindac (206). Triacsin C also reduces the viability of DLD-1 and SW620 cells, with an IC_{50} of approximately 2 μM (208). Furthermore, the combination of Triacsin C

with an SCD inhibitor at low concentrations synergistically reduces viability in multiple CRC cell lines, including DLD-1, SW620, HT-29, and LS174T. Notably, this combined treatment reverses the mesenchymal phenotype observed in DLD-1 cells overexpressing ACSL4, ACSL1, and SCD. In addition, the combination is also effective on CRC cells resistant to conventional chemotherapy. Importantly, the same inhibitors concentrations that drastically reduce CRC cell viability are completely ineffective on normal colonocytes (CCD18CO and CCD841). Therefore, targeting ACSL4, in combination with other treatments, offers a potential therapeutic approach for CRC.

6.4.3. Breast cancer

Breast cancer (BC) is subcategorized based on the expression of hormone receptors, including estrogen receptor (ER), progesterone receptor (PR), human epidermal growth factor receptor 2 (HER2), and androgen receptor (AR) (209). Cancers that do not express ER, PR, and HER2 are classified as triple-negative breast cancers (TNBC), whereas those lacking all four receptors are referred to as quadruple-negative breast cancers (QNBC). While the majority of BC express ER, TNBC and QNBC exhibit a more aggressive phenotype and currently lack targeted treatment options. Observational analyses in both cells and tumor samples reveal that there is an inverse relationship between expression of ACSL4 and steroid hormone/HER2 receptors in BC (210,211). ACSL4 is overexpressed in TNBC and particularly in QNBC, where it has been proposed as a biomarker (211).

Additionally, immunohistochemical analysis of patient tissues reveals that ACSL4 expression correlates with N stage, distant metastasis, and poor overall survival (212).

In MCF-7 cells, which are ER-positive and ACSL4-negative, forced ACSL4 expression induces a reduction in ER, PR and AR levels, while silencing ER induces ACSL4 expression. Conversely, forced expression of ER in naturally ER-negative MDA-MB-231 cells downregulates ACSL4 (213). This inverse relationship affects the response to targeted therapies. Forced ACSL4 expression in estrogen-dependent MCF-7 cells and in HER2-positive SKBr3 cells induces resistance to tamoxifen and lapatinib, respectively (211). However, forced expression of ACSL4 also confers resistance to non-targeted therapies, including etoposide (211), cisplatin, doxorubicin, and paclitaxel, likely through the upregulation of multidrug resistance transporters (214).

ACSL4 also influences the progression of BC. Forced expression of ACSL4 in ACSL4-negative BC cells results in an increased growth, invasion and migration (211,215). Conversely, knockdown of *ACSL4* in MDA-MB-231 cells has the opposite effect, reducing cell proliferation, invasion, and migration (215). Notably, the increased migration of TNBC cells is ACSL4-specific, as silencing other *ACSL* isoforms does not produce a significant effect (216).The growth-promoting effect mediated by ACSL4 is also observed *in vivo* across different xenograft mouse models (211,216–218). Additionally, ACSL4 facilitates TNBC metastasis, as its depletion in tumors

derived from MDA-MB-231 and 4T1 cells significantly reduces metastatic burden in the lungs and liver of nude mice (212,216).

Different mechanisms underlie the role of ACSL4 in driving a more aggressive and metastatic form of BC. It has been proposed that ACSL4 mediates the intramitochondrial transport of arachidonate through a pathway involving ACOT2, as steroidogenic cells do (215). This leads to the production of 5-LOX metabolites, which upregulate COX-2 expression and facilitate the synthesis of PGE2. PGE2 in turn plays a pivotal role in shaping the inflammatory microenvironment that fosters cancer initiation and progression, as evidenced across various cancer types (219). ACSL4 also promotes the PUFA-PL production, which levels are particularly elevated in TNBC cells (212). This alters the physical properties of membranes, increasing their fluidity and facilitating the recruitment of activated integrin β1 into lipid rafts, thereby enhancing the metastatic potential of cancer cells.

Pharmacological targeting of ACSL4 produces results similar to those observed with genetic ablation. Inhibiting ACSL4 activity with PRGL493 suppresses the proliferation (IC_{50} = 23 μM), restricts the migration of MDA-MB-231 cells, and reduces tumor growth in a xenograft mouse model (92). PRGL493 treatment also significantly reduces the metastatic burden following orthotopic implantation of MDA-MB-231 cells (212). Although, another study reports that PRGL493 does not significantly impact the proliferation of 4T1 and MDA-MB-231 cells, the compound effectively

impairs their invasiveness and migratory capabilities both *in vitro* and *in vivo* in this experimental setup (216).

In addition, inhibiting ACSL4 in combination with various other therapies has demonstrated beneficial effects. Inhibition of ACSL4 with PRGL493 sensitizes MDA-MB-231 cells to hormonal therapy (92). The combination of ACSL4 inhibitors, such as PRGL493 or Triacsin C, with chemotherapeutic agents like doxorubicin, paclitaxel, or cisplatin demonstrates a strong synergistic effect in inhibiting MDA-MB-231 cell proliferation (92,214). Moreover, the combination of PRGL493 with paclitaxel and cisplatin in mice leads to greater tumor growth reduction and a more pronounced decrease in lung and liver metastatic burden compared to individual treatments (212). Similarly, the combination of ACSL4 inhibition using ROSI, TRO, or Triacsin C, along with a 5-LOX inhibitor and a COX inhibitor, synergistically suppresses MDA-MB-231 cell proliferation and migration while also reducing tumor growth *in vivo* (217). Intriguingly, however, Triacsin C alone shows higher cytotoxicity in BC cells that lack ACSL4 expression, suggesting that its effects may involve other targets, as it is also known to inhibit ACSL1 and ACSL3 (210,211).

In summary, these findings suggest that ACSL4 acts as a biomarker for specific breast cancer subtypes, drives resistance to hormonal therapy and chemotherapy, and promotes the progression of BC. This positions ACSL4 as a promising target for TNBC and QNBC, particularly in adjuvant therapies.

6.4.4. Prostate cancer

Patients with advanced prostate cancer (PC) initially respond well to androgen deprivation therapy (220). However, the treatment eventually selects for cancer cells that adapt to androgen deprivation, resulting in the development of castration-resistant prostate cancer (CRPC), the leading cause of PC-related mortality. Importantly, CRPC preserves AR signaling through diverse mechanisms, one of which involves acquiring steroidogenic capabilities (221). Similarly to BC, in PC, there is an inverse correlation between androgen receptor (AR) expression and ACSL4 levels, as observed in different PC cells (190,210). Mechanistically, AR transcriptionally represses *ACSL4* by binding to the androgen response element within its promoter region (77). Immunohistochemical analysis of PC tissues reveals that ACSL4 expression is elevated in malignant cells compared to benign epithelial cells, especially in CRPC (190). Further evidence suggests that ACSL4 directly contributes to the development of CRPC. Forced expression of ACSL4 in androgen-dependent LNCaP cells, which do not naturally express ACSL4, decreases their sensitivity to antiandrogen treatment (190).

ACSL4 is also associated with progression of PC. Forced expression of ACSL4 in LNCaP cells results in an increased proliferation, migration and invasion (190). Conversely, *ACSL4* knockdown in androgen-independent PC cells (PC-3 and DU145), which endogenously express ACSL4, reduces proliferation, migration and invasion (77,190). Consistent with in vitro findings, LNCaP xenografts with forced ACSL4 expression exhibit a

significantly accelerated tumor growth rate in mice, whereas *ACSL4* knockdown in PC-3 and DU145-derived tumors markedly inhibits growth.

Pharmacological inhibition of ACSL4 in PC-3 cells by PRGL493 significantly reduces steroidogenesis as evidenced with decreased StAR and progesterone levels (92). In addition, PRGL493 treatment inhibits proliferation (IC_{50} = 27 μM) and migration in PC-3 cells while also reducing proliferation in primary cell cultures derived from tumor tissue samples of PC patients. Furthermore, the combination of PRGL493 and docetaxel synergizes in inhibiting cell proliferation. Finally, PRGL493 reduces the growth of PC-3-derived tumors in mice. This suggests that ACSL4 inhibition represents a viable pharmacological target in CRPC.

6.4.5. Ovarian cancer

Recently, a correlation has been established between metastatic potential and ferroptosis sensitivity in several cancers, including ovarian, liver and head and neck cancers (222). Further analysis through *in vivo* genetic screens in an ovarian cancer (OC) distal metastasis mouse model identified ACSL4 as a pro-metastatic gene. Notably, ACSL4 depletion in selected pro-metastatic OC cells (ES-2-MC2-Hep) significantly reduces the lung metastasis burden after intraperitoneal implantation, without affecting cell proliferation *in vitro* and subcutaneous tumor growth. Mechanistically, ACSL4 facilitates extravasation during hematogenous metastasis, as suggested by the reduced number and size of metastatic lung lesions following intravenous implantation of *ACSL4* knockout ES-2-MC2-Hep cells. This is further

supported by the observation that deep lung perfusion more efficiently clears *ACSL4* knockout metastatic cells, as they remain trapped in the lung capillaries. Consistently, PRGL493-mediated ACSL4 inhibition reduces cancer cell burden in the lung parenchyma following perfusion, whereas in the absence of perfusion, the total metastatic burden remains unchanged. The evaluation of membrane fluidity using a fluorescent probe compatible with live cells demonstrates that ACSL4 depletion leads to a decrease in membrane fluidity that is restored in ACSL4-rescuing cells. ACSL4 depletion also reduces invasiveness *in vitro*. Furthermore, increasing arachidonate content in parent ovarian cancer cell (ES-2-*GFP*-luc) phenocopies ACSL4's function and promotes metastatic extravasation after intravenous implantation. Together, these results suggest that ACSL4 facilitates ovarian metastatic extravasation, likely by increasing PUFA-PL content, which enhances membrane fluidity and promotes invasiveness.

Although ACSL4 promotes extravasation by increasing PUFA-PL content in metastatic cells, it also creates dependencies on enzymes involved in preparing PUFAs for β-oxidation, which is crucial for the early stages of colonization. These enzymes include isomerases and reductases such as enoyl-CoA isomerase 1 (EC1) and enoyl-CoA hydratase 1 (ECH1), respectively. Depleting these enzymes in ES-2-MC2-Hep cells reduces subcutaneous tumor growth in mice, while having no effect on cell proliferation *in vitro*, suggesting a role in colonization. As a result, the double knockout of *ACSL4* and *ECH1* in ES-2-MC2-Hep cells further reduces lung metastatic burden after intravenous injection compared to single-gene

deletion. Additional investigations are needed to determine whether dual inhibition of ACSL4 and ECH1 could offer a viable pharmacological option.

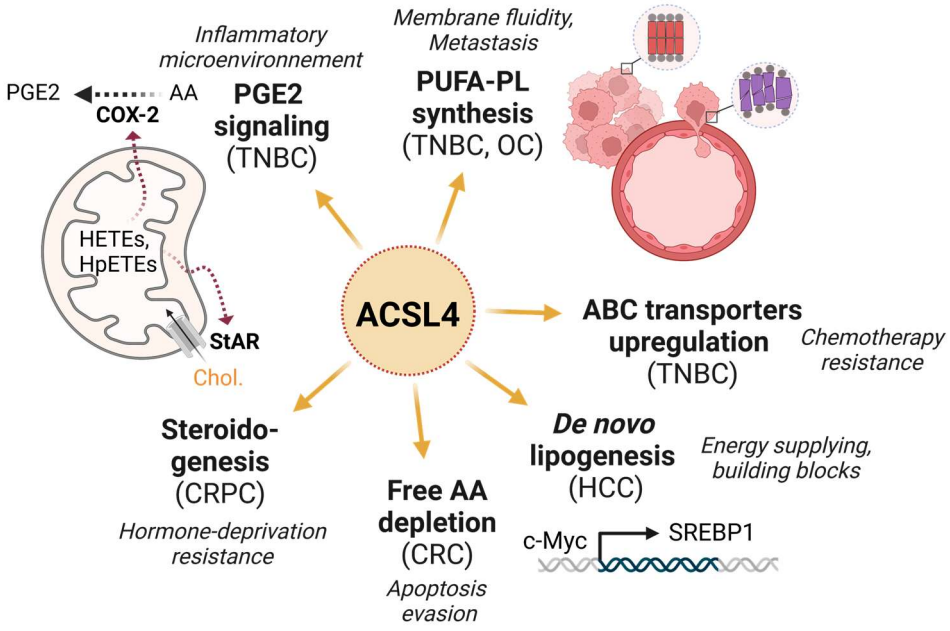

Figure 19. Pro-tumoral roles of ACSL4. ACSL4 promotes PUFA-PL synthesis, increasing membrane fluidity and facilitating metastasis in triple-negative breast cancer (TNBC) and ovarian cancer (OC). ACSL4 contributes to chemotherapy resistance, potentially by upregulating ABC transporters involved in drug efflux in TNBC. In hepatocellular carcinoma (HCC), ACSL4 enhances *de novo* lipogenesis by stabilizing c-Myc, which stimulates SREBP1 expression, leading to upregulation of lipogenic enzymes. By depleting unesterified arachidonate (AA), ACSL4 prevents induction of apoptosis in colorectal cancer (CRC). ACSL4 supports abnormal steroidogenesis in castration-resistant prostate cancer (CRPC), enabling tumor cell survival in androgen-deprived conditions. Lastly, ACSL4 fosters a pro-inflammatory microenvironment by upregulating COX-2 and promoting PGE2 synthesis in TNBC.

Targeting ACSL4 represents an appealing therapeutic approach in HCC, CRC, TNBC, CRPC, and OC, as it limits tumor growth, impairs metastatic potential, or both. **Figure 19** illustrates examples of the advantages conferred to cancer cells by ACSL4. The numerous synergistic effects observed when ACSL4 inhibitors are combined with various compounds, including conventional chemotherapies and targeted therapies, offer great promise for adjuvant treatment strategies. However, these ACSL4-overexpressing cancers generally exhibit high ferroptosis sensitivity, as the two are closely linked (141). Ferroptosis induction in cancer may result from tumor-suppressive mechanisms or, at the very least, it provides a potent alternative strategy that critically depends on ACSL4 activity. Thus, ACSL4 plays a dual role in these cancers: promoting cancer progression through lipid metabolism reprogramming, while also exhibiting antitumoral activity by enhancing ferroptosis vulnerability. This highlights the complexity of targeting ACSL4 in cancer. It is conceivable that the benefit of inhibiting ACSL4 versus inducing ferroptosis largely depends on the specific context. Future studies will define the conditions under which each approach is most effective.

7. ACSL4 inhibitors

Given the growing recognition of ACSL4 as an attractive therapeutic target, recent efforts have focused on developing novel, optimized pharmacological inhibitors. In this section, we first examine the early identified ACSL4

inhibitors, such as ROSI and Triacsin C, followed by a discussion of more recently developed compounds with notable properties. The structures and pharmacological characteristics of these inhibitors are summarized in **Figure 20**.

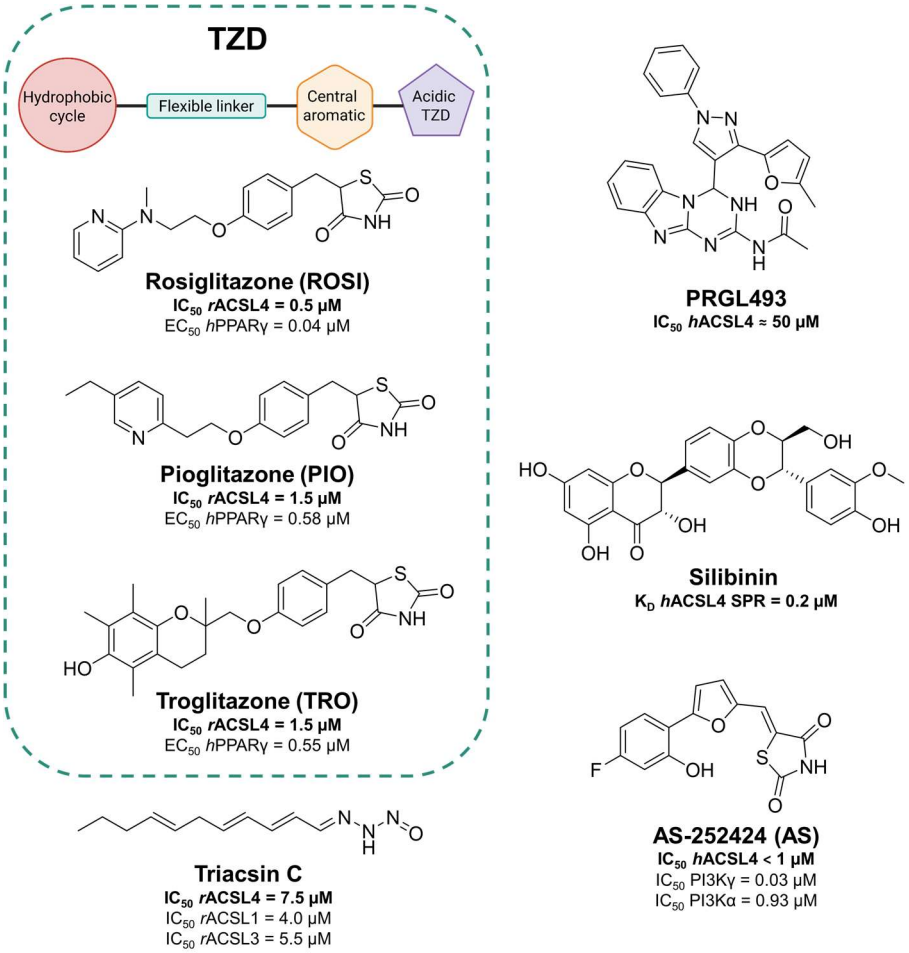

Figure 20. Structure and pharmacological properties of ACSL4 inhibitors.

7.1. Thiazolidinediones (TZD)

ROSI is the reference ACSL4 inhibitor, widely used overall and especially in studies related to ferroptosis. It belongs to the thiazolidinedione (TZD) family, a class of oral insulin-sensitizing agents used in the treatment of type 2 diabetes owing to their potent PPARγ agonist activity (223,224).

The TZD pharmacophore features a hydrophobic cyclic moiety connected via a flexible linker to a central aromatic ring, which is *para*-substituted with an acidic TZD group (**Figure 20**).

Among the TZD family, ROSI, TRO and PIO have been thoroughly studied for their ACSL4 inhibitory activity (39,225–227). ROSI is the most potent, with an IC_{50} of 0.5 µM, while TRO and PIO show IC_{50} values of 1.5 µM (226). TRO displays a mixed inhibition mechanism with respect to palmitate and ATP, and an uncompetitive mechanism toward CoA.

An interesting feature of ROSI is its selectivity for ACSL4 within the ACSL family (39,226). It displays over 15-fold greater activity toward ACSL4 compared to ACSL1 and ACSL5, and shows no significant inhibition of ACSL3 and ACSL6.

TZDs are frequently used as reference compounds to inhibit ferroptosis via ACSL4 targeting (101). Among them, TRO shows the most pronounced antiferroptotic activity, despite being a less potent ACSL4 inhibitor. This effect is likely attributable to its chromanol moiety, shared with vitamin E, which has inherent antioxidant properties. However, given the central role of lipid metabolism in ferroptosis, the potent PPARγ activity of TZDs represents

a significant liability, as PPARγ is an important regulator of lipid metabolism (228). In fact, several recent publications report that PPARγ activation inhibits ferroptosis, using the same TZD compounds that serve as reference ACSL4 inhibitors in other studies (229–232).

Thus, their lack of selectivity represents a critical issue for their use as pharmacological tools inhibiting ACSL4. It has been noticed that the acidic TZD head group in ROSI is essential for its binding to PPARγ, as methylation of the TZD nitrogen, which neutralizes its acidity, abolishes ROSI's ability to bind PPARγ (233). Therefore, TZD modification to gain ACSL4 selectivity might be possible. Moreover, ROSI, TRO, and PIO differ in their western moieties, suggesting that this region of the scaffold tolerates modifications and could be further optimized to enhance ACSL4 inhibition. The finding that the sulfo-conjugated metabolite of TRO, modified at the hydroxyl group of the chromanol ring, is ten times more potent than the parent compound further supports this notion (225).

Due to their potent activity toward ACSL4, selectivity within the ACSL family, tolerance for scaffold modifications, and synthetic tractability, TZDs represent a promising starting point for medicinal chemistry efforts aimed at optimizing ACSL4 inhibition.

7.2. Triacsins

Triacsins are metabolites of *Streptomyces aureofaciens* that were first described to inhibit ACSL activity in the late 1980s (234,235). There are four different triacsins (A, B, C, and D) that share an unsaturated 11-carbon chain

and a terminal *N*-hydroxytriazene moiety, but differ in the number and position of double bonds within the chain. Among the four structures, only Triacsin A and C (**Figure 20**) significantly inhibit ACSL activity in purified *Pseudomonas aeruginosa* enzyme and in microsomal fractions from rat liver, with Triacsin C being the most potent (235). The N-hydroxytriazene motif has been proposed as essential for ACSL inhibition, as hydrolysis-derived aldehyde analogs lack activity. Mechanistic studies reveal that Triacsin A inhibits ACSL noncompetitively with respect to ATP and CoA, while displaying competitive inhibition toward FAs, consistent with its structural resemblance. The first indirect evidence of Triacsin C inhibiting ACSL4 comes from observations showing that it prevents the incorporation of radiolabeled arachidonate into rat neutrophils, and that upon stimulation with a calcium ionophore, these treated neutrophils release increased amounts of eicosanoids (236). Further evaluation on purified recombinant ACSL isoforms revealed that Triacsin C inhibits ACSL1 (IC_{50} = 4 μM), ACSL3 (IC_{50} = 5.5 μM), and ACSL4 (IC_{50} = 7.5 μM), while showing no activity against ACSL5 and ACSL6 (39). Despite their lack of selectivity, numerous studies focus solely on the ACSL4-related activity of Triacsin C when drawing conclusions, introducing a significant bias.

The *N*-hydroxytriazene motif remains poorly explored in medicinal chemistry. As a result, little is known about its reactivity and stability *in vivo*. Notably, Triacsin C exhibits time-dependent inhibition that cannot be fully reversed by washing, suggesting an irreversible or slowly reversible mechanism (237). Moreover, the synthetic routes of Triacsins result in overall

low yields, and their biosynthesis involves 15 distinct enzymes (238), limiting their synthetic tractability. Thus, they are poorly suited as starting points in drug discovery.

7.3. PRGL493

PPRGL493 exhibited the highest docking score in the virtual screening of over 400,000 drug-like compounds, using a homology model of ACSL4 focused on the entrance of the putative FA tunnel (92). To improve solubility in organic solvent, an acetylated derivative of PPRGL493, PRGL493 (**Figure 20**), was synthesized. PRGL493 inhibits ACSL4 with an IC_{50} of approximatively 50 μM, while showing no activity against ACSL1 and ACSL3. The compound was extensively studied in biological models, showing inhibition of arachidonoyl-CoA (AA-CoA) formation in Leydig cells, as well as in BC and PC cell lines. The compound reduces steroidogenesis both *in vitro* and *in vivo*, inhibits proliferation and migration in BC and PC cells, and decreases tumor growth in *in vivo* models. PRGL493 is commonly used in studies targeting ACSL4 in cancer research. However, its IC_{50} is relatively high and does not consistently correlate with the biological effects, which can occur at much lower or higher concentrations. This, coupled with the fact that target engagement has not been determined, makes it difficult to confirm that its action is mediated through direct ACSL4 inhibition.

7.4. Silibinin

Silibinin is a natural compound extracted from *Silybum marianum*, widely used in the treatment of liver diseases due to its antioxidant, anti-inflammatory, and antiapoptotic properties. Recently, studies have investigated Silibinin's targets using living-cell-target accessibility profiling (LC-TRAP) (239). The TRAP approach examines the proteome-level accessibility changes induced by ligand binding, identifying the responsive proteins as targets. Analysis of the targetome in living HepG2 cells highlighted different enriched clusters, including ferroptosis regulators such as ACSL4. Further analysis revealed that Silibinin prevents RSL3-induced ferroptosis in an ACSL4-dependent manner. ACSL4 target engagement was confirmed in HepG2 cell lysates through two independent methods. A pull-down assay using an alkyne-labeled Silibinin derivative bearing a photo-cross-linking diazirine group, and a cellular thermal shift assay. Silibinin's binding affinity to ACSL4 was determined using surface plasmon resonance (SPR), yielding a dissociation constant (K_D) of 0.21 μM. The compound inhibited AA-CoA formation in HEK293T cell lysates with an IC_{50} of 14.14 μM; however, even at the highest tested concentration (50 μM), only a 40% reduction in AA-CoA levels was observed. Additionally, Silibinin decreased the incorporation of arachidonate into phosphatidylethanolamine (PE) in living HepG2 cells.

Silibinin is known to exhibit a multifaceted mechanism of action, functioning as a direct radical scavenger (240) and modulating various signaling pathways, including PI3K/AKT and NF-κB (241), which also play a role in

ferroptosis and cancer (242,243). Therefore, the use of Silibinin as a tool to selectively inhibit ACSL4 is limited by its broad mechanism of action.

7.5. AS-252424

Phenotypic screening of a kinase inhibitor library in HT-1080 cells under ferroptotic conditions identified AS-252424 (AS) (**Figure 20**) as a novel compound with antiferroptotic activity (93). The compound was subsequently validated for its ability to inhibit ferroptosis across various cell lines, where ferroptosis was induced through different mechanisms. AS is a potent inhibitor of PI3K (IC_{50} PI3Kγ = 0.033, μM IC_{50} PI3Kα = 0.93 μM) (244), and PI3K/AKT signaling is known to play a role in regulating ferroptosis (242). However, since the ferroptosis protection was not replicated by other PI3Kγ inhibitors, genetic ablation of PI3Kγ, or AKT inhibitors, this suggests that AS exerts its effects through an alternative mechanism (93). Moreover, AS neither functions as an iron chelator nor exhibits intrinsic antioxidant activity. Further investigations into AS target using a biotin-tagged derivative of the compound in a pull-down assay, identified ACSL4 as the most enriched protein. The target engagement of AS was then confirmed by drug affinity-responsive target stability and by cellular thermal shift assay. AS potently inhibits recombinant ACSL4, with an IC_{50} below 1 μM, while showing no activity against ACSL1 and ACSL3.

AS contains a pan-assay interference motif (PAINS), specifically an ene-rhodanine–like moiety potentially capable of covalently reacting with nucleophiles (245). Accordingly, the reversibility of its antiferroptotic

activity was assessed and subsequently confirmed (93). To investigate the compound's binding site on ACSL4, docking studies were performed using an AlphaFold model of the protein, which predicted interaction within the ATP-binding pocket.

Because AS is a poorly soluble compound with a short half-life ($t_{1/2}$ = 1 hour) and a high clearance rate (244), the authors developed a copolymer-based nanoparticle formulation to improve its delivery *in vivo* (93). The formulation successfully inhibited ferroptosis *in vitro* and conferred protection against ischemia-reperfusion injury (IRI) in both kidney and liver mouse models.

Although the compound demonstrates a promising activity *in vivo*, it also presents several limitations that may hinder its broader pharmacological application. First, the presence of an acrylamide moiety raises a structural alert, as this motif may participate in irreversible reactions with nucleophiles. Second, the antiferroptotic activity of AS might still be mediated by other PI3K isoforms, as the compound remains a submicromolar inhibitor of PI3Kα, and PI3Kα inhibitors potently suppress ferroptosis (246). Additionally, PI3Kγ plays a significant role in cancer, where its inhibition represents an antitumoral strategy (247). Therefore, the selectivity issues of AS compromise its utility in studying ACSL4 in pathological models. Finally, its poor ADME properties, which require nanoparticle-based delivery, limit its convenience as a pharmacological tool.

Although several novel compounds have been reported since 2020, the most commonly used inhibitors remain ROSI and Triacsin C.

The newly identified ACSL4 inhibitors fail to address the major limitation of earlier compounds: their lack of selectivity. The development of more potent and selective ACSL4 inhibitors would greatly benefit the scientific community by enabling more precise investigations into the enzyme's role in pathological settings.

8. Possible adverse outcomes of targeting ACSL4

When considering ACSL4 as a pharmacological target, it is crucial to anticipate potential adverse effects of its inhibition. This can be approached by analyzing the toxicity profiles of reference inhibitors, examining the physiological functions disrupted by ACSL4 inhibition, and studying phenotypes of knockout mouse models.

For ACSL4, the prediction of adverse effects based on the toxicity profiles of known inhibitors is limited by their poor selectivity. For instance, the side effects of ROSI (e.g., weight gain, edema, and cardiomegaly) are attributed primarily to its full PPARγ agonist activity rather than inhibition of ACSL4 (248). Similarly, triacsins exhibit hypotensive vasodilatory effects, but these appear to be independent of ACSL inhibition since triacsin D, which weakly inhibits ACSLs, has a significantly stronger vasodilatory activity than triacsin C (234).

As discussed in sections 5.3 to 5.5, ACSL4 plays a key role in regulating both the synthesis and activity of eicosanoids. Consequently, its inhibition could interfere with related physiological processes, including inflammation, steroidogenesis and insulin secretion. In line with this, ACSL4 inhibitors may exacerbate inflammatory responses following proinflammatory stimulation, as evidenced by increased systemic inflammation in global *ACSL4* knockout mice challenged with LPS (104). In addition, given ACSL4's role in brain development and the association between null mutations and mental retardation (see section 5.6), inhibitors targeting this enzyme may have teratogenic potential.

However, the observation that hemizygous male mice ($ACSL4^{-/y}$) present a normal phenotype and are fertile suggests that ACSL4 is not strictly essential in vivo (249). In contrast, heterozygous female mice ($ACSL4^{+/-}$) exhibit reduced fertility, and their offspring carrying disrupted alleles face a high risk of embryonic lethality. These findings indicate that a combined deficiency in both mother and pups may underlie the elevated embryonic death rate.

Finally, given the overlapping substrate specificities among ACSL isoforms, it is plausible that other family members may partially compensate for complete ACSL4 inhibition, thereby mitigating severe disruption of physiological pathways and limiting drastic adverse effects.

9. Conclusions

ACSL4 is a crucial enzyme that activates PUFAs, driving multiple downstream metabolic pathways and linking it to various physiological and pathological processes. We first introduced FAs, focusing on their metabolism and emphasizing the essential role of ACSLs in their initial activation to acyl-CoA. Next, we discussed the similarities among ACSL isoforms, highlighting their shared catalytic mechanisms and structures while noting their distinct roles in FA partitioning. We then provided a detailed overview of ACSL4's unique properties that define its specialized function, including its tissue distribution, subcellular localization, preference for specific PUFAs such as arachidonate, and the multiple layers of regulation. Those properties underlie the diverse physiological roles of ACSL4, including its involvement in PUFA uptake, their channeling into PLs, and the regulation of steroidogenesis and eicosanoid synthesis. Beyond its physiological functions, we explored ACSL4's role in pathophysiology, emphasizing diseases where its pharmacological inhibition represents a compelling therapeutic strategy. As a key regulator of ferroptosis, ACSL4 is implicated in conditions such as ischemia-reperfusion injury and neurodegenerative diseases. Additionally, by driving lipid metabolism reprogramming, ACSL4 confers proliferative advantages and facilitates EMT in specific cancers. Finally, we reviewed the different reported ACSL4 inhibitors, detailing their development, properties, advantages, and

limitations, underscoring the need for more potent and selective compounds to firmly establish ACSL4 as a therapeutic target.

OBJECTIVES AND STRATEGIES

This research falls within the scope of the Medicinal Chemistry Research Group (CMFA) at Université Catholique de Louvain and the Innovative Therapeutics for Brain Diseases (IT4BD) team at Université de Lille, aligning with their thematic focus on drug discovery, with IT4BD specifically dedicated to therapeutic strategies for brain diseases. Over the years, both groups have developed expertise in discovering novel molecular scaffolds targeting various proteins and optimizing their properties to design potent pharmacological tools.

This multidisciplinary expertise integrates various complementary approaches: biotechnological methods for protein production and purification, biochemical and biophysical techniques for *in vitro* characterization, organic chemistry for scaffold optimization, chemical biology for binding site identification, bioinformatics for rational drug design, and cellular biology for evaluation in pathological models.

In this context, this work focuses on ACSL4, with the first two chapters dedicated to designing novel inhibitors more potent and selective, with the goal of further establishing ACSL4 inhibition as a viable therapeutic approach. The strategy pursued to achieve these objectives is illustrated in **Figure 21.**

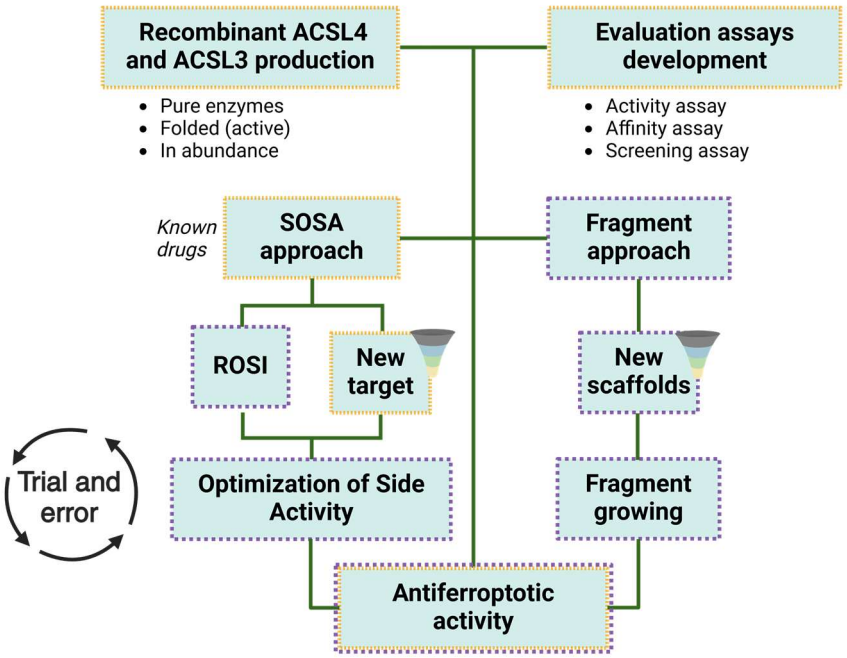

Figure 21. Strategy for the design and optimization of ACSL4 inhibitors. Yellow-highlighted boxes correspond to the results presented in the first chapter, while the results corresponding to purple-highlighted boxes will be briefly discussed in the second section. Funnels represent the screening process conducted.

The initial objective was to build a robust foundation for screening and evaluation. This involved producing recombinant ACSL4 and ACSL3, and developing both biophysical and biochemical assays to monitor ligand binding and inhibitory activity.

To optimize ACSL4 inhibitors, we implemented two complementary medicinal chemistry strategies in parallel. The first approach focused on selectively optimizing the side activity (SOSA) of existing drugs, either by

modifying the reference compound ROSI or by screening a commercial library of FDA-approved compounds, with the objective of eliminating their primary activity while enhancing ACSL4 inhibition. The second approach followed a fragment-based strategy, where small molecular fragments were identified through screening and subsequently elaborated into more potent inhibitors.

Inhibitor optimization was primarily driven by iterative medicinal chemistry efforts aimed at enhancing potency for ACSL4 while assessing selectivity against ACSL3. Finally, the most promising inhibitors were evaluated for their antiferroptotic activity in cell-based models of Parkinson's disease, serving as an initial proof of concept for their therapeutic potential in pathological settings.

Chapter I describes the development of the evaluation platform and the identification of a novel inhibitor scaffolds through a screening campaign based on the SOSA approach. Chapter II provides (i) a brief overview of the optimization efforts for the new inhibitor series identified in Chapter I, (ii) the outcomes of structural modifications of ROSI, and (iii) the fragment-based strategy, serving as a transition between chapters I and III. The objectives of chapter III stem from insights gained during the drug discovery program and will be presented following the first two chapters.

CONTRIBUTIONS

Throughout this PhD, we initiated a highly collaborative project involving three principal investigators, five PhD students, numerous master's students, and several research groups. My personal contributions to this collective effort included developing methods for the efficient production of pure enzymes and establishing a range of biophysical assays to evaluate ligand binding. I actively participated in screening campaigns and contributed modestly to the synthesis of analogs during the optimization phase, with my primary focus being the assessment of binding affinities. While I was a primary contributor to the results presented in Chapters I and III, the results summarized in Chapter II were predominantly generated by other members of the team.

RESULTS – CHAPTER I

To initiate a medicinal chemistry project aimed at developing improved ACSL4 inhibitors with antiferroptotic activity, it was first necessary to establish an experimental framework. Chapter I details the development of this methodology, starting with the production and purification of recombinant ACSL4 and ACSL3, followed by validation of their proper folding and enzymatic activity. It then describes the biochemical and biophysical assays optimized to enable the progression from large-scale chemical library screening to the validation of selective inhibitors. The applicability of the approach is demonstrated through the screening of an FDA-approved library, which led to the identification of a novel inhibitor series with antiferroptotic properties in a cell-based model of Parkinson's disease.

Biochemical Pharmacology 204 (2022) 115239

Contents lists available at ScienceDirect

Biochemical Pharmacology

journal homepage: www.elsevier.com/locate/biochempharm

Repositioning of FDA-Approved antifungal agents to interrogate Acyl-CoA synthetase long chain family member 4 (ACSL4) in ferroptosis

Romain Marteau [a,1], Séverine Ravez [b,1], Darius Mazhari Dorooee [a,2], Hind Bouchaoui [b,2], Karine Porte [a], Jean-Christophe Devedjian [b,c], Patricia Melnyk [b], David Devos [b], Raphaël Frédérick [a,*], Jamal El Bakali [b,*]

[a] Medicinal Chemistry Research Group (CMFA), Louvain Drug Research Institute (LDRI), Université catholique de Louvain (UCLouvain), 73 Avenue Mounier, B1.73.10, 1200 Bruxelles, Belgium
[b] Univ. Lille, Inserm, CHU Lille, UMR-S-U1172 - LilNCog - Lille Neuroscience & Cognition, F-59000 Lille, France
[c] Université du Littoral Côte d'Opale-1, place de l'Yser, BP 72033, 59375 Dunkerque Cedex, France

The results presented in this chapter have been adapted from the publication in *Biochemical Pharmacology* (250).

1. Abstract

Ferroptosis, first coined in 2012, is an iron-dependent regulated cell death (RCD) characterized by the accumulation of lipid peroxides to toxic levels. This mechanism is currently being evaluated as a target for a variety of diseases offering new opportunities for drug design and development. Recent reports uncovered acyl-CoA synthetase long-chain 4 (ACSL4) as a critical contributor to ferroptosis execution. Therefore, ACSL4 inhibitors are emerging as attractive antiferroptotic agents. Herein, we developed a robust screening cascade with orthogonal biophysical and biochemical techniques to identify original human ACSL4 inhibitors. By screening an FDA-approved drug library, we were able to identify and validate new inhibitors with micromolar-range activity against ACSL4. With an IC_{50} of 280 nM against *h*ACSL4, antifungal agent sertaconazole is to our knowledge, the most potent ACSL4 inhibitor identified so far. In addition, sertaconazole significantly reduced lipid peroxidation and ferroptosis in human differentiated dopaminergic neurons (Lund human mesencephalic LUHMES cells), demonstrating that it is a valuable chemical tool for further investigating the role of ACSL4 in ferroptosis. This study highlights phenethyl-imidazole scaffold as a novel and promising starting point for the development of antiferroptotic agents targeting ACSL4.

Table of Contents graphic

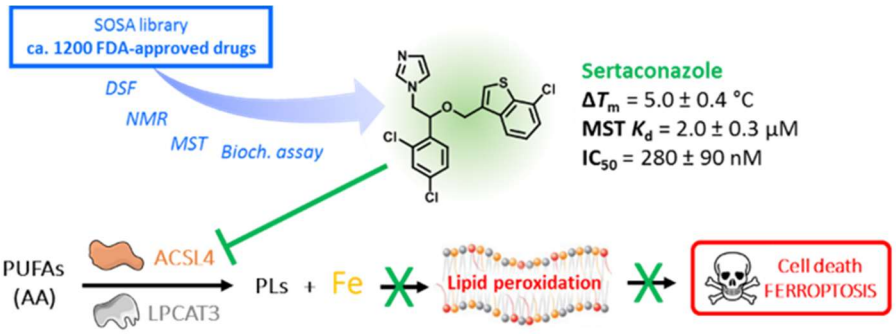

2. Introduction

Ferroptosis, is a non-apoptotic iron-dependent regulated cell death (RCD, **Figure 22**) first coined in 2012 (122,123). It is characterized by the accumulation of toxic membrane lipid peroxides leading eventually to membrane damage and cell lysis (124,251). This RCD is highly dependent on lipid composition of the membrane (101). Indeed, membrane phospholipids (PLs), particularly phosphatidylethanolamines (PE) enriched in polyunsaturated fatty acids (PUFAs) such as arachidonate are highly susceptible to peroxidation (57). Therefore, the enrichment of PLs with PUFAs is a key step in determining ferroptosis sensitivity (101). PLs are enriched in PUFAs through the action of acyl-CoA synthetase long chain family member 4 (ACSL4) which activates PUFAs in acyl-CoA, which in

turn are incorporated in PLs thanks to lysophosphatidylcholine acyltransferase 3 (LPCAT3).

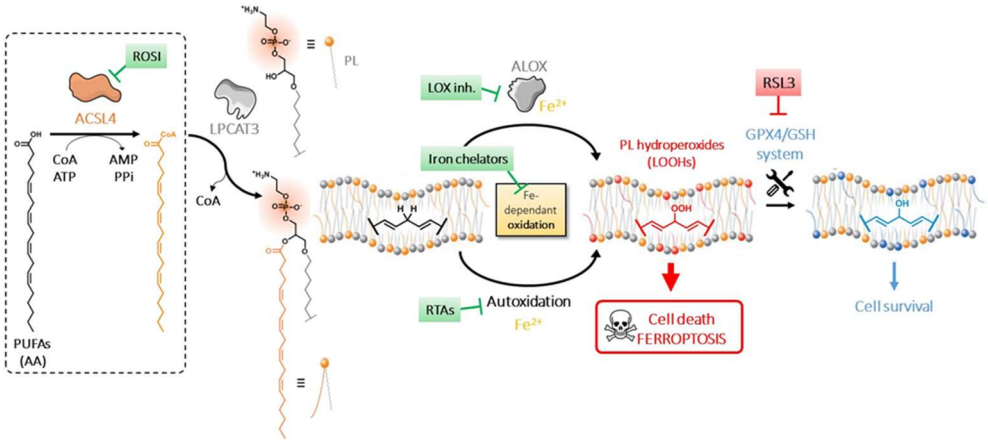

Figure 22. Simplified overview of the ferroptotic pathway. Ferroptosis inhibitors and inducer are colored in green and red, respectively. AA, arachidonic acid; ACSL4, acyl-CoA synthetase long chain 4; ALOX, arachidonate lipoxygenase; AMP, adenosine monophosphate; ATP, adenosine triphosphate; CoA, coenzyme A; GPX4, glutathione peroxidase 4; GSH, glutathione; LOX, lipoxygenase; LPCAT3, lysophosphatidylcholine acyltransferase 3; PL, phospholipids, PPi, pyrophosphate; PUFAs, polyunsaturated fatty acids; ROSI, rosiglitazone; RSL3, RAS-selectively lethal 3; RTAs, radical-trapping antioxidants.

During ferroptosis, PUFAs containing PLs are subjected to peroxidation through distinct iron-dependent mechanisms. Non-heme iron-containing enzymes such as arachidonate lipoxygenases (ALOX) can initiate lipid peroxidation, forming substrates for the Fenton reaction (125,252). Lipid peroxidation then propagates through autoxidation catalyzed by labile iron. Additionally, heme enzymes such as the cytochrome P450 oxidoreductase (POR) can generate H_2O_2 and promote lipid peroxidation (126). In a physiological context, peroxidized lipids are neutralized by endogenous

antioxidant systems, mainly glutathione peroxidase 4 (GPX4) which uses glutathione as co-factor to reduce peroxides to non-toxic alcohols (253). Under ferroptotic conditions, increased lipid peroxidation is not sufficiently compensated by endogenous antioxidant systems resulting in the accumulation of toxic lipid peroxides. This step is considered as the major event leading to cell death by ferroptosis (101). Experimentally, ferroptosis is generally induced by small molecules like (*1S*,*3R*)-RSL3 (RSL3), a covalent GPX4 inhibitor or by Erastin, which acts at the cystine-glutamate antiporter system xc^- and voltage dependent anion channels 2 and 3 (254,255).

Over the past years, ferroptosis has attracted considerable attention owing to its important role in several diseases (256). Since the early days of the field, cancer cells sensitivity to ferroptosis encouraged the development of ferroptosis inducers as an appealing strategy to selectively kill cancer cells (257). Interestingly, this increased sensitivity particularly affects dedifferentiated as well as persister cancer cells and seems to result from a more intense metabolic activity associated with a higher reactive oxygen species (ROS) generation (155,258). In addition, cancer cells often need high amount of iron, thereby increasing their sensitivity to ferroptosis. However, cancer cells are not the only cells sensitive to ferroptosis. Metabolic adaptations during the ischemic period of ischemia-reperfusion injuries (IRI) impair several ROS scavenging mechanisms and the reperfusion phase induces a ROS "burst" which leads to cell death, notably by ferroptosis (259). In addition, accumulating evidence points at an important role of ferroptosis

in neurodegenerative diseases such as Alzheimer's, Parkinson's diseases and amyotrophic lateral sclerosis (260). The pathologic iron overload observed in these diseases catalyzes Fenton chemistry in tissues particularly rich in PUFAs, which leads to excessive lipid peroxidation and subsequent ferroptosis (261). Therefore, blocking ferroptosis with small molecules accounts for an innovative approach in the potential treatment of ferroptosis-related diseases. For example, ferroptotic cell death can be dramatically reduced by iron chelators (such as deferiprone) and radical-trapping antioxidants such as liproxstatin-1 (**Figures 22** and **23**) (262,263).

In this context, ACSL4 inhibition has attracted much attention lately. Indeed, free PUFAs must be activated by ACSL4 to be incorporated into PLs membranes to participate in the ferroptotic cell death (**Figure 22**). ACSL4 belongs to the ACSL family of enzymes that play a crucial role in the metabolism of FAs (30). They activate FAs into their acyl-CoA analogues following a Bi Uni Uni Bi Ping Pong mechanism. Some of the activated FAs fuel the lipid biosynthesis and are precursors of structural membrane components or signaling molecules such as diacylglycerol and lysophosphatidic acid. In mammals, there are five ACSLs isoforms (ACSL 1, 3, 4, 5 and 6). ASCL3 and 4 share approximately 63% sequence identity and only about 30% with other ACSL isoforms (38). ACSLs have specific preferences for FA with particular chain lengths and saturations. This specificity seems to arise from crucial amino acids in the FA binding pocket. By preferentially metabolizing PUFAs such as arachidonate, ACSL4 is involved in several biological processes including inflammation,

steroidogenesis, cancer and ferroptosis (264). The key role of ACSL4 in ferroptosis execution was first demonstrated in a genome-wide screening in 2015 (140). In 2017, Doll et al. validated ACSL4 as an appealing target in the control of ferroptosis by a genome-wide CRISPR-based genetic screen (101). They further demonstrated that knockout or pharmacological inhibition of ACSL4 with thiazolidinediones (TZDs) such as rosiglitazone (ROSI) conferred a strong protection against ferroptosis (**Figure 23**).

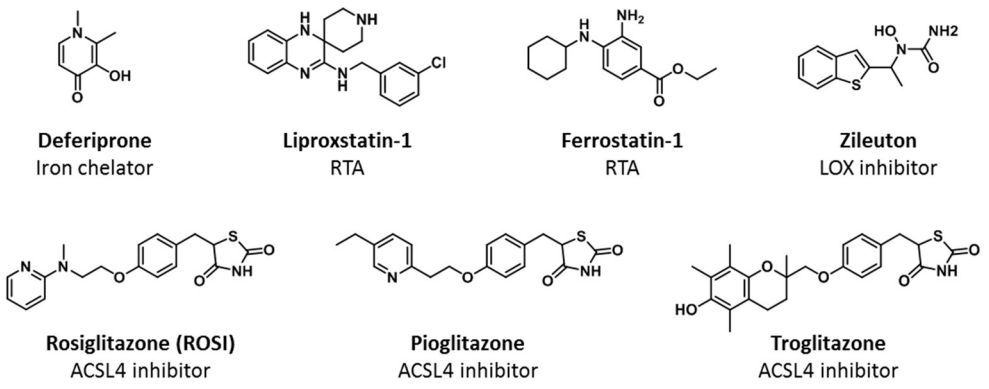

Figure 23. Structures of main ferroptosis inhibitors.

More recently, ACSL4 was reported to be further activated through phosphorylation by PKCβII that senses initial lipid peroxidation events. Therefore, ACSL4 is an important protagonist in ferroptosis involved in a feedforward loop (86). In addition, ACSL4 was shown to exacerbate ischemic stroke by promoting ferroptosis-induced brain injury and neuroinflammation (265). Another recent study showed that inhibition of ACSL4 attenuates ferroptotic damage after pulmonary ischemia-reperfusion (160).

Together, these data validate ACSL4 as a key regulator of ferroptosis, paving the way to the development of novel ACSL4 inhibitors. Up to now, only three PPAR-γ agonists (TZDs), namely, ROSI, pioglitazone and troglitazone were described as micromolar-range inhibitors of rat ASCL4 (selective vs. other ACSL isoforms) (39,226). Therefore, there is a need for the discovery of novel selective ACSL4 inhibitors. To that end, we developed a robust screening cascade with orthogonal biophysical and biochemical techniques to identify original ACSL4 inhibitors. We report here the identification of a novel series of human ACSL4 inhibitors, which best representative compound displays potent antiferroptotic activity in cells.

3. Materials and methods

3.1. Chemicals and reagents.

ROSI, ECO and FLUCO were purchased from TCI chemicals (Belgium). SERTA nitrate was purchased from Sigma Aldrich (France). All salts, buffers and ATP were purchased from Sigma Aldrich (France). Dimethylsulfoxide (DMSO-d_6) was purchased from Eurisotop (France). Chemicals used for protein production were purchased from Sigma Aldrich (France or Belgium). RSL3 was purchased from Sigma Aldrich (France). For screening, 1134 FDA-approved drugs were obtained from Selleckchem (Germany). All FDA-

approved drugs were dissolved in DMSO (Sigma Aldrich, France), and stock solutions were stored at -80 °C.

3.2. Recombinant expression and purification of human ACSL4 and ACSL3.

The plasmid pET-28(a)+ coding for the short isoform of the human His-tagged ACSL4 at its *N*-terminal part was purchased from GeneCust™ and transformed into *E. coli* BL21 (DE3). Transformants were grown in LB supplemented with 50 µg/mL kanamycine and 34.2 µg/mL chloramphenicol at 37 °C until they reached an OD_{600} of 0.9-1. Recombinant expression of ACSL4 proteins was then induced with isopropyl-β-D thiogalactopyranoside (IPTG; 1 mM, final concentration) and the incubation continued at 20 °C during 18 h. Bacterial cells were then harvested by centrifugation (5,000 rpm, 4 °C, 20 min).

Bacterial cells were sonicated in ice-cooled lysate buffer containing 20 mM Tris pH 7.5, 1% triton X-100, 0.1% sodium cholate and further processed by centrifugation (10,000 rpm, 4 °C, 30 min). The Ni-NTA resin was pre-equilibrated with wash buffer (50 mM Tris pH 8.5, 10 mM $MgCl_2$, 300 mM NaCl, 10% glycerol, 30 mM imidazole). The resulting supernatant was supplemented with 20 mM imidazole to avoid non-specific interactions and was then incubated with the pre-equilibrated resin for 1 h under stirring. The column was subsequently washed with the wash buffer to elute unbound proteins. His-tagged ACSL4 proteins were eluted with elution buffer (50 mM Tris pH 8.5, 10 mM $MgCl_2$, 300 mM NaCl, 10% glycerol, 500 mM

imidazole). Finally, purified proteins were dialyzed at 4 °C for 18 h against a stock buffer (50 mM Tris pH 7, 10 mM $MgCl_2$, 300 mM NaCl, 20% Glycerol, 1 mM DTT). The different steps of the purification process were controlled by SDS-PAGE stained with Coomassie blue and apparent molecular weight (MW) was determined by comparison to the Biorad™ pre-stained protein ladders. The protein quality and the batch similarity were confirmed by nanoDSF on Tycho NT.6 instrument. The *h*ACSL3 was produced and purified using a similar protocol as for ACSL4.

3.3. Nano differential scanning fluorimetry

Proteins diluted at 10 µM in stock buffer were introduced in adapted capillaries, placed in a Tycho NT.6 instrument (Nanotemper) and submitted to the thermal gradient. Data were analyzed using GraphPad Prism® to determine the denaturation temperature (T_m). Each condition was measured in triplicate.

3.4. Differential scanning fluorimetry.

DSF was conducted on a QuantStudio 3 real time PCR detection system (Applied Biosystems, Life Technologies). A total of 20 µL/well solution was prepared containing 2 µM ACSL4, 1 mM ATP, 10 µM of tested compound or DMSO and 2 X fluorescent dye (Protein Thermal Shift™ Dye Kit, reference 4461146, Applied Biosystems, Life Technologies) in a buffer containing 50 mM Tris pH 7, 100 mM NaCl and 1 mM $MgCl_2$. After thoroughly mixing and sealing, the plate was heated at 1% of ramp rate (~ 2

°C/min) from 25 to 70 °C. Filters were adapted to correspond to the optimal excitation (x4) and emission (m4) wavelengths for fluorescent dye and Rox was selected as reporter for detection of fluorescence intensity. Results were analyzed and expressed as the first derivative of the fluorescent emission plotted against temperature using a trial version of the Protein Thermal Shift™ Software v1.4 (Applied Biosystems, Life Technologies).

3.5. Microscale thermophoresis experiments.

The measurements were conducted on a NanoTemper Monolith NT.115 instrument (NanoTemper Technologies, GmbH, Munich, Germany) with red filter. ACSL4 was labeled with the RED-tris-NTA 2nd generation fluorescent dye (MO-L018, NanoTemper Technologies, GmbH, Munich, Germany) and applied at a final concentration of 500 nM. Serial dilution of ligand was prepared in the optimized buffer (PBS: 8 mM Na_2HPO_4, 2 mM KH_2PO_4, 150 mM NaCl, 3 mM KCl; 10 mM $MgCl_2$; 5% DMSO; 0.05% Tween) with 1 mM ATP. A volume of 10 µL of labeled ACSL4 was mixed with 10 µL of each dilution of ligand and the samples were loaded into standard capillaries. Measurements were performed at 23 °C using 100% LED power and 60% MST power. Laser *on* and *off* times were set at 20 s and 5 s, respectively. The curves were extracted from the MST traces at 4 to 5 sec MST on time. Data analysis was performed using the NanoTemper® analysis software.

3.6. 1D-^{1}H NMR-Line broadening experiments.

All experiments were performed on a Bruker Ascend Avance III 600 MHz system equipped with a broadband cryoprobe (Bruker). Spectra were collected at 298 K using 8 transients, a 7239 Hz spectral width, 15.2 K data points, and a relaxation delay of 3.0 s. Water signal suppression was achieved using an excitation-sculpting scheme. The total experiment time was approximately 5 min. *h*ACSL4-6His protein for 1D NMR was expressed and purified from *E. coli*, as described above. The protein was then buffer-exchanged in commercial phosphate buffer solution (PBS, ThermoFischer, Germany) and diluted to reach final concentrations of 0, 0.075, 0.15, 0.30, 0.60, 1.2 and 2.4 µM in PBS containing 6% DMSO-d_6, 1 mM $MgCl_2$, 0.05% Tween-20 and 100 µM of ligand. NMR Spectra were phase-adjusted and baseline-corrected with TopSpin® 4.09.

3.7. ACSL4 and ACSL3 enzymatic assay.

Inorganic pyrophosphate (PPi) production was monitored with a Varioskan Flash spectrophotometer (Thermo Scientific) using the EnzChek® pyrophosphate assay kit (E-6645). Each condition was measured in triplicate at 25 °C. The total reaction volume was 100 µL and ACSL4 activity was assayed in a buffer containing 50 mM Tris pH 7.5, 200 mM NaCl, 1 mM $MgCl_2$, 200 µM MESG, 50 µM ATP, 100 µM CoA, 1 mM DTT, 10% DMSO (or tested compound), 1 U/mL PNP, 0.03 U/mL pyrophosphatase, and 50 nM purified enzyme. ACSL3 activity was assessed under similar conditions, except in the absence of NaCl and using 600 nM enzyme. Reactions were

initiated by the addition of a palmitate solution, typically to a final concentration of 100 µM (0.06% triton, 1% EtOH). A control experiment was performed in which a control solution (0.06% triton, 1% EtOH) was added instead of palmitate solution. The plate was mixed manually, and the absorbance change was recorded every 30 s for 30 min at 360 nm. For data analysis, initial rates were calculated during the linear portion. The slope of the control experiment was subtracted from each slope and the corrected slope was converted to the rate of pyrophosphate (PPi) production by use of PPi standard curve. Results were analyzed using GraphPad Prism®.

3.8. Cell line and culture conditions.

LUHMES cells were a generous gift from Pr. Marcel Leist (In vitro Toxicology and Biomedicine, University of Konstanz, Germany). LUHMES cells are neuronal precursor cells, conditionally-immortalized which can be differentiated in 5 days into post-mitotic dopaminergic neurons by shutting-down the *myc* transgene. For LUHMES cell culture, Nunclon™ cell culture flasks and well-plates were pre-coated with 50 µg/mL of poly-L-ornithine (Sigma-aldrich) and 1 µg/mL fibronectin (Sigma-Aldrich) in distilled water overnight then washed twice. Cells were grown at 37 °C in a humidified 95% air, 5% CO_2 atmosphere. Proliferating cells were maintained in Advanced Dulbecco modified Eagle's Medium/F12 (Advanced DMEM/F12) supplemented with 1 X N-2 supplement, 2 mM L-glutamine and 40 ng/mL rBFGF (recombinant basic fibroblast growth factor) purchased from ThermoFisher. Cell differentiation was performed following a published

protocol (266). Briefly, $2x10^6$ cells were seeded in a T75 flask for 2 days then the differentiation started (d0) by replacing the proliferative media with the differentiation media containing Advanced DMEM/F12, 1 X N2 supplement, 2 mM L- glutamine, 1 mM dibutyryl cAMP (Sigma-Aldrich), 1 µg/mL tetracycline (Sigma-Aldrich) and 2 ng/mL recombinant human GDNF (Bio-Techne). After 2 days of pre-differentiation (d2), cells were harvested with Trypsine-EDTA 0.05% (ThermoFisher, France), centrifuged for 5 min at 300 g, seeded in appropriate supports in differentiation media. Cells were left to fully differentiate for 3 more days (d5).

3.9. Measurement/imaging of lipid ROS.

LUHMES cells were seeded at d2 in 24 well-plates at a density of 250 000 cells per well and left to fully differentiate until d5. Cells were pretreated with 5 µM ECO, 5 µM SERTA, 5 µM FLUCO or media for 14 h before induction of ferroptosis with RSL3 (30 nM, 6 h). Following treatments, cells were harvested by trypsinization and transferred to a 5 mL tube, pelleted (300 g, 5 min, 4 °C), resuspended in 200 µL PBS containing a LIVE/DEAD VIOLET probe (ThermoFisher, France) at 0.8 µL per tube and incubated for 15 min at 37°C. Then cell suspensions were incubated with an additional 200 µL of PBS containing C11-BODIPY 581/591 probe (ThermoFisher, France) at a final concentration of 1 µM for another 15 min at 37 °C. Cells were analyzed using the flow cytometer LSR FORTESSA X20 (BD Biosciences) with FITC and PE-Texas Red, for detecting green and red fluorescence respectively. Lipid peroxidation was measured from green fluorescence detected in the living cell

population (cells unlabeled for the LIVE DEAD probe). At least 10 000 cells were analyzed per sample and data analyses was conducted using the Kaluza Analysis Software (Beckmann Coulter) and three independent biological replications were performed for each condition. Of note, in this cell line, a sharp decrease in lipid ROS was observed upon Liproxsatin-1 treatment (1 µM) after inducing ferroptosis with 20 nM of RLS3.

3.10. Cell viability assay.

Cell viability analysis was measured in 96 well-plates where cells were seeded at d2 of differentiation at a density of 40 000 cells per well. At d5, cells were pretreated with 5 µM ECO, 5 µM SERTA, 5 µM FLUCO or media for 14 h before to induce ferroptosis with a concentration range of RSL3 (0, 8, 10, 12, 15 and 20 nM) for 24 h. Then, cell viability was determined incubating with 100 µg/mL of Resazurin (Sigma-Aldrich, France) for 2 h at 37 °C in dark. Fluorescence signals were measured using the Mithras LB 950 Device with a lamp energy of 5000, excitation 560 nm and emission 600 nm. Fluorescence values were normalized by setting fluorescence values of control wells as 100% of cell viability. Of note, in this cell line, a strong protection was observed upon Liproxsatin-1 treatment (1 µM) after inducing ferroptosis with 20 nM of RLS3.

3.11. 2,2-Diphenyl 1-picrylhydrazyl (DPPH) assay.

Radical-trapping antioxidant activity of ECO, SERTA, Fer-1 (40, 20, 10 and 5 µM) and Trolox (40, 32, 24, 16 µM) was assessed in 96 well-plates with a

SpectraMax M2e spectrophotometer using the 2,2-diphenyl 1-picrylhydrazyl (DPPH) antioxidant assay kit from Dojindo (Germany). Following the provided protocol, compounds were incubated with the DPPH reagent for 30 minutes in the dark at 25°C then absorbance was read at 517 nm. Each condition was measured in triplicate. Results were analyzed using GraphPad Prism®.

3.12. Iron chelation assay.

Iron chelation potential of ECO and SERTA was evaluated at 5 and 12.5 µM using the ferrous iron chelating assay kit from Amsbio (Netherlands). EDTA (0.5, 5, 12.5 and 25 µM) was used as a positive control. Compounds were solubilized in the provided buffer containing 5% DMSO, $FeSO_4$, and ferrozine. After incubation for 10 minutes, absorbance was read at 562 nm with a SpectraMax M2e spectrophotometer. Each condition was measured in triplicate. Results were analyzed using GraphPad Prism®.

4. Results

4.1. Human ACSL4 is a tractable target amenable to screening.

4.1.1. Enzymatic production of hACSL4 and hACSL3.

We produced the short isoform of the human ACSL4 (*h*ACSL4, 670 amino acids) and a truncated version of the human ACSL3 (*h*ACSL3, 678 amino

acids) lacking the transmembrane domain (41 first amino acids) in *E. coli* BL21(DE3). The recombinant proteins containing an *N*-terminal his-tag were purified by Ni^{2+}-affinity chromatography. Using this expression and purification procedure, we obtained a typical yield of purified protein around 10 mg/L of culture for both isoforms. Purified ACSLs were produced with good purity as judged by SDS-PAGE and migrated at the expected value of ca. 75 kDa (**Figure 24A-B**). Quality of both proteins were regularly controlled in nano differential scanning fluorimetry (nDSF) and displayed a melting temperature (T_m) in native conditions of 55.0 and 47.9 °C for ACSL4 and ACSL3, respectively (**Figure 24C-D**). Enzymatic activity was also regularly measured thanks to an optimized biochemical assay.

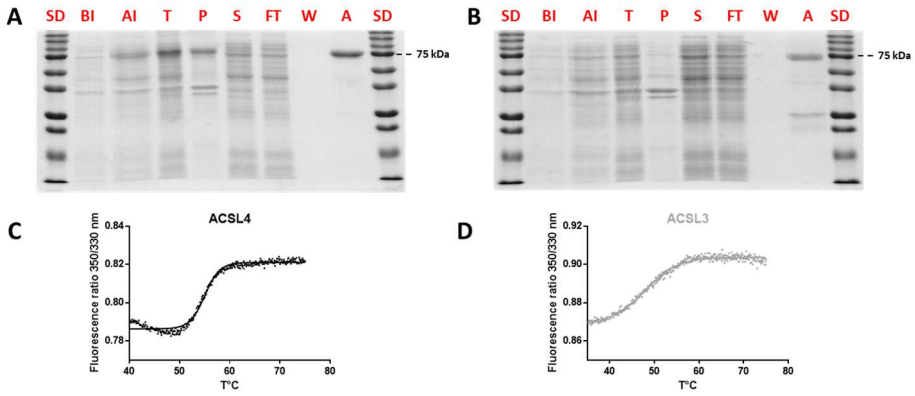

Figure 24. Quality control of ACSL4 and ACSL3. Coomassie blue-stained SDS-PAGE analysis throughout the purification process of ACSL4 (**A**) and ACSL3 (**B**). Lane 1 and 10, molecular mass standards (SD); lane 2, before induction (BI); lane 3, after induction (AI); lane 4 total lysate (T); lane 5, pellet (P); lane 6, supernatant (S); lane 7, flow through (FT); lane 8, wash (W), lane 9, purified ACSL. nDSF of purified ACSL4 (**C**) and ACSL3 (**D**) at 10 µM in the stock buffer. T_m of 55.0 and 47.9 °C were determined for ACSL4 and ACSL3 (*n=3*), respectively.

4.1.2. Biochemical assay optimization.

We adapted the spectrophotometric EnzChek® pyrophosphate assay (267). Briefly, this enzymatic coupled assay quantifies the pyrophosphate (PPi) produced by ASCL4 or ACSL3 which is converted into two equivalents of orthophosphate (Pi) by the pyrophosphatase. The produced Pi and the 2-amino-6-mercapto-7-methylpurine riboside are then consumed by the purine ribonucleoside phosphorylase to generate ribose-1-phosphate and 2-amino-6-mercapto-7-methyl purine, which is detected by an increase in absorbance at 360 nm (**Figure 25A**). Since the absorbance at 360 nm remained linear with PPi concentrations only up to 80 µM in the coupling system (**Figure 25B**), ATP concentration was limited to 50 µM in subsequent experiments to prevent signal saturation and ensure accurate monitoring of ACSL activity. To optimize the assay, we first monitored reaction velocity as a function of ACSL concentration under initial conditions: 50 mM Tris.HCl (pH 7), 500 mM NaCl, 5 mM $MgCl_2$, 0.03% Triton X-100, 10% DMSO, 50 µM ATP, 100 µM CoA and 100 µM palmitate (**Figure 25C**). ACSL activity was directly proportional to enzyme concentration in the range of 25-500 nM for ACSL4 and 50-1200 nM for ACSL3. Based on these results, concentrations of 50 nM ACSL4 and 600 nM ACSL3 were selected for further assay optimization. We then fine-tuned parameters sequentially, adopting the best condition at each step before advancing. For ACSL4, the concentration of Triton X-100 (0.06%) was optimized first, followed by pH (7.5), divalent ions (1 mM $MgCl_2$), NaCl (200 mM), DTT (1 mM), DMSO (10%), and finally the temperature (25 °C) (**Figure 25D–J**).

Optimized conditions for ACSL3 were similar, except that NaCl was excluded from the buffer. These optimized conditions were used for the evaluation of inhibitors.

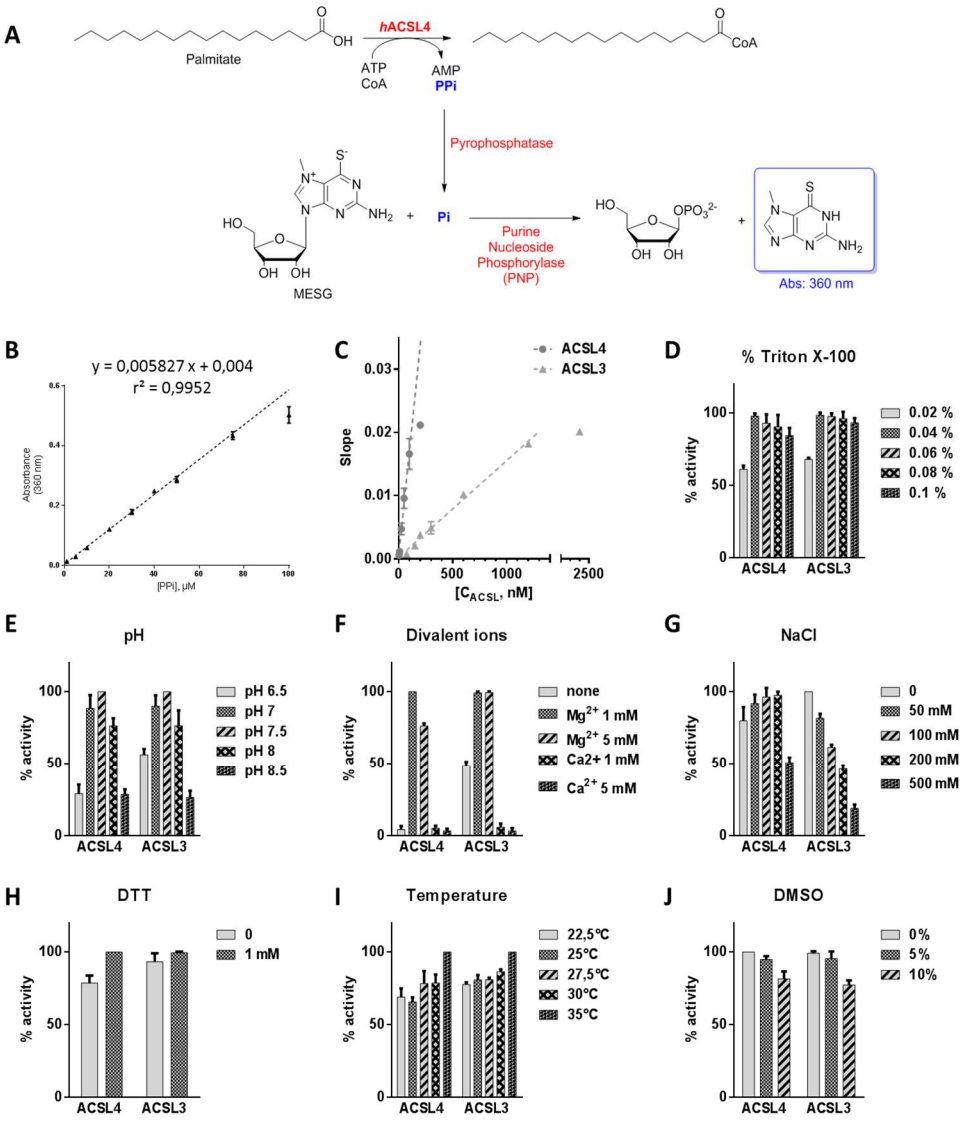

Figure 25. Biochemical assay conditions optimization. (**A**) Scheme illustrating real-time monitoring of the ACSL-catalyzed reaction. Pyrophosphatase catalyzes the conversion of the released PPi by ACSL into two equivalents of Pi. Then, Pi and MESG are consumed by the PNP to generate the product which is detected at 360 nm. (**B**) PPi Standard curve obtained from various concentrations of $Na_4P_2O_7$ in

standard assay conditions in the presence of the coupling system comprising pyrophosphatase and purine nucleoside phosphorylase. (**C**) Measurement of ACSL activity in the presence of different amounts of enzyme. Influence of the Triton X-100 (**D**), pH (**E**), divalent ions (**F**), NaCl (**G**), DTT (**H**), temperature (**I**), DMSO (**J**) on ACSL4 and ACSL3 activity. The parameters were sequentially optimized, starting from standard conditions and selecting the optimal setting for each before moving on to the next. The reaction rates were calculated over the first five minutes (mean ± SEM, *n*=3).

4.1.3. Development of a screening cascade

With the aim of screening chemical libraries, we developed a screening cascade composed of orthogonal biophysical and biochemical assays (**Figure 26**).

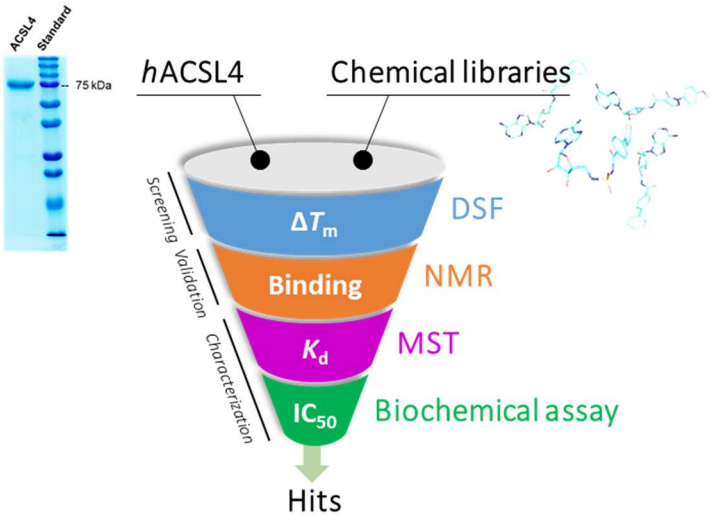

Figure 26: Screening cascade for the identification of ACSL4 inhibitors.

Differential Scanning Fluorometry (DSF) was developed to serve as the first line screening method. DSF relies on the binding of a fluorescent dye to

hydrophobic regions of the protein exposed to the solvent upon thermal denaturation. In DSF, molecules that stabilize the folded state of the protein cause an increase of the denaturation temperature of the protein, indicative of a binding event. Assay conditions were optimized with reference inhibitor ROSI. Based on the results, we selected an assay mixture containing 2 µM ACSL4, 1 mM ATP, 2 X fluorescent Protein Thermal Shift™ Dye in buffer containing 50 mM Tris pH 7, 100 mM NaCl and 1 mM $MgCl_2$. Under these conditions, ROSI showed a significant thermal shift (ΔT_m = 5.0 ± 0.1 °C at 10 µM) consistent with a binding event (**Figure 27A**). ROSI-ACSL4 binding was then confirmed using an adaptation of the traditional 1D ^{1}H NMR line broadening (268). Indeed, a decrease in NMR signals intensity of ROSI was observed with increasing ACSL4 concentration indicating protein-ligand binding (**Figure 27B**). To complement these first line screening assays, in addition to the biochemical assay described above, MicroScale Thermophoresis (MST) was developed to quantify the binding of ligands to ACSL4. MST measures binding affinities by monitoring differential movement in a microscopic temperature gradient. The thermophoretic movement of particles is detected through fluorescence of one of the binding partners. For this experiment, His-tagged ACSL4 (500 nM) was labeled with a fluorescent dye according to the supplier protocol. Thermographs of ROSI binding to ACSL4 provided well-defined curves and related dose-response curve gave a K_D of 2.2 ± 0.2 µM (**Figure 27C**).

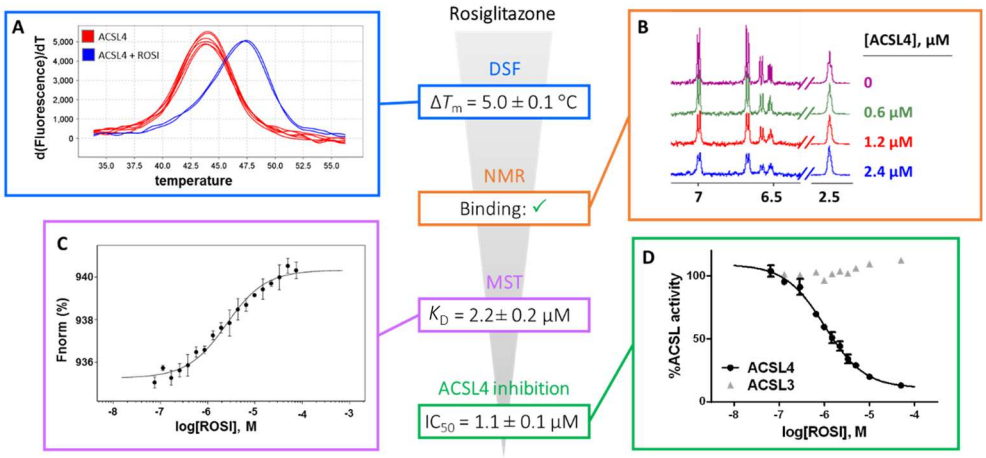

Figure 27. Assay validation with ROSI. (**A**) Thermal denaturation profile of ACSL4 (red curve, *n*=4) and ACSL4 in presence of 10 µM ROSI (blue curve, *n*=4). Results are expressed as derivative of fluorescence emission against temperature. (**B**) Selected region of the ^{1}H NMR spectra of ROSI (100 µM) at different concentrations of ACSL4. (**C**) MST dose-response curve for the binding interaction between ROSI and ACSL4 [extracted from the MST traces at 4 to 5 s MST on time]. The concentration of protein is kept constant at 500 nM, while ROSI concentration varies from 0.075 µM to 74 µM. Fitting of the binding curve gives a K_D of 2.2 ± 0.2 µM (*n*=4). (**D**) Dose-response curve of ROSI on ACSL4 activity (ACSL4 IC_{50} = 1.1 ± 0.1 µM, *n*=3).

In parallel, we measured the inhibitory activity of ROSI against *h*ACSL4 using the spectrophotometric EnzChek® pyrophosphate assay described above. ACSL4 inhibitors dose-dependently decreased the absorbance at 360 nm. Under optimized conditions, ROSI displayed an IC_{50} value of 1.1 ± 0.1 µM when tested against 50 nM of *h*ACSL4 (**Figure 27D**). The same experiment was performed against *h*ACSL3. As expected, ROSI showed no inhibition of *h*ASCL3 at tested concentrations (IC_{50} > 50 µM) confirming its selectivity over this isoform. Taken together these data validate the screening cascade composed of orthogonal biochemical and biophysical techniques.

4.2. Screening of FDA-approved drugs led to the identification of novel ACSL4 inhibitors.

4.2.1. Evaluation of an FDA-approved library against hACSL4.

A set of ca. 1200 FDA-approved drugs were screened to identify ACSL4 inhibitors using a screening cascade composed of the developed orthogonal methods described above (**Figure 28A**). Thus, compounds were first screened at 10 µM using DSF. This step led to the identification of 11 compounds that can be divided into three series. Among them, we identified ROSI (which was part of the library), acitretin, an oral retinoid used in the treatment of psoriasis (ΔT_m = 3.0 ± 0.3 °C) and a cluster of nine antifungal drugs with ΔT_m ranging from 1.7 to 5.7 °C.

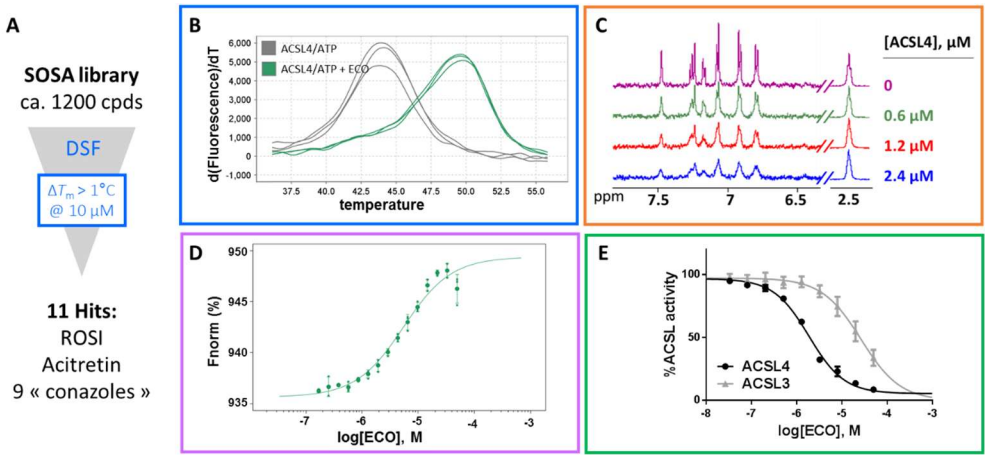

Figure 28. Econazole (ECO) identification and validation. (**A**) Flowchart describing TSA screening results. (**B**) Thermal denaturation profile of ACSL4 (grey curve, *n*=3) and ACSL4 in presence of 10 µM ECO (green curve, *n*=3). Results are expressed as derivative of fluorescence emission against temperature. (**C**) Selected region of the 1D ^{1}H NMR spectra of ECO (100 µM) at different concentrations of ACSL4. (**D**) MST dose-response curve for the binding interaction between ECO and ACSL4

[extracted from the MST traces at 4 to 5 s MST on time]. The concentration of protein is kept constant at 500 nM, while the ECO concentration varies from 0.17 µM to 74 µM. Fitting of the binding curve gives a K_D of 5.2 ± 1.1 µM (n=4). (**E**) Dose-response curves of ECO on ACSL activity (ACSL4 IC_{50} = 2.0 ± 0.2 µM, n=3; ACSL3 IC_{50} = 22.7 ± 1.7 µM, n=3).

Among the latter, econazole (ECO, ΔT_m = 5.7 ± 0.1 °C, **Figure 28B**) was selected as a representative compound for further validation. Therefore, it was assayed in ^{1}H NMR line broadening, MST and enzymatic assay. ECO binding to ACSL4 was confirmed in ^{1}H NMR line broadening experiment (**Figure 28C)** and a K_D of 5.2 ± 1.1 µM was measured by MST (**Figure 28D**). ECO was shown to inhibit ACSL4 with an IC_{50} value of 2.0 ± 0.2 µM in the presence of 0.06 % Triton X-100 (**Figure 28E**).

4.2.2. Preliminary Structure−Activity Relationships (SARs) of conazole series revealed a sub-micromolar selective ACSL4 inhibitor.

To validate the outcome of the screening process, the nine antifungal derivatives and some analogues were evaluated (**Table 1**). The most predominant feature of this series is the presence of an azole ring (imidazole or triazole) which is a key structural feature of antifungal derivatives. Despite this common feature, we set out to understand the key structural elements that were responsible for ACSL4 inhibitory potency. Triazole compounds (voriconazole, fluconazole, itraconazole, posaconazole) were inactive in DSF experiment as well as in orthogonal assays. The 1,3-dioxolane derivative ketoconazole showed a thermal shift value of 0.8 °C at 10 µM and a weak ACSL4 inhibition (45% of inhibition at 50 µM). Interestingly, phenethyl-

imidazole compounds investigated in the series revealed promising ACSL4 inhibitory activity.

Table 1. Structure−Activity Relationships of conazole series. [a]ΔT_m value was determined by three independent experiments for each compound (10 μM) in the presence of 1 mM ATP. [b]MST K_D value was determined by three independent experiments for each compound in the presence of 1 mM ATP. [c]IC_{50} value was determined by three independent experiments performed in duplicate for each compound concentration. nd: not determined.

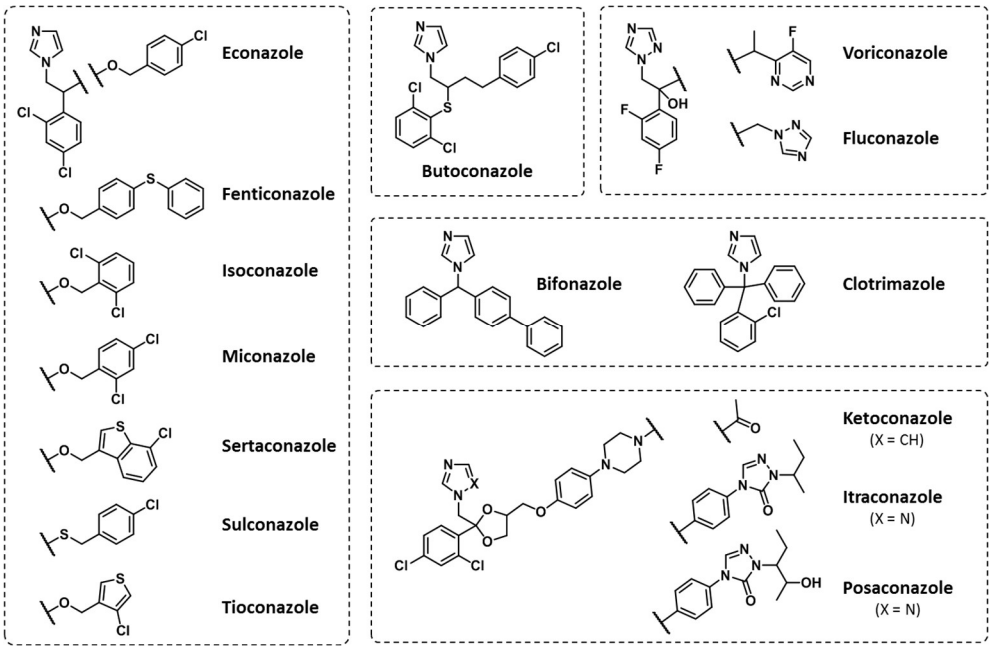

Compound	ΔT_m (°C)[a]	MST K_D (μM)[b]	IC_{50} values (μM) or % of inhibition at 50 μM[c]	
			*h*ACSL4	*h*ACSL3
Rosiglitazone	5.0 ± 0.1	2.2 ± 0.2	1.0 ± 0.02	0%
Econazole	5.7 ± 0.1	5.2 ± 1.1	2.0 ± 0.2	22.7 ± 3.9
Fenticonazole	2.8 ± 0.1	2.6 ± 0.5	8.8 ± 1.3	9%
Isoconazole	2.4 ± 0.1	3.0 ± 0.5	1.4 ± 0.5	0%
Miconazole	3.4 ± 0.3	1.1 ± 0.2	1.5 ± 0.3	0%
Sertaconazole	5.0 ± 0.4	2.0 ± 0.3	0.28 ± 0.09	29%
Sulconazole	1.7 ± 0.2	4.5 ± 0.9	15.2 ± 2.3	0%
Tioconazole	1.9 ± 0.3	8.1 ± 1.4	1.8 ± 0.2	9%
Butoconazole	2.3 ± 0.3	> 50	10.9 ± 1.3	0%
Bifonazole	3.2 ± 0.1	> 50	1.1 ± 0.3	0%
Clotrimazole	< 0.2	nd	nd	nd
Voriconazole	< 0.2	nd	nd	nd
Fluconazole	< 0.2	> 50	0%	0%
Ketoconazole	0.8 ± 0.2	> 50	45%	0%
Itraconazole	< 0.2	nd	nd	nd
Posaconazole	< 0.2	nd	nd	nd

For example, close analogues of ECO (isoconazole, miconazole and tioconazole) are characterized by an interesting micromolar-range IC_{50} and

K_D values. In addition, sertaconazole (SERTA) provided a significant thermal shift value (5.0 ± 0.4 °C at 10 μM), a submicromolar IC_{50} value (280 ± 90 nM) and a K_D value of 2.0 ± 0.3 μM. Biphenyl analogue bifonazole showed an inhibition in the micromolar-range but no binding could be observed in MST at tested concentrations. Interestingly, phenethyl-imidazole derivatives fenticonazole and sulconazole, as well as butoconazole and clotrimazole displayed no or reduced ACSL4 inhibitory activity. With the notable exception of ECO (IC_{50} ACSL3 = 22.7 ± 3.9 μM), all of the evaluated compounds were found selective for ACSL4 versus ACSL3.

4.2.3. ECO and SERTA prevent RSL3-induced lipid peroxidation and protect cells from ferroptosis.

We evaluated whether the most promising inhibitors ECO and SERTA were able to prevent RSL3-induced lipid peroxidation in LUHMES cells, a cell line highly sensitive to ferroptosis (179). We measured the levels of lipid ROS induced by RSL3 (30 nM) in LUHMES cells using the fluorescent probe BODIPY-C11 581/591 in the presence of 5 μM of ECO, SERTA and FLUCO (negative control). As shown in **Figure 29A** and **B**, treatment with RSL3 induced the lipid ROS accumulation in LUHMES cell line. Lipid ROS accumulation was significantly reduced when cells were treated with ECO or SERTA but not with FLUCO. Based on these encouraging results, we tested whether SERTA could prevent RSL3-induced ferroptosis in LUHMES cell line. We incubated the cells with ECO, SERTA and negative control (FLUCO) at 5 μM and subjected them to RSL3 treatment (0-20 nM). As

represented in **Figure 29C**, both ECO and SERTA significantly inhibited RSL3-induced ferroptosis whereas FLUCO (inactive on ACSL4) failed to rescue cells from ferroptosis.

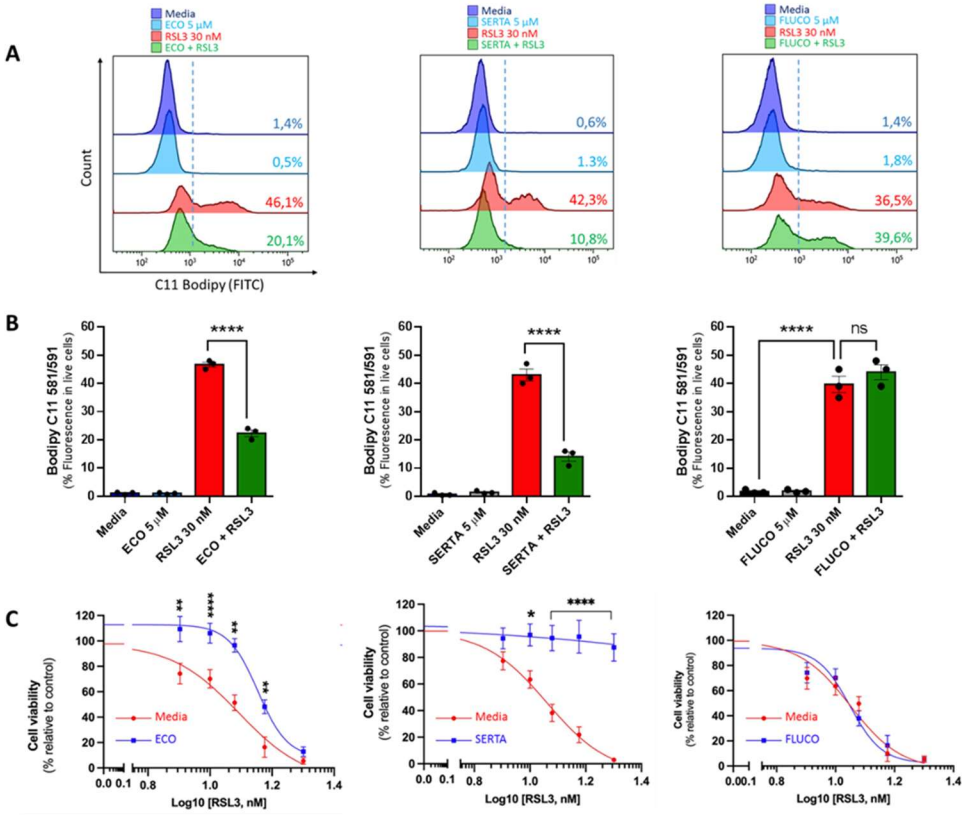

Figure 29. Cellular evaluation of ECO, SERTA and FLUCO. (**A**) Protection of LUHMES cells from RSL3-induced lipid peroxidation. LUHMES cells were treated with 5 µM ECO, 5 µM SERTA, 5 µM FLUCO, or media for 14 hours before induction of lipid peroxidation with 30 nM RSL3. After 6 hours, lipid peroxidation in live cells was measured by flow cytometry using the C11 BODIPY 581/591 probe. The staining data obtained at 530 nm (oxidized BODIPY 581/591-C11) are plotted as a histogram (**B**). Results are expressed in mean ± SEM, *n*=3 independent experiments. Statistical analyses were performed using one-way ANOVA followed by Dunnett's multiple comparisons test. **** $p < 0.0001$. (**C**) Protection of

LUHMES cells against RSL3-induced ferroptosis cell death. Dose dependent toxicity of RSL3 (0, 8, 10, 12, 15, 20 nM; 24 hours) after a pretreatment with 5 µM ECO, 5 µM SERTA, 5 µM FLUCO (*blue curves*) or media (*red curves*) for 14 hours. Results are expressed in mean ± SEM, *n*=3 independent experiments. Statistical analyses were performed using two-way ANOVA followed by Sidak's multiple comparison test. *$p < 0.05$; **$p < 0.01$; **** $p < 0.0001$.

Finally, to exclude that SERTA and ECO inhibit ferroptosis through other mechanisms such as ROS scavenging or iron chelation, we evaluated their ability to reduce 2,2-diphenyl-1-picrylhydrazyl (DPPH) radical (**Figure 30A**) and to displace Fe(II)-ferrozine complexe (**Figure 30B**). We observed no significant ROS-scavenging activity for ECO and SERTA compared to the two RTAs ferrostatin-1 (Fer-1) and trolox. In addition, iron chelation was negligible at the tested antiferroptotic concentrations.

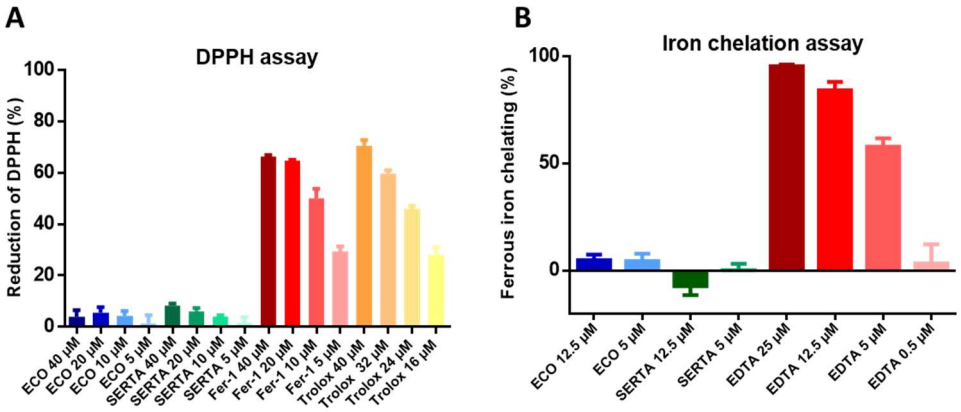

Figure 30. Evaluation of radical-trapping and iron-chelating activity of ECO and SERTA. (**A**) Assessment of antioxidant activity of ECO and SERTA (5, 10, 20 and 40 µM) compared to Fer-1 (5, 10, 20 and 40 µM) and trolox (16, 24, 32 and 40 µM) using the DPPH assay. Compounds were incubated with DPPH reagent (kit from Dojindo™) for 30 min at 25°C in the dark. Absorbance was read at 517 nm. The percent inhibition of DPPH for each condition was plotted as a histogram expressed in mean ± SEM, *n*=3 independent experiments. (**B**) Iron-chelation assesssment of

ECO, SERTA (5 and 12.5 μM) compared to EDTA (0.5, 5, 12.5 and 25 μM) monitored by displacement of Fe(II)-Ferrozine complex (kit from Amsbio™). Following ten minutes incubation, absorbance was read at 562 nm. Ferrous iron chelating (%) was plotted as a histogram expressed in mean ± SEM, *n=3* experiments.

5. Discussion

Ferroptosis, a recently coined regulated cell death, has attracted considerable attention owing to its important role in several diseases. Particularly, inhibiting ferroptosis accounts for an innovative approach in the potential treatment of neurodegenerative diseases and ischaemia reperfusion injuries (256). ACSL4 recently emerged as a key enzyme in ferroptosis execution (86,101). Knockout (KO) or pharmacological inhibition of ACSL4 was shown to confer a strong protection against ferroptosis. The research work presented here aims at developing orthogonal biochemical and biophysical tools for the identification of novel selective ACSL4 inhibitors with antiferroptotic properties.

Even though ACSLs from different organisms have been studied for decades, little is known about human ACSL4. Most studies on recombinant ACSL4 were performed using the rat enzyme (226). The production of human recombinant ACSL4 was reported only once and the purification was only partial (72). Here, we provide a robust protocol allowing the production of pure ACSL4 (purity > 95%) with a typical yield of 10 mg/L of culture volume.

In the perspective of screening chemical libraries to find new ACSL4 inhibitors, potential hits need to be validated through orthogonal methods. Therefore, we developed four different techniques to assess potential inhibitor. DSF was developed to serve as the first line screening method. This technique was optimized with reference inhibitor ROSI which displayed a significant thermal shift ($\Delta T_m = 5.0 \pm 0.1$ °C) when tested at 10 µM, indicating an increased stability of the protein upon ROSI binding. In 1D ^{1}H NMR line broadening experiments, a decrease in NMR signals intensity of ROSI was observed with increasing concentrations of ACSL4 consistent with a binding event. These qualitative results were further supported by quantitative data obtained from MST and an enzymatic assay. MST experiments were set up in order to determine the binding affinity of ACSL4 inhibitors. Experiments were optimized with ROSI which displayed a K_D value of 2.2 µM. Finally, although numerous studies have reported experimental setup to monitor ACSLs activity, only a few allow a continuous determination of the synthetase activity (39,46,72,226). To address this limitation, we adapted the spectrophotometric EnzChek® pyrophosphate assay (267). This robust enzymatic coupled assay which quantifies the pyrophosphate (PPi) formation, allowed an easy monitoring of ACSL4 activity. Under optimized conditions, reference ACSL4 inhibitor ROSI displayed an IC_{50} value of 1.0 µM, in good agreement with the data described against the rat ACSL4 (39,226).

Because ACSL4 is the only ACSL that increases ferroptosis sensitivity in presence of endogenous FA (101,141), selectivity over other ACSLs is desirable for the new ACSL4 inhibitors. In mammals, there are five ACSLs

isoforms (members 1, 3, 4, 5 and 6). The isoforms 3 and 4 share approximatively 63% sequence identity and only about 30% with other ACSLs (38). Therefore, in order to evaluate the selectivity profile of future inhibitors, a truncated and soluble *h*ACSL3 was produced and purified using a similar protocol as for ACSL4. As expected, ROSI showed no inhibition of ASCL3 at tested concentrations (IC_{50} > 50 μM).

Using a screening cascade composed of the developed orthogonal methods described above, an FDA-approved drug library was screened and allowed for the identification of 11 hits including a family of antifungal drugs. The main representative compound of this series (ECO) was shown to bind ACSL4 in DSF (ΔT_m = 5.7 ± 0.1 °C), ^{1}H NMR line broadening and in MST experiments (K_D = 5.2 ± 1.1 μM), and to inhibit ACSL4 activity with an IC_{50} value of 2.0 ± 0.2 μM. Because ECO is known to form colloidal aggregates, we double-checked that the inhibition was not the result of an aggregation-based inhibition mechanism which is a leading cause of false positives in screening campaigns (269). Aggregation-based inhibition is often characterized by a steep dose-response curve and is strongly attenuated by addition of non-ionic detergent such as Triton X-100 (often used at 0.01%) (270,271). ECO, when tested in the presence of up to 0.1% Triton X-100, kept its inhibitory activity with an appropriate dose–response curve (Hill slope = 1.1) (272), suggesting a specific inhibition mechanism. Early SAR studies highlighted the phenethyl-imidazole moiety as being important for ACSL4 inhibition. With an IC_{50} value of 280 nM, SERTA is, to the best of our

knowledge, among the most potent *h*ACSL4 inhibitor described so far. It was also shown to be selective over *h*ACSL3.

It is worth noting that for several compounds, such as ROSI, ECO, and SERTA, the measured IC_{50} values are lower than their corresponding K_D values. Theoretically, this should not occur, as inhibition requires the compound to be bound to the enzyme, implying that the K_D should be equal to or lower than the IC_{50}. This discrepancy may arise from differences in experimental conditions between the two assay types, particularly regarding enzyme concentration. In the MST assay, a relatively high concentration of ACSL4 (500 nM) is used. Although only 5% of the enzyme is fluorescently labeled (25 nM), constituting the "target", the remaining 95%, which is unlabeled, can still bind ligands. This excess of untagged enzyme may sequester compounds, effectively reducing the concentration available to interact with the labeled fraction and thus leading to an underestimation of the true binding affinity. This underestimation becomes more pronounced with increasing binding affinity, making it difficult to accurately determine K_D values that approach or fall below the total enzyme concentration. Therefore, MST K_D values should be viewed as an orthogonal method to assess relative binding affinities through dose-response analysis, rather than as absolute measures of affinity.

Antiferroptotic effect of both ECO and SERTA was then evaluated in LUHMES cells. These immortalized cells, derived from embryonic human mesencephalon, can be differentiated into dopaminergic-like neurons with expression of specific biochemical markers, extensive neurites, and the

capability to release and uptake dopamine (273). LUHMES cells exhibit high physiological relevance and retain practical culture requirements, which justifies their frequent use as a Parkinson's disease model when exposed to toxins.

This differentiated cell line is also particularly sensitive to ferroptosis (179), and *ACSL4* knockdown was shown to protect cells against ferroptosis induced by Erastin or RSL3 or AA + Fe (274). Because lipid peroxidation is considered the major event leading to ferroptosis, we measured the levels of lipid peroxidation induced by RSL3 using BODIPY-C11 581/591 in the presence of 5 μM of either ECO or SERTA. We found that these two ACSL4 inhibitors significantly reduced lipid peroxidation. They were also able to protect LUHMES cells against RSL3-induced ferroptosis.

Because, conazoles are reported to be cytochrome P450 (CYP) inhibitors, we wondered whether the protective effects were at least in part related to this CYP activity. We demonstrated that FLUCO (inactive on ACSL4) did not decrease lipid peroxidation and did not rescue cells from RSL3-induced ferroptosis. We also examined whether ECO and SERTA act as radical trapping antioxidants (RTAs) besides inhibiting ACSL4, which could explain the antiferroptotic activity. DPPH assay is the most straightforward method to evaluate the antioxidant/radical-trapping activity of compounds. In this assay, both ECO and SERTA did not reduce the absorbance of DPPH solution at 517 nm, indicating that they do not behave as RTAs. In addition, we excluded the possibility of an iron chelating mechanism that could contribute to the antiferroptotic effect at 5 μM.

Together, these results suggest that ECO and SERTA can effectively suppress lipid peroxidation and protect cells from ferroptosis likely through an ACSL4-dependent mechanism.

In summary, with the aim of identifying novel ACSL4 inhibitors, we developed a robust screening cascade composed of orthogonal biophysical and biochemical techniques that allowed the screening of an FDA-approved drug library. Identified hit inhibitors were successfully validated and the most promising compound (SERTA) displayed an IC_{50} of 280 nM against *h*ACSL4 and a good selectivity over *h*ACSL3. In addition, SERTA decreased lipid peroxidation and protected cells from RSL3-induced ferroptosis in a non-oncogenic neuronal cell line that is sensitive to ferroptosis (LUHMES). These results suggest that SERTA is not only an interesting tool for studying the biological role of ACSL4 in ferroptosis but may also serve as a starting point for the development of novel potent antiferroptotic compounds.

6. Acknowledgments

We thank Prof. Jean-François Goossens and Prof. Benoit Foligne for access to their laboratory equipment. This work was supported by the French Community of Belgium (ARC 21/26-115), the Belgian Fonds National de la Recherche Scientifique (F.R.S.-FNRS; PDR grant 40003810), the Télévie (Grant 40007387), the University of Lille and INSERM. D.M.D. is a Télévie research fellow. The authors thank the Nuclear and Electron Spin Technology

(NEST) platform for providing access to the Bruker Ascend Avance III 600 MHz system.

RESULTS - CHAPTER II

In Chapter I, we established a methodology to evaluate ACSL4 ligands and inhibitors, which enabled the identification of a novel phenethyl-imidazole inhibitor series with antiferroptotic activity. Chapter II builds on this foundation by presenting the team's efforts across diverse medicinal chemistry approaches aimed at further optimizing inhibitors through iterative cycles of scaffold modification and evaluation. The first section of Chapter II outlines the SOSA strategy, beginning with a brief exploration of phenethyl-imidazole modifications, followed by a thorough investigation of the ROSI scaffold, which led to the development of improved ACSL4 inhibitors (33). The second part of this chapter discusses the fragment-based drug design (FBDD) strategy, initiated with the screening of a fragment library and culminating in the design of a potent novel inhibitor. Finally, the last part of Chapter II highlights a common limitation across all inhibitor series, their reduced activity against ACSL4's preferred substrates.

1. Selective optimization of side activity (SOSA) approach

An early objective of the SOSA approach is to chemically modify the scaffold to eliminate the compound's original pharmacological activity while preserving or improving the desired activity. In this context, two strategies were pursued in parallel: modification of the newly identified phenethyl-imidazole series (see Chapter I) and optimization of the reference inhibitor, ROSI.

1.1. Modulating the phenethyl-imiadzole scaffold

To optimize phenethyl-imidazole series, we used SERTA and ECO as starting points, with the primary objective of eliminating their original pharmacological activities. Notably, azole antifungals are known to inhibit lanosterol 14α-demethylase, a cytochrome P450 (CYP) enzyme essential for ergosterol biosynthesis (275). Azole inhibitors occupy the active site typically reserved for CYP substrates, with their imidazole/triazole moiety coordinating directly with the heme iron, thereby blocking oxygen binding and inhibiting the enzyme (276). However, there is a cross-over inhibition of human sterol 14α-demethylase (CYP51) involved in cholesterol biosynthesis (277). **Figure 31** illustrates the binding between econazole and CYP51.

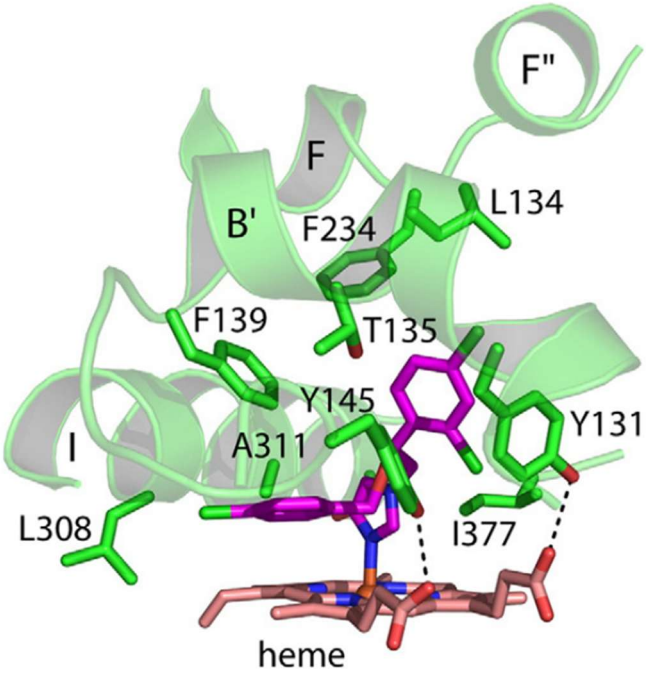

Figure 31. Crystal structure of human CYP51 in complex with Econazole (ECO). The protein is shown in green, with amino acid residues located within 4 Å of ECO represented as sticks. ECO and the heme group are shown as sticks with carbon atoms colored magenta and salmon, respectively. Oxygen, nitrogen, iron, and chlorine atoms are colored red, blue, orange, and green. Black dashed lines indicate hydrogen bonds. From (277).

In addition, azole antifungals inhibit various other CYP enzymes involved in xenobiotic metabolism, including CYP3A4 (278), and also target other heme-containing proteins such as indoleamine 2,3-dioxygenase (279), as well as iron-dependent non-heme enzymes like thromboxane synthase (280).

Given that these off-targets likely involve iron coordination, efforts to optimize ACSL4 inhibition focused primarily on replacing the imidazole moiety with less chelating alternatives. The removal of the imidazole group from the ECO scaffold (**1**) led to a significant decrease in activity (with an estimated IC_{50} of 25 μM), although inhibition remained present (**Figure 32**). In line with the imidazole modulation strategy, a recent study aimed at minimizing CYP3A4 inhibition by itraconazole (ITRA), explored a series of azole and non-azole derivatives (281). They initially observed that replacing the 1,2,4-triazole moiety of ITRA with the imidazole found in SERTA or ECO did not affect CYP3A4 inhibition, suggesting that both heterocycles possess comparable metal-chelating properties. However, introducing alkyl groups such as methyl, ethyl, or isopropyl at the 2-position of the imidazole ring progressively reduced CYP inhibition, likely due to increased steric hindrance interfering with iron coordination. Additionally, substituting imidazole with pyrazole or tetrazole significantly diminished CYP inhibition.

Based on this, we investigated similar modulations on SERTA scaffold and evaluated their inhibitory activity against ACSL4 (**Figure 32**).

The introduction of alkyl groups at the 2-position (**2**,**3**,**4**) led to a drastic reduction in activity (IC_{50} **2** ≈ 50 μM), with the bulkier the alkyl group, the greater the decrease in inhibition. Replacing the imidazole with a pyrazole (**5**) or tetrazole (**6**,**7**) also reduced activity, though to a lesser extent, with IC_{50} values around 15 μM. Although this represents a 50-fold reduction compared to the parent SERTA, these findings suggest that it is possible to reduce CYP inhibition while retaining meaningful activity against ACSL4. However, the coordinating properties of the scaffold may be important for interacting with the magnesium cofactor within the ACSL4 catalytic pocket, potentially complicating the selective optimization of ACSL4 activity.

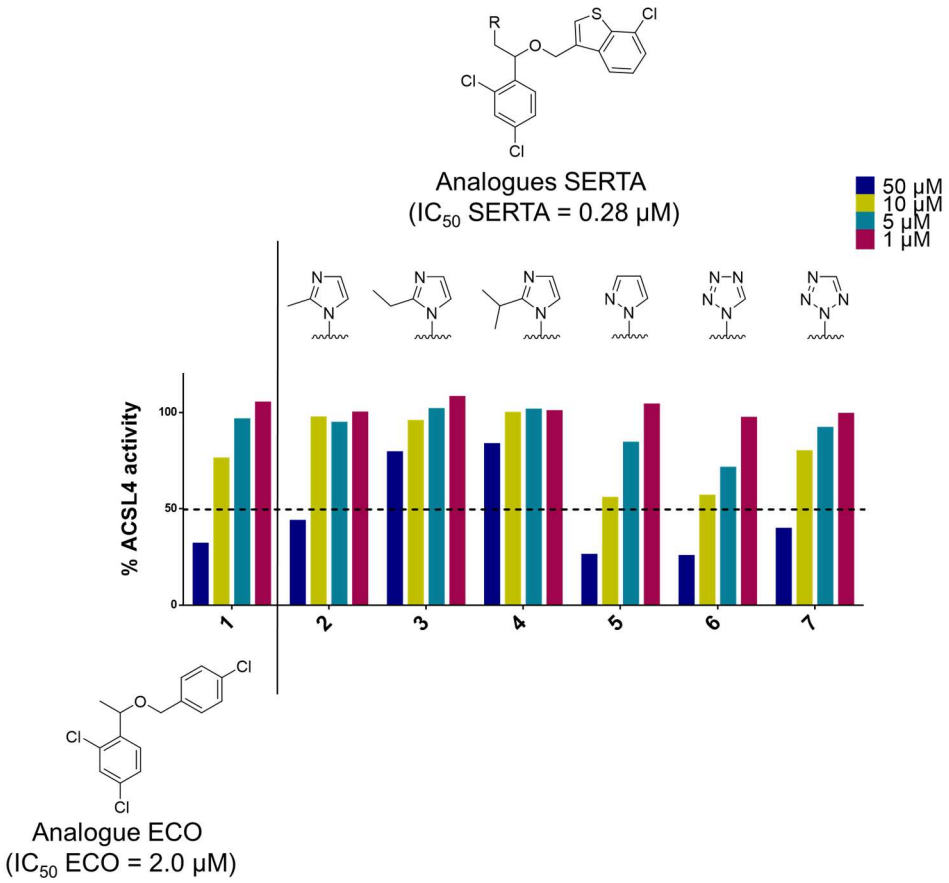

Figure 32. Pilot study on imidazole modification. Compounds were tested at 50 µM (blue), 10 µM (yellow), 5 µM (cyan), and 1 µM (magenta). Each bar is the result of a single experiment.

Another limitation of the phenetyl-imidazole scaffold is its high lipophilicity, which appears to correlate with its activity against ACSL4. All the hits in **Table 1** have a predicted partition coefficient (logP) above 4.5, with the most potent SERTA also being among the most lipophilic compound, showing a logP of 5.6. In contrast, ketoconazole, which exhibits low activity, has a lower predicted logP of 3.6, while completely inactive FLUCO has a value below 1

(**Table 2**). Additionally, SERTA exhibits a low fraction of sp^3-hybridized carbons (Fsp^3 = 0.15), leading to pronounced planarity that adversely affects its solubility (282).

Table 2. Relationship between lipophilicity and activity for conazole derivatives. Physicochemical properties are predicted using SwissADME.ch. LogP value is the average of five predictive models. Activity values represent the mean of three independent experiments. MW, molecular weight; Fsp3, fraction of sp^3 cabons; nd, not determined.

	IC_{50} (μM)	MW (g/mol)	LogP	Fsp^3
SERTA	0.28	437.8	5.6	0.15
KETO	≈ 50	531.4	3.6	0.38
FLUCO	nd	306.3	0.9	0.23

Therefore, future optimization efforts should also aim to reduce the lipophilicity and enhance the 3D features of the SERTA scaffold.

1.2. Modulation of ROSI-scaffold

While early attempts to improve the phenethyl-imidazole series were unsuccessful, the SOSA approach starting from ROSI led to significant optimization of ACSL4 inhibition. The results presented here provide a brief overview of this work, as reported in *Angewandte Chemie* (33).

How to cite: *Angew. Chem. Int. Ed.* **2025**, e202500518
doi.org/10.1002/anie.202500518

Drug Discovery

LIBX-A401: A Novel Selective Inhibitor of Acyl-CoA Synthetase Long Chain Family Member 4 (ACSL4) and Its Binding Mode

Darius Mazhari Dorooee, Séverine Ravez, Didier Vertommen, Nicolas Renault, Nicolas Papadopoulos, Romain Marteau, Emeline Charnelle, Karine Porte, Alexandre Gobert, Nathalie Hennuyer, Gaetan Herinckx, Maëla Pautric, Aurélie Jonneaux, Jean Christophe Devedjian, David Devos, Bart Staels, Patricia Melnyk, Stefan N. Constantinescu, Raphaël Frédérick, and Jamal El Bakali**

ROSI is the most widely used ACSL4 inhibitor in the literature. However, its potent primary activity as a PPARγ agonist, a central regulator of lipid homeostasis, represents a major limitation to its use as a selective ACSL4 inhibitor. To overcome this limitation, we initiated a medicinal chemistry campaign to optimize the ROSI scaffold with the goal of eliminating its PPARγ activity while preserving its inhibitory effect on ACSL4. The TZD ring, particularly its acidic character, is essential for PPARγ activity (233), so our initial approach focused on replacing it on ROSI scaffold or its phenyl analogue (**8**) (**Table 3**). Simply removing it led to a complete loss of activity (**9**, IC_{50} > 50 μM). However, N-methylation of the TZD, which removes its acidic properties, retained activity (**10**, IC_{50} = 4.5 μM). This suggested that it was possible to eliminate PPARγ activity while preserving ACSL4 inhibition. Next, we considered opening the TZD ring with ester analogues. Interestingly, the ethylene ester analogue preserved activity (**11**, IC_{50} = 8.5 μM), and the linker showed an optimal size, as both smaller (**12**, IC_{50} = 24 μM) and larger (**13**, IC_{50} > 50 μM) linkers resulted in decreased activity. Rigidifying compound **11** by forming a methylacrylate derivative resulted in activity (**14**, IC_{50} = 1.5 μM) comparable to the parent compound ROSI.

Finally, replacing the amine in the linker connecting the two phenyl groups by an amide further improved the activity (**15**, IC_{50} = 0.38 μM). Remarkably, compound **15** showed no activity against PPARγ or ACSL3 at the tested concentrations. The binding of **15** to ACSL4 was further confirmed by nDSF (ΔT_m = 5.3 °C) and by MST (K_D = 0.72 μM) and, similarly to ROSI and SERTA, was dependent on the presence of ATP. This is consistent with the requirement of ATP for FA binding in *tt*LC-FACS, suggesting that these inhibitors may engage the enzyme in an analogous manner.

Table 3. Modulations around ROSI scaffold. IC_{50}, K_D and ΔT_m values (± SD) represent the mean of three independent experiments.

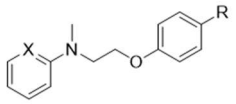

Entry	X	R	ACSL4 IC_{50}, µM
ROSI	N	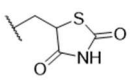	1.1 ± 0.1
8	CH		0.4 ± 0.1
9	N	H	> 50
10	N	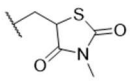	4.5 ± 1.1
11	CH	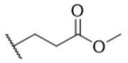	8.5 ± 3.5
12	CH	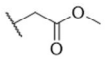	24.1 ± 0.6
13	CH	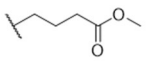	> 50
14	CH	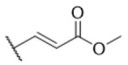	1.5 ± 0.6
15	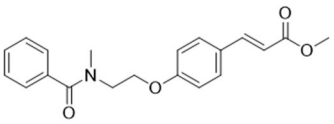		

LIBX-A401
IC_{50} (ACSL4) = 0.38 ± 0.03 µM
MST K_D (ACSL4) = 0.72 ± 0.12 µM
ΔT_m (ACSL4) = 5.3 ± 0.2 °C
IC_{50} (ACSL3) > 50 µM
Inactive on PPARγ at 10 µM

To investigate the binding site of **15**, photoaffinity labeling (PAL) experiments were conducted using a derivative bearing a *para*-substituted trifluoromethyl diazirine moiety on the benzamide. Following trypsin digestion and LC-MS/MS analysis, Ala329 was found to be the modified residue. This residue aligns with Leu236 in *tt*LC-FACS, positioned at the distal end of the FA tunnel. Based on these results, we initiated *in sillico* studies using a refined AlphaFold 2 model. Blind docking of compound **15** revealed the best pose within the orthosteric FA binding site. Furthermore, molecular dynamics (MD) simulations performed to refine ACSL4-**15** complex model highlighted an interaction by sustained hydrogen bonds between the amide of **15** and Gln302 side chain (**Figure 33**). Additional interactions include hydrophobic contacts within the lipophilic tunnel, notably involving residue Leu325.

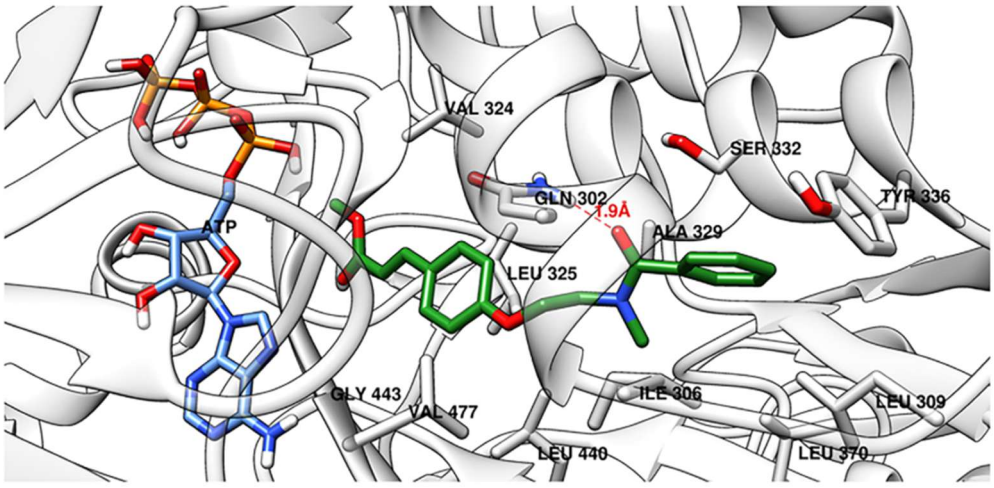

Figure 33. Putative binding mode of compound **15** on ACSL4. ASCL4-compound **15** complex after docking and an additional 100 ns MD simulation.

To assess the importance of these residues in compound **15** binding, different ACSL4 mutants, including Gln302Ala, Gln302Met and Leu325Phe were generated and evaluated. While the Gln302Ala and Gln302Met mutations disrupt the ability to form hydrogen bonds with the amide group of compound **15**, the Leu325Phe mutation introduces steric hindrance within the FA tunnel, impairing ligand accommodation. All these mutants exhibited a significant reduction in both inhibitory activity and binding affinity of **15**. Together, these data strongly support the binding of **15** into the FA pocket.

Finally, the antiferroptotic activity of compound **15** was assessed across various cell lines, including LHUMES. It effectively prevented lipid peroxidation (**Figure 34A**) and the associated cell death (**Figure 34B**) triggered by co-treatment with arachidonate and iron, in a manner comparable to *ACSL4* knockdown. ACSL4 engagement by compound **15** in cells was monitored by cellular thermal shift assay (CETSA). CETSA is based on the same principle as conventional TSA, but ligand-induced stabilization is assessed at the target level in more complex environments, such as intact cells (283). This is possible because, in these settings, proteins generally unfold and precipitate sufficiently independently of one another. Thus, after treating cells with the drug, followed by heating, lysis, and removal of aggregates, western blot analysis allows for the determination of remaining soluble or folded protein.

Treatment of LUHMES cells with **15** significantly stabilized ACSL4, demonstrating that the compound reaches its target in a cellular context and supporting the enzyme's role in its antiferroptotic activity (**Figure 34C**).

Overall, compound **15** (**LIBX-A401**) is a promising tool for studying the role of ACSL4 in various pathological settings.

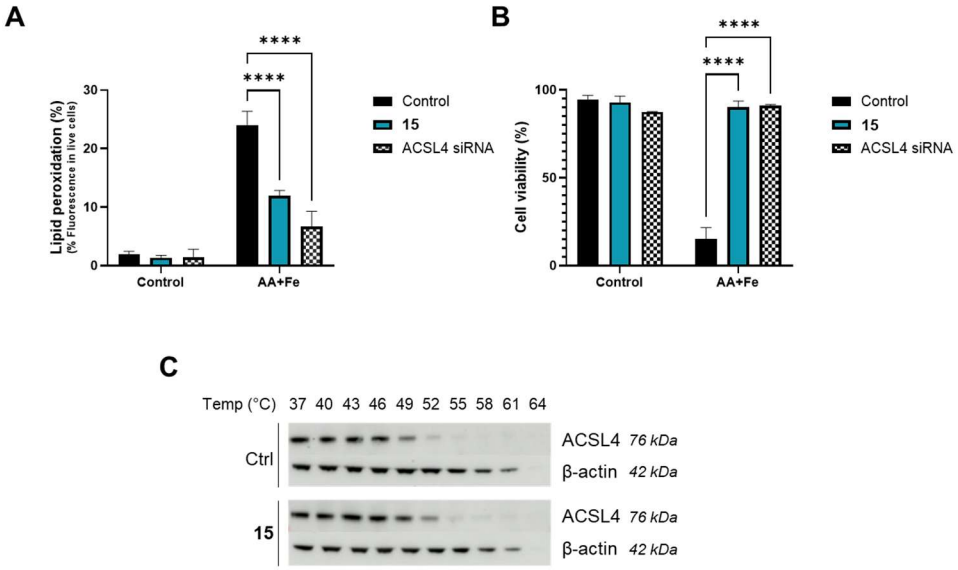

Figure 34. Compound **15** prevents ferroptosis in LHUMES cells by targeting ACSL4. (**A**) Percentage of lipid peroxidation in LUHMES cells transfected with ACSL4 siRNA or pretreated with 2.5 µM of **15** for 4 h, followed by treatment with AA+Fe for 24 h. Lipid peroxidation was assessed by flow cytometry using the C11 BODIPY 581/591 probe. The fluorescence signal at 530 nm (oxidized C11 BODIPY) is shown as a histogram. Data represent mean ± SEM (n = 4). (**B**) Cell viability of LUHMES cells assessed by flow cytometry using LIVE/DEAD™ Violet stain. Cells were transfected with ACSL4 siRNA or pretreated with 2.5 µM of **15** for 4 h, followed by treatment with AA+Fe for 48 h. Data represent mean and SEM (n = 3). (**C**) Representative western blots showing thermal stability of ACSL4 in LUHMES cell line in the presence of DMSO or compound **15** at 10 µM. ACSL4 was quantified by immunoblotting. Statistical analyses were performed using two-way ANOVA followed by Tukey's multiple comparisons test. **** $p < 0.001$.

Optimization of the inhibitor series has continued beyond the initial publication. One limitation of **LIBX-A401** is its methylacrylate moiety, a Michael acceptor that can potentially form covalent bonds with nucleophiles

(284,285). Although the reversibility of ACSL4 inhibition was confirmed via a jump-dilution assay and minimal reactivity was observed in the presence of nucleophiles such as GSH, potential reactivity in more complex biological systems cannot be excluded.

Therefore, the subsequent focus in optimizing the series was directed toward modifying this methylacrylate group. Replacing the central phenyl group by a naphtyl (**16**), which retains scaffold rigidity while eliminating the Michael acceptor character, resulted in activity comparable to **LIBX-A401** (**Figure 35**). However, the ester moiety in compound **16** remains problematic, as it may be susceptible to hydrolysis by circulating esterases *in vivo*. This concern is particularly relevant given that the corresponding acid analogue (**17**) completely loses activity. Considerable efforts were devoted to modulating this ester, culminating in the development of a methyl-oxadiazole derivative (**18**) with potent ACSL4 activity (IC_{50} = 0.10 μM).

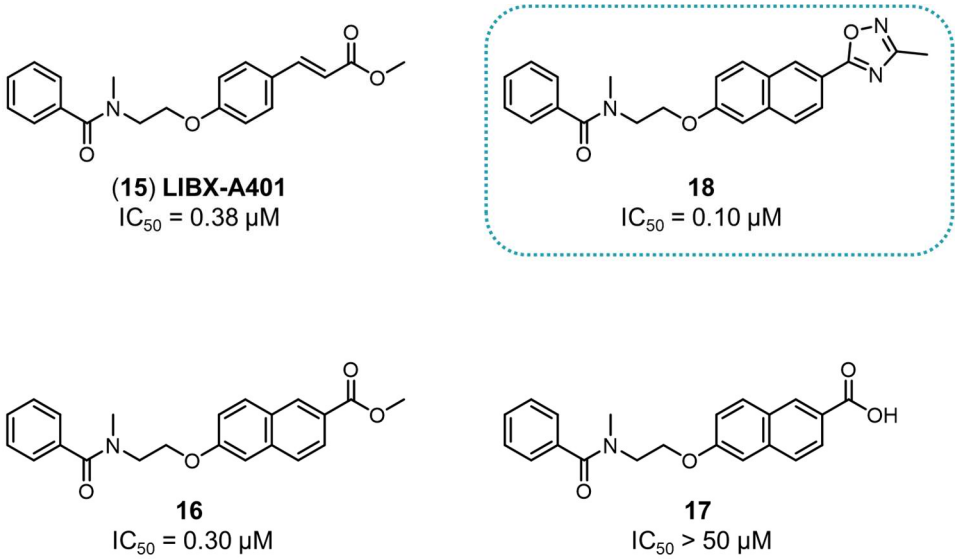

Figure 35. Modifying the methylacrylate group of LIBX-A401. The figure depicts three LIBX-A401 analogues and presents their inhibitory activity against ACSL4. IC_{50} are the results of three replicates.

Similar to the conazole analogues, optimization of the ROSI series also tends to favor lipophilic and planar scaffolds, as reflected by the increasing LogP and decreasing Fsp^3 when progressing from ROSI, to LIBX-A401, and ultimately compound **18** (**Table 4**). To address these physicochemical limitations, ongoing lead optimization is pursuing a scaffold-hopping strategy, focusing on modifications to the central core of **18**, such as heterocycle replacement or ring opening.

Table 4. Relationship between potency, lipophily and planarity for ROSI derivatives. Physicochemical properties are predicted using SwissADME.ch. LogP value is the average of five predictive models. IC_{50} represent the mean of three independent experiments. MW, molecular weight; Fsp^3, fraction of sp^3 cabons.

	IC_{50} (μM)	MW (g/mol)	LogP	Fsp^3
ROSI	1.1	357.4	2.3	0.28
(**15**) LIBX-A401	0.38	339.4	3.2	0.20
18	0.10	387.4	4.0	0.17

I personally contributed to this work by synthesizing a few ROSI derivatives, including compound **13**, and by evaluating the binding interactions of **LIBX-A401** with both wild-type ACSL4 and the mutants using MST and nDSF.

2. Fragment-based drug discovery

The successful use of the AI-based structural model of ACSL4 with the ROSI series motivated us to pursue the development of inhibitors through a fragment-based drug discovery (FBDD) strategy. Indeed, this approach, which aims to identify low-affinity chemical starting points, is greatly facilitated by structural information that enables the rational evolution of fragments into lead compounds (286).

The results presented here provide an overview of the FBDD approach applied to ACSL4, as reported in the *Journal of Medicinal Chemistry* (287).

We began our FBDD program by screening a library of 640 fragments (Maybridge library, Fischer Scientific), which were visually pre-selected to maximize chemical diversity, using the screening cascade we had previously established (250). Following the initial DSF screening in the presence of ATP, fragments that stabilized ACSL4 by more than 1 °C at 2 mM, or by more than 0.5 °C at 0.5 mM for the less soluble compounds, were selected.

Among these, 31 fragments showed at least 50% inhibition of ACSL4 activity at 500 μM. **Figure 36A** presents four of the most appealing fragments, all exhibiting ligand efficiency (LE) greater than 0.3. Ligand efficiency (LE) is a parameter frequently monitored during fragment-to-lead optimization (288). It represents the binding energy of a compound normalized by its number of heavy atoms (non-hydrogen atoms). In practice, binding energies can be approximated using IC_{50} values obtained in a given assay system. During optimization, maintaining or improving LE as the fragment is grown ensures that improvements in potency are not offset by a disproportionate increase in molecular weight. Benzofuran **19** was prioritized for optimization due to its potency (IC_{50} = 33 μM), multiple potential sites for derivatization, and synthetic accessibility (**Figure 36B**).

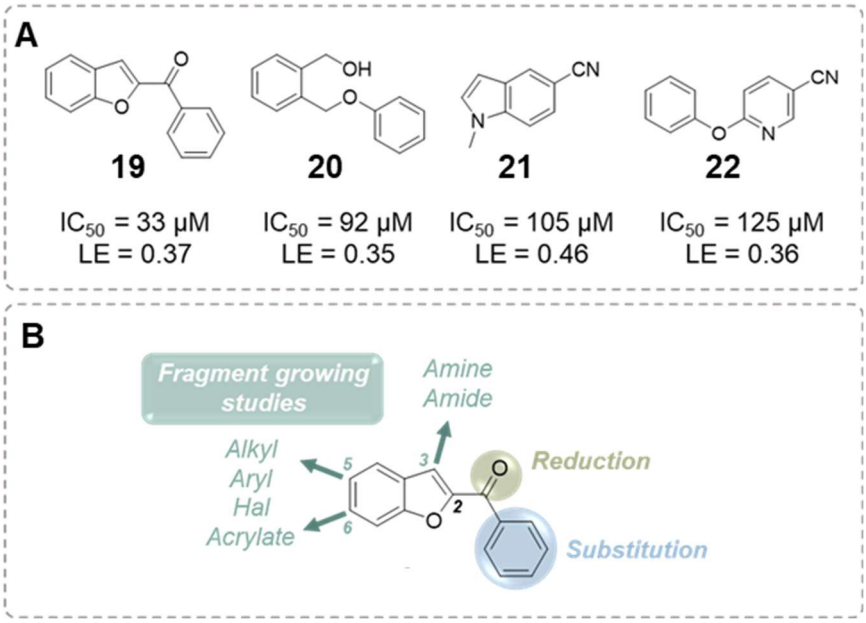

Figure 36. Identification of benzofuran (**19**) as a promising starting fragment. (**A**) Representative fragment hits selected from the primary screening cascade. (**B**) Initial structural modifications explored around compound **19**.

Figure 37 illustrates the key intermediates involved in the optimization of fragment **19**. SAR exploration began with modifications at the C-3 position of the benzofuran ring. An amino group was initially introduced due to the tractable synthesis and the potential for further functionalization. While this modification was tolerated, it did not enhance the activity of the parent compound **19**. However, acetylation of the amine led to a six-fold improvement in potency (**23**: IC_{50} = 5.6 µM).

The ketone moiety present on the fragment was found to be essential for ACSL4 inhibition. Its reduction to either a secondary alcohol or a methylene

group led to a complete loss of activity. Likewise, the phenyl ring of the acetophenone was critical to activity.

Further SAR exploration focused on substituting the benzofuran core. Substitution at C-5 with a methyl group (**24**: IC_{50} = 0.33 µM) significantly enhanced ACSL4 inhibition. Notably, the incorporation of a methylacrylate moiety, as seen in **LIBX-A401**, resulted in a marked improvement in activity (**25**: IC_{50} of 0.049 µM). Elongation of the methyl ester did not have a positive impact on the inhibitory activity, while replacing the ester by a carboxylic acid led to a total loss of potency. Thus, compound **25** was selected for further characterization.

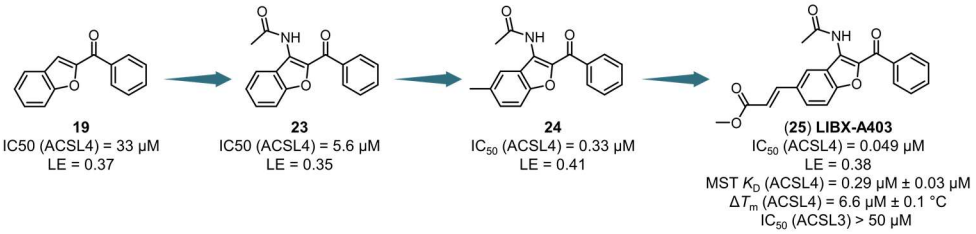

Figure 37. Fragment evolution toward compound **25**.

Initial selectivity profiling revealed that **25** does not inhibit ACSL3. Furthermore, the binding of **25** to ACSL4 was validated by nDSF (ΔT_m = 6.6 °C) and by MST (K_D = 0.29 µM). As with previous inhibitors, binding was ATP-dependent, suggesting a similar binding mode to **LIBX-A401**. Based on this hypothesis, *in silico* docking within the FA pocket of the refined ACSL4 model we previously reported (33), followed by molecular dynamics simulations, revealed that compound **25** primarily engages in hydrophobic interactions. As observed for **LIBX-A401**, Leu325 was among the key

interacting residues, whereas Gln302 was not involved. Consistently, evaluation of **25** against the Gln302Met mutant did not alter potency, while its activity was reduced by tenfold against Leu325Phe mutant. Collectively, these findings support the hypothesis that compound **25** binds within the FA pocket of ACSL4.

Finally, compound **25** was evaluated for its antiferroptotic activity across two different cell models. In MDA-MB231 cancer cells, **25** dose-dependently prevented cell death (EC_{50} = 172 nM) (**Figure 38A**), with ACSL4 engagement confirmed through cellular thermal shift assay (**Figure 38B**). Furthermore, in LHUMES cells, compound **25** reduced lipid peroxidation (**Figure 38C**) and preserved cell viability under ferroptotic conditions (**Figure 38D**), similarly to *ACSL4* knockdown.

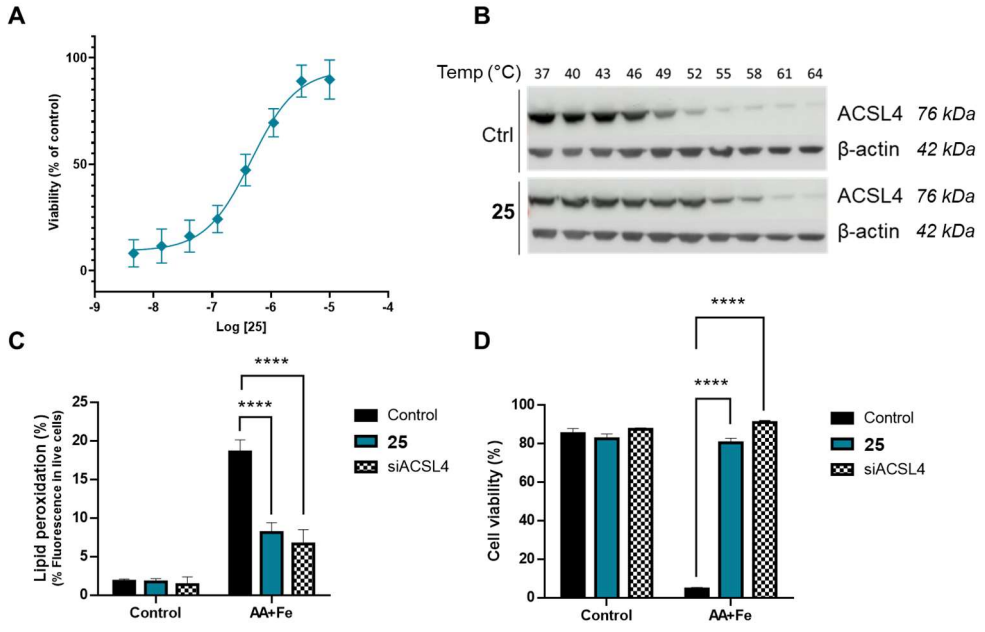

Figure 38. Compound **25** prevents ferroptosis by targeting ACSL4 in different cellular models. (**A**) Cell viability of MDA-MB-231 cells assessed by MTS assay. Cells were pretreated with increasing concentrations of compound **25** for 18 h, followed by treatment with 800 nM RSL3 for 24 h. Data represent mean and SEM (n = 3). (**B**) Representative western blots showing thermal stability of ACSL4 in MDA-MB-231 cell line in the presence of DMSO or compound **25** at 10 µM. ACSL4 was quantified by immunoblotting. (**C**) Percentage of lipid peroxidation in LUHMES cells transfected with ACSL4 siRNA or pretreated with 2.5 µM of **25** for 4 h, followed by treatment with AA+Fe for 24 h. Lipid peroxidation was assessed by flow cytometry using the C11 BODIPY 581/591 probe. The fluorescence signal at 530 nm (oxidized C11 BODIPY) is shown as a histogram. Data represent mean ± SEM (n = 4). (**D**) Cell viability of LUHMES cells assessed by flow cytometry using LIVE/DEAD™ Violet stain. Cells were transfected with ACSL4 siRNA or pretreated with 2.5 µM of **25** for 4 h, followed by treatment with AA+Fe for 48 h. Data represent mean and SEM (n = 3). Statistical analyses were performed using two-way ANOVA followed by Tukey's multiple comparisons test. **** $p < 0.001$.

Compound **25** (**LIBX-A403**) is the most potent ACSL4 inhibitor reported to date, exhibiting nanomolar activity. Its development constitutes a strong foundation for further lead optimization.

Nonetheless, the physicochemical profile of **LIBX-A403** remains suboptimal. With a logP above 3 and a high molecular planarity ($Fsp^3 = 0.1$), the compound exhibits poor solubility. Current efforts therefore focus on optimizing solubility by modifying the scaffold to introduce polar groups that lower the logP, and to reduce the planarity by increasing the content of sp^3 carbons (**Figure 39**).

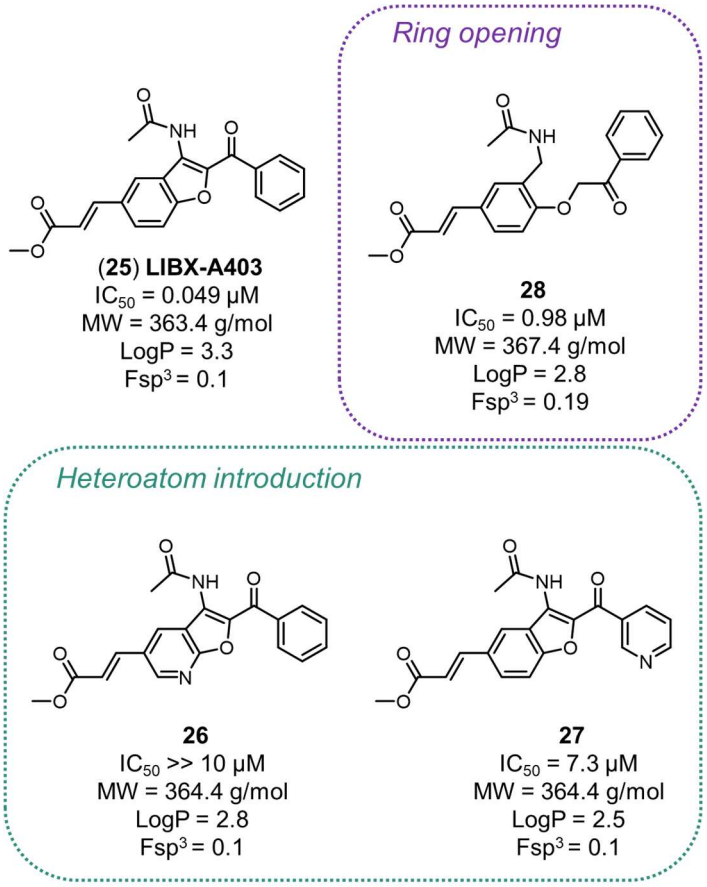

Figure 39. Enhancing solubility of the **LIBX-A403** scaffold. The figure shows three **LIBX-A403** analogues and presents their activity on ACSL4 as well as key physicochemical properties predicted using SwissADME.ch. IC_{50} are the results of three replicates.

Introducing nitrogens, either at the 7-position on the benzofuran ring (**26**), or at the *meta* position of the phenyl (**27**) reduced logP by 0.5 and 0.8 respectively. However, these modest modifications resulted in a substantial loss of ACSL4 inhibitory activity, with compound **27** exhibiting an IC_{50} over 90-fold higher, and compound **26** showing only 3% inhibition at 10 µM.

Interestingly, opening the benzofuran ring (**28**) to increase Fsp^3 preserved ACSL4 inhibitory activity (IC_{50} = 0.98 μM), although with a 20-fold reduction in potency. Therefore, while the inhibitory activity of benzofuran analogues appears intrinsically linked to the lipophilicity and planarity of their scaffold, there may be room to optimize these parameters without substantially affecting potency.

My contribution to this work involved participating in the initial fragment screening and performing biophysical characterizations of **LIBX-A403** and compound **24** binding to ACSL4.

3. FA-dependent inhibition

In recent years, significant progress has been made in the development of ACSL4 inhibitors, with compounds exhibiting up to a twenty-fold increase in potency and enhanced selectivity compared to reference inhibitors. However, we made a disappointing, yet intriguing discovery when assessing ACSL4 inhibition against its preferential substrate arachidonate. We found that the developed molecules were significantly less active in the presence of arachidonate (20:4ω-6) compared to palmitate (16:0), which had been the substrate used in the activity assays up to that point. To further investigate this phenomenon, we evaluated several ACSL4 inhibitors, both in-house compounds such as LIBX-A403 and compound **18**, and those from the literature, against a panel of structurally diverse FAs (**Table 5**). Initially, we

observed that several recently reported inhibitors, such as PRGL493 or silibiline, were completely inactive in our experimental setup, regardless of the FA used. In addition, for all the compounds that did show inhibition, we noted a clear FA-dependent pattern in their activity. ACSL4 inhibition was strongest for SFAs and MUFAs and progressively declined with increasing unsaturation (up to four double bonds) reaching its lowest level with HUFAs, including arachidonate (20:4ω-6), eicosapentaenoate (20:5ω-3) and adrenate (22:4ω-6).

Surprisingly, AS-252424, previously reported to inhibit ACSL4 in the presence of arachidonate (93), was completely inactive with this FA in our assay.

Although significantly less potent, LIBX-A403 and compound **18** were among the most effective ACSL4 inhibitors in the presence of PUFAs, suggesting that improved inhibition with palmitate (16:0) may correlate with enhanced activity in the presence of PUFAs as well.

Table 5. FA dependency of ACSL4 inhibitors**.** Evaluation of several reported and in-house ACSL4 inhibitors (10 μM) against nine structurally distinct FAs: palmitate (16:0), stearate (18:0), oleate (18:1ω-9), linoleate (18:2ω-6), eicosenoate (20:1ω-9), arachidonate (20:4ω-6), eicosapentaenoate (20:5ω-3), docosenoate (22:1ω-9), and adrenate (22:4ω-6). Results are presented as mean % inhibition relative to control. Each value represents the average of two independent experiments performed duplicates.

	16:0	18:0	18:1ω-9	18:2ω-6	20:1ω-9	20:4-ω6	20:5ω-3	22:1ω-9	22:4ω-6
Rosiglitazone	90	92	85	73	64	0	10	93	7
Triacsine C	100	98	88	35	27	29	7	97	0
AS-252424	79	82	60	37	25	2	6	80	3
PRGL493	2	1	9	1	0	0	2	13	0
Silibinine	6	4	0	1	0	0	1	8	0
Sertaconazole	67	98	87	48	50	0	6	93	2
18	90	100	100	100	93	17	55	100	56
LIBX-A403	94	90	90	90	91	16	51	87	65

This trend, where inhibition diminishes as the FA more closely resembles the preferred substrate, suggests a competitive relationship between the inhibitor and the FA for binding to ACSL4. Such a competitive mechanism would be consistent with the proposed binding site of LIBX-A401 and LIBX-A403 within the FA pocket, as well as with the ATP-dependency observed for the binding of most of these inhibitors. However, the detailed mechanism of ACSL4 inhibition remains uncharacterized for any of these compounds. The Triacsin C analogue Triacsin A was reported to act as a competitive inhibitor with respect to oleate in *Pseudomonas aeruginosa* ACSL (235). In contrast,

the TZD analogue troglitazone (TRO) was unexpectedly reported as a mixed inhibitor toward palmitate (49). We re-evaluated the inhibition mechanism of TRO and confirmed the mixed inhibition pattern for palmitate (16:0) in our experimental setup. This suggests that the inhibitor binds ACSL4 whether palmitate (16:0) is present or not, which may point to distinct binding sites between the two ligands. Nevertheless, mixed inhibition does not preclude the possibility of inhibitor binding within the enzyme's active site (289). It was even recently proposed that mixed inhibitors exclusively bind to active sites (290). As conclusions could not be drawn from kinetic studies alone, we turned to biophysical methods for further insight.

We initiated the development of a saturation transfer difference nuclear magnetic resonance (STD NMR) assay to perform competition between FAs and inhibitors. In this technique, a selective saturation pulse is applied to the target protein, and saturation is transferred to nearby ligands, resulting in a reduction of their proton NMR signals (291). Compounds showing proton signal attenuation under these conditions are identified as binders. As results are presented as the absolute difference between spectra acquired with and without protein saturation, stronger STD signals for a given ligand-protein complex indicate more substantial interactions with the protein.

We observed that in the presence of arachidonate (20:4ω-6), aromatic STD signals of ROSI were significantly reduced by roughly 62%, whereas palmitate (16:0) caused only a 17% reduction (**Figure 40**).

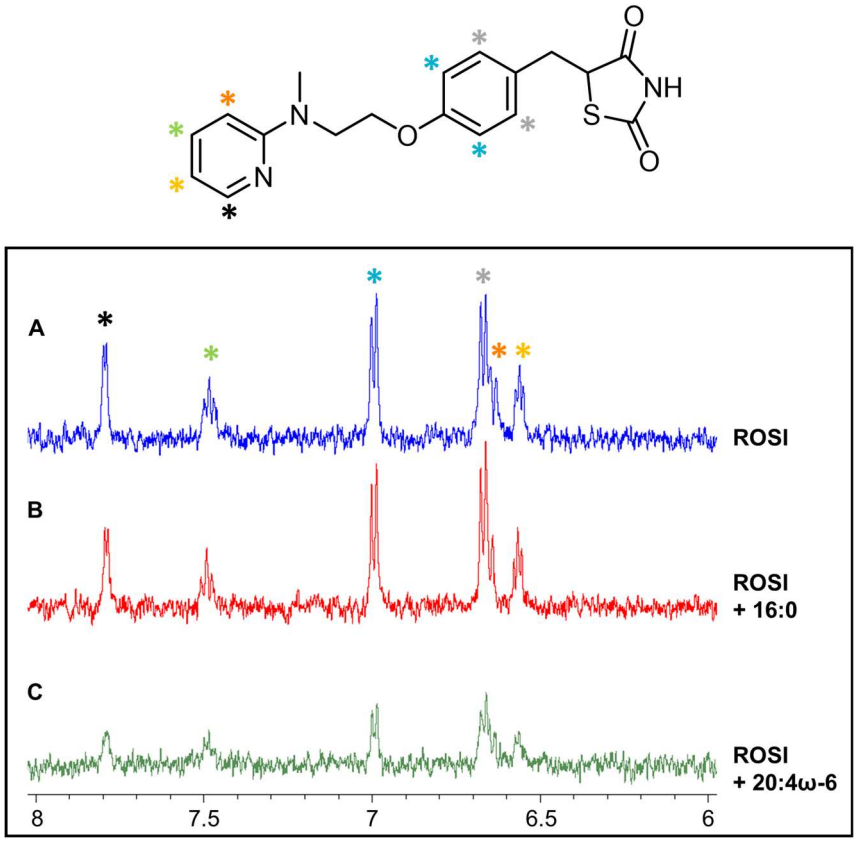

Figure 40. STD NMR competition assay between ROSI and FAs. The figure depicts ^{1}H STD spectra of ROSI (50 µM) in the aromatic region (6–8 ppm) in the presence of ACSL4 (1 µM): (**A**) alone, (**B**) with palmitate (150 µM), and (**C**) with arachidonate (150 µM). Spectra are the results of a single experiment each time.

It demonstrates that arachidonate (20:4ω-6), but not palmitate (16:0), efficiently displaces ROSI from ACSL4. This may explain why ROSI inhibits ACSL4 in the presence of palmitate but not in the presence of arachidonate. However, even a three-fold excess of arachidonate relative to ROSI was insufficient to fully displace the inhibitor, with approximately 40% of the

signal remaining. This residual binding suggests incomplete competition, potentially indicating the presence of additional, non-selective binding sites that are not displaced by arachidonate. Thus, although the method supports the hypothesis of a competitive relationship between ACSL4-specific FAs and the inhibitors, uncertainty remains.

Ultimately, this investigation into a potential competitive mode of inhibition raised more questions than it answered, highlighting discrepancies between the different techniques used (**Figure 41**).

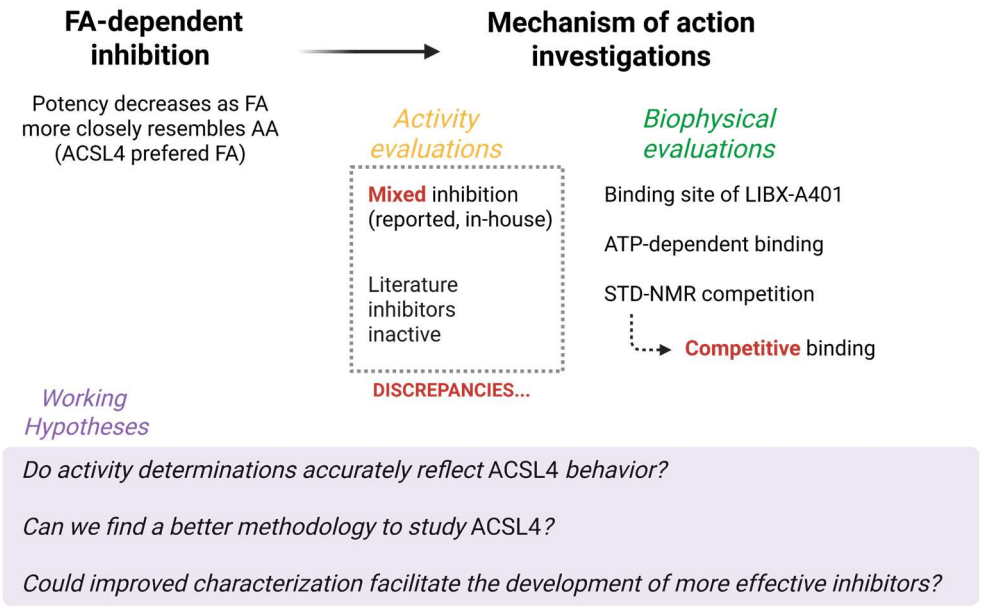

Figure 41. Hypotheses arising from observations that inhibitor activity is FA-dependent.

While biophysical methods suggest that FAs and inhibitors share a common binding site, kinetic studies indicating a mixed mode of inhibition with respect to FAs do not support this conclusion. Further highlighting the limitations of activity-based assays, some compounds previously described as inhibitors in the literature (93,239) showed no detectable inhibitory effect in our system. Moreover, there is a notable disconnect between the overall modest differences in FA preference observed in specificity studies (29,34,39,46), and the drastic loss of inhibitor activity in the presence of certain PUFAs we observe. Taken together, these findings suggest that ACSL4 activity measurements may not reliably reflect the enzyme's true kinetic behavior, and that alternative methods could be better suited for determining its FA preference. In addition, given that the potency of inhibitors appears intrinsically linked to ACSL4 substrate specificity, a deeper understanding of the molecular mechanisms underlying its FA preference could greatly facilitate lead optimization. To gain insight into these mechanisms, we conducted substrate specificity studies.

4. Supplemental methods

4.1. STD NMR

All NMR experiments were conducted on a Bruker Ascend Avance III 600 MHz spectrometer equipped with a broadband cryoprobe (Bruker).

Recombinant *h*ACSL4 was expressed and purified from *E. coli* as previously described (250). The purified protein was buffer-exchanged into phosphate-buffered saline (PBS, ThermoFisher, Germany) and diluted to a final concentration of 1 µM in PBS supplemented with 5% DMSO-d_6, 1 mM $MgCl_2$, 400 µM ATP, and 50 µM ROSI, either in the presence or absence of 150 µM of the FA. Initial ^{1}H NMR spectra were recorded at 298 K using 8 scans, a spectral width of 7239 Hz, 15.2 K data points, and a relaxation delay of 3.5 s to accurately determine the position of the water resonance. 1D STD NMR spectra were acquired using the stddiffesgp.3 pulse program, which includes a spoil sequence, water suppression via excitation sculpting, a T_2 filter and a spin-lock (D29 = 5 ms) to minimize protein background signals. STD spectra were acquired at 298 K with 4096 scans, a spectral width of 7239 Hz, 15.2 K data points, a saturation time of 3 s, and a relaxation delay of 3.5 s. On-resonance and off-resonance saturation frequencies were set to 0 ppm and -40 ppm, respectively. The total acquisition time per experiment was approximately 12 hours. All spectra were processed using TopSpin® 4.0.9. Phase correction and baseline adjustment were applied. The aromatic region of ROSI in the STD difference spectra (6–8 ppm) was integrated, and values were normalized to the corresponding off-resonance spectrum for comparative analysis.

RESULTS-CHAPTER III

Chapter II described the drug design strategies that led to the development of improved ACSL4 inhibitors, achieving nanomolar-range IC_{50} values and enhanced selectivity profiles. However, these potent inhibitions appear to correlate with the enzyme's substrate specificity, resulting in drastically reduced potencies in the presence of arachidonate, the physiologically relevant FA. Given its implication for the inhibitors significance, we undertook an in-depth exploration of ACSL4 FA specificity, anticipating that a clearer understanding would provide a rational basis for further chemical optimization. Chapter III presents the results of this investigation into ACSL4 substrate specificity, evaluating the enzyme's activity and affinity for various FAs using the previously developed biochemical and biophysical assays, along with a novel LC-MS-based competition assay. This in-depth study ultimately challenges the conventional approaches previously used. It proposes alternative methodologies and emphasizes the importance of considering the acyl-CoA products when determining ACSL4 specific substrates.

Characterization of acyl-CoA synthetase long-chain family member 4 (ACSL4) fatty acid preference reveals product-governed substrate specificity

Romain Marteau, Alexandre Gobert, Noah Cossou, Darius Mazhari, Martin Roumain, Jamal El Bakali, Raphaël Frédérick, Séverine Ravez

The results discussed in this chapter are set to be submitted to the *Journal of Lipid Research*.

1. Abstract

ACSL4 is one of five isoforms that activate long-chain fatty acids (FAs) by catalyzing their conversion into acyl-CoA thioesters, enabling their participation in diverse metabolic pathways. ACSL4 is widely recognized for its preference for polyunsaturated fatty acids (PUFAs), especially arachidonate (20:4ω-6), linking it to eicosanoid synthesis, ferroptosis, and associated pathophysiological processes. However, the molecular mechanisms underlying this preference remain poorly understood. Moreover, biochemical characterizations of FA specificity are insufficient to explain ACSL4's marked selectivity for PUFAs observed in biological systems. In this study, we employed complementary approaches to thoroughly investigate

ACSL4 FA specificity. Conventional biochemical assays measuring enzymatic activity with individual FAs revealed minimal differences among substrates. In contrast, binding affinity assessments clearly differentiated FAs based on their chain length and degree of unsaturation. To further elucidate ACSL4 substrate preference, we developed an LC-MS competition assay to monitor specific FA consumption when the enzyme is exposed to mixtures of FAs. This approach enabled the establishment of a FA preference ranking that more accurately captures the diversity of the biological context. The competition experiments revealed that the preferential formation of PUFA-derived products strongly inhibits the conversion of lower-priority FAs. Further investigation revealed a significant correlation between product inhibition and the established FA preference ranking. Collectively, these findings uncovered a product-inhibition mechanism that regulates ACSL4 substrate specificity, offering new insights into how the enzyme plays its specialized role. By highlighting the importance of the product in determining which FA ACSL4 converts, this work also provides a foundation for future investigations into the substrate specificities of other ACSL isoforms.

2. Introduction

Polyunsaturated fatty acids (PUFAs) are essential lipid components that contribute to the structural integrity and functionality of cell membranes (12). Their preferential incorporation at the *sn*-2 position of phospholipids (PLs) by lysophospholipid acyltransferases provides enhanced structural plasticity compared to other FAs (10). In addition to their structural role, certain PUFAs also act as precursors for lipid mediators. Arachidonate, for instance, is released from membranes by phospholipase A2 and serves as substrate for the synthesis of eicosanoids, a diverse class of signaling molecules involved in inflammation, brain function, platelet aggregation and various other processes (27).

At the crossroads of FA metabolism, long-chain acyl-Coenzyme A synthetases (ACSLs) play a crucial role by catalyzing the formation of a thioester bond between a FA and Coenzyme A (CoA), producing acyl-CoAs. Key insights into their catalytic mechanism have primarily come from the crystallographic structure of *Thermus thermophilus* long chain fatty acyl-CoA synthetase (*tt*LC-FACS), the only ACSL family member with a resolved three-dimensional structure (37). The latter supports an ordered Bi Uni Uni Bi ping-pong catalytic mechanism, in which ATP binding induces a conformational shift that allows FA entry into the active site. The reaction proceeds through the formation of an acyl-AMP intermediate, which then reacts with CoA to generate fatty acyl-CoA (**Figure 42**).

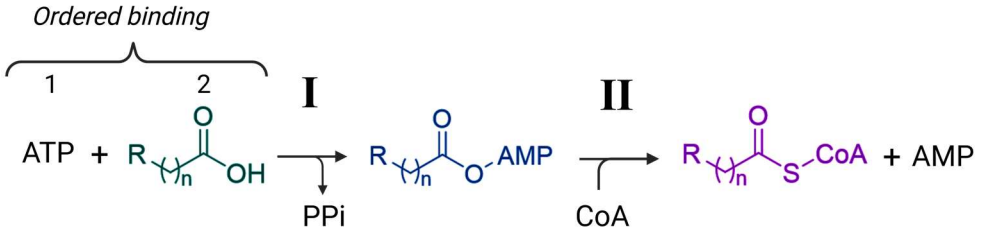

Figure 42. Catalytic Mechanism of ACSLs. The reaction proceeds through two sequential steps: (I) ATP binds first, followed by the FA, forming an acyl-AMP intermediate and releasing PPi. (II) CoA then replaces AMP, resulting in the formation of acyl-CoA and AMP.

The formation of acyl-CoAs by ACSLs facilitates diverse metabolic processes, including PL synthesis, β-oxidation, and protein acylation, while also modulating the availability of free PUFAs for eicosanoid biosynthesis (30). In mammals, the ACSL family consists of five isoforms (ACSL1, 3, 4, 5, and 6), which, despite substantial sequence divergence, share highly conserved functional domains (39). Each isoform displays distinct patterns of tissue distribution, subcellular localization, and FA preferences (29,42–45). While ACSLs exhibit a broad FA utilization, it has been proposed that individual isoforms channels specific FA toward distinct metabolic pathways (30). Understanding these substrate preferences is critical to elucidate how the different ACSLs contribute to lipid metabolism.

To investigate their specific contribution to FA partitioning, numerous biochemical studies have analyzed the activities of recombinant ACSLs in response to various FA substrates (39,46). However, efforts to characterize FA preferences of ACSLs have met significant challenges. Biochemical

evaluations often reveal overlapping substrate utilization across isoforms, making it difficult to delineate clear metabolic roles. Moreover, notable discrepancies have been reported across studies as well as between different constructs examined within the same study (34,46). Despite these inconsistencies, several reports emphasize ACSL4's marked preference for 20-carbon PUFAs, such as arachidonate (20:4ω-6) and eicosapentaenoate (20:5ω-3) (29,58), supporting its key role in regulating eicosanoid biosynthesis (98,99,115). ACSL4 also activates a diverse array of saturated, monounsaturated, and other polyunsaturated FAs ranging from 14 to 22 carbons, albeit generally with lower efficiency (29,39,46).

More recently, ACSL4 has attracted considerable attention due to its role in ferroptosis, a form of iron-dependent regulated cell death (RCD) characterized by excessive lipid peroxidation within membrane PLs. By selectively activating arachidonate and other PUFAs containing bis-allylic positions, ACSL4 promotes the formation of oxidizable phospholipids, which serve as essential substrates for lipid peroxidation and drive ferroptosis. This RCD is implicated in various pathologies, including cancer, ischemic organ injury and neurodegenerative diseases (101,124). Given the importance of ACSL4 in shaping the phospholipidome and its direct link to ferroptosis, further investigation is needed to understand how its substrate specificity influences cell fate decisions.

To gain deeper insights into ACSL4's marked preference for arachidonate, we explored several complementary approaches. Here, we present an in-depth

study comparing ACSL4's activity and affinity toward eight structurally diverse FAs. Using a novel LC-MS-based competition assay, we evaluated ACSL4-mediated utilization of FA within mixtures, providing a model that better reflects the complexity of the cellular environment. Surprisingly, arachidonoyl-CoA (AA-CoA) product potently inhibited the conversion of lower-priority substrates, revealing a previously unrecognized mechanism of product-governed substrate specificity. These findings offer fresh insights into how ACSL4 prioritizes PUFAs and may inform future studies on lipid metabolism and ferroptosis regulation.

3. Materials and methods

3.1. Reagents

Palmitate, eicosadienoate, γ-linolenate and arachidonoyl-CoA lithium salt were purchased from Merck (Belgium or France). α-linolenate was purchased from Selleckchem (Germany), Mead acid from Cayman (USA), Elaidate from Fischer Scientific (Belgium), Adrenate from Cambridge Bioscience (UK), and arachidonate and AMP from Doug Discovery (UK). Palmitoyl-CoA lithium salt was purchased from Santa Cruz Biotechnology and ApCpp was purchased from Jenna Bioscience.

3.2. ACSL4 expression and purification

Recombinant *N*-terminally His-tagged ACSL4_v1 protein expression and purification were carried out following previously described protocols (250). Briefly, *E. coli* BL21 (DE3) transformants were cultured in LB medium containing kanamycin and chloramphenicol. Protein expression was induced with 1 mM IPTG at 20 °C for 18 h. Cells were harvested by centrifugation, lysed in an ice-cooled buffer containing 20 mM Tris pH 7.5, 1% triton X-100, 0.1% sodium cholate, and clarified by centrifugation. His-tagged ACSL4 proteins were purified using Ni-NTA affinity chromatography, with elution performed in a buffer containing 50 mM Tris pH 8.5, 10 mM $MgCl_2$, 300 mM NaCl, 10% glycerol, 500 mM imidazole. Purified proteins were dialyzed overnight at 4 °C against stock buffer (50 mM Tris pH 7, 10 mM $MgCl_2$, 300 mM NaCl, 20% Glycerol, 1 mM DTT) for final preparation.

3.3. Spectrophotometric ACSL4 activity assay

ACSL4 Activity Assay. ACSL4 activity was assessed using a previously described procedure (250) with the EnzChek® Pyrophosphate Assay Kit (Thermo Scientific) on a Varioskan Flash spectrophotometer. Enzyme activity was monitored in a reaction buffer containing 50 mM Tris (pH 7.5), 200 mM NaCl, 1 mM $MgCl_2$, 200 µM MESG, 50 µM ATP, 100 µM CoA, 1 mM DTT, 10% DMSO, 0.06% Triton-X 100, 1 U/mL PNP, 0.03 U/mL pyrophosphatase, and 50 nM purified ACSL4. Reactions were initiated by the addition of a FA solution, to a final concentration of 100 µM (final concentration: 0.06% triton, 1% EtOH). A control experiment was performed

in which a solution (0.06% triton, 1% EtOH) was added instead of a FA solution. The plate was mixed manually, and the absorption change was recorded every 30 s for 30 min at 360 nm. Reaction rates were determined from the linear phase, typically using 10 data points between 2 and 10 minutes of the reaction. The slope of the control experiment was subtracted from each measured slope to obtain corrected values, which were then expressed as a percentage of the enzyme's activity relative to the uninhibited control.

The first step of ACSL4 activity was measured under the same conditions, except that CoA was excluded, and ACSL4 and pyrophosphatase concentrations were adjusted to 4 μM and 0.075 U/mL, respectively.

Michaelis−Menten Kinetics. Steady-state kinetic parameters for FAs were determined at saturating concentrations of the other two substrates (100 μM) using the standard assay conditions described above. Initial velocities (v_0) were measured as a function of substrate concentration to generate a saturation curve, which was then fitted to the Michaelis-Menten equation using nonlinear regression analysis.

3.4. Nano differential scanning fluorimetry (nDSF)

NanoDSF measurements were performed as described (33), with a Prometheus NT.48 fluorimeter (Nanotemper Technologies, GmbH, Munich, Germany) using Prometheus standard capillaries. ACSL4 was diluted at 8 μM in assay buffer (PBS: 8 mM Na_2HPO_4, 2 mM KH_2PO_4, 150 mM NaCl, 3 mM KCl, 10 mM $MgCl_2$, 5% Glycerol, 0.05% Tween, 5% DMSO) supplemented

with 1 mM ATP or non-hydrolyzable α,β-methyleneadenosine-5'-triphosphate (ApCpp) if indicated. The FAs were diluted at 100 µM in the same assay buffer. The solutions were mixed (1:1) and transferred to capillaries. Thermal protein stability was assessed by monitoring the fluorescence derivative signal (330 nm) over a temperature range of 25 to 80 °C (at a rate of 7 °C/min) with the excitation power set to 100%.

3.5. Microscale thermophoresis (MST) assay

MST measurements were performed as previously described (33) using a NanoTemper Monolith NT.115 instrument with a red filter. ACSL4 (500 nM) was labeled with 25 nM RED-tris-NTA 2nd generation dye (NanoTemper Technologies). Ligand serial dilutions were prepared in assay buffer (PBS: 8 mM Na_2HPO_4, 2 mM KH_2PO_4, 150 mM NaCl, 3 mM KCl, 10 mM $MgCl_2$, 5% Glycerol, 0.05% Tween, 5% DMSO) supplemented with 1 mM ATP or ApCpp if indicated. Labeled ACSL4 (10 µL) was mixed with 10 µL of each ligand dilution, and samples were loaded into standard capillaries. Measurements were conducted at 23 °C with 100% LED power and 60% MST power, using laser on/off times of 20 s and 5 s, respectively. Data were extracted from the 5th run at 9-10 s MST on-time.

3.6. LC-MS measurement of ACSL4 FA consumption

Single time-point analysis. Specific FA consumption by ACSL4 was evaluated in various FA mixtures, each containing 25 µM of individual FAs, across a range of ATP concentrations (0 to 250 µM). The reaction was

initiated by adding the ATP solution to a buffer containing the FA mixture, with final concentrations of 50 mM Tris (pH 7.5), 200 mM NaCl, 1 mM $MgCl_2$, 250 µM CoA, 1 mM DTT, 10% DMSO, 0.06% Triton-X 100, and 100 nM purified ACSL4. The reaction was incubated for 90 minutes at 30°C and terminated by adding an equal volume (1:1) of acetonitrile spiked with 100 µM eicosadienoate (20:2ω-6) as an internal standard. Following centrifugation at 20,000 × g for 20 minutes, the supernatants were analyzed by LC-MS to quantify the remaining FAs. Analysis was conducted using an Agilent 1100 series LC-MS single quadrupole (InfinityLab) equipped with electrospray ionization in negative mode. Briefly, 40 µl of sample was injected into Ascentis Express C18 column (100 × 4.6 mm; 2.7 µm, Sigma). The LC flow was maintained at 0.5 ml/min and elution was conducted in isocratic mode using mobile phase consisting of 90% acetonitrile, 10% water and 1 mM ammonium acetate. FAs $(M\text{-}H)^-$ were extracted, and their levels normalized to the 0 µM ATP condition.

Kinetic analysis. Kinetic measurements were performed at 50 µM ATP over 1, 2, 5, and 10 minutes under the same conditions, except with 50 µM of individual fatty acids and 25 nM purified ACSL4.

3.7. Statistical analysis

All experiments were conducted for a minimum of three times unless mentioned otherwise. Data are presented as mean ± SD. Unpaired t-tests are used as indicated in the legend to calculate *p*-values. Statistical significance was determined with a *p*-value under 0.05. Graphs and statistical analyses

were performed using GraphPad Prism software version 10.0. nDSF and MST data were analyzed using PR.ThermControl software (Nanotemper Technologies, GmbH, Munich, Germany) and MO.Affinity Analysis v2.3 software (Nanotemper Technologies, GmbH, Munich, Germany), respectively.

4. Results

4.1. Biochemical analysis of ACSL4 substrate preference reveals limited differentiation among FAs

Yamamoto and colleagues identified the different ACSL isoforms present in mammals and initially characterized their FAs specificities by evaluating a set of FAs at a single concentration (29,42–45). To compare their findings on the rat ACSL4 with our human construct of ACSL4_v1, consisting of the short variant His-tagged at its N-terminal, we evaluated the activity of 20 FAs using a previously described assay (250). In brief, inorganic pyrophosphate (PPi) production during the first catalytic step is monitored at 360 nm using an enzymatic coupling system with pyrophosphatase and purine nucleoside phosphorylase.

As reported, arachidonate (20:4ω-6) exhibited increased activity compared to palmitate (16:0) (**Figure 43A**). However, the increase in activity observed with *h*ACSL4 was modest compared to *r*ACSL4, with respective activity

levels of 127% and over 200% (29). Two FAs namely, arachidate (20:0) and α-linolenate, exhibited notably low activity. Beyond these exceptions, the enzymatic activities with the remaining FAs showed minimal differentiation.

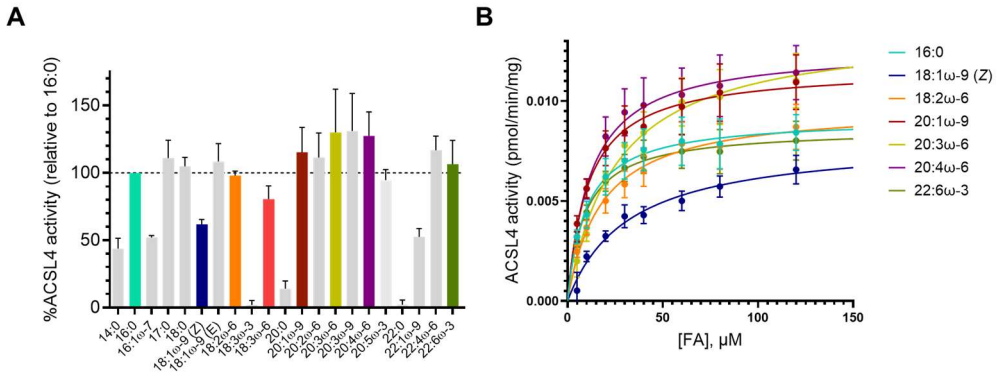

Figure 43. FA activity profiling of ACSL4. Activity measurements were performed using the EnzChek® pyrophosphate assay. (**A**) ACSL4 enzymatic activity in the presence of various FAs (50 μM). Results are expressed as percentage of activity relative to palmitate (16:0). Each bar is the result of two independent experiments performed in duplicate. Eight representative FAs from the entire panel were selected for further characterization (indicated by colored bars). 16:0 palmitate; 14:0 myristate; 17:0 heptadecanoate; 18:0 stearate; 20:0 arachidate; 16:1ω-7 palmitoleate; 18:1ω-9 (Z) oleate; 18:1ω-9 (E) elaidate; 18:2ω-6 linoleate; 18:3ω-3 α-linolenate; 18:3ω-6 γ-linolenate; 20:1ω-9 eicosenoate; 20:2ω-6 eicosadienoate; 20:3ω-6 dihomo-γ-linolenate; 20:3ω-9 eicosatrienoate; 20:4ω-6 arachidonate; 20:5ω-3 eicosapentaenoate; 22:1ω-9 docosenoate; 22:4ω-6 Adrenate; 22:6ω-3 docosahexaenoate. (**B**) Michaelis-Menten curves for eight representative FAs at saturating concentrations (100 μM) of ATP and CoA. Associated kinetic parameters are reported in **Table 6**. Each curve is the result of three independent experiments performed in duplicate.

We evaluated the kinetic parameters of ACSL4 using eight structurally diverse FAs selected from the previous experiment: palmitate (16:0), oleate (18:1ω-9), linoleate (18:2ω-6), γ-linolenate (18:3ω-6), eicosenoate (20:1ω-9),

dihomo-γ-linolenate (20:3ω-6), arachidonate (20:4ω-6), and docosahexaenoate (22:6ω-3) (**Table 6, Figure 43B**).

Under our assay conditions, the K_m values for palmitate ($K_{m\ 16:0}$ = 10 μM), arachidonate ($K_{m\ 20:4\omega\text{-}6}$ = 12 μM), eicosenoate ($K_{m\ 20:1\omega\text{-}9}$ = 11 μM) and docosahexaenoate ($K_{m\ 22:6\omega\text{-}3}$ = 9 μM) were similar. ACSL4 showed a distinct K_m for oleate ($K_{m\ 18:1\omega\text{-}9}$ = 38 μM), linoleate ($K_{m\ 18:2\omega\text{-}6}$ = 18 μM), and dihomo-γ-linolenate ($K_{m\ 20:3\omega\text{-}6}$ = 25 μM), which were 2- to 4-fold higher than the K_m value for arachidonate (20:4ω-6). The maximum initial velocity for the FAs ranged from 0.8 to 1.5 μM.min^{-1}, with the highest V_{max} observed for 20-carbon FAs. Substrate specificity is conventionally assessed using the kinetic parameters ratio k_{cat}/K_m (catalytic efficiency), as it captures enzyme behavior both when substrate binding is rate-limiting (*via* K_m) and when the substrate is at saturating concentrations (*via* k_{cat}) (289).

Table 6. Biochemical characterizations of ACSL4 substrates. Kinetic parameters were determined using the Enzchek® pyrophosphate assay at saturating concentrations of ATP and CoA. The reported values (± SD) are the results of three independent experiments. The ranking associated with the parameter is indicated in **bold**.

Fatty acid	V_{max} (μM.min^{-1})	K_m (μM)	k_{cat}/K_m (M^{-1} s^{-1})
16:0	0.89 ± 0.17 (**4**)	9.74 ± 0.63 (**1**)	2213 ± 428 (**3**)
18:1ω-9	0.82 ± 0.06 (**4**)	38.39 ± 3.49 (**7**)	520 ± 107 (**7**)
18:2ω-6	0.98 ± 0.19 (**4**)	17.78 ± 1.64 (**5**)	1314 ± 129 (**6**)
20:1ω-9	1.24 ± 0.24 (**1**)	10.79 ± 0.77 (**1**)	2737 ± 288 (**1**)
20:3ω-6	1.52 ± 0.34 (**1**)	25.36 ± 4.08 (**6**)	1445 ± 150 (**5**)
20:4ω-6	1.37 ± 0.25 (**1**)	11.98 ± 1.05 (**1**)	2739 ± 291 (**1**)
22:6ω-3	0.82 ± 0.18 (**4**)	9.02 ± 1.54 (**1**)	2205 ± 219 (**3**)

The highest catalytic efficiencies were obtained for arachidonate (20:4ω-6) and eicosenoate (20:1ω-9), but these were only 1.2-fold higher than those for palmitate (16:0) and docosahexaenoate (22:6ω-3). The lowest catalytic efficiency was observed for oleate (18:1ω-9) with a k_{cat}/K_m ratio 5-fold lower than that of arachidonate (20:4ω-6). The determination of these kinetic parameters did not explain the marked preference of ACSL4 for arachidonate. However, it has been suggested that k_{cat}/K_m may not fully reflect the efficiency of enzymes like ACSL4, which catalyze reactions involving multiple substrates and products (292). Recently, the crucial role of binding affinity in determining the substrate specificity of enzymes has been emphasized (293),

prompting us to characterize FA binding by two biophysical methods: nano differential scanning fluorimetry (nDSF) and microscale thermophoresis (MST).

4.2. Characterization of binding events highlights distinctions among FAs

We performed nDSF experiments following a procedure we previously described for assessing inhibitor binding (33) (**Figure 44A**, **Figures S1-S2**). Based on the structure of *tt*LC-FACS, ATP initially binds to the enzyme, inducing the opening of the FA tunnel (37). This facilitates the entry of the FA into the catalytic cavity, leading to the formation of an acyl-AMP intermediate. The binding of selected FAs was therefore evaluated both with and without 1 mM ATP (saturating concentration), as well as in the presence of 1 mM of the non-hydrolyzable ATP analog, α,β-methyleneadenosine-5'-triphosphate (ApCpp). As observed for *tt*LC-FACS, FA binding required the prior binding of ATP (37), as minimal stabilization was detected for any of the eight FAs in its absence (**Figure 44A**). However, in the presence of ApCpp, a distinct stabilization pattern emerged (**Figure 44A**). Interestingly, the highest stabilization was observed with arachidonate (20:4ω-6), showing a ΔT_m of 6.9 °C. This was followed by other PUFAs, including 18:3ω-6 (ΔT_m = 4.7 °C), 22:6ω-3 (ΔT_m = 4.7 °C), 20:3ω-6 (ΔT_m = 3.9 °C), and 18:2ω-6 (ΔT_m = 2.3 °C). Monounsaturated FAs (MUFAs) showed lower stabilization, with 18:1ω-9 yielding a ΔT_m of 1.7 °C and 20:1ω-9 a ΔT_m of 1.2 °C, while saturated 16:0 exhibited the least stabilization effect, with a ΔT_m of 0.4 °C.

This suggests that FAs with a higher degree of unsaturation exhibit stronger binding to ACSL4. In the presence of ATP, the stabilization trend followed a similar pattern. Among the tested FAs, arachidonate (20:4ω-6) induced the highest stabilization (ΔT_m = 9.6 °C), whereas palmitate (16:0) exhibited the lowest (ΔT_m = 0.8 °C). Compared to the ApCpp condition, we observed improved stabilization for all FAs, except for γ-linolenate (18:3ω-6), which exhibited the same ΔT_m values (**Figure 44A**). We speculated that the differences between the two conditions were due to the formation of the acyl-AMP intermediate in the presence of ATP (**Figure S3A**). To challenge this hypothesis, we evaluated ACSL4 activity under conditions comparable to the nDSF assay, in the absence of the final substrate CoA (**Figure S3B**). We observed low but measurable PPi generation, demonstrating that the acyl-AMP intermediate could be formed even without CoA. In contrast, ACSL4 was confirmed to be inactive when ATP was replaced by ApCpp (**Figure S3C**). Consequently, we inferred that nDSF experiments in the presence of ATP partly reflect the formation of the acyl-AMP intermediate.

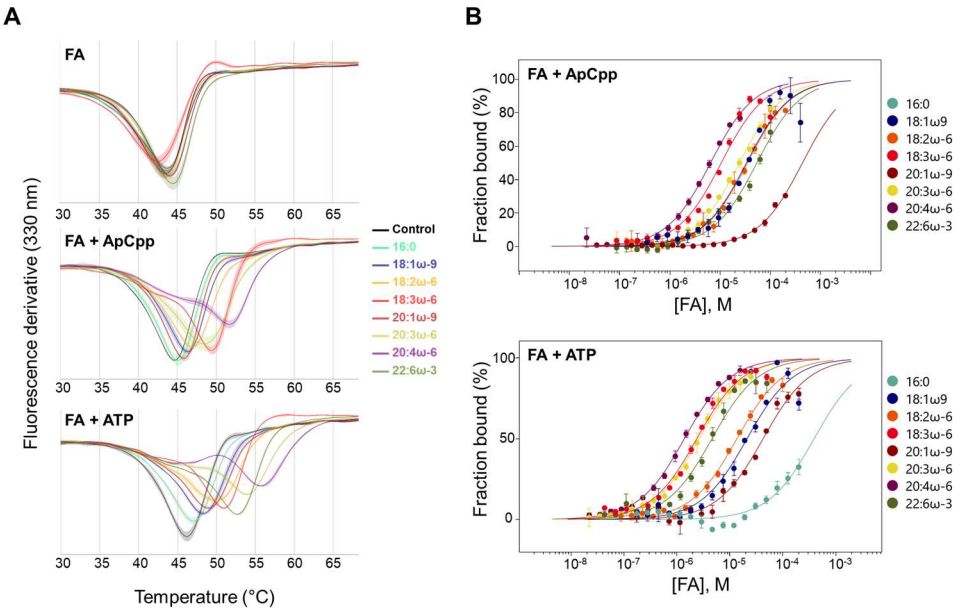

Figure 44. Assessment of FA binding to ACSL4. (**A**) Thermal shift assay of eight representative FAs on *h*ACSL4. nDSF traces of ACSL4 (4 µM) with each FA (50 µM) under apo condition or in the presence of 1 mM ApCpp or ATP. Each curve is the result of three independent experiments. Associated ΔT_m values are reported in **Table 7**. (**B**) Determination of FA affinities. MST traces for the binding interaction of FAs with 1 mM ApCpp or ATP. Each curve is the result of three independent experiments. Associated K_Ds or $_{app}K_D$s are reported in **Table 7**.

Given that stabilization in nDSF showed clear patterns, we further investigated FA binding by determining their K_D values using the MST method we had previously developed (33) (**Figure 44B**, **Figure S4**). The affinity determined in the presence of ATP is referred to as $_{app}K_D$, as it includes the contribution of intermediate formation. Consistent with the nDSF results, binding events were either undetectable or observed only at high concentrations in the absence of ATP or ApCpp (data not shown). In

contrast, their presence enabled the measurement of binding affinities for most tested FAs, except for palmitate (16:0) in the presence of ApCpp, presumably due to its very low affinity under these conditions (**Table 7**, **Figure 44B**). As observed in the nDSF experiments, affinity was consistently higher in the presence of ATP compared to ApCpp, further supporting the hypothesis that the acyl-AMP intermediate forms and enhances binding. In both conditions, arachidonate (20:4ω-6) presented the highest affinity, while palmitate (16:0) showed the lowest (when measurable). The overall trend in MST aligned with that observed in nDSF experiments, showing a comparable influence of the degree of unsaturation (**Table 7**, **Figure 44B**). Thus, while activity-based comparisons failed to effectively differentiate substrates, biophysical characterizations of FA binding to ACSL4 revealed clear distinctions and structure-based tendencies. However, the biophysical methods differed in the precise ranking of intermediate FAs (**Table 7**).

Table 7. Biophysical characterization of eight representative FAs binding to ACSL4. [a]ΔT_m values (± SD) were determined in nDSF by three independent experiments for each FA in the presence of 1 mM ApCpp or ATP. [b]K_D and [c]$_{app}K_D$ values (± SD) were determined using MST by three independent experiments for each FA in the presence of 1 mM ApCpp or ATP, respectively. The ranking associated with the parameter is indicated in **bold**.

Fatty acid	[a]ΔT_m (°C)		[b]K_D (μM)	[c]$_{app}K_D$ (μM)
	+ ApCpp	+ ATP	+ ApCpp	+ ATP
16:0	0.45 ± 0.1 (**8**)	0.84 ± 0.1 (**8**)	n.d.	390.3 ± 461 (**8**)
18:1ω-9	1.7 ± 0.1 (**6**)	2.1 ± 0.2 (**7**)	33.6 ± 9.1 (**4**)	21.1 ± 6.3 (**6**)
18:2ω-6	2.3 ± 0.1 (**5**)	3.7 ± 0.1 (**5**)	35.3 ± 3.8 (**4**)	13.6 ± 1.4 (**5**)
18:3ω-6	4.7 ± 0.2 (**2**)	4.7 ± 0.1 (**4**)	10.5 ± 2.3 (**2**)	2.4 ± 0.3 (**2**)
20:1ω-9	1.2 ± 0.1 (**7**)	2.8 ± 0.1 (**6**)	437.3 ± 145 (**7**)	42.4 ± 7.7 (**7**)
20:3ω-6	3.9 ± 0.1 (**4**)	7.7 ± 0.1 (**2**)	24.3 ± 2.2 (**3**)	2.6 ± 0.2 (**2**)
20:4ω-6	6.9 ± 0.0 (**1**)	9.6 ± 0.1 (**1**)	6.5 ± 0.6 (**1**)	1.4 ± 0.1 (**1**)
22:6ω-3	4.7 ± 0.3 (**2**)	6.4 ± 0.1 (**3**)	54.0 ± 14 (**6**)	4.6 ± 0.8 (**4**)

4.3. FA competition for ACSL4-mediated activation establishes a preference ranking

A recognized limitation of conventional activity measurements is their inability to account for the mixtures of FAs typically processed by ACSLs (46). To further investigate substrate preference, we developed an LC-MS-based competition assay to monitor ACSL4's specific FA consumption when exposed to a mixture of the eight selected FAs. This assay involved

incubating the enzyme with the FA mixture (25 μM of each FA), excess CoA (250 μM), and a range of ATP concentrations, from limiting to excess levels (0 to 250 μM) (**Figure S5A**). After a non-limiting incubation period (90 min), the reaction was quenched, and the remaining specific FAs were quantified relative to the control. Calibration curves verified the linearity of the response, and two distinct controls confirmed that FA consumption was dependent on both the presence of ATP and ACSL4 (**Figures S5B-S5C**).

As shown in **Figure 45A**, arachidonate (20:4ω-6) and dihomo-γ-linolenate (20:3ω-6) were the only FAs converted at low ATP concentrations, highlighting ACSL4's preference for these two substrates within the mixture of eight FAs. Further increasing the concentration of ATP enabled the consumption of other PUFAs, such as docosahexaenoate (22:6ω-3), γ-linolenate (18:3ω-6) and linolenate (18:2ω-6), as well as the MUFA eicosenoate (20:1ω-9). However, even at excess ATP levels (250 μM), the conversion of γ-linolenate (18:3ω-6), linolenate (18:2ω-6) and eicosenoate (20:1ω-9) remained incomplete, while palmitate (16:0) and oleate (18:1ω-9) were largely unaffected.

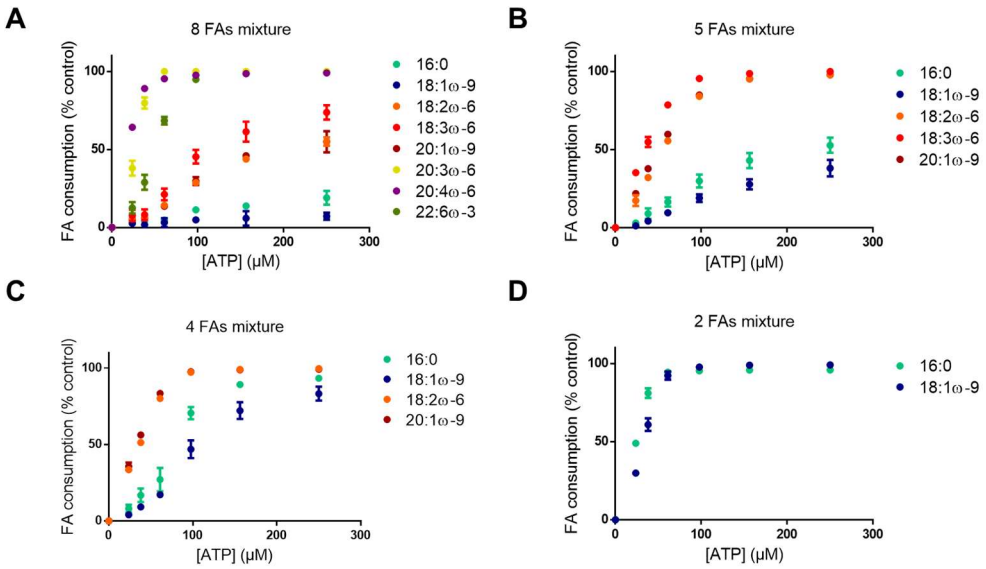

Figure 45. FA competition for ACSL4 activity. LC-MS monitoring of ACSL4 specific FA consumption (25 μM of each) in different FA mixtures with ranging ATP concentrations (from 0 to 250 μM). Higher-priority FAs from a mixture were not included in subsequent experiments. (**A**) Mixture of eight representative FAs. (**B**) Mixture of five FAs excluding 20:4ω-6, 20:3ω-6 and 22:6ω-3. (**C**) Mixture of four FAs excluding 18:3ω-6. (**D**) Mixture of 18:1ω-9 and 16:0.

We hypothesized that the acyl-CoAs produced from high-priority PUFAs such as arachidonate (20:4ω-6), dihomo-γ-linolenate (20:3ω-6) and docosahexaenoate (22:6ω-3) inhibited the conversion of lower-priority FAs. To test this hypothesis, we removed these three PUFAs and repeated the experiment using a combination of the remaining five FAs (**Figure 45B**). Under these conditions, conversion of all five FAs increased markedly. γ-Linolenate (18:3ω-6) was preferentially consumed, followed closely by linoleate (18:2ω-6) and eicosenoate (20:1ω-9), whereas consumption of

oleate (18:1) and palmitate (16:0) remained incomplete at highest ATP concentration.

Continuing our stepwise elimination strategy, we next evaluated a four-FA mixture excluding γ-linolenate (18:3ω-6) (**Figure 45C**). This resulted in a significant increase in the utilization of remaining FAs. Since the consumption of the two lowest-priority FAs, oleate (18:1ω-9) and palmitate (16:0), was still not complete, we evaluated them together (**Figure 45D**). This time, their conversion reached completion at an ATP concentration close to the equimolar condition.

To better define substrate preferences, we analyzed closely competing FAs together by monitoring their specific consumption over time using an adapted LC-MS method (**Figure S6**). The two preferential substrates could be distinguished, as the slope for arachidonate (20:4ω-6) consumption over time was significantly higher than that of dihomo-γ-linolenate (20:3ω-6). Similarly, palmitate (16:0) showed a steeper slope compared to oleate (18:1ω-9), while γ-linolenate (18:3ω-6) exhibited a slightly higher consumption rate than linoleate (18:2ω-6) and eicosenoate (20:1ω-9). However, the slopes for eicosenoate (20:1ω-9) and linoleate (18:2ω-6) were similar.

At this point, we could establish a ranking of the eight FAs based on their preferential consumption by ACSL4 (**Table 8**). When certain PUFAs are present, the enzyme preferentially utilizes them in a specific order: arachidonate (20:4ω-6), followed closely by dihomo-γ-linolenate (20:3ω-6), and then docosahexaenoate (22:6ω-3). Following these, ACSL4 prioritizes γ-

linolenate (18:3ω-6) over eicosenoate (20:1ω-9) and linoleate (18:2ω-6), with no clear preference between the latter two. At the bottom of the ACSL4 preference list, palmitate (16:0) ranks just above oleate (18:1ω-9).

Table 8. Comparison between different parameters for the ranking of ACSL4 FA preference.

Competition		**20:4 > 20:3 > 22:6 > 18:3 >18:2 = 20:1 > 16:0 > 18:1**
AA-CoA inhibition		20:4 < 20:3 < 22:6 < 18:3 < 18:2 < 20:1 < 16:0 = 18:1
k_{cat}/K_m		20:4 = 20:1 >16:0 = 22:6 > 20:3 = 18:2 > 18:1 - (18:3?)
ΔT_m	+ ApCpp	20:4 > 18:3 = 22:6 > 20:3 > 18:2 > 18:1 > 20:1 > 16:0
	+ ATP	20:4 > 20:3 > 22:6 > 18:3 > 18:2 > 20:1 > 18:1 > 16:0
K_D	+ ApCpp	20:4 > 18:3 > 20:3 > 18:1 > 18:2 > 22:6 > 20:1 > (16:0)
	+ ATP	20:4 > 18:3 = 20:3 > 22:6 > 18:2 > 20:1 > 18:1 > 16:0

4.4. Inhibition by preferential products shapes ACSL4 FA specificity

The LC-MS competition assay suggested that certain products influence ACSL4's FA specificity. To test the product inhibition hypothesis, we

monitored the specific FA consumption within a mixture of four lower-priority FAs (20:1ω-9, 18:2ω-6, 18:1ω-9 and 16:0) in the presence of one reaction product: arachidonoyl-CoA (AA-CoA), palmitoyl-CoA (PA-CoA), AMP, or PPi (**Figure 46A**). Among the four products investigated, AA-CoA stood out by drastically inhibiting the consumption of all four FAs, while the inhibitory effects of the other products remained minimal.

The inhibition of ACSL4 activity by AA-CoA and PA-CoA (10 μM) was further assessed across the eight FAs using the spectrophotometric activity assay (**Figure 46B**). AA-CoA completely inhibited the conversion of palmitate (16:0) and oleate (18:1ω-9), while the inhibition of higher-ranked FAs, linoleate (18:2ω-6), γ-linolenate (18:3ω-6) and eicosenoate (20:1ω-9), was less significant. In contrast, the conversion of preferential PUFAs (20:3ω-6, 20:4ω-6 and 22:6ω-3) was minimally affected by AA-CoA. Strikingly, the percentage of inhibition by AA-CoA correlated with the established FA ranking from the LC-MS competition assay. On the other hand, inhibition of ACSL4 by PA-CoA, the product of a lower-priority FA, was negligible. We further evaluated the inhibitory potential of AA-CoA by determining its IC_{50} for the conversion of three representative FAs from the panel: a saturated FA (palmitate, 16:0), a MUFA (eicosenoate, 20:1ω-9), and a PUFA (arachidonate, 20:4ω-6) (**Figure 46C**). While AA-CoA potently inhibited palmitate (16:0, IC_{50} = 0.35 μM), its effect was less pronounced against eicosenoate (20:1ω-9, IC_{50} = 1.6 μM), and no inhibition was observed in the presence of arachidonate (20:4ω-6).

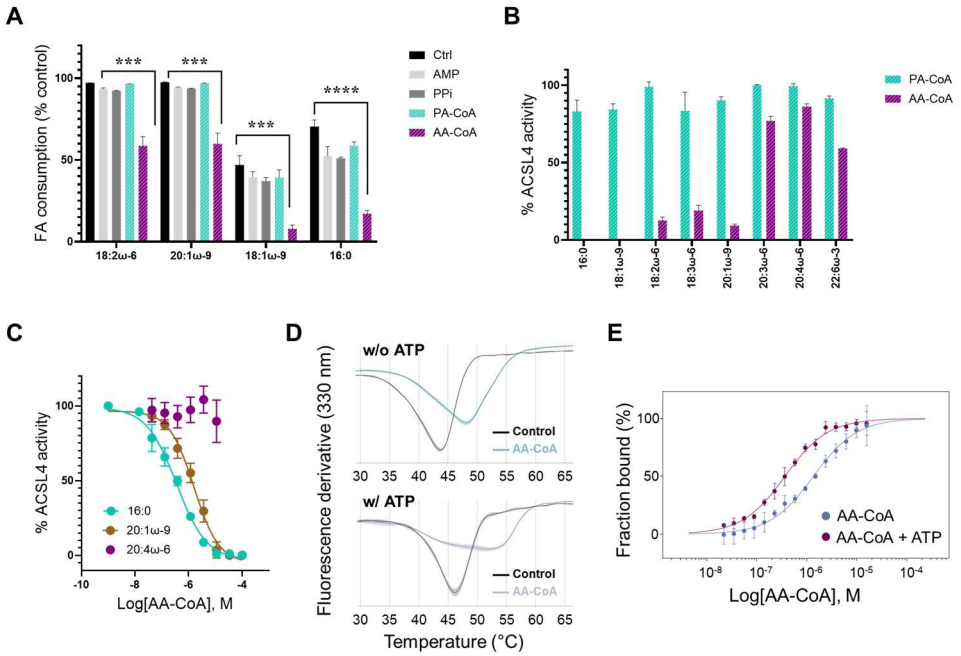

Figure 46. AA-CoA governs ACSL4 substrate specificity (**A**) LC-MS analysis of ACSL4-mediated FA consumption in a mixture of 18:2ω-6, 20:1ω-9, 18:1ω-9 and 16:0 (25 µM of each) with 98 µM of ATP in the presence of 200 µM AMP (light grey), 200 µM PPi (dark grey), 50 µM of PA-CoA (cyan) or 50 µM of AA-CoA (purple). Each bar is the result of three independent experiments. Statistical analysis was determined using unpaired t-test,*** $p < 0.001$; **** $p < 0.0001$ (**B**) ACSL4 activity for eight distinct FAs (100 µM) measured using the EnzChek® pyrophosphate assay, in the presence of either PA-CoA, AA-CoA (10 µM), or control conditions. Each bar is the result of two independent experiments performed in duplicate. (**C**) Dose-response inhibition of ACSL4 by AA-CoA, measured using the EnzChek® pyrophosphate assay, for three representative FAs: palmitate (16:0, IC_{50} = 0.35 µM), eicosenoate (20:1ω-9, IC_{50} = 1.6 µM) and, arachidonate (20:4ω-6) at 100 µM of FA. Each curve is the results of three independent experiments performed in duplicate. (**D**) nDSF traces of ACSL4 with AA-CoA in apo condition (blue curve, $\Delta T_m = 4.4 \pm 0.1$ °C) or in the presence of ATP (purple curve, $\Delta T_m = 5.5 \pm 0.4$ °C) compared to respective controls (black curves). ΔT_m values were determined by three independent experiments. (**E**) MST traces for the binding interaction between ACSL4 and AA-CoA in the presence (purple curve, K_D = 0.35

± 0.03 μM) or absence (blue curve, K_D = 1.3 ± 0.1 μM) of ATP. K_D values were determined by three independent experiments.

To deepen the characterization of AA-CoA, we monitored its binding interaction with ACSL4 using nDSF and MST (**Figure 46D-E**). Interestingly, we observed that, in contrast to FAs, AA-CoA could bind with high affinity in the absence of ATP (ΔT_m = 4.4 ± 0.1 °C, K_D = 1.3 ± 0.1 μM). Furthermore, its affinity increases in the presence of ATP (ΔT_m = 5.5 ± 0.4 °C, K_D = 0.35 ± 0.03 μM), resulting in a 3-fold higher affinity compared to the corresponding substrate, arachidonate (K_D = 1.4 ± 0.1) under the same conditions.

5. Discussion

ACSLs play a central role in lipid metabolism by catalyzing the initial activation of FAs, a crucial step for their utilization in various downstream metabolic pathways (30). Based on their unique properties, it is widely accepted that each ACSL isoform plays a distinct role in directing selective FAs toward specific metabolic fates. What sets ACSL4 apart is its preference for PUFAs, particularly arachidonate, positioning it at the intersection of eicosanoid regulation, ferroptosis, and various associated pathologies (99). However, the mechanisms underlying ACSL4's preference for arachidonate remain poorly understood. Here, we provide extensive characterization

demonstrating that product inhibition plays a key role in shaping ACSL4's substrate specificity.

To gain insights into the mechanisms governing ACSL4 FA preference, we initially followed the conventional approach used in earlier studies by screening structurally distinct FAs for activity. Although ACSL4 exhibited the highest activity toward arachidonate, the differences among FAs were modest. For instance, when comparing arachidonate (20:4ω-6) to palmitate (16:0), only a 1.27-fold increase in activity at 50 μM and a 1.2-fold difference in catalytic efficiency was observed. Given that palmitate is the most abundant FA, accounting for 20–30% of total FAs in humans (294), such differences appear negligible. These observations contrast with the initial characterization of *r*ACSL4 (29), in which a nearly 2-fold increase in activity was reported at 100 μM, along with more than a tenfold increase in k_{cat}/K_m for arachidonate (20:4ω-6) compared to palmitate (16:0). However, apparent similar activities between the two FAs have also been reported in other publications (39,46), highlighting the impact of methodological conditions on observed results.

Although the k_{cat}/K_m ratio serves as a valuable comparative parameter for enzymes with unimolecular mechanisms, its relevance in the assessment of multireactant systems is often unwarranted (292). Following the strategy employed by (293) to differentiate two substrates with comparable k_{cat}/K_m, we assessed ACSL4 binding interactions with eight FAs using nDSF and MST. Using these two orthogonal methods, we showed that, similar to *tt*LC-

FACS, ACSL4 requires a primary conformational change induced by ATP to bind a FA. By comparing the FA binding events observed in the presence of ATP with those in the presence of a non-hydrolyzable analogue, we likely captured two distinct steps in the catalysis: intermediate formation and FA binding.

Both methods, under both conditions, revealed clear differentiation between FAs, allowing general tendencies to be established (**Table 7**). ACSL4 exhibited the highest affinity for PUFAs, with arachidonate (20:4ω-6) showing the strongest binding, followed by MUFAs, and lastly the saturated FA palmitate (16:0), which displayed the weakest affinity. The more than eleven-fold difference in ΔT_m and over two log units difference in $_{app}K_D$ between arachidonate (20:4ω-6) and palmitate (16:0) stand in stark contrast to the minimal variations observed in kinetic studies.

Previously, Coleman et al. reported a marked inhibition of palmitate (16:0) conversion when co-incubated with arachidonate (20:4ω-6), despite both substrates exhibiting comparable k_{cat}/K_m values in their study (39). This suggests that kinetic parameters may not accurately reflect ACSL4 behavior when exposed to mixtures of FAs, as is typically the case in the cellular environment. To account for this competition scenario, we developed a novel LC-MS assay to monitor specific FA consumption by ACSL4 within mixtures of up to eight FAs. Using this assay, we observed that the preferential consumption of specific PUFAs such as arachidonate (20:4ω-6) and dihomo-γ-linolenate (20:3ω-6) inhibits the conversion of other FAs. Successive

removal of the preferential FAs from the mixtures gradually unlocked the conversion of lower-priority FAs, suggesting that a product-inhibition mechanism governs ACSL4's substrate specificity. We pursued the investigation of this phenomenon by evaluating ACSL4 inhibition in the presence of two representative products: AA-CoA, corresponding to a preferential substrate, and PA-CoA, representing the product of a lower-priority substrate. While inhibition by PA-CoA was minimal, AA-CoA displayed potent inhibitions against lower-priority FAs. Remarkably, the intensity of this inhibition was inversely correlated with the FA ranking determined in the LC-MS competition assays (**Table 8**), strongly supporting the role of product inhibition in shaping ACSL4's FA preference.

Product inhibition is a well-established negative feedback mechanism that plays a crucial role in regulating metabolic balance (295). However, to our knowledge, this is the first time that product inhibition of an enzyme has been implicated in controlling its substrate specificity. Such mechanism confers a highly specialized role to ACSL4 in activating arachidonate and related PUFAs. It possibly prevents the saturation of the ACSL4 active site by constitutively abundant FAs, thereby facilitating the rapid reesterification of arachidonate. This may be crucial, considering that low dose (10 μM) of arachidonate can induce apoptosis (296) and that eicosanoid synthesis, an intrinsically transient process, is limited by arachidonate availability (102). Preventing the activation of lower-priority FAs may also facilitate the formation of specialized membranes enriched in PUFAs, which is essential for maintaining proper membrane fluidity. Membrane fluidity, in turn,

influences the activity of specific membrane proteins, supports cellular and organelle integrity, and regulates vascular permeability, factors believed to be critical for numerous brain functions (297). On the other hand, ACSL4's high specificity for arachidonate underpins its unique role, compared to other isoforms, in sensitizing cells to ferroptosis (101).

We also characterized AA-CoA interaction and found that it binds tightly to ACSL4 in the absence of ATP (ΔT_m = 4.4 °C, K_D = 1.3 μM), a condition that reflects the end of one catalytic cycle and the initiation of the next. AA-CoA affinity further increases (ΔT_m = 5.5 °C, K_D = 0.35 μM) following the ATP-induced conformational shift necessary for the binding of a new FA, leading to nearly a 3-fold stronger affinity compared to the corresponding substrate. With the product already bound, this may result in an unfair competition that prevents lower affinity FAs from binding.

The higher affinity of AA-CoA compared to arachidonate is likely due to the synergy between the fatty acyl and CoA moieties. Together, these components strengthen the binding, an effect presumably attributable to most FAs. This implies that FAs with higher affinities are converted into products that are more potent inhibitors, balancing the overall reaction rates among FAs. Such phenomenon may explain why the conventional biochemical methodologies show limited differentiation between FAs, often resulting in comparable k_{cat}/K_m values for the preferential arachidonate (20:4ω-6) and the lower-priority palmitate (16:0) (39,46). Product inhibition also likely contributes to the discrepancies observed in the substrate preference rankings

from previous studies, as variations in protein purity and FA concentrations can lead to significantly different levels of inhibition. For instance, in the more complex medium of Sf-9 cell lysate supernatants with overexpressed ACSL4 and low levels of FAs (0.1-1 μM), only highly unsaturated FAs are converted (58), possibly due to the presence of endogenous products inhibiting activity for lower-priority FAs.

The regulation of substrate specificity by product inhibition suggests that relying solely on the kinetic parameters of isolated FAs is inadequate for accurately determining ACSL4's FA preference. To account for all the interactions that occur when mixtures of FAs are presented to the enzyme, it is crucial to use an assay capable of monitoring the specific FA activities.

Other ACSL isoforms also exhibit inconsistencies across studies, and reported FA specificity profiles often lack clear or consistent patterns (34,46). Despite these inconclusive results, each ACSL likewise fulfill specialized roles in FA channeling (298). For instance, ACSL3 plays an opposing role to ACSL4 by channeling MUFAs into membrane phospholipids, thereby displacing oxidizable PUFAs and protecting cells from ferroptosis (299). Previous studies have reported that PA-CoA inhibits nonspecific ACSL activity in rat liver microsomal fractions (300). Given the minimal inhibition of ACSL4 by PA-CoA, it is likely that other ACSL isoforms are also regulated by product inhibition.

Evidence that preferential products influence ACSL4's FA specificity pave the way for future investigations into other isoforms. A precise determination

of the specific substrates for each ACSL will enhance our knowledge of their specific roles in FA metabolism.

6. Acknowledgments

The authors thank Prof. Jean-François Goossens for providing access to the Varioskan Flash spectrophotometer. This work was supported by l'agence nationale de la recherche (ANR-23-CE18-0051) (EGID ANR-10-LABX-046), the Région Hauts-de-France (Start-AIRR FerInh4Park), the French Community Of Belgium (ARC 21/26–115), the Belgian Fonds National de la Recherche Scientifique (F.R.S.-FNRS; PDR grant 40003810), the Télévie (Grant 40007387). D.M.D. is a Télévie research fellow. N.P. received an Aspirant Ph.D Fellowship from FRS-FNRS (Belgium).

7. Supplementary material

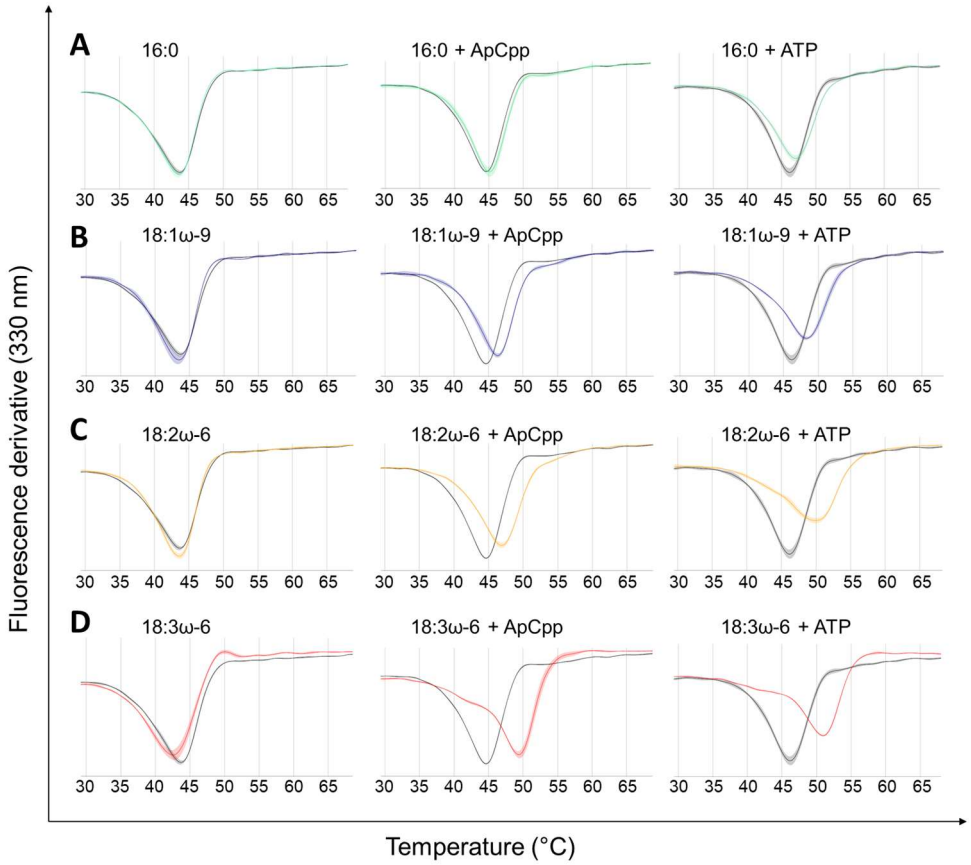

Figure S1. Thermal shift assays of four representative FAs on ACSL4. nDSF traces of ACSL4 (4 µM) with 50 µM of (**A**) palmitate (16:0), (**B**) oleate (18:1ω-9), (**C**) linoleate (18:2ω-6), and (**D**) γ-linolenate (18:3ω-6) under apo condition or in the presence of 1 mM ApCpp or ATP (colored curves) compared to the corresponding control (black curves). Each curve represents the average of three independent experiments. Corresponding ΔT_m values are reported in **table 5**[a].

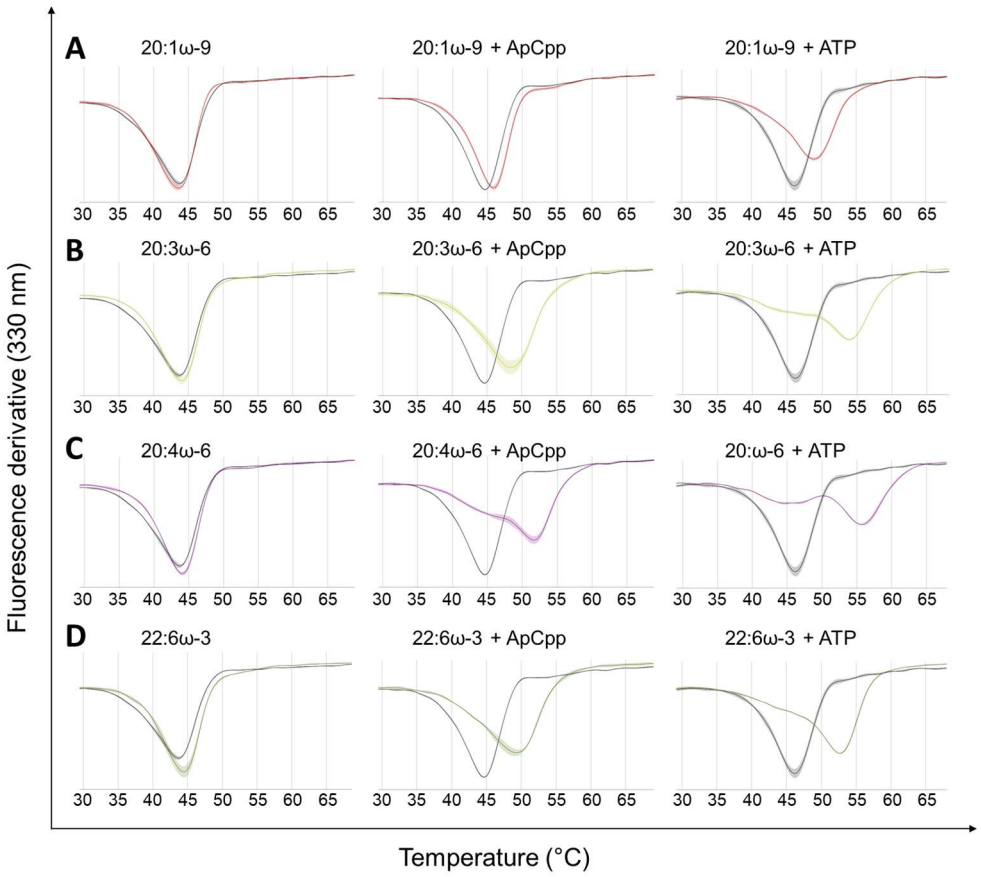

Figure S2. Thermal shift assays of four representative FAs on ACSL4. nDSF traces of ACSL4 (4 µM) with 50 µM of (**A**) eicosenoate (20:1ω-9), (**B**) dihomo-γ-linolenate (20:3ω-6), (**C**) arachidonate (20:4ω-6), and (**D**) docosahexaenoate (22:6ω-3) under apo condition or in the presence of 1 mM ApCpp or ATP (colored curves) compared to the corresponding control (black curves). Each curve represents the average of three independent experiments. Corresponding ΔT_m values are reported in **table 5**[a].

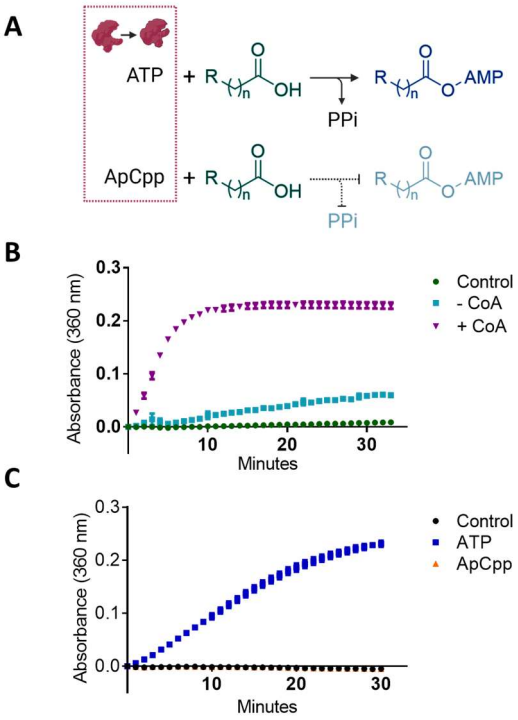

Figure S3. The ATP and ApCpp conditions capture two distinct FA binding events. (**A**) Schematic representation of the hypothesis proposing that ApCpp allows the observation of FA binding alone, while ATP enables both FA binding and acyl-AMP formation. (**B**) ACSL4 retains residual activity in the absence of CoA, indicating acyl-AMP formation. Enzymatic activity was assessed in conditions analogue to nDSF, with 4 µM ACSL4, using palmitate (16:0) as a substrate, with or without 100 µM CoA. The plot represents one of three independent experiments performed in duplicate. (**C**) ApCpp is not a substrate of ACSL4. ACSL4 (50 nM) activity assay was performed in the presence of ATP or ApCpp (50 µM). The plot represents one of three independent experiments performed in triplicate.

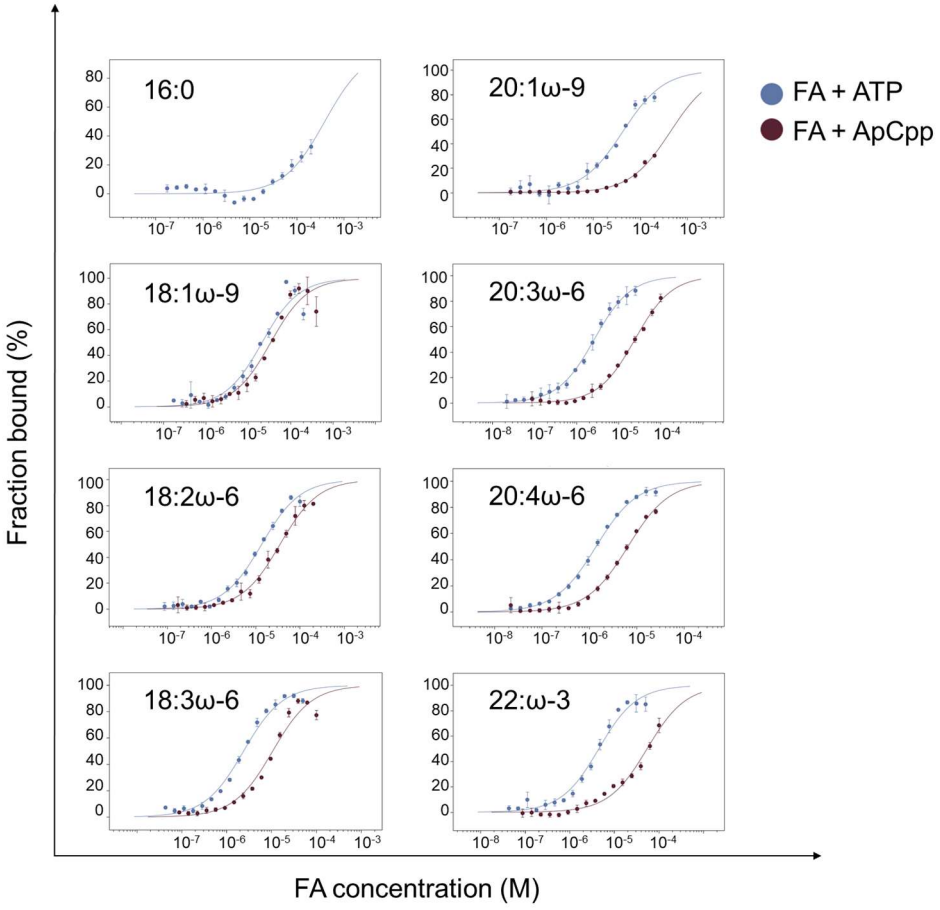

Figure S4. MST traces showing the binding interactions of eight FAs. Binding interactions of palmitate (16:0), oleate (18:1ω-9), linoleate (18:2ω-6), γ-linolenate (18:3ω-6), eicosenoate (20:1ω-9), dihomo-γ-linolenate (20:3ω-6), arachidonate (20:4ω-6), and docosahexaenoate (22:6ω-3) with ACSL4 in the presence of 1 mM ATP (blue curves) or ApCpp (purple curves). Each curve represents the average of three independent experiments. Associated K_Ds or $_{app}K_D$s are reported in **table 5**[b,c].

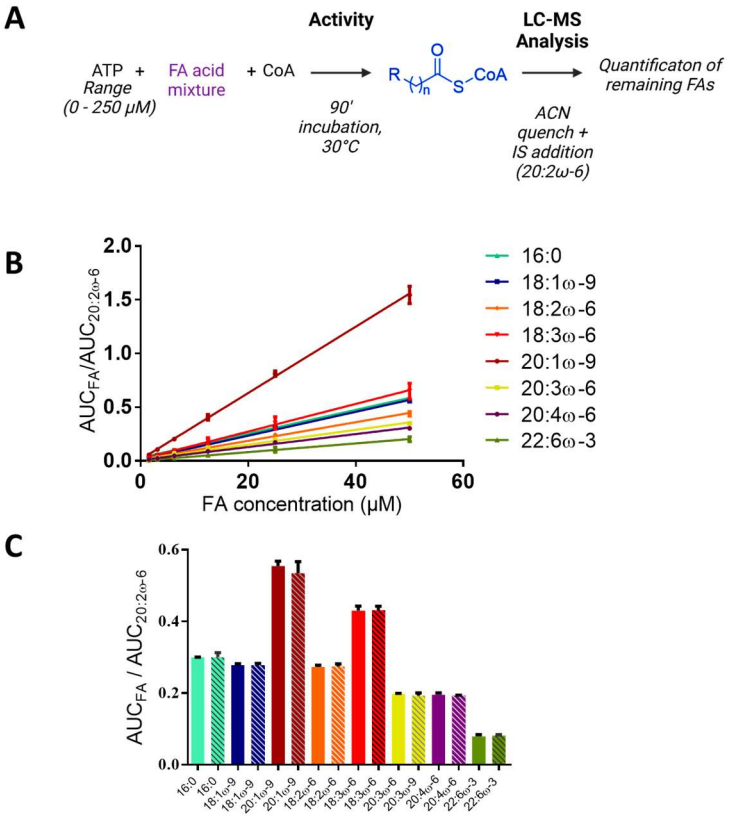

Figure S5. Development of a LC-MS-based competition assay to monitor specific FA consumption by ACSL4. (**A**) Schematic representation of the competition assay. (**B**) Calibration curves of eight FAs. LC-MS responses for serial dilutions of an eight-FA mixture, demonstrating linearity across concentration range (50 to 1.56 µM). Each point is the result of three independent experiments. (**C**) Control experiments for FA consumption in eight-FAs mixtures. Comparison of FAs levels between a control experiment with ACSL4 in the absence of ATP (solid bars) and another control without ACSL4 but with 250 µM ATP (striped bars), demonstrating that FA consumption is dependent on both ACSL4 and ATP. Each bar is the result of three independent experiments. ACN, acetonitrile; IS, internal standard.

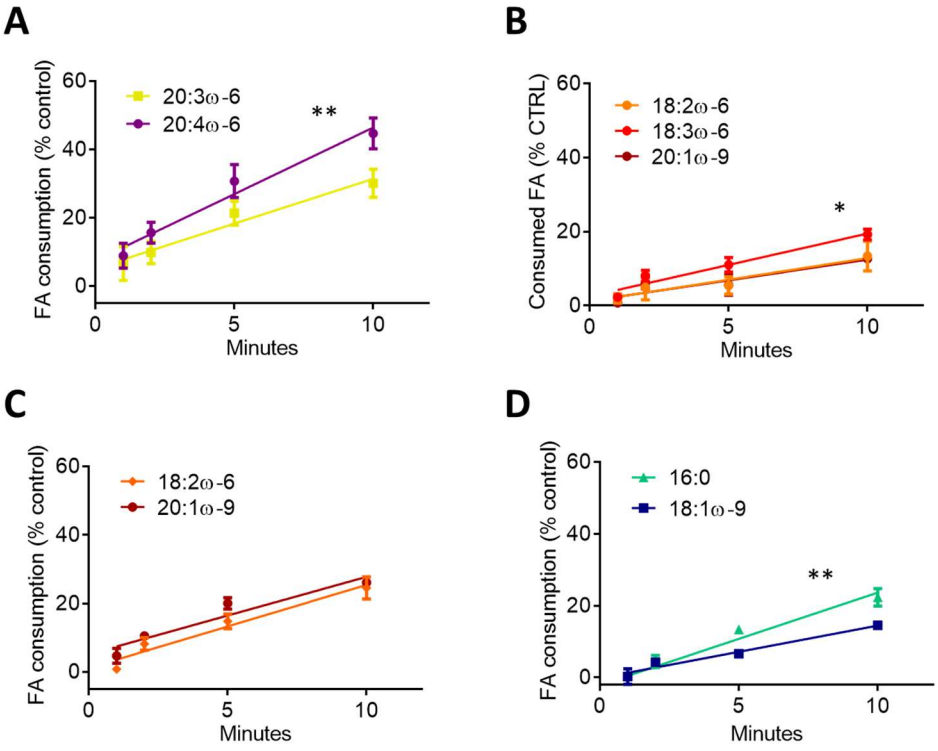

Figure S6. Kinetic LC-MS monitoring of ACSL4's consumption of closely competing FAs. (**A**) Mixture of 20:4ω-6 and 20:3ω-6. (**B**) Mixture of 18:2ω-6, 18:3ω-6 and 20:1ω-9. (**C**) Mixture of 18:2ω-6 and 20:1ω-9. (**D**) Mixture of 18:1ω-9 and 16:0. Each point is the result of three independent experiments. Statistical analysis was determined using unpaired t-test, * $p < 0.05$; ** $p < 0.01$.

GENERAL DISCUSSION AND PERSPECTIVES

In this work, we focused on ACSL4, an enzyme involved in the initial activation step of PUFAs. Given its relevance in cancer and ferroptosis-related diseases, ACSL4 represents a compelling therapeutic target. Our aim was therefore to develop optimized inhibitors with improved potency and selectivity profiles compared to the reference compounds.

In the first chapter, we initiated the project by producing recombinant ACSL4 and ACSL3 constructs and developing a screening cascade integrating both biophysical and biochemical methods. Since false positives are a significant burden in screening campaigns, the use of multiple orthogonal methods represents a major advantage that limits the risk of non-specificity. We thus developed four techniques that we validated with ROSI, the most used reference inhibitor. Intriguingly, during this validation, we observed that binding of the reference inhibitor was ATP-dependent in DSF and MST. From that point onward, we considered a potential analogy with FAs, which, based on the *tt*LC-FACS structure, require an ATP-induced conformational change to bind.

Using the screening platform developed, we assessed an FDA-approved library to identify novel inhibitor scaffolds. The underlying approach aimed to repurpose existing drugs by identifying new activity against ACSL4. As noted by Nobel laureate Sir James Black, “The most fruitful basis for the discovery of a new drug is to start with an old drug.” Drug repurposing is particularly popular among pharmaceutical companies, as it offers a lower-cost and potentially faster alternative to *de novo* drug discovery and

development. In recent years, drug repurposing has contributed to approximately 30% of newly FDA-approved drugs (301). Beyond these considerations, the primary advantage for us was the ability to start from scaffolds presumed to possess more drug-like properties, while also benefiting from a wealth of existing information, such as synthesis procedures and physicochemical characteristics.

A primary screening of the library using DSF yielded 11 hits, corresponding to a hit rate of approximately 1%, which is consistent with expectations for this type of screening strategy (302,303). To identify potential ATP competitors, we also screened the library in the absence of the nucleotide. However, no compounds induced a significant thermal shift under these conditions, highlighting the difficulty of targeting ACSL4 in its *apo* form. The hits included the reference inhibitor ROSI and acitretin, a vitamin A analogue.

Notably, nine of the hits identified belonged to the same azole antifungal family. Among them, only the compounds bearing a phenethyl-imidazole moiety passed all validation assays, showing the importance of this structural element for ACSL4 inhibition. The most potent compound of the series, SERTA (**Figure 47**), exhibited an activity 3-fold increased (IC_{50} = 280 nM) compared to ROSI and demonstrated selectivity for ACSL4 over ACSL3.

Additionally, SERTA reduced lipid peroxidation and protected LUHMES cells from ferroptosis. Since the antiferroptotic activities paralleled ACSL4 inhibition (SERTA > ECO > FLUCO), and were independent of iron-

chelation and antioxidant effects, it is likely that the protective effects are mediated through ACSL4 inhibition. However, its target engagement remains to be validated.

In conclusion, this work established a robust methodology that bridges the investigation of large compound libraries to their evaluation in cellular pathological models. We validated the approach by identifying a novel inhibitor series able to prevent ferroptosis in a cell-based model of Parkinson's disease. The most potent compound, SERTA, does not only constitute an interesting tool but may serve as a starting point for the development of novel antiferroptotic compounds.

Noteworthy, during this work, we observed that the affinity of SERTA measured by MST (K_D = 2.0 µM) appeared significantly weaker than the IC_{50} value (IC_{50} = 0.28 µM), which is theoretically inconsistent, as specific inhibition presupposes target binding, implying that K_D should always be equal to or lower than the IC_{50} (**Equation 1**). This discrepancy may arise from differences in experimental conditions between the two methods, particularly the high enzyme concentration (500 nM) required for MST experiments, which limits the accurate determination of K_D below this threshold.

$$IC_{50} = \frac{[E]_0}{2} + K_D(app) \qquad (\mathbf{1})$$

Where $[E]_0$ is the total enzyme concentration.

Nonetheless, MST remains a valuable dose-response orthogonal technique to validate hit binding and rank them by relative affinity. To better estimate the absolute affinity, we could determine the inhibition constant (K_i), which represents the K_D obtained through inhibition kinetic analysis. K_i measurements would allow independence from enzyme and substrate concentrations, enabling better comparisons. For example, in selectivity studies, where ACSL3 concentration is 12-fold higher than ACSL4, K_i values would provide a more accurate comparison across isoforms than IC_{50}. However, *K*i values only accurately reflects a binding constant when the mode of inhibition is correctly identified, which can be challenging to establish for an enzyme, such as ACSL4, with a complex catalytic mechanism and strong product inhibition. Alternatively, other biophysical methods, such as surface plasmon resonance (SPR) or isothermal titration calorimetry (ITC), could provide accurate K_D values while also generating valuable binding kinetic and thermodynamic contribution data, respectively.

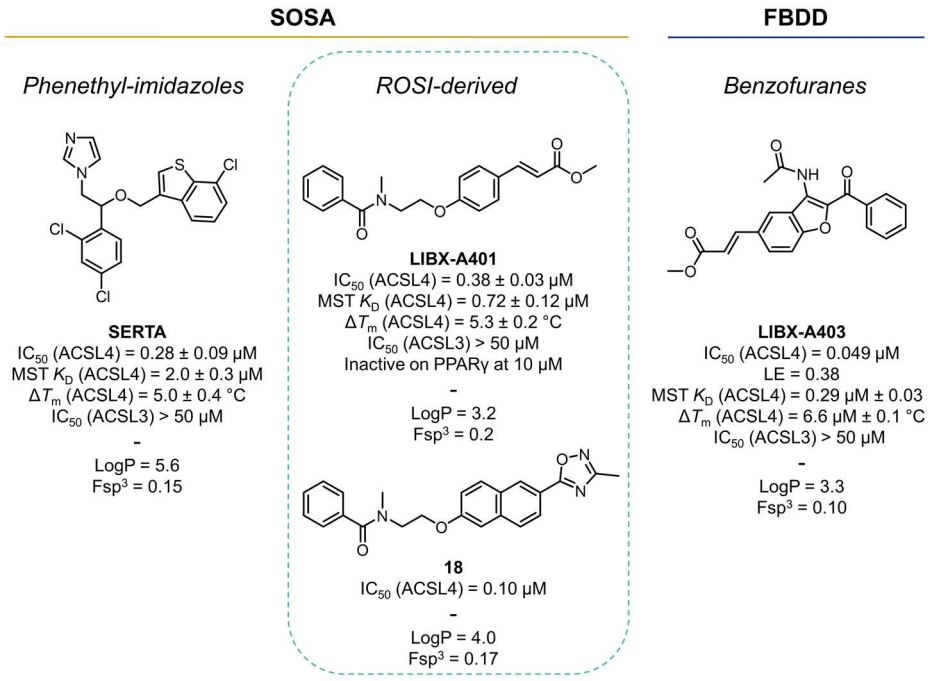

Figure 47. Structure and properties of developed ACSL4 inhibitors.

In the second chapter, which serves as a transition, we briefly discussed the medicinal chemistry efforts employed to optimize compounds from three distinct inhibitor series. We also highlighted a significant limitation shared by all ACSL4 inhibitors: FA-dependency.

Starting from the scaffold of a known drug often requires reducing its typically high activity toward the original target in order to enhance selectivity for the new target of interest. To reduce CYP inhibition by the SERTA series, we investigated modifications around the imidazole moiety, known to coordinate the CYP heme iron. Replacing it with non- or less-

chelating moieties either completely abolished ACSL4 inhibition or significantly reduced it, by approximately 50- to 100-fold. Thus, although CYP inhibition can be reduced, it comes at the cost of a drastic loss in ACSL4 inhibition. This suggests that a chelating group may be crucial in this region of the scaffold, potentially to coordinate the magnesium ion required for ACSL4 enzymatic activity (37). Thus, future efforts to optimize the SERTA scaffold should continue to focus on reducing CYP inhibition, while preserving ACSL4 inhibitory potency. A dedicated assay to monitor CYP activity would be required to conduct selectivity optimization.

Starting from the widely used ROSI, strategies were developed to eliminate its PPARγ agonist activity. The acidic TZD head group present in ROSI is crucial for its binding and functional activity on PPARγ (233). To our satisfaction, removal of the acidic character preserved ACSL4 inhibitory activity. Optimization efforts led to LIBX-A401 (**Figure 47**), a compound that, compared to ROSI, exhibits improved ACSL4 activity (IC_{50} = 0.38 μM), lacks PPARγ agonist activity, and maintains selectivity over ACSL3. As with all inhibitors investigated so far, LIBX-A401 binding to ACSL4 is ATP-dependent. A thorough investigation of its binding site, using integrated chemical biology approaches, in silico studies, and mutagenesis analysis, demonstrated that LIBX-A401 binds within the predicted FA pocket. LIBX-A401 also confers protection against ferroptosis in cell-based models, with target engagement further supporting ACSL4 involvement in this activity. The methylacrylate moiety in LIBX-A401 is a liability as it may react irreversibly with nucleophiles in biological systems. Consequently, strategies

targeting the replacement of the methylacrylate moiety led to the development of compound **18**, which exhibits nearly a fourfold increase in activity compared to LIBX-A401 (**Figure 47**). Lead optimization is currently progressing through a scaffold-hopping approach, aimed at modifying the central core to incorporate hydrophilic elements and boost the sp^3 character of the molecule. Although only a few key molecules are presented here, over a hundred analogues were synthesized and evaluated to reach the potent compound **18**, establishing a structure-activity relationship (SAR) that will be detailed in a forthcoming publication later this year.

The valuable structural insights obtained during ROSI optimization encouraged us to pursue a fragment-based drug discovery (FBDD) program. After a screening of 640 fragments using the screening cascade we developed, we validated 31 hits. Fragment **19**, which showed the most potent activity (IC_{50} = 33 μM) and a good ligand efficiency (LE = 0.37), was selected for hit optimization, although other compounds with promising properties could also have served as suitable starting points. Optimization of fragment **19** led to LIBX-A403 (**Figure 47**), the most potent ACSL4 inhibitor reported to date (IC_{50} = 0.049 μM; LE = 0.38). As with LIBX-A401, the ATP-dependency of binding, along with molecular modeling and site-directed mutagenesis, suggests that LIBX-A403 may also bind within the FA pocket, where it is predicted to engage primarily in hydrophobic interactions. In addition, the compound potently prevents ferroptosis (EC_{50} = 0.172 μM), while showing target engagement in cells. Like LIBX-A401, LIBX-A403 contains a methylacrylate moiety with potential reactivity concerns, and modifications

of this group are currently being considered. A major limitation of LIBX-A403 is its poor aqueous solubility, which restricts its use in biological models. Early attempts to improve the physicochemical properties of the benzofuran series, either by introducing heteroatoms to reduce lipophilicity or by opening the benzofuran ring to decrease planarity, resulted in a significant loss of activity. Thus, inhibition by benzofuran analogues appears to correlate with both lipophilicity and planarity. However, the open-ring analogue preserves substantial potency (**28**, IC_{50} = 0.98 µM), and may serve as a new starting point to improve the drug-likeliness of the chemical series.

Although this issue is clearly illustrated by the benzofuran derivatives, it may extend to all inhibitor series studied. Phenethyl-imidazole drugs are even more lipophilic, restricting their application primarily to topical use. Within the broader azole antifungal family, the most potent compound, SERTA, displays one of the highest logP and among the lowest Fsp^3 values. Optimization of the LIBX-A401 scaffold also favors the development of compounds with increased lipophilicity and planarity, as illustrated by comparing LIBX-A401 (IC_{50} = 0.38 µM, LogP = 3.17, Fsp^3 = 0.20) to the compound **18** (IC_{50} = 0.10 µM, LogP = 4, Fsp^3 = 0.17). Given the tropism of ACSL4 for the cell's lipophilic compartments and the inherent lipophilicity of its FA substrates, it is not surprising that the inhibitors also tend to be highly lipophilic. However, to maximize the likelihood of favorable ADME properties, balancing low oxidative and renal clearance with sufficient solubility and passive permeability, the logD of a compound should ideally fall within the range of 1 to 3 (304). In addition, the high degree of planarity

observed in the most potent inhibitors across all series represents not only a liability in terms of solubility but may also restrict their ability to occupy greater 3D chemical space (282). Adding complexity to the scaffolds, by the means of saturation and chiral centers could result in compounds that better complement the spatial subtleties of ACSL4, potentially enhancing both potency and selectivity. In fact, the average Fsp^3 value has been shown to increase throughout drug development, rising from 0.36 at the discovery stage to 0.47 in approved drugs (282). Thus, the three inhibitor series share common physicochemical liabilities, which should be addressed by incorporating hydrophilic features and increasing molecular complexity. Future lead optimization efforts will need to strike a careful balance between improving drug-likeness while preserving potency.

As we further characterized the developed ACSL4 inhibitors, we unexpectedly found that they were nearly inactive *in vitro* against the enzyme's preferred substrate, arachidonate. This prompted us to evaluate a range of inhibitors against a panel of FAs, revealing FA-dependent inhibition across all active compounds tested, with arachidonate showing the lowest level of inhibition.

Although FA-dependency of inhibition was anticipated based on the putative binding sites of some inhibitors, the magnitude of the effect was unexpected. A 100- to 1000-fold increase in IC_{50} was estimated when comparing palmitate (16:0) to arachidonate (20:4ω-6), which contrasts sharply with the more

moderate activity differences between FAs in substrate specificity studies (29),(39),(46).

We investigated a potential potent competitive mechanism to account for these drastic differences. Kinetic studies with TRO revealed a mixed inhibition pattern, which, by nature, remains inconclusive. Preliminary STD NMR competition studies showed that arachidonate (20:4ω-6), but not palmitate (16:0), was able to significantly displace ROSI binding. However, displacement by arachidonate was only partial, suggesting that the competition is not complete. Further optimization of the method or the use of an orthogonal technique is needed to clarify the competitive mechanism.

Realizing that all known ACSL4 inhibitors exhibit poor *in vitro* inhibition when assessed against the enzyme's preferred FA substrates, raises critical questions: **what is their value if they fail to effectively inhibit the isoform's physiologically relevant activity?** The therapeutic potential of ACSL4 is closely tied to its activity toward arachidonate and the selective inhibition of its activity toward SFAs or MUFAs would likely be ineffective.

How does the inhibition of purified ACSL4 correlate with the activity of these inhibitors in more complex models? Are they capable of inhibiting arachidonoyl-CoA synthetase activity in cellular systems or *in vivo*? LIBX-A401 and LIBX-A403 were shown to bind ACSL4 in cells (33), while AS-252424 and the Silibinin probe effectively target ACSL4 in cell lysates (93,239). Furthermore, ROSI and PRGL493 were shown to decrease the formation of AA-CoA in cells (92), whereas Silibinin reduced AA-CoA

formation in cell lysates (239). These findings confirm that the compounds do inhibit arachidonoyl-CoA synthetase activity in cellular contexts.

Given that AS-252424 (93) **and PRGL493** (92) **were reported to inhibit purified ACSL4 in the presence of arachidonate but failed to show activity in our assay, could the issue lie in our experimental setup?** The importance of experimental methodology has been highlighted in studies of ACSL substrate specificity, as variations in protein purification protocols and activity assays can result in significant discrepancies (34,46). In our setup, while the potency of the inhibitors varies depending on the FA used, the relative ranking of their inhibitory effects tends to be conserved across different FAs. Therefore, monitoring inhibition using palmitate (16:0) seems relevant, as it enables meaningful comparison between different inhibitors.

Because ACSL4 is considerably more difficult to inhibit in the presence of arachidonate (20:4ω-6) than with palmitate (16:0), gaining a deeper understanding of the molecular mechanisms underlying its preference for arachidonate could significantly aid lead optimization. To this end, we initiated substrate specificity studies.

In chapter III, we investigated the mechanisms governing ACSL4's FA preference. We first adopted a conventional approach by screening structurally distinct FAs for activity. Although ACSL4 showed the highest activity toward arachidonate, the differences among FAs were modest. Comparing arachidonate (20:4ω-6) to palmitate (16:0) revealed only a 1.27-

fold increase in activity at 50 µM and a 1.2-fold difference in catalytic efficiency.

We further investigated substrate specificity by monitoring ACSL4 binding interactions with eight FAs using nDSF and MST. These two orthogonal methods revealed that, similar to *tt*LC-FACS, ACSL4 undergoes a primary ATP-induced conformational change necessary for FA binding. In addition, by comparing FA binding events in the presence of ATP versus a non-hydrolyzable analogue, we likely distinguished two catalytic steps: FA binding and intermediate formation.

Both methods, under both conditions, were consistent and revealed clear distinctions between FAs. ACSL4 showed the highest affinity for PUFAs, with arachidonate (20:4ω-6) binding most strongly, followed by MUFAs, and finally palmitate (16:0). The more than eleven-fold difference in ΔT_m and over two log units in apparent K_D between arachidonate (20:4ω-6) and palmitate (16:0) sharply contrast with the minimal differences observed in kinetic studies.

Although all biophysical methods resulted in a similar overall FA ranking, the exact positioning of intermediate FAs varied between approaches. To serve as a benchmark method, we developed a novel LC-MS assay to monitor specific FA consumption by ACSL4 within mixtures of FAs. Using this assay, we observed that the preferential consumption of specific PUFAs such as arachidonate (20:4ω-6) and dihomo-γ-linolenate (20:3ω-6) strongly inhibited the conversion of other FAs. The successive removal of fully

consumed FAs from the mixtures progressively enabled the conversion of lower-priority FAs, suggesting that product inhibition may play a role in regulating ACSL4's substrate specificity. Using four different mixtures, we established a preference ranking that better captures the complexity of a physiological environment. Among the different ranking methods, nDSF in the presence of ATP most closely approximates the ranking observed in the competition assay.

We validated the product-inhibition mechanism by evaluating ACSL4 activity in the presence of two representative products: AA-CoA, corresponding to a preferential substrate, and PA-CoA, product of a lower-priority substrate. While inhibition by PA-CoA was minimal, AA-CoA potently inhibited lower-priority FAs conversion. The inhibition remarkably correlated with the FA ranking determined in the LC-MS competition assays, supporting the role of product inhibition in shaping ACSL4's FA preference.

It is well established that product inhibition plays a key role in maintaining metabolic balance through negative feedback mechanisms (295). However, we found no other reports of this type of mechanism contributing to substrate specificity in any enzymatic system. It clearly confers upon ACSL4 a highly specialized role *in vitro* in the activation of arachidonate and related PUFAs. The physiological advantages of such specificity control remain speculative, but may involve the need for a rapid response to tightly regulate arachidonate levels, thereby preventing apoptosis (296) or halting eicosanoid synthesis (102). Alternatively, this tight specificity might be required to support the

biosynthesis of PUFA-rich membrane domains with specialized functions, ultimately contributing to ferroptosis sensitivity (101).

We characterized AA-CoA interaction and found that it binds with high affinity to ACSL4 in the absence of ATP (K_D = 1.3 μM), a condition that reflects the end of one catalytic cycle and the initiation of the next. Following the ATP-induced conformational change that enables binding of a new FA, AA-CoA affinity further increases (K_D = 0.35 μM), resulting in nearly threefold stronger binding compared to the most preferred substrate. With the product already bound, this may result in an unfair competition that prevents lower affinity FAs from binding. Thus, a new model can be proposed in which the catalytic cavity is never truly empty, but instead occupied by a preferential product (**Figure 48**). PUFAs may be less affected by the constitutive presence of their products, either due to their inherently higher affinity, or perhaps due to their ability to navigate a partially occupied cavity thanks to greater structural flexibility. Obtaining structural insights would be instrumental in clarifying this phenomenon.

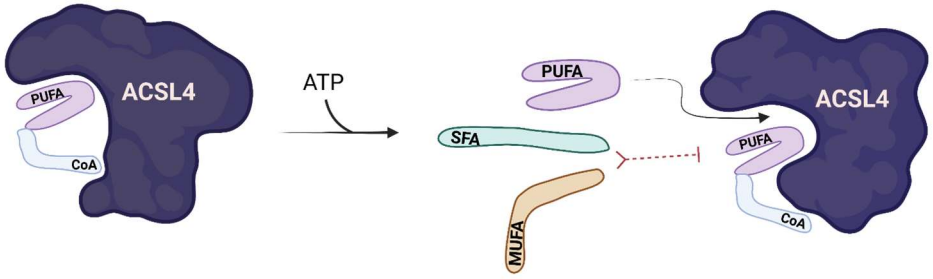

Figure 48. Preferential products remain bound to ACSL4, preventing processing of lower-priority FAs.

One might question the relevance of product-governed substrate specificity in more complex biological systems. Numerous gain- and loss-of-function have demonstrated that ACSL4 exclusively metabolizes PUFAs in cellular contexts (58,59,68) which support the existence of a regulatory mechanism when considering the ability of recombinant enzymes to use other type of FAs. In addition, previous studies have reported that PA-CoA inhibits nonspecific ACSL activity in rat liver microsomal (300) or mitochondrial (305) fractions, validating the effect in more complex media. However, the presence of ACBP, a small cytosolic protein with nanomolar affinity for acyl-CoAs (306) and the ability to mitigate ACSL inhibition by PA-CoA (305) might temper the efficiency of product inhibition. Further investigation into ACBP's role in modulating ACSL4 product inhibition and its influence on FA preference will provide deeper insights into the relevance of this regulatory mechanism *in vivo*.

Based on the results we obtained, it can be assumed that FAs with higher affinities are converted into products with stronger binding, which act as more potent inhibitors, thereby balancing the overall reaction rates across different FAs. Such phenomenon may explain why the conventional biochemical methodologies show limited differentiation between FAs, often resulting in comparable k_{cat}/K_m values for the preferential arachidonate (20:4ω-6) and the lower-priority palmitate (16:0) (39,46). Thus, relying solely on the kinetic parameters of isolated FAs is inadequate for accurately determining ACSL4's substrate preference.

These assumptions likely extend to other ACSL isoforms, whose reported FA specificity profiles, based on kinetic measurements, often lack clear and consistent patterns (34,46). Given the previously reported ACSL inhibition by PA-CoA (300,305) and the minimal ACSL4 inhibition we observed with the same product, it is probable that other isoforms are also subject to regulation via product inhibition. Therefore, it would be valuable to re-evaluate the FA preferences of other ACSLs by accounting for product inhibition, using a methodology similar to that developed for ACSL4.

However, whether this approach on purified proteins provides a meaningful advantage over cell-based evaluations is open to discussion. To explore this further, we will discuss the respective limitations of each approach.

ACSL activity is tightly regulated by post-translational modifications, such as phosphorylation, which can even influence oligomeric states, as observed for ACSL4 (86). These transient modifications cannot be recapitulated in purified proteins, especially when expressed in simple organisms such as bacteria.

Furthermore, as with other proteins that operate at the water-lipid interface, accurately assessing their activity presents a major challenge, as purification procedures inevitably create an artificial environment that differs significantly from their native cellular context (34). To obtain sufficient amounts of protein from *E. coli* lysates, we had to use Triton X-100 at concentrations way above its critical micellar concentration. We also observed that both the enzymatic activity and apparent oligomeric state of

ACSL4 were highly sensitive to the type and concentration of detergent used (data not shown). In addition, these enzymes use FAs as substrates, which are likely sequestered within the artificial micelles, and generate detergent-like products that can potentially alter the micellar environment.

Another limitation is that we cannot determine the FA concentration at the enzyme's active site in a cellular context, as it is not uniformly distributed (46). The majority of the intracellular unesterified FA pool is bound with high affinity to abundant fatty acid-binding proteins (FABPs), restricting free FA concentrations to the low nanomolar range (9). This suggests that enzymes utilizing FAs may require dedicated delivery mechanisms, for example through interactions with FABPs. Moreover, the release of certain esterified FAs, such as arachidonate, is a transient process that is highly dependent on the (patho)physiological conditions (307). Altogether, these considerations make it challenging to reproduce a cellular environment containing a physiologically relevant mixture of FAs. Considering that FABPs can accommodate FA concentrations up to 300 µM (9), and that unesterified arachidonate levels range from low (0.5-15 µM) under resting conditions to high micromolar levels (100-500 µM) following stimulation (307), using 200 µM total FAs, distributed as 25 µM each for eight representative species, provides a reasonable physiological approximation. For more specific contexts, the composition of this mixture could still be adjusted accordingly.

Finally, working with purified proteins does not capture the advantages of multi-protein assemblies that typically enhance pathway efficiency, as

substrates and intermediates remain concentrated near potential downstream proteins rather than being diluted into the bulk phase (298). This mechanism has been proposed in the context of the ACSL1-GPAT1 interactome and could also involve FABPs and ACBP.

Therefore, future studies using purified proteins should focus on evaluating their activity in well-defined systems that incorporate membranes closely resembling their native environment, along with key components of their interactome.

Although cellular evaluations better mimic a physiologically relevant environment and allow for the assessment of the metabolic fate of FAs, gain- and loss-of-function studies come with their own set of drawbacks. A major caveat of gain- and loss-of-function studies concerning ACSLs is that long-term changes in gene expression may affect other enzymes or proteins involved in FA transport and metabolism (97). As a result, interpretations may be confounded by secondary alterations in gene expression or posttranslational modifications affecting other proteins involved in lipid metabolism.

Evidence from overexpression studies is particularly questionable due to the potential mislocalization of the overexpressed ACSL, which may significantly alter FA channeling (30). Downstream pathways may become saturated and unable to process an excess flux of acyl-CoA substrates. The surplus acyl-CoA could then aberrantly inhibit metabolic enzymes and damage cellular membranes due to its detergent-like properties. Thus, studies

employing transient inhibition, either through inducible knockout or selective pharmacological inhibitors, are preferable.

Another limitation is that the distribution of FAs and the function of ACSL isoforms may vary across tissues and cell types, meaning that conclusions might be restricted to the specific models studied.

Additionally, the FA profile of cultured cells differs markedly from that of natural cells, typically containing twice the MUFA and half the PUFA levels, due to limited availability of PUFAs in culture media (308). This discrepancy can significantly alter lipid metabolism in cell-based models.

Finally, the diverse metabolic roles of ACSLs, from FA uptake to their channeling into multiple distinct pathways, make it challenging to comprehensively track their functional contributions. Sensitive methods capable of simultaneously measuring *in vivo* fluxes of free FAs and acyl-CoAs are therefore required to clearly delineate their specific roles.

In conclusion, both biological and biochemical models come with inherent limitations, as is the case with any experimental system. Evaluating the metabolic fate of FAs is simply not possible using purified proteins alone and requires more complex biological models. However, defining a clear substrate spectrum or investigating the molecular determinants underlying it is far more feasible in biochemical systems, where strict control over experimental parameters enables clearer interpretation of results. For instance, uncovering a product-inhibition mechanism is challenging in

biological systems, since introducing the product would substitute for the enzyme natural activity.

Because this work spanned from medicinal chemistry to biochemistry, beginning with the observation that ACSL4 inhibition is intrinsically linked to substrate specificity, it is natural to question whether the product inhibition underlying this specificity contributes to the FA-dependent inhibition. First, it is reasonable to assume that the substrate and product share at least a partially overlapping binding site, given their common fatty acyl moiety. Thus, a potential competition mechanism between the FA and the inhibitor may also be preserved by the product. This might explain why TRO displays a mixed inhibition pattern, as its binding wouldn't be affected by the FA alone. Investigating this will require a robust biophysical competition method that provides clear signals for inhibitors, FAs and their derivatives. Alternatively, should ACBP facilitate the removal of the product, this could restore the inhibitory effect of pharmacological compounds on ACSL4 in the presence of arachidonate. If so, it would strongly suggest that the product impairs the compounds' binding. This would also support the idea that ACSL4 inhibition in the presence of arachidonate is facilitated in biological systems by the downstream processing of acyl-CoAs, potentially explaining the discrepancies observed between biochemical and cellular models.

Recognizing the role of the product in ACSL4 catalysis does not provide a straightforward solution to the lack of inhibition by pharmacological

compounds in the presence of arachidonate. However, it opens new avenues for the design of optimized ACSL4 inhibitors.

Through the study of product binding and product inhibition, we observed for the first time an inhibitor capable of binding ACSL4 in the absence of ATP. This presents an opportunity to design ligands that replicate this mechanism. A product-mimetic compound could extend the window of the catalytic cycle during which the inhibitor can bind, potentially enhancing potency. Moreover, the CoA-binding pocket provides additional hotspot residues capable of forming non-hydrophobic interactions, compensating for the limited interaction diversity within the predominantly lipophilic FA-binding pocket. Consequently, this approach could facilitate the improvement of drug-like properties during lead optimization. As a proof of concept, a hybrid molecule combining a LIBX derivative linked through the cinnamic ester group to a CoA moiety is envisioned. However, the synthesis of such amphiphilic compounds may be challenging, and the rational design of CoA modulations could prove difficult during later optimization steps.

It is possible that ACBP alleviates product inhibition by interacting with ACSLs and extracting acyl-CoAs. If so, disrupting this interaction could represent a novel inhibitory strategy. Achieving this would require a detailed understanding of the putative binding interface between ACSL4 and ACBP. Nevertheless, since exogenous AA-CoA seems to have minimal inhibitory effect on ACSL4 arachidonoyl-CoA synthetase activity, strategies based on

mimicking the product or blocking the putative alleviating mechanisms may prove ineffective.

Alternatively, we could consider the hypothesis in which PUFAs are selectively processed in the presence of AA-CoA due to their structural flexibility, enabling them to slip into a partially obstructed catalytic cavity. According to this hypothesis, AA-CoA blocks the entry of lower-priority FAs and possibly that of inhibitors as well, thereby preventing their action. In this context, developing 'contortionist' inhibitors that mimic the bis-allylic features of PUFAs to access the partially blocked cavity may prove valuable. To support this idea, Triacsin C, which resembles a FA and contains a bis-allylic carbon, is the most effective inhibitor in the presence of arachidonate. However, up to now, we have rather observed that rigidifying the scaffolds tends to enhance inhibitory activity, but this may be due to the fact that evaluations during the drug optimization process were conducted using palmitate (16:0). Reevaluating the SAR of key analogues in the presence of arachidonate (20:4ω-6) would be valuable and necessary to ensure the relevance of this strategy.

A more classical approach to improving inhibition in the presence of arachidonate would be to identify key residues specifically involved in arachidonate binding and to design inhibitors that target or extend toward those residues. For such studies, docking of representative FAs and inhibitors, followed by molecular dynamics simulations using the refined AlphaFold 2 model of ACSL4 that we developed (33), may yield valuable insights.

Moreover, the recently updated AlphaFold 3 further enhances prediction capabilities for protein-ligand complexes, as it was shown to outperform state-of-the-art docking tools (309). This version also enables the assessment of how post-translational modifications (PTMs) influence the predicted protein structure, which could be especially relevant for ACSL4, considering the numerous PTMs reported (69,76,82–87). However, one limitation of AI-based prediction methods for proteins with multiple distinct conformations is that they tend to generate "in-between" models by averaging across resolved structures in different conformational states. To address this limitation, the set of structures used to generate models for each distinct state should be carefully curated. For example, only apo structures could be selected for one state and ATP-bound structures for another. Finally, the generated model should also reflect the correct oligomeric state, which can be achieved using different tools, such as AlphaFold-Multimer (310).

It is noteworthy that such deep-learning-predicted structures are only as good as the quality and similarity of the available data. In this case, the closest homologous structure available, *tt*LC-FACS, differs substantially from ACSL4, sharing only 20% sequence identity. Because of this, the newly optimized model would need to be validated using experimental data, for example from mutagenesis studies.

In any case, resolving the ACSL4 structure through X-ray crystallography or cryo-EM remains a primary objective. Capturing the distinct conformational states of ACSL4 by determining structures of the enzyme complexed with

arachidonate, intermediates, and product derivatives would be instrumental in fully elucidating the catalytic mechanism. Furthermore, resolving structures of ACSL4 bound to inhibitors would provide a precise definition of the binding sites and facilitate rational drug design. To achieve this goal, two different approaches are currently being pursued in parallel by the team and collaborators from the Centre de Biologie Structurale (CBS). Following the optimization of negative-stain electron microscopy conditions to obtain a well-populated, monodispersed sample, cryo-EM experiments have now been initiated. The other strategy aims to crystallize a chimeric protein comprising the catalytic domain of ACSL4 embedded within the scaffold of the *tt*LC-FACS structure, to maximize the likelihood of obtaining crystals.

Most of the proposed perspectives above aim to outcompete the specific substrate of an enzyme that, as we have observed, is highly specialized in its metabolism. Moreover, as mentioned before, a notable weakness of compounds binding in the FA pocket is the highly hydrophobic nature of the cavity, which tends to favor the development of highly lipophilic inhibitors. For these reasons, it might be wiser to move away from FA competition. Since FAs require ATP to bind, one strategy to identify FA-independent inhibitors would be to screen for compounds that can bind in the absence of ATP. Because no hits were identified under these conditions in our initial screenings, such compounds appear to be rare, and exploring larger chemical libraries will likely be necessary to discover them. An alternative strategy would be to screen compounds directly in an activity assay conducted with

arachidonate as the substrate. Thus, the journey may continue as it began, with new screenings paving the way forward.

REFERENCES

1. Nelson DL, Cox MM, Hoskins AA. Lipids. In: Lehninger Principles of biochemistry. 8th ed. New-York: Macmillan Learning; 2021. p. 1283–365.

2. Tvrzicka E, Kremmyda LS, Stankova B, Zak A. Fatty acids as biocompounds: Their role in human metabolism, health and disease - a review. part 1: Classification, dietary sources and biological functions. Biomed Pap. 2011;155(2):117–30.

3. Bond LM, Makoto M, O'Neill LM, Ding F, Ntambi JM. Fatty Acid Desaturation and Elongation in Mammals. In: Ridgway ND, McLeod RS, editors. Biochemistry of Lipids, Lipoproteins and Membranes. 6th ed. Amsterdam: Elsevier B.V.; 2016. p. 185–208.

4. Vannice G, Rasmussen H. Position of the academy of nutrition and dietetics: Dietary fatty acids for healthy adults. J Acad Nutr Diet. 2014;114(1):136–53.

5. Kihara A. Very long-chain fatty acids: Elongation, physiology and related disorders. J Biochem. 2012;152(5):387–95.

6. Rustan AC, Drevon CA. Fatty Acids: Structures and Properties. Encycl Life Sci. 2005;1(2):1–7.

7. Legrand P, Rioux V. The complex and important cellular and metabolic functions of saturated fatty acids. Lipids. 2010;45(10):941–6.

8. Fulco AJ, Mead JF. Metabolism of Essential Fatty Acids. J Biol Chem. 1959;234(6):1411–6.

9. Lehner R, Quiroga AD. Fatty Acid Handling in Mammalian Cells. In: Ridgway ND, McLeod RS, editors. Biochemistry of Lipids, Lipoproteins and Membranes. 6th ed. Amsterdam: Elsevier B.V; 2016. p. 149–84.

10. Antonny B, Vanni S, Shindou H, Ferreira T. From zero to six double bonds: Phospholipid unsaturation and organelle function. Trends Cell Biol. 2015;25(7):427–36.

11. Yin H, Xu L, Porter NA. Free radical lipid peroxidation: Mechanisms and analysis. Chem Rev. 2011;111(10):5944–72.

12. Harayama T, Shimizu T. Roles of polyunsaturated fatty acids, from mediators to membranes. J Lipid Res. 2020;61(8):1150–60.

13. Ham. Fast flip-flop of cholesterol and fatty acids in membranes: implications for membrane transport proteins. Curr Opin Lipidol. 2003;263–71.

14. Doege H, Stah A. Protein-mediated fatty acid uptake: Novel insights from in vivo models. Physiology. 2006;21(4):259–68.

15. Knudsen J, Neergaard TBF, Gaigg B, Jensen MV, Hansen JK. Role of acyl-CoA binding protein in acyl-CoA metabolism and acyl-CoA-mediated cell signaling. J Nutr. 2000;130(2 SUPPL.):294S-298S.

16. Paiva P, Medina FE, Viegas M, Ferreira P, Neves RPP, Sousa JPM, et al. Animal Fatty Acid Synthase: A Chemical Nanofactory. Chem Rev. 2021;121(15):9502–53.

17. Cerone M, Smith TK. Desaturases: Structural and mechanistic insights into the biosynthesis of unsaturated fatty acids. IUBMB Life. 2022;74(11):1036–51.

18. Su HM, Moser AB, Moser HW, Watkins PA. Peroxisomal Straight-chain Acyl-CoA Oxidase and D-bifunctional Protein Are Essential for the Retroconversion Step in Docosahexaenoic Acid Synthesis. J Biol Chem. 2001;276(41):38115–20.

19. Houten SM, Violante S, Ventura F V., Wanders RJA. The Biochemistry and Physiology of Mitochondrial Fatty Acid β-Oxidation and Its Genetic Disorders. Annu Rev Physiol. 2016;78:23–44.

20. Schulz H, Kunau WH. Beta-oxidation of unsaturated fatty acids: a revised pathway. Trends Biochem Sci. 1987;12:403–6.

21. Yen CLE, Stone SJ, Koliwad S, Harris C, Farese R V. DGAT enzymes and triacylglycerol biosynthesis. J Lipid Res. 2008;49(11):2283–301.

22. Ridgway ND. Phospholipid Synthesis in Mammalian Cells. In: Ridgway ND, McLeod RS, editors. Biochemistry of Lipids, Lipoproteins and Membranes. 6th ed. Amsterdam: Elsevier B.V.; 2016. p. 209–36.

23. William Dowhan, Mikhail Bogdanov EM. Functional Roles of Lipids in Membranes. In: Ridgway ND, McLeod RS, editors. Biochemistry of Lipids, Lipoproteins and Membranes. 6th ed. Amsterdam: Elsevier B.V.; 2016. p. 1–40.

24. Coleman RA, Lee DP. Enzymes of triacylglycerol synthesis and their regulation. Prog Lipid Res. 2004;43(2):134–76.

25. Fagone P, Jackowski S. Membrane phospholipid synthesis and endoplasmic reticulum function. J Lipid Res. 2009;50(SUPPL.):S311–6.

26. Hishikawa D, Hashidate T, Shimizu T, Shindou H. Diversity and function of membrane glycerophospholipids generated by the remodeling pathway in mammalian cells. J Lipid Res. 2014;55(5):799–807.

27. Shimizu T. Lipid mediators in health and disease: Enzymes and receptors as therapeutic targets for the regulation of immunity and inflammation. Annu Rev Pharmacol Toxicol. 2009;49:123–50.

28. Smith WL, Murphy RC. The Eicosanoids: Cyclooxygenase, Lipoxygenase and Epoxygenase Pathways. In: Ridgway ND, McLeod RS, editors. Biochemistry of Lipids, Lipoproteins and Membranes. 6th ed. Amsterdam: Elsevier B.V.; 2016. p. 259–96.

29. Kang MJ, Fujino T, Sasano H, Minekura H, Yabuki N, Nagura H, et al. A novel arachidonate-preferring acyl-CoA synthetase is present in steroidogenic cells of the rat adrenal, ovary, and testis. Proc Natl Acad Sci U S A. 1997;94(7):2880–4.

30. Grevengoed TJ, Klett EL, Coleman RA. Acyl-CoA Metabolism and Partitioning. Anu Rev Nutr. 2014;34:1–30.

31. Schmelz S, Naismith JH. Adenylate-forming enzymes. Curr Opin Struct Biol. 2009;19(6):666–71.

32. Gulick AM. Conformational dynamics in the acyl-CoA synthetases, adenylation domains of non-ribosomal peptide synthetases, and firefly luciferase. ACS Chem Biol. 2009;4(10):811–27.

33. Mazhari Dorooee D, Ravez S, Vertommen D, Renault N, Papadopoulos N, Marteau R, et al. LIBX-A401: A Novel Selective Inhibitor of Acyl-CoA Synthetase Long Chain Family Member 4 (ACSL4) and Its Binding Mode. Angew Chemie - Int Ed. 2025;e202500518.

34. Soupene E, Kuypers FA. Mammalian long-chain acyl-CoA synthetases. Exp Biol Med. 2008;233(5):507–21.

35. Rose G, Brandes R, Shapiro B, Pong P, Centre R. Palmitoyl-Coenzyme A Synthetase. Biochem J. 1973;131:199–209.

36. Li H, Melton EM, Quackenbush S, DiRusso CC, Black PN. Mechanistic studies of the long chain acyl-CoA synthetase Faa1p from Saccharomyces cerevisiae. Biochim Biophys Acta - Mol Cell Biol Lipids. 2007;1771(9):1246–53.

37. Hisanaga Y, Ago H, Nakagawa N, Hamada K, Ida K, Yamamoto M, et al. Structural basis of the substrate-specific two-step catalysis of long chain fatty acyl-CoA synthetase dimer. J Biol Chem. 2004;279(30):31717–26.

38. Malhotra KT, Malhotra K, Lubin BH, Kuypers FA. Identification and molecular characterization of acyl-CoA synthetase in human erythrocytes and erythroid precursors. Biochem J. 1999;344(1):135–43.

39. Van Horn CG, Caviglia JM, Li LO, Wang S, Granger DA, Coleman RA. Characterization of recombinant long-chain rat Acyl-CoA synthetase isoforms 3 and 6: Identification of a novel variant of isoform 6. Biochemistry. 2005;44(5):1635–42.

40. Watkins PA, Maiguel D, Jia Z, Pevsner J. Evidence for 26 distinct acyl-coenzyme A synthetase genes in the human genome. J Lipid Res. 2007;48(12):2736–50.

41. Black PN, Zhang Q, Weimar JD, DiRusso CC. Mutational analysis of a fatty acyl-coenzyme a synthetase signature motif identifies seven amino acid residues that modulate fatty acid substrate specificity. J Biol Chem. 1997;272(8):4896–903.

42. Iijima H, Fujino T, Minekura H, Suzuki H, Kang MJ, Yamamoto T. Biochemical studies of two rat acyl-CoA synthetases, ACS1 and ACS2. Eur J Biochem. 1996;242(2):186–90.

43. Fujino T, Rang MJ, Suzuki H, Iijima H, Yamamoto T. Molecular characterization and expression of rat Acyl-CoA synthetase 3. J Biol Chem. 1996;271(28):16748–52.

44. Oikawa E, Iijima H, Suzuki T, Sasano H, Kamataki A, Nagura H, et al. A novel acyl-CoA synthetase, ACS5, expressed in intestinal epithelial cells and proliferating preadipocytes. J Biochem. 1998;124(3):679–85.

45. Fujino T, Yamamoto T. Cloning and functional expression of a novel long-chain acyl-CoA synthetase expressed in brain. J Biochem. 1992;111(2):197–203.

46. Klett EL, Chen S, Yechoor A, Lih FB, Coleman RA. Long-chain acyl-CoA synthetase isoforms differ in preferences for eicosanoid species and long-chain fatty acids. J Lipid Res. 2017;58(5):884–94.

47. Coleman R a, Lewin TM, Horn CG Van, Gonzalez-baro MR. Do Long-Chain Acyl-CoA Synthetases Regulate Fatty Acid Entry into Synthetic Versus Degradative Pathways? Recent Adv Nutr Sci. 2002;132(8):2123–6.

48. Igal RA, Wang P, Coleman RA. Triacsin C blocks de novo synthesis of glycerolipids and cholesterol esters but not recycling of fatty acid into phospholipid: Evidence for functionally separate pools of acyl-CoA. Biochem J. 1997;324(2):529–34.

49. Lewin TM, Kim JH, Granger DA, Vance JE, Coleman RA. Acyl-CoA synthetase isoforms 1, 4, and 5 are present in different subcellular membranes in rat liver and can be inhibited independently. J Biol Chem. 2001;276(27):24674–9.

50. Li LO, Mashek DG, An J, Doughman SD, Newgard CB, Coleman RA. Overexpression of rat long chain acyl-CoA synthetase 1 alters fatty acid metabolism in rat primary hepatocytes. J Biol Chem. 2006;281(48):37246–55.

51. Lobo S, Wiczer BM, Bernlohr DA. Functional analysis of long-chain Acyl-CoA synthetase 1 in 3T3-L1 adipocytes. J Biol Chem. 2009;284(27):18347–56.

52. Ellis JM, Li LO, Wu PC, Koves TR, Ilkayeva O, Stevens RD, et al. Adipose Acyl-CoA synthetase-1 directs fatty acids toward β-oxidation and is required for cold thermogenesis. Cell Metab. 2010;12(1):53–64.

53. Bu SY, Mashek DG. Hepatic long-chain acyl-CoA synthetase 5 mediates fatty acid channeling between anabolic and catabolic pathways. J Lipid Res. 2010;51(11):3270–80.

54. Melton EM, Cerny RL, Watkins PA, DiRusso CC, Black PN. Human fatty acid transport protein 2a/very long chain Acyl-CoA synthetase 1 (FATP2a/Acsvl1) has a preference in mediating the channeling of exogenous n-3 fatty acids into phosphatidylinositol. J Biol Chem. 2011;286(35):30670–9.

55. Xu X, Gopalacharyulu P, Seppänen-Laakso T, Ruskeepää AL, Aye CC, Carson BP, et al. Insulin signaling regulates fatty acid catabolism at the level of CoA activation. PLoS Genet. 2012;8(1):e1002478.

56. Küch EM, Vellaramkalayil R, Zhang I, Lehnen D, Brügger B, Stremmel W, et al. Differentially localized acyl-CoA synthetase 4 isoenzymes mediate the metabolic channeling of fatty acids towards phosphatidylinositol. Biochim Biophys Acta - Mol Cell Biol Lipids. 2014;1841(2):227–39.

57. Kagan VE, Mao G, Qu F, Angeli JPF, Doll S, Croix CS, et al. Oxidized arachidonic and adrenic PEs navigate cells to ferroptosis. Nat Chem Biol. 2017;13(1):81–90.

58. Kuwata H, Nakatani E, Shimbara-Matsubayashi S, Ishikawa F, Shibanuma M, Sasaki Y, et al. Long-chain acyl-CoA synthetase 4 participates in the formation of highly unsaturated fatty acid-containing phospholipids in murine macrophages. Biochim Biophys Acta - Mol Cell Biol Lipids. 2019;1864(11):1606–18.

59. Killion EA, Reeves AR, El Azzouny MA, Yan QW, Surujon D, Griffin JD, et al. A role for long-chain acyl-CoA synthetase-4 (ACSL4) in diet-induced phospholipid remodeling and obesity-associated adipocyte dysfunction. Mol Metab. 2018;9:43–56.

60. Cao Y, Traer E, Zimmerman GA, McIntyre TM, Prescott SM. Cloning, expression, and chromosomal localization of human long-chain fatty acid-CoA ligase 4 (FACL4). Genomics. 1998;49(2):327–30.

61. Piccini M, Vitelli F, Bruttini M, Pober BR, Jonsson JJ, Villanova M, et al. FACL4, a new gene encoding long-chain acyl-CoA synthetase 4, is deleted in a family with Alport syndrome, elliptocytosis, and mental retardation. Genomics. 1998;47(3):350–8.

62. Lewin TM, Van Horn CG, Krisans SK, Coleman RA. Rat liver acyl-CoA synthetase 4 is a peripheral-membrane protein located in two distinct subcellular organelles, peroxisomes, and mitochondrial-associated membrane. Arch Biochem Biophys. 2002;404(2):263–70.

63. Meloni I, Parri V, De Filippis R, Ariani F, Artuso R, Bruttini M, et al. The XLMR gene ACSL4 plays a role in dendritic spine architecture. Neuroscience. 2009;159(2):657–69.

64. Ndiaye H, Liu JY, Hall A, Minogue S, Morgan MY, Waugh MG. Immunohistochemical staining reveals differential expression of ACSL3 and ACSL4 in hepatocellular carcinoma and hepatic gastrointestinal metastases. Biosci Rep. 2020;40(4):BSR20200219.

65. Radif Y, Ndiaye H, Kalantzi V, Jacobs R, Hall A, Minogue S, et al. The endogenous subcellular localisations of the long chain fatty acid-activating enzymes ACSL3 and ACSL4 in sarcoma and breast cancer cells. Mol Cell Biochem. 2018;448(1–2):275–86.

66. von Krusenstiern AN, Robson RN, Qian N, Qiu B, Hu F, Reznik E, et al. Identification of essential sites of lipid peroxidation in ferroptosis. Nat Chem Biol. 2023;19(6):719–30.

67. Fujimoto Y, Itabe H, Sakai J, Makita M, Noda J, Mori M, et al. Identification of major proteins in the lipid droplet-enriched fraction isolated from the human hepatocyte cell line HuH7. Biochim Biophys Acta - Mol Cell Res. 2004;1644(1):47–59.

68. Tuohetahuntila M, Spee B, Kruitwagen HS, Wubbolts R, Brouwers JF, Van De Lest CH, et al. Role of long-chain acyl-CoA synthetase 4 in formation of polyunsaturated lipid species in hepatic stellate cells. Biochim Biophys Acta - Mol Cell Biol Lipids. 2015;1851(2):220–30.

69. Smith ME, Saraceno GE, Capani F, Castilla R. Long-chain acyl-CoA synthetase 4 is regulated by phosphorylation. Biochem Biophys Res Commun. 2013;430(1):272–7.

70. Kristi L. Stringer, Bulent Turan, Lisa McCormick, Modupeoluwa Durojaiye, Laura Nyblade, Mirjam-Colette Kempf, Bronwen Lichtenstein and JMT. Characterization of Acyl-CoA Synthetase Isoforms In Pancreatic Beta Cells: Gene Silencing Shows Participation of ACSL3 and ACSL4 In Insulin Secretion. Physiol Behav. 2017;618:32–43.

71. Shimshoni JA, Basselin M, Li LO, Coleman RA, Stanley I, Modi HR. Valproate uncompetitively inhibits arachidonic acid acylation by rat acyl-CoA synthetase 4: Relevance to valproate's efficacy against bipolar disorder. Biochim Biophys Acta. 2011;1811(3):163–9.

72. Shimbara-Matsubayashi S, Kuwata H, Tanaka N, Kato M, Hara S. Analysis on the substrate specificity of recombinant human Acyl-CoA synthetase ACSL4 variants. Biol Pharm Bull. 2019;42(5):850–5.

73. Li Y, Feng D, Wang Z, Zhao Y, Sun R, Tian D, et al. Ischemia-induced ACSL4 activation contributes to ferroptosis-mediated tissue injury in intestinal ischemia/reperfusion. Cell Death Differ. 2019;26(11):2284–99.

74. Wu J, Minikes AM, Gao M, Bian H, Li Y, Stockwell BR, et al. Intercellular interaction dictates cancer cell ferroptosis via NF2–YAP signalling. Nature. 2019;572(7769):402–6.

75. Kan CFK, Singh AB, Dong B, Shende VR, Liu J. PPARδ activation induces hepatic long-chain acyl-CoA synthetase 4 expression in vivo and in vitro. Biochim Biophys Acta - Mol Cell Biol Lipids. 2015;1851(5):577–87.

76. Kan CFK, Singh AB, Stafforini DM, Azhar S, Liu J. Arachidonic acid downregulates acyl-CoA synthetase 4 expression by promoting its ubiquitination and proteasomal degradation. J Lipid Res. 2014;55(8):1657–67.

77. Ma Y, Zhang X, Alsaidan OA, Yang X, Sulejmani E, Zha J, et al. Long-Chain Acyl-CoA synthetase 4–mediated fatty acid metabolism sustains androgen receptor pathway–independent prostate cancer. Mol Cancer Res. 2021;19(1):124–35.

78. Maciel FC, Maloberti P, Neuman I, Cano F, Castilla R, Castillo F, et al. An arachidonic acid-preferring acyl-CoA synthetase is a hormone-dependent and obligatory protein in the signal transduction pathway of steroidogenic hormones. J Mol Endocrinol. 2005;34(3):655–66.

79. Mele PG, Duarte A, Paz C, Capponi A, Podestá EJ. Role of intramitochondrial arachidonic acid and acyl-CoA synthetase 4 in angiotensin II-regulated aldosterone synthesis in NCI-H295R adrenocortical cell line. Endocrinology. 2012;153(7):3284–94.

80. Ding K, Liu C, Li L, Yang M, Jiang N, Luo S, et al. Acyl-CoA synthase ACSL4: An essential target in ferroptosis and fatty acid metabolism. Chin Med J (Engl). 2023;136(21):2521–37.

81. Sen P, Kan CFK, Singh AB, Rius M, Kraemer FB, Sztul E, et al. Identification of p115 as a novel ACSL4 interacting protein and its role in regulating ACSL4 degradation. J Proteomics. 2020;229:103926.

82. Feng S, Rao Z, Zhang J, She X, Chen Y, Wan K, et al. Inhibition of CARM1-Mediated Methylation of ACSL4 Promotes Ferroptosis in Colorectal Cancer. Adv Sci. 2023;10(36):e2303484.

83. Xie G, Li N, Li K, Xu Y, Zhang Y, Cao S, et al. Phosphatase LHPP confers prostate cancer ferroptosis activation by modulating the AKT-SKP2-ACSL4 pathway. Cell Death Dis. 2024;15(9):665.

84. Bai YT, Xiao FJ, Wang H, Ge RL, Wang LS. Hypoxia protects H9c2 cells against ferroptosis through senp1-mediated protein desumoylation. Int J Med Sci. 2021;18(7):1618–27.

85. Wang J, Wang Z, Yuan J, Wang J, Shen X. The positive feedback between ACSL4 expression and O-GlcNAcylation contributes to the growth and survival of hepatocellular carcinoma. Aging (Albany NY). 2020;12(9):7786–800.

86. Zhang H-L, Hu B-X, Li Z-L, Du T, Shan J-L, Ye Z-P, et al. PKCβII phosphorylates ACSL4 to amplify lipid peroxidation to induce ferroptosis. Nat Cell Biol. 2022;24(1):88–98.

87. Li Z, Xu ZM, Chen WP, Du XJ, Ou CX, Luo ZK, et al. Tumor-repopulating cells evade ferroptosis via PCK2-dependent phospholipid remodeling. Nat Chem Biol. 2024;20(10):1341–52.

88. Andersson CS, Lundgren CAK, Magnúsdóttir A, Ge C, Wieslander Å, Molina DM, et al. The Mycobacterium tuberculosis very-long-chain fatty acyl-CoA synthetase: Structural basis for housing lipid substrates longer than the enzyme. Structure. 2012;20(6):1062–70.

89. Kochan G, Pilka ES, von Delft F, Oppermann U, Yue WW. Structural Snapshots for the Conformation-dependent Catalysis by Human Medium-chain Acyl-coenzyme A Synthetase ACSM2A. J Mol Biol. 2009;388(5):997–1008.

90. Dykstra H, Fisk C, LaRose C, Waldhart A, Meng X, Zhao G, et al. Mouse long-chain acyl-CoA synthetase 1 is active as a monomer. Arch Biochem Biophys. 2021;700:108773.

91. Jumper J, Evans R, Pritzel A, Green T, Figurnov M, Ronneberger O, et al. Highly accurate protein structure prediction with AlphaFold. Nature. 2021;596(7873):583–9.

92. Castillo AF, Orlando UD, Maloberti PM, Prada JG, Dattilo MA, Solano AR, et al. New inhibitor targeting Acyl-CoA synthetase 4 reduces breast and prostate tumor growth, therapeutic resistance and steroidogenesis. Cell Mol Life Sci. 2020;78(6):2893–910.

93. Huang Q, Ru Y, Luo Y, Luo X, Liu D, Ma Y, et al. Identification of a targeted ACSL4 inhibitor to treat ferroptosis-related diseases. Sci Adv. 2024;10(13):eadk1200.

94. Mashek DG, McKenzie MA, Van Horn CG, Coleman RA. Rat long chain acyl-CoA synthetase 5 increases fatty acid uptake and partitioning to cellular triacylglycerol in McArdle-RH7777 cells. J Biol Chem. 2006;281(2):945–50.

95. Milger K, Herrmann T, Becker C, Gotthardt D, Zickwolf J, Ehehalt R, et al. Cellular uptake of fatty acids driven by the ER-localized acyl-CoA synthetase FATP4. J Cell Sci. 2006;119(22):4678–88.

96. Poppelreuther M, Rudolph B, Du C, Großmann R, Becker M, Thiele C, et al. The N-terminal region of acyl-CoA synthetase 3 is essential for both the localization on lipid droplets and the function in fatty acid uptake. J Lipid Res. 2012;53(5):888–900.

97. Mashek DG, Coleman RA. Cellular fatty acid uptake: The contribution of metabolism. Curr Opin Lipidol. 2006;17(3):274–8.

98. Reeves AR, Sansbury BE, Pan M, Han X, Spite M, Greenberg AS. Myeloid-Specific Deficiency of Long-Chain Acyl CoA Synthetase 4 Reduces Inflammation by Remodeling Phospholipids and Reducing Production of Arachidonic Acid–Derived Proinflammatory Lipid Mediators. J Immunol. 2021;207(11):2744–53.

99. Kuwata H, Yoshimura M, Sasaki Y, Yoda E, Nakatani Y. Role of long-chain acyl-coenzyme A synthetases in the regulation of arachidonic acid metabolism in interleukin 1β-stimulated rat fibroblasts. BBA - Mol Cell Biol Lipids. 2014;1841(1):44–53.

100. Golej DL, Askari B, Kramer F, Barnhart S, Vivekanandan-Giri A, Pennathur S, et al. Long-chain acyl-CoA synthetase 4 modulates prostaglandin E2 release from human arterial smooth muscle cells. J Lipid Res. 2011;52(4):782–93.

101. Doll S, Proneth B, Tyurina YY, Panzilius E, Kobayashi S, Ingold I, et al. ACSL4 dictates ferroptosis sensitivity by shaping cellular lipid composition. Nat Chem Biol. 2017;13(1):91–8.

102. Irvine RF. How is the level of free arachidonic acid controlled in mammalian cells? Biochem J. 1982;204(1):3–16.

103. Kuwata H, Hara S. Inhibition of long-chain acyl-CoA synthetase 4 facilitates production of 5,11-dihydroxyeicosatetraenoic acid via the cyclooxygenase-2 pathway. Biochem Biophys Res Commun. 2015;465(3):528–33.

104. Kuwata H, Nakatani E, Tomitsuka Y, Ochiai T, Sasaki Y, Yoda E, et al. Deficiency of long-chain acyl-CoA synthetase 4 leads to lipopolysaccharide-induced mortality in a mouse model of septic shock. FASEB J. 2023;37(12):e23330.

105. Maloberti P, Maciel FC, Castillo AF, Castilla R, Duarte A, Toledo MF, et al. Enzymes involved in arachidonic acid release in adrenal and Leydig cells. Mol Cell Endocrinol. 2007;265–266:113–20.

106. Privalle CT, Crivello JF, Jefcoate CR. Regulation of intramitochondrial cholesterol transfer to side-chain cleavage cytochrome P-450 in rat adrenal gland. Proc Natl Acad Sci U S A. 1983;80(3):702–6.

107. Clark BJ, Wells J, King SR, Stocco DM. The purification, cloning, and expression of a novel luteinizing hormone-induced mitochondrial protein in MA-10 mouse leydig tumor cells: Characterization of the steroidogenic acute regulatory protein (star). J Biol Chem. 1994;269(45):28314–22.

108. Maloberti P, Lozano RC, Mele PG, Cano F, Colonna C, Mendez CF, et al. Concerted regulation of free arachidonic acid and hormone-induced steroid synthesis by acyl-CoA thioesterases and acyl-CoA synthetases in adrenal cells. Eur J Biochem. 2002;269(22):5599–607.

109. Fernanda Castillo A, Cornejo Maciel F, Castilla R, Duarte A, Maloberti P, Paz C, et al. cAMP increases mitochondrial cholesterol transport through the induction of arachidonic acid release inside this organelle in Leydig cells. FEBS J. 2006;273(22):5011–21.

110. Wang XJ, Dyson MT, Jo Y, Eubank DW, Stocco DM. Involvement of 5-lipoxygenase metabolites of arachidonic acid in cyclic AMP-stimulated steroidogenesis and steroidogenic acute regulatory protein gene expression. J Steroid Biochem Mol Biol. 2003;85(2–5):159–66.

111. Wang XJ, Walsh LP, Reinhart AJ, Stocco DM. The role of arachidonic acid in steroidogenesis and steroidogenic acute regulatory (StAR) gene and protein expression. J Biol Chem. 2000;275(26):20204–9.

112. Wang X, Shen CL, Dyson MT, Yin X, Schiffer RB, Grammas P, et al. The involvement of epoxygenase metabolites of arachidonic acid in cAMP-stimulated steroidogenesis and steroidogenic acute regulatory protein gene expression. J Endocrinol. 2006;190(3):871–8.

113. Squire LR. Cholesterol Ester Droplets and Steroidogenesis. Mol Cell Endocrinol. 2013;371(1–2):15–9.

114. Wang W, Hao X, Han L, Yan Z, Shen WJ, Dong D, et al. Tissue-Specific Ablation of ACSL4 Results in Disturbed Steroidogenesis. Endocrinology. 2019;160(11):2517–28.

115. Cho YY, Kang MJ, Sone H, Suzuki T, Abe M, Igarashi M, et al. Abnormal uterus with polycysts, accumulation of uterine prostaglandins, and reduced fertility in mice heterozygous for Acyl-CoA synthetase 4 deficiency. Biochem Biophys Res Commun. 2001;284(4):993–7.

116. Klett EL, Chen S, Edin ML, Li LO, Ilkayeva O, Zeldin DC, et al. Diminished Acyl-CoA synthetase isoform 4 activity in INS 832/13 cells reduces cellular epoxyeicosatrienoic acid levels and results in impaired glucose-stimulated insulin secretion. J Biol Chem. 2013;288(30):21618–29.

117. Meloni I, Muscettola M, Raynaud M, Longo I, Bruttini M, Moizard MP, et al. FACL4, encoding fatty acid-CoA ligase 4, is mutated in nonspecific X-linked mental retardation. Nat Genet. 2002;30(4):436–40.

118. Zhang Y, Chen D, Wang Z. Analyses of mental dysfunction-related ACSl4 in Drosophila reveal its requirement for Dpp/BMP production and visual wiring in the brain. Hum Mol Genet. 2009;18(20):3894–905.

119. Liu Z, Huang Y, Zhang Y, Chen D, Zhang YQ. Drosophila Acyl-CoA synthetase long-chain family member 4 regulates axonal transport of synaptic vesicles and is required for synaptic development and transmission. J Neurosci. 2011;31(6):2052–63.

120. Cho YY. A novel role of brain-type ACS4 isotype in neuronal differentiation. Biochem Biophys Res Commun. 2012;419(3):505–10.

121. Li W, Shan BQ, Zhao HY, He H, Tian ML, Cheng X, et al. MiR-130a-3p regulates neural stem cell differentiation in vitro by targeting Acsl4. J Cell Mol Med. 2022;26(9):2717–27.

122. Dixon SJ, Lemberg KM, Lamprecht MR, Skouta R, Zaitsev EM, Gleason CE, et al. Ferroptosis: An iron-dependent form of nonapoptotic cell death. Cell. 2012;149(5):1060–72.

123. Stockwell BR. Ferroptosis turns 10: Emerging mechanisms, physiological functions, and therapeutic applications. Cell. 2022;185(14):2401–21.

124. Jiang X, Stockwell BR, Conrad M. Ferroptosis: mechanisms, biology and role in disease. Nat Rev Mol Cell Biol. 2021;22(4):266–82.

125. Yang WS, Kim KJ, Gaschler MM, Patel M, Shchepinov MS, Stockwell BR. Peroxidation of polyunsaturated fatty acids by lipoxygenases drives ferroptosis. Proc Natl Acad Sci U S A. 2016;113(34):E4966–75.

126. Zou Y, Li H, Graham ET, Deik AA, Eaton JK, Wang W, et al. Cytochrome P450 oxidoreductase contributes to phospholipid peroxidation in ferroptosis. Nat Chem Biol. 2020;16(3):302–9.

127. Abrams RP, Carroll WL, Woerpel KA. Five-Membered Ring Peroxide Selectively Initiates Ferroptosis in Cancer Cells. ACS Chem Biol. 2016;11(5):1305–12.

128. Seiler A, Schneider M, Förster H, Roth S, Wirth EK, Culmsee C, et al. Glutathione Peroxidase 4 Senses and Translates Oxidative Stress into 12/15-Lipoxygenase Dependent- and AIF-Mediated Cell Death. Cell Metab. 2008;8(3):237–48.

129. Friedmann Angeli JP, Schneider M, Proneth B, Tyurina YY, Tyurin VA, Hammond VJ, et al. Inactivation of the ferroptosis regulator Gpx4 triggers acute renal failure in mice. Nat Cell Biol. 2014;16(12):1180–91.

130. Zilka O, Shah R, Li B, Friedmann Angeli JP, Griesser M, Conrad M, et al. On the Mechanism of Cytoprotection by Ferrostatin-1 and Liproxstatin-1 and the Role of Lipid Peroxidation in Ferroptotic Cell Death. ACS Cent Sci. 2017;3(3):232–43.

131. Gao M, Monian P, Quadri N, Ramasamy R, Jiang X. Glutaminolysis and Transferrin Regulate Ferroptosis. Mol Cell. 2015;59(2):298–308.

132. Hou W, Xie Y, Song X, Sun X, Lotze MT, Zeh HJ, et al. Autophagy promotes ferroptosis by degradation of ferritin. Autophagy. 2016;12(8):1425–8.

133. Tuo QZ, Lei P, Jackman KA, Li XL, Xiong H, Li XL, et al. Tau-mediated iron export prevents ferroptotic damage after ischemic stroke. Mol Psychiatry. 2017;22(11):1520–30.

134. Brown CW, Amante JJ, Chhoy P, Elaimy AL, Liu H, Zhu LJ, et al. Prominin2 Drives Ferroptosis Resistance by Stimulating Iron Export. Dev Cell. 2019;51(5):575–86.

135. Chemistry B, Marzolo V. The selenoenzyme phospholipid hydroperoxide glutathione peroxidase. Biochem Biophys Acta. 1985;839(1):62–70.

136. Yang WS, Sriramaratnam R, Welsch ME, Shimada K, Skouta R, Viswanathan VS, et al. Regulation of ferroptotic cancer cell death by GPX4. Cell. 2014;156(1–2):317–31.

137. Dixon SJ, Patel D, Welsch M, Skouta R, Lee E, Hayano M, et al. Pharmacological inhibition of cystine-glutamate exchange induces endoplasmic reticulum stress and ferroptosis. Elife. 2014;2014(3):e02523.

138. Bersuker K, Hendricks JM, Li Z, Magtanong L, Ford B, Tang PH, et al. The CoQ oxidoreductase FSP1 acts parallel to GPX4 to inhibit ferroptosis. Nature. 2019;575(7784):688–92.

139. Doll S, Freitas FP, Shah R, Aldrovandi M, da Silva MC, Ingold I, et al. FSP1 is a glutathione-independent ferroptosis suppressor. Nature. 2019;575(7784):693–8.

140. Dixon SJ, Winter GE, Musavi LS, Lee ED, Snijder B, Rebsamen M, et al. Human Haploid Cell Genetics Reveals Roles for Lipid Metabolism Genes in Nonapoptotic Cell Death. ACS Chem Biol. 2015;10(7):1604–9.

141. Yuan H, Li X, Zhang X, Kang R, Tang D. Identification of ACSL4 as a biomarker and contributor of ferroptosis. Biochem Biophys Res Commun. 2016;478(3):1338–43.

142. Shindou H, Shimizu T. Acyl-CoA:lysophospholipid acyltransferases. J Biol Chem. 2009;284(1):1–5.

143. Magtanong L, Ko PJ, To M, Cao JY, Forcina GC, Tarangelo A, et al. Exogenous Monounsaturated Fatty Acids Promote a Ferroptosis-Resistant Cell State. Cell Chem Biol. 2019;26(3):420–32.

144. Tesfay L, Paul BT, Konstorum A, Deng Z, Cox AO, Lee J, et al. Stearoyl-CoA desaturase 1 protects ovarian cancer cells from ferroptotic cell death. Cancer Res. 2019;79(20):5355–66.

145. Jiang L, Kon N, Li T, Wang SJ, Su T, Hibshoosh H, et al. Ferroptosis as a p53-mediated activity during tumour suppression. Nature. 2015;520(7545):57–62.

146. Wang SJ, Li D, Ou Y, Jiang L, Chen Y, Zhao Y, et al. Acetylation Is Crucial for p53-Mediated Ferroptosis and Tumor Suppression. Cell Rep. 2016;17(2):366–73.

147. Wang W, Green M, Choi JE, Gijón M, Kennedy PD, Johnson JK, et al. CD8+ T cells regulate tumour ferroptosis during cancer immunotherapy. Nature. 2019;569(7755):270–4.

148. Liao P, Wang W, Wang W, Kryczek I, Li X, Bian Y, et al. CD8+ T cells and fatty acids orchestrate tumor ferroptosis and immunity via ACSL4. Cancer Cell. 2022;40(4):365-378.

149. Co HKC, Wu CC, Lee YC, Chen SH. Emergence of large-scale cell death through ferroptotic trigger waves. Nature. 2024;631(8021):654–62.

150. Dolma S, Lessnick SL, Hahn WC, Stockwell BR. Identification of genotype-selective antitumor agents using synthetic lethal chemical screening in engineered human tumor cells. Cancer Cell. 2003;3(3):285–96.

151. Yang WS, Stockwell BR. Synthetic Lethal Screening Identifies Compounds Activating Iron-Dependent, Nonapoptotic Cell Death in Oncogenic-RAS-Harboring Cancer Cells. Chem Biol. 2008;15(3):234–45.

152. Zhou Q, Meng Y, Li D, Yao L, Le J, Liu Y, et al. Ferroptosis in cancer: From molecular mechanisms to therapeutic strategies. Signal Transduct Target Ther. 2024;9(1):55.

153. Lei G, Zhang Y, Koppula P, Liu X, Zhang J, Lin SH, et al. The role of ferroptosis in ionizing radiation-induced cell death and tumor suppression. Cell Res. 2020;30(2):146–62.

154. Viswanathan VS, Ryan MJ, Dhruv HD, Gill S, Eichhoff OM, Seashore-Ludlow B, et al. Dependency of a therapy-resistant state of cancer cells on a lipid peroxidase pathway. Nature. 2017;547(7664):453–7.

155. Tsoi J, Robert L, Paraiso K, Galvan C, Sheu KM, Lay J, et al. Multi-stage Differentiation Defines Melanoma Subtypes with Differential Vulnerability to Drug-Induced Iron-Dependent Oxidative Stress. Cancer Cell. 2018;33(5):890–904.

156. Hangauer MJ, Viswanathan VS, Ryan MJ, Bole D, Eaton JK, Matov A, et al. Drug-tolerant persister cancer cells are vulnerable to GPX4 inhibition. Nature. 2017;551(7679):247–50.

157. Eltzschig HK, Eckle T. Ischemia and reperfusion-from mechanism to translation. Nat Med. 2011;17(11):1391–401.

158. Chu LK, Cao X, Wan L, Diao Q, Zhu Y, Kan Y, et al. Autophagy of OTUD5 destabilizes GPX4 to confer ferroptosis-dependent kidney injury. Nat Commun. 2023;14(1):8393.

159. Tang LJ, Luo XJ, Tu H, Chen H, Xiong XM, Li NS, et al. Ferroptosis occurs in phase of reperfusion but not ischemia in rat heart following ischemia or ischemia/reperfusion. Naunyn Schmiedebergs Arch Pharmacol. 2021;394(2):401–10.

160. Xu Y, Li X, Cheng Y, Yang M, Wang R. Inhibition of ACSL4 attenuates ferroptotic damage after pulmonary ischemia-reperfusion. FASEB J. 2020;34(12):16262–75.

161. Ma XH, Liu JHZ, Liu CY, Sun WY, Duan WJ, Wang G, et al. ALOX15-launched PUFA-phospholipids peroxidation increases the susceptibility of ferroptosis in ischemia-induced myocardial damage. Signal Transduct Target Ther. 2022;7(1):288.

162. Cai W, Liu L, Shi X, Liu Y, Wang J, Fang X, et al. Alox15/15-HpETE Aggravates Myocardial Ischemia-Reperfusion Injury by Promoting Cardiomyocyte Ferroptosis. Circulation. 2023;147(19):1444–60.

163. Fang X, Wang H, Han D, Xie E, Yang X, Wei J, et al. Ferroptosis as a target for protection against cardiomyopathy. Proc Natl Acad Sci U S A. 2019;116(7):2672–80.

164. Linkermann A, Skouta R, Himmerkus N, Mulay SR, Dewitz C, De Zen F, et al. Synchronized renal tubular cell death involves ferroptosis. Proc Natl Acad Sci U S A. 2014;111(47):16836–41.

165. Tuo Q zhang, Liu Y, Xiang Z, Yan HF, Zou T, Shu Y, et al. Thrombin induces ACSL4-dependent ferroptosis during cerebral ischemia/reperfusion. Signal Transduct Target Ther. 2022;7(1):59.

166. Jin Z, Li J, Dong W, Fei G, Xiucheng Y, Bingqing Y, et al. Liproxstatin-1 Alleviates Lung Transplantation-induced Cold Ischemia–Reperfusion Injury by Inhibiting Ferroptosis. Transplantation. 2023;107(10):2190–202.

167. Kojima H, Hirao H, Kadono K, Ito T, Yao S, Torgerson T, et al. Cold stress–induced ferroptosis in liver sinusoidal endothelial cells determines liver transplant injury and outcomes. JCI Insight. 2024;9(3):e174354.

168. Li W, Feng G, Gauthier JM, Lokshina I, Higashikubo R, Evans S, et al. Ferroptotic cell death and TLR4/Trif signaling initiate neutrophil recruitment after heart transplantation. J Clin Invest. 2019;129(6):2293–304.

169. Ward RJ, Zucca FA, Duyn JH, Crichton RR, Zecca L. The role of iron in brain ageing and neurodegenerative disorders. Lancet Neurol. 2014;13(10):1045–60.

170. Hambright WS, Fonseca RS, Chen L, Na R, Ran Q. Ablation of ferroptosis regulator glutathione peroxidase 4 in forebrain neurons promotes cognitive impairment and neurodegeneration. Redox Biol. 2017;12:8–17.

171. Chen L, Dar NJ, Na R, McLane KD, Yoo K, Han X, et al. Enhanced defense against ferroptosis ameliorates cognitive impairment and reduces neurodegeneration in 5xFAD mice. Free Radic Biol Med. 2022;180:1–12.

172. Majerníková N, Marmolejo-Garza A, Salinas CS, Luu MDA, Zhang Y, Trombetta-Lima M, et al. The link between amyloid β and ferroptosis pathway in Alzheimer's disease progression. Cell Death Dis. 2024;15(10):782.

173. Zha X, Liu X, Wei M, Huang H, Cao J, Liu S, et al. Microbiota-derived lysophosphatidylcholine alleviates Alzheimer's disease pathology via suppressing ferroptosis. Cell Metab. 2024;37(1):169–86.

174. Zhu Z yun, Liu Y dong, Gong Y, Jin W, Topchiy E, Turdi S, et al. Mitochondrial aldehyde dehydrogenase (ALDH2) rescues cardiac contractile dysfunction in an APP/PS1 murine model of Alzheimer's disease via inhibition of ACSL4-dependent ferroptosis. Acta Pharmacol Sin. 2022;43(1):39–49.

175. Fusco G, Chen SW, Williamson PTF, Cascella R, Perni M, Jarvis JA, et al. Structural basis of membrane disruption and cellular toxicity by a-synuclein oligomers. Science (80-). 2017;358(6369):1440–3.

176. Zakharov SD, Hulleman JD, Dutseva EA, Antonenko YN, Rochet JC, Cramer WA. Helical α-synuclein forms highly conductive ion channels. Biochemistry. 2007;46(50):14369–79.

177. Song L-M, Xiao Z-X, Zhang N, Yu X-Q, Cui W, Xie J-X, et al. Apoferritin improves motor deficits in MPTP-treated mice by regulating brain iron metabolism and ferroptosis. iScience. 2021;24(5):102431.

178. Tang F, Ping Z, Ling L, Chen K, Xu G. Inhibition of ACSL4 Alleviates Parkinsonism Phenotypes by Reduction of Lipid Reactive Oxygen Species. Neurotherapeutics. 2023;20(4):1154–66.

179. Do Van B, Gouel F, Jonneaux A, Timmerman K, Gelé P, Pétrault M, et al. Ferroptosis, a newly characterized form of cell death in Parkinson's disease that is regulated by PKC. Neurobiol Dis. 2016;94:169–78.

180. Akagawa M, Ishii Y, Ishii T, Shibata T, Yotsu-yamashita M. Metal-Catalyzed Oxidation of Protein-Bound Dopamine. Biochemistry. 2006;45(50):15120–8.

181. Hauser DN, Dukes AA, Mortimer AD, Hastings TG. Dopamine quinone modifies and decreases the abundance of the mitochondrial selenoprotein glutathione peroxidase 4. Free Radic Biol Med. 2013;65:419–27.

182. Sun J, Lin XM, Lu DH, Wang M, Li K, Li SR, et al. Midbrain dopamine oxidation links ubiquitination of glutathione peroxidase 4 to ferroptosis of dopaminergic neurons. J Clin Invest. 2023;133(13):e165228.

183. Angelova PR, Choi ML, Berezhnov A V., Horrocks MH, Hughes CD, De S, et al. Alpha synuclein aggregation drives ferroptosis: an interplay of iron, calcium and lipid peroxidation. Cell Death Differ. 2020;27(10):2781–96.

184. Zhang B, Chen K, Dai Y, Luo X, Xiong Z, Zhang W, et al. Human α-synuclein aggregation activates ferroptosis leading to parvalbumin interneuron degeneration and motor learning impairment. Commun Biol. 2024;7(1):1227.

185. Schriever SC, Zimprich A, Pfuhlmann K, Baumann P, Giesert F, Klaus V, et al. Alterations in neuronal control of body weight and anxiety behavior by glutathione peroxidase 4 deficiency. Neuroscience. 2017;357:241–54.

186. Chen L, Hambright WS, Na R, Ran Q. Ablation of the ferroptosis inhibitor glutathione peroxidase 4 in neurons results in rapid motor neuron degeneration and paralysis. J Biol Chem. 2015;290(47):28097–106.

187. Wang T, Tomas D, Perera ND, Cuic B, Luikinga S, Viden A, et al. Ferroptosis mediates selective motor neuron death in amyotrophic lateral sclerosis. Cell Death Differ. 2022;29(6):1187–98.

188. Lee H, Lee JJ, Park NY, Dubey SK, Kim T, Ruan K, et al. Multi-omic analysis of selectively vulnerable motor neuron subtypes implicates altered lipid metabolism in ALS. Nat Neurosci. 2021;24(12):1673–85.

189. Song S, Su Z, Kon N, Chu B, Li H, Jiang X, et al. ALOX5-mediated ferroptosis acts as a distinct cell death pathway upon oxidative stress in Huntington's disease. Genes Dev. 2023;37(5–6):204–17.

190. Wu X, Deng F, Li Y, Daniels G, Du X, Ren Q, et al. ACSL4 promotes prostate cancer growth, invasion and hormonal resistance. Oncotarget. 2015;6(42):44849–63.

191. Liang YC, Wu CH, Chu JS, Wang CK, Hung LF, Wang YJ, et al. Involvement of fatty acid-CoA ligase 4 in hepatocellular carcinoma growth: Roles of cyclic AMP and p38 mitogen-activated protein kinase. World J Gastroenterol. 2005;11(17):2557–63.

192. Young KS, Mi KP, Su HH, Sun YH, Mi HK, Jung CK, et al. Regulation of cell growth by fatty acid-CoA ligase 4 in human hepatocellular carcinoma cells. Exp Mol Med. 2007;39(4):477–82.

193. Cao Y, Dave KB, Doan TP, Prescott SM. Fatty acid CoA ligase 4 is up-regulated in colon adenocarcinoma. Cancer Res. 2001;61(23):8429–34.

194. Zhang Y, Li S, Li F, Lv C, Yang Q kai. High-fat diet impairs ferroptosis and promotes cancer invasiveness via downregulating tumor suppressor ACSL4 in lung adenocarcinoma. Biol Direct. 2023;16(1):10.

195. Chen WC, Wang CY, Hung YH, Weng TY, Yen MC, Lai MD. Systematic analysis of gene expression alterations and clinical outcomes for long-chain acyl-coenzyme A synthetase family in cancer. PLoS One. 2016;11(5):e0155660.

196. Liu S, Fan S, Wang Y, Chen R, Wang Z, Zhang Y, et al. ACSL4 serves as a novel prognostic biomarker correlated with immune infiltration in Cholangiocarcinoma. BMC Cancer. 2023;23(1):444.

197. Hou J, Jiang C, Wen X, Li C, Xiong S, Yue T, et al. ACSL4 as a Potential Target and Biomarker for Anticancer: From Molecular Mechanisms to Clinical Therapeutics. Front Pharmacol. 2022;13:949863.

198. Sung YK, Hwang SY, Park MK, Bae HI, Kim WH, Kim JC, et al. Fatty acid-CoA ligase 4 is overexpressed in human hepatocellular carcinoma. Cancer Sci. 2003;94(5):421–4.

199. Sun XJ, Xu GL. Overexpression of Acyl-coA ligase 4 (ACSL4) in patients with hepatocellular Carcinoma and its prognosis. Med Sci Monit. 2017;23:4343–50.

200. Chen J, Ding C, Chen Y, Hu W, Lu Y, Wu W, et al. ACSL4 promotes hepatocellular carcinoma progression via c-Myc stability mediated by ERK/FBW7/c-Myc axis. Oncogenesis. 2020;9:42.

201. Chen J, Ding C, Chen Y, Hu W, Yu C, Peng C, et al. ACSL4 reprograms fatty acid metabolism in hepatocellular carcinoma via c-Myc/SREBP1 pathway. Cancer Lett. 2021;502:154–65.

202. Röhrig F, Schulze A. The multifaceted roles of fatty acid synthesis in cancer. Nat Rev Cancer. 2016;16(11):732–49.

203. Li H, Song J, He Y, Liu Y, Liu Z, Sun W, et al. CRISPR/Cas9 Screens Reveal that Hexokinase 2 Enhances Cancer Stemness and Tumorigenicity by Activating the ACSL4-Fatty Acid β-Oxidation Pathway. Adv Sci. 2022;9(21):e2105126.

204. Louandre C, Ezzoukhry Z, Godin C, Barbare JC, Mazière JC, Chauffert B, et al. Iron-dependent cell death of hepatocellular carcinoma cells exposed to sorafenib. Int J Cancer. 2013;133(7):1732–42.

205. Feng J, Lu P zhi, Zhu G zhi, Hooi SC, Wu Y, Huang X wei, et al. ACSL4 is a predictive biomarker of sorafenib sensitivity in hepatocellular carcinoma. Acta Pharmacol Sin. 2021;42(1):160–70.

206. Cao Y, Pearman TA, Zimmerman GA, McIntyre TM, Prescott SM. Intracellular unesterified arachidonic acid signals apoptosis. Proc Natl Acad Sci U S A. 2000;97(21):11280–5.

207. Dai G, Wang D, Ma S, Hong S, Ding K, Tan X, et al. ACSL4 promotes colorectal cancer and is a potential therapeutic target of emodin. Phytomedicine. 2022;102:154149.

208. Sánchez-Martínez R, Cruz-Gil S, de Cedrón MG, Álvarez-Fernández M, Vargas T, Molina S, et al. A link between lipid metabolism and epithelial-mesenchymal transition provides a target for colon cancer therapy. Oncotarget. 2015;6(36):38719–36.

209. Bhattarai S, Saini G, Gogineni K, Aneja R. Quadruple-negative breast cancer: novel implications for a new disease. Breast Cancer Res. 2020;22(1):127.

210. Monaco ME, Creighton CJ, Lee P, Zou X, Topham MK, Stafforini DM. Expression of long-chain fatty Acyl-CoA synthetase 4 in breast and prostate cancers is associated with sex steroid hormone receptor negativity. Transl Oncol. 2010;3(2):91–8.

211. Wu X, Li Y, Wang J, Wen X, Marcus MT, Daniels G, et al. Long Chain Fatty Acyl-CoA Synthetase 4 Is a Biomarker for and Mediator of Hormone Resistance in Human Breast Cancer. PLoS One. 2013;8(10):e77060.

212. Qiu Y, Wang X, Sun Y, Jin T, Tang R, Zhou X, et al. ACSL4-Mediated Membrane Phospholipid Remodeling Induces Integrin b1 Activation to Facilitate Triple-Negative Breast Cancer Metastasis. Cancer Res. 2024;84(11):1856–71.

213. Dattilo MA, Benzo Y, Herrera LM, Prada JG, Castillo AF, Orlando UD, et al. Regulatory mechanisms leading to differential Acyl-CoA synthetase 4 expression in breast cancer cells. Sci Rep. 2019;9(1):10324.

214. Orlando UD, Castillo AF, Medrano MAR, Solano AR, Maloberti PM, Podesta EJ. Acyl-CoA synthetase-4 is implicated in drug resistance in breast cancer cell lines involving the regulation of energy-dependent transporter expression. Biochem Pharmacol. 2019;159:52–63.

215. Maloberti PM, Duarte AB, Orlando UD, Pasqualini ME, Solano AR, Lopez-Otín C, et al. Functional interaction between acyl-coa synthetase 4, lipooxygenases and cyclooxygenase-2 in the aggressive phenotype of breast cancer cells. PLoS One. 2010;5(11):e15540.

216. Sinha A, Saini KK, Kiran T, Khan MA, Satrusal SR, Verma A, et al. ACSL4 activity drives TNBC metastasis by positively regulating Histone H3 Acetylation mediated SNAIL expression. Proc Natl Acad Sci U S A. 2024;121(52):e2408049121.

217. Orlando UD, Garona J, Ripoll G V., Maloberti PM, Solano ÁR, Avagnina A, et al. The functional interaction between acyl-coa synthetase 4, 5-lipooxygenase and cyclooxygenase-2 controls tumor growth: A novel therapeutic target. PLoS One. 2012;7(7):e40794.

218. Sinha A, Saini KK, Chandramouli A, Tripathi K, Khan MA, Satrusal SR, et al. ACSL4-mediated H3K9 and H3K27 hyperacetylation upregulates SNAIL to drive TNBC metastasis. Proc Natl Acad Sci U S A. 2024;121(52):e2408049121.

219. Finetti F, Travelli C, Ercoli J, Colombo G, Buoso E, Trabalzini L. Prostaglandin E2 and cancer: Insight into tumor progression and immunity. Biology (Basel). 2020;9(12):434.

220. Le TK, Duong QH, Baylot V, Fargette C, Baboudjian M, Colleaux L, et al. Castration-Resistant Prostate Cancer: From Uncovered Resistance Mechanisms to Current Treatments. Cancers (Basel). 2023;15(20):5047.

221. Gordon JA, Noble JW, Midha A, Derakhshan F, Wang G, Adomat HH, et al. Upregulation of scavenger receptor B1 is required for steroidogenic and nonsteroidogenic cholesterol metabolism in prostate cancer. Cancer Res. 2019;79(13):3320–31.

222. Wang Y, Hu M, Cao J, Wang F, Han JR, Wu TW, et al. ACSL4 and polyunsaturated lipids support metastatic extravasation and colonization. Cell. 2025;188(2):412–29.

223. Lehmann JM, Moore LB, Smith-Oliver TA, Wilkison WO, Willson TM, Kliewer SA. An antidiabetic thiazolidinedione is a high affinity ligand for peroxisome proliferator-activated receptor γ (PPARγ). J Biol Chem. 1995;270(22):12953–6.

224. Willson TM, Brown PJ, Sternbach DD, Henke BR. The PPARs: From orphan receptors to drug discovery. J Med Chem. 2000;43(4):527–50.

225. Fulgencio JP, Kohl C, Girard J, Pégorier JP. Troglitazone inhibits fatty acid oxidation and esterification, and gluconeogenesis in isolated hepatocytes from starved rats. Diabetes. 1996;45(11):1556–62.

226. Kim JH, Lewin TM, Coleman RA. Expression and characterization of recombinant rat acyl-CoA synthetases 1, 4, and 5: Selective inhibition by triacsin C and thiazolidinediones. J Biol Chem. 2001;276(27):24667–73.

227. Askari B, Kanter JE, Sherrid AM, Golej DL, Bender AT, Liu J, et al. Rosiglitazone inhibits Acyl-CoA synthetase activity and fatty acid partitioning to diacylglycerol and triacylglycerol via a peroxisome proliferator-activated receptor-γ - Independent mechanism in human arterial smooth muscle cells and macrophages. Diabetes. 2007;56(4):1143–52.

228. Varga T, Czimmerer Z, Nagy L. PPARs are a unique set of fatty acid regulated transcription factors controlling both lipid metabolism and inflammation. Biochim Biophys Acta - Mol Basis Dis. 2011;1812(8):1007–22.

229. Duan C, Jiao D, Wang H, Wu Q, Men W, Yan H, et al. Activation of the PPARγ Prevents Ferroptosis-Induced Neuronal Loss in Response to Intracerebral Hemorrhage Through Synergistic Actions With the Nrf2. Front Pharmacol. 2022;13:869300.

230. Xue X, Dai T, Chen J, Xu Y, Yang Z, Huang J, et al. PPARγ activation suppresses chondrocyte ferroptosis through mitophagy in osteoarthritis. J Orthop Surg Res. 2023;18(1):620.

231. Lai W, Yu L, Deng Y. PPARγ alleviates preeclampsia development by regulating lipid metabolism and ferroptosis. Commun Biol. 2024;7(1):429.

232. Zhang S, Wang Y, Gu J, Yang Y, Liang J, Wang Y, et al. PPARγ Antagonists Exhibit Antitumor Effects by Regulating Ferroptosis and Disulfidptosis. Biomolecules. 2024;14(5):596.

233. Liu K, Black RM, Acton JJ, Mosley R, Debenham S, Abola R, et al. Selective PPARγ modulators with improved pharmacological profiles. Bioorganic Med Chem Lett. 2005;15(10):2437–40.

234. S Omura, H Tomoda, Q M Xu, Y Takahashi YI. Triacsins, new inhibitors of acyl-CoA synthetase produced by Streptomyces sp. J Antibiot (Tokyo). 1986;39(9):1211–8.

235. Hiroshi T, Kazuaki I, Satoshi O. Inhibition of acyl-CoA synthetase by triacsins. Biochim Biophys Acta (BBA)/Lipids Lipid Metab. 1987;921(3):595–8.

236. Oh-ishi S, Yamaki K, Abe M, Tomoda H, Omura S. The acyl-CoA synthetase inhibitor triacsin C enhanced eicosanoid release in leukocytes. Jpn J Pharmacol. 1992;59(3):417–8.

237. Pillai VC, Chen YQ, Crumley J, Bazinet RP, Rapoport SI, Weis MT. Triacsin C is a time dependent inhibitor of Long Chain Fatty Acyl CoA Synthetase (Acsl) in endothelial cells. FASEB J. 2008;22(S1):792.12.

238. Del Rio Flores A, Twigg FF, Du Y, Cai W, Aguirre DQ, Sato M, et al. Biosynthesis of triacsin featuring an N-hydroxytriazene pharmacophore. Nat Chem Biol. 2021;17(12):1305–13.

239. Yan W, Wang D, Wan N, Wang S, Shao C, Zhang H, et al. Living Cell-Target Responsive Accessibility Profiling Reveals Silibinin Targeting ACSL4 for Combating Ferroptosis. Anal Chem. 2022;94(43):14820–6.

240. Surai PF. Silymarin as a natural antioxidant: An overview of the current evidence and perspectives. Antioxidants. 2015;4(1):204–47.

241. Ray PP, Islam MA, Islam MS, Han A, Geng P, Aziz MA, et al. A comprehensive evaluation of the therapeutic potential of silibinin: a ray of hope in cancer treatment. Front Pharmacol. 2024;15:1349745.

242. Li S, He Y, Chen K, Sun J, Zhang L, He Y, et al. RSL3 Drives Ferroptosis through NF- κ B Pathway Activation and GPX4 Depletion in Glioblastoma. Oxid Med Cell Longev. 2021;2915019.

243. Su H, Peng C, Liu Y. Regulation of ferroptosis by PI3K/Akt signaling pathway: a promising therapeutic axis in cancer. Front Cell Dev Biol. 2024;12:1372330.

244. Pomel V, Klicic J, Covini D, Church DD, Shaw JP, Roulin K, et al. Furan-2-ylmethylene thiazolidinediones as novel, potent, and selective inhibitors of phosphoinositide 3-kinase γ. J Med Chem. 2006;49(13):3857–71.

245. Baell J, Walters MA. Chemistry: Chemical con artists foil drug discovery. Nature. 2014;513:481–843.

246. Kang Y, Tiziani S, Park G, Kaul M, Paternostro G. Cellular protection using Flt3 and PI3Ka inhibitors demonstrates multiple mechanisms of oxidative glutamate toxicity. Nat Commun. 2014;5:3672.

247. Mognol GP, Ghebremedhin A, Varner JA. Targeting PI3Kγ in cancer. Trends in Cancer. 2025;xx(xx):1–13.

248. Kroker AJ, Bruning JB. Review of the structural and dynamic mechanisms of PPAR γ partial agonism. PPAR Res. 2015;816856.

249. Zheng J, Conrad M. Ferroptosis: when metabolism meets cell death. Physiol Rev. 2024;105(2):651–706.

250. Marteau R, Ravez S, Mazhari Dorooee D, Bouchaoui H, Porte K, Devedjian JC, et al. Repositioning of FDA-Approved antifungal agents to interrogate Acyl-CoA synthetase long chain family member 4 (ACSL4) in ferroptosis. Biochem Pharmacol. 2022;204:115239.

251. Riegman M, Sagie L, Galed C, Levin T, Steinberg N, Dixon SJ, et al. Ferroptosis occurs through an osmotic mechanism and propagates independently of cell rupture. Nat Cell Biol. 2020;22(9):1042–8.

252. Shah R, Shchepinov MS, Pratt DA. Resolving the Role of Lipoxygenases in the Initiation and Execution of Ferroptosis. ACS Cent Sci. 2018;4(3):387–96.

253. Giovanni C. Forcina and Scott J. Dixon. GPX4 at the Crossroads of Lipid Homeostasis and Ferroptosis. Proteomics. 2013;18:e1800311.

254. Lei P, Bai T, Sun Y. Mechanisms of ferroptosis and relations with regulated cell death: A review. Front Physiol. 2019;10:139.

255. Xie Y, Hou W, Song X, Yu Y, Huang J, Sun X, et al. Ferroptosis: Process and function. Cell Death Differ. 2016;23(3):369–79.

256. Li J, Cao F, Yin H liang, Huang Z jian, Lin Z tao, Mao N, et al. Ferroptosis: past, present and future. Cell Death Dis. 2020;11(2):88.

257. Liang C, Zhang X, Yang M, Dong X. Recent Progress in Ferroptosis Inducers for Cancer Therapy. Adv Mater. 2019;31(51):e1904197.

258. Rodriguez R, Schreiber SL, Conrad M. Persister cancer cells: Iron addiction and vulnerability to ferroptosis. Mol Cell. 2022;82(4):728–40.

259. Chen Y, Fan H, Wang S, Tang G, Zhai C, Shen L. Ferroptosis: A Novel Therapeutic Target for Ischemia-Reperfusion Injury. Front Cell Dev Biol. 2021;9:688605.

260. Masaldan S, Bush AI, Devos D, Rolland AS, Moreau C. Striking while the iron is hot: Iron metabolism and ferroptosis in neurodegeneration. Free Radic Biol Med. 2019;133:221–33.

261. Ren JX, Sun X, Yan XL, Guo ZN, Yang Y. Ferroptosis in Neurological Diseases. Front Cell Neurosci. 2020;14:218.

262. Angeli JPF, Shah R, Pratt DA, Conrad M. Ferroptosis Inhibition: Mechanisms and Opportunities. Trends Pharmacol Sci. 2017;38(5):489–98.

263. Santana-Codina N, Gikandi A, Mancias JD. The Role of NCOA4-Mediated Ferritinophagy in Ferroptosis. In: Florez AF, Alborzinia H, editors. Ferroptosis: mechanism and diseases. Cham: Springer Nature Switzerland; 2019. p. 41–57.

264. Kuwata H, Hara S. Role of acyl-CoA synthetase ACSL4 in arachidonic acid metabolism. Prostaglandins Other Lipid Mediat. 2019;144:106363.

265. Cui Y, Zhang Y, Zhao X, Shao L, Liu G, Sun C, et al. ACSL4 exacerbates ischemic stroke by promoting ferroptosis-induced brain injury and neuroinflammation. Brain Behav Immun. 2021;93:312–21.

266. Scholz D, Pöltl D, Genewsky A, Weng M, Waldmann T, Schildknecht S, et al. Rapid, complete and large-scale generation of post-mitotic neurons from the human LUHMES cell line. J Neurochem. 2011;119(5):957–71.

267. Webb MR. A continuous spectrophotometric assay for inorganic phosphate and for measuring phosphate release kinetics in biological systems. Proc Natl Acad Sci U S A. 1992;89(11):4884–7.

268. Shortridge MD, Hage DS, Harbison GS, Powers R. Estimating protein-ligand binding affinity using high-throughput screening by NMR. J Comb Chem. 2008;10(6):948–58.

269. Ganesh AN, Donders EN, Shoichet BK, Shoichet MS. Colloidal aggregation: From screening nuisance to formulation nuance. Nano Today. 2018;19:188–200.

270. Feng BY, Toyama BH, Wille H, Colby DW, Collins SR, May BCH, et al. Small-molecule aggregates inhibit amyloid polymerization. Nat Chem Biol. 2008;4(3):197–9.

271. Feng BY, Shoichet BK. A detergent-based assay for the detection of promiscuous inhibitors. Nat Protoc. 2006;1(2):550–3.

272. Lloyd MD. High-Throughput Screening for the Discovery of Enzyme Inhibitors. J Med Chem. 2020;63(19):10742–72.

273. Zhang XM, Yin M, Zhang MH. Cell-based assays for Parkinson's disease using differentiated human LUHMES cells. Acta Pharmacol Sin. 2014;35(7):945–56.

274. Mahoney-Sanchez L, Bouchaoui H, Boussaad I, Jonneaux A, Timmerman K, Berdeaux O, et al. Alpha synuclein determines ferroptosis sensitivity in dopaminergic neurons via modulation of ether-phospholipid membrane composition. Cell Rep. 2022;40(8):111231.

275. Ghannoum M., Rice L. Antifungal Agents: Mode of Action, Mechanisms of Resistance, and Correlation of These Mechanisms with Bacterial Resistance. Clin Microbiol Rev. 1999;12(4):501–17.

276. Balding PR, Porro CS, McLean KJ, Sutcliffe MJ, Maréchal JD, Munro AW, et al. How do azoles inhibit cytochrome P450 enzymes? A density functional study. J Phys Chem A. 2008;112(50):12911–8.

277. Strushkevich N, Usanov SA, Park HW. Structural basis of human CYP51 inhibition by antifungal azoles. J Mol Biol. 2010;397(4):1067–78.

278. Yamaguchi Y, Akiyoshi T, Kawamura G, Imaoka A, Miyazaki M, Guengerich FP, et al. Comparison of the inhibitory effects of azole antifungals on cytochrome P450 3A4 genetic variants. Drug Metab Pharmacokinet. 2021;38:100384.

279. Röhrig UF, Majjigapu SR, Chambon M, Bron S, Pilotte L, Colau D, et al. Detailed analysis and follow-up studies of a high-throughput screening for indoleamine 2,3-dioxygenase 1 (IDO1) inhibitors. Eur J Med Chem. 2014;84:284–301.

280. Steinhilber D, Jaschonek K, Knospe J, Morof O, Roth HJ. Effects of novel antifungal azole derivatives on the 5-lipoxygenase and cyclooxygenase pathway. Arzneimittelforschung. 1990;40(11):1260–3.

281. Li Y, Pasunooti KK, Li RJ, Liu W, Head SA, Shi WQ, et al. Novel Tetrazole-Containing Analogues of Itraconazole as Potent Antiangiogenic Agents with Reduced Cytochrome P450 3A4 Inhibition. J Med Chem. 2018;61(24):11158–68.

282. Lovering F, Bikker J, Humblet C. Escape from flatland: Increasing saturation as an approach to improving clinical success. J Med Chem. 2009;52(21):6752–6.

283. Jafari R, Almqvist H, Axelsson H, Ignatushchenko M, Lundbäck T, Nordlund P, et al. The cellular thermal shift assay for evaluating drug target interactions in cells. Nat Protoc. 2014;9(9):2100–22.

284. Citarella A, Moi D, Pedrini M, Pérez-Peña H, Pieraccini S, Dimasi A, et al. Synthesis of SARS-CoV-2 Mpro inhibitors bearing a cinnamic ester warhead with in vitro activity against human coronaviruses. Org Biomol Chem. 2023;21(18):3811–24.

285. Jackson PA, Widen JC, Harki DA, Brummond KM. Covalent Modifiers: A Chemical Perspective on the Reactivity of α,β-Unsaturated Carbonyls with Thiols via Hetero-Michael Addition Reactions. J Med Chem. 2017;60(3):839–85.

286. Erlanson DA, Davis BJ, Jahnke W. Fragment-Based Drug Discovery: Advancing Fragments in the Absence of Crystal Structures. Cell Chem Biol. 2019;26(1):9–15.

287. Charnelle E, Gobert A, Marteau R, Pautric M, Renault N, Jonneaux A, et al. Discovery of Potent Acyl-CoA Synthetase Long-Chain Family Member 4 (ACSL4) Inhibitors with Antiferroptotic Properties. J Med Chem. 2025;

288. Vol DDT, May N. Ligand efficiency : a useful metric for lead selection. Drug Discov Today. 2004;9(10):430–1.

289. Robert A. Copeland. Steady-State Kinetics of Single-Substrate Enzyme Reactions. In: ENZYMES: a practical introduction to structure, mechanism and data analysis. 3rd ed. Chennai: Wiley; 2023. p. 125–53.

290. Pesaresi A. Mixed and non-competitive enzyme inhibition: underlying mechanisms and mechanistic irrelevance of the formal two-site model. J Enzyme Inhib Med Chem. 2023;38(1):2245168.

291. Mayer M, Meyer B. Characterization of ligand binding by saturation transfer difference NMR spectroscopy. Angew Chemie - Int Ed. 1999;38(12):1784–8.

292. Banta S, Wheeldon I. Theory-Based Development of Performance Metrics for Comparing Multireactant Enzymes. ACS Catal. 2020;10(2):1123–32.

293. Su D, Kosciuk T, Yang M, Price IR, Lin H. Binding Affinity Determines Substrate Specificity and Enables Discovery of Substrates for N-Myristoyltransferases. ACS Catal. 2021;11(24):14877–83.

294. Carta G, Murru E, Banni S, Manca C. Palmitic acid: Physiological role, metabolism and nutritional implications. Front Physiol. 2017;8:902.

295. Liu Y, Zhang F, Jiang L, Perry JJP, Zhao Z, Liao J. Product inhibition kinetics determinations - Substrate interaction affinity and enzymatic kinetics using one quantitative FRET assay. Int J Biol Macromol. 2021;193(Pt B):1481–7.

296. Pérez R, Matabosch X, Llebaria A, Balboa MA, Balsinde J. Blockade of arachidonic acid incorporation into phospholipids induces apoptosis in U937 promonocytic cells. J Lipid Res. 2006;47(3):484–91.

297. Tallima H, El Ridi R. Arachidonic acid: Physiological roles and potential health benefits – A review. J Adv Res. 2018;11:33–41.

298. Coleman RA. It takes a village: Channeling fatty acid metabolism and triacylglycerol formation via protein interactomes. J Lipid Res. 2019;60(3):490–7.

299. Rodencal J, Dixon SJ. A tale of two lipids: Lipid unsaturation commands ferroptosis sensitivity. Proteomics. 2023;23(6):e2100308.

300. Pande S V. Reversal by CoA of palmityl-CoA inhibition of long chain Acyl-CoA synthetase activity. Biochem Biophys Acta. 1973;306(1):15–20.

301. Pillaiyar T, Meenakshisundaram S, Manickam M, Sankaranarayanan M. A medicinal chemistry perspective of drug repositioning: Recent advances and challenges in drug discovery. Eur J Med Chem. 2020;195:112275.

302. Bakowski MA, Beutler N, Wolff KC, Kirkpatrick MG, Chen E, Nguyen TTH, et al. Drug repurposing screens identify chemical entities for the development of COVID-19 interventions. Nat Commun. 2021;12(1):3309.

303. Buitrago L, Menezes MR, Larson C, Li J, Kartika T, Banerjee P, et al. Unbiased high-throughput screening of drug-repurposing libraries identifies small-molecule inhibitors of clot retraction. Blood Adv. 2025;9(5):1049–68.

304. Johnson TW, Gallego RA, Edwards MP. Lipophilic Efficiency as an Important Metric in Drug Design. J Med Chem. 2018;61(15):6401–20.

305. Rasmussen JT, Rosendal J, Knudsen J. Interaction of acyl-CoA binding protein (ACBP) on processes for which acyl-CoA is a substrate, product or inhibitor. Biochem J. 1993;292(3):907–13.

306. Færgeman NJ, Knudsen J. Role of long-chain fatty acyl-CoA esters in the regulation of metabolism and in cell signalling. Biochem J. 1997;323(1):1–12.

307. Brash AR. Arachidonic acid as a bioactive molecule. J Clin Invest. 2001;107(11):1339–45.

308. Else PL. The highly unnatural fatty acid profile of cells in culture. Prog Lipid Res. 2020;77:101017.

309. Abramson J, Adler J, Dunger J, Evans R, Green T, Pritzel A, et al. Accurate structure prediction of biomolecular interactions with AlphaFold 3. Nature. 2024;630(8016):493–500.

310. Evans R, Neill MO, Pritzel A, Antropova N, Senior A, Green T, et al. Protein complex prediction with AlphaFold-Multimer. bioRxiv. 2022;